Etude de la filamentation d'impulsions laser à haute cadence pour le développement d'un paratonnerre laser

Pierre Walch

INSTITUT POLYTECHNIQUE DE PARIS

ENSTA IP PARIS

NNT : 2022IPPAE022

Thèse de doctorat

Study of high repetition rate laser filamentation for the development of a laser lightning rod

Thèse de doctorat de l'Institut Polytechnique de Paris
Préparée à l'École nationale supérieure de techniques avancées

École doctorale n°626 de l'Institut Polytechnique de Paris
Spécialité de doctorat: Optique, laser et plasma

Thèse présentée et soutenue à Palaiseau, le 29/11/2022, par

Pierre Walch

Composition du Jury :

Pascal Chabert Professeur, LPP, École Polytechnique, France (UMR 7648)	Président
Stelios Tzortzakis Professor, FORTH, University of Crete, Greece	Rapporteur
Julien Labaune Chercheur, ONERA, France	Rapporteur
Jean-Pierre Wolf Professeur, GAP-Biophotonics, Université de Genève, Suisse	Examinateur
Bruno Esmiller Chercheur, ArianeGroup, France	Examinateur
Aurélien Houard Chercheur, LOA, École Polytechnique, France (UMR 7639)	Directeur de thèse
André Mysyrowicz Professeur, LOA, École Polytechnique, France (UMR 7639)	Invité

La passion et les rêves sont comme le temps, rien ne peut les arrêter
et il en sera ainsi tant qu'il y aura des hommes prêts à donner un sens au mot « liberté » !

Remerciements

La filamentation laser, la foudre, la propagation des streamers-leaders, la thermodynamique des décharges, les effets cumulatifs à haut taux de répétition, etc. Tant de sujets sur lesquels j'ai écrit dans ce manuscrit de thèse et c'est maintenant, alors qu'il ne me reste qu'à ajouter les remerciements, que je reste bloqué devant une page blanche.

La physique me semble bien simple d'approche en comparaison de l'exercice d'exprimer mes remerciements envers tous ceux auxquels je suis redevable à la suite de ma thèse… car comme toute bonne histoire, celle-ci compte une abondance de personnages fantastiques. Et pour ce qui est d'une histoire, j'ai le sentiment que ma thèse tient plus d'une épopée ! Épopée qui m'a fait arpenter un long et sinueux chemin côtoyant la félicité, l'émerveillement, la grandeur, la tourmente, l'adversité, la déchéance, et même à de rares moments l'ennui !

Mais qui pourrait s'attendre à moins quand on se choisit pour objectif de contrôler la foudre ? Enfin, assez parlé de moi dans une section de remerciements qui sont justement dévoués aux autres.

Je tiens d'abord à remercier Aurélien Houard, mon directeur de thèse lors de cette longue aventure. Merci d'avoir accepté de répondre à ce premier mail envoyé à 3h du matin pour demander de visiter le labo pour me renseigner sur un stage, demande ayant pour seul argument le fait que «je trouve le concept [du paratonnerre laser] génial ». Merci d'avoir ensuite répondu d'un autre « oui » impassible quand j'ai demandé un fatidique mercredi matin si ce serait possible de continuer et faire une thèse après avoir passé les derniers mois à dire à tout va que je comptais faire autre chose (« oui » que je me suis permis de demander à confirmer le soir en quittant le labo). Merci pour ta bienveillance quand j'ai fait mes premières armes et mes premières erreurs, tout en me faisant rapidement prendre confiance en moi en tant que scientifique. Et surtout, merci encore pour ton indéfectible patience et soutien quand, possiblement après avoir peut-être légèrement trop pris confiance en moi, je m'éloignais trop des sentiers battus, déraillais complètement et partais dans le décor, la limite entre être indépendant et incontrôlable ayant toujours été bien trop flou dans mon esprit. Nous avons formé un duo à la dynamique pour le moins atypique, mais ce fut un plaisir d'avoir réalisé cette thèse avec toi.

Merci à André Mysyrowicz pour les nombreuses discussions scientifiques que nous avons pu avoir tout au long de ma thèse. En y repensant, je me dis que nous aurions dû en avoir encore beaucoup plus car il reste encore de nombreux sujets que nous avions évoqués depuis le début de ma thèse et qui sont toujours pour moi un mystère. Merci pour ton regard éclairé sur ces nombreux sujets et sur ta vision de la recherche que tu as toujours allègrement partagés avec moi.

Merci à Leonid Arantchouk pour les nombreuses expériences que nous avons réalisé ensemble. Nous avons passé bien trop de temps à argumenter entre nous avant de réaliser que nous étions en fait d'accord depuis le début, mais je pense néanmoins que nous formions une bonne paire d'expérimentateurs. Merci d'avoir partagé avec moi ton dévouement sans limite pour la Science, et de m'avoir inculqué le respect qui est nécessaire et dû au domaine de la haute tension.

Merci à Yves-Bernard André pour m'avoir toujours soutenu lors de ma thèse. Je sais que tu refuseras toujours ton titre de « vrai héros de l'histoire », mais tu m'as en bien trop d'occasions sorti de situations difficiles pour que je change d'avis. Merci d'avoir toujours répondu positivement à l'appel quand plus aucune option ne me semblait bonne et qu'il me fallait sortir un joker.

Merci à Benoît Mahieu pour avoir réalisé tant d'expériences avec moi. Comme promis, je fais maintenant une référence à ton enseignement approfondi sur l'utilisation des lasers d'alignement, éléments si importants mais pourtant bien trop souvent négligés dans les montages optiques. Merci

d'avoir toujours été accessible même lorsque je te posais les questions les plus basiques, avais simplement envie de discuter, ou cherchais en urgence quelqu'un pour réaliser une expérience.

Merci à Rostyslav Danylo pour nos nombreux échanges sur « la vie de doctorant dans l'équipe ILM » et bien d'autres sujets. Bien que nos domaines de recherche ne se croisaient que trop rarement, notre quotidien avait tant de similarités qu'il était toujours intéressant d'en discuter pour en souligner les haut et les bas.

Merci à tous les autres membres de l'équipe ILM qui l'on rejoint ou quitté pendant ma thèse, que j'aime appeler « ceux partis trop tôt, arrivés trop tard, ou bien un peu des deux ». Merci à Magali Lozano pour m'avoir épaulé lors de nombreuses expériences et pour avoir supporté nos incessantes digressions avec Leonid. Merci à Laurent Bizet pour avoir accepté de m'aider après avoir été parfois quelque peu parachuté en plein milieu du chaos d'une campagne expérimentale, et quel dommage que nous n'ayons pas pu travailler ensemble sur les manips micro-ondes car nous aurions surement été efficaces. Merci à Sylvain Albert pour avoir toujours été ouvert à la discussion sur à peu près tout et n'importe quoi, même si j'avoue que nous ne parlions que trop rarement de physique. Merci à Celia Millon pour m'avoir toujours fourni une parfaite raison (excuse ?) pour faire une pause aux alentours de 16h30, bien que je ne t'ai que trop souvent partagé ma théorie selon laquelle les crevettes feraient une bien meilleure alternative à la filamentation laser pour produire de la sonoluminescence.

En plus de l'équipe ILM, Je tiens aussi à remercier tous les membres du LOA, laboratoire bien atypique dont l'ambiance conviviale et le doux sentiment de liberté font que l'on se sent rapidement chez soi. Merci à Antoine Rousse pour m'avoir chaleureusement accueilli lorsqu'il était directeur du laboratoire et merci à Stéphane Sebban d'avoir continué avec la même sympathie lorsqu'il lui a succédé. Merci aux membres du secrétariat pour m'avoir aidé à régler bien des problèmes administratifs, avec une intention particulière pour Catherine Buljore et Patricia Toullier que j'ai maintes fois sollicitées lors de mes nombreux départs en mission. Merci à Cédric Thaury avec qui j'ai encadré le modal plasmon de surface, qui a été une des expériences d'enseignements les plus libres et sympathiques que j'ai réalisées.

Au-delà du laboratoire, te tiens à remercier les membres du consortium LLR que j'ai beaucoup côtoyé lors de ma thèse au gré des nombreuses campagnes expérimentales, en particulier les membres du GAP-Biophotonics de Genève, les membres de l'EMC Laboratory à Lausanne, et les membres de Trumpf scientific lasers. Je ne pourrais penser au projet LLR sans penser à des moments et sentiments si marquants tels que l'étrange quiétude des pauses cigarettes au crépuscule d'Ugo Andral avec comme toile de fonds les lumières des villes visibles depuis le mont Säntis, la profonde stupeur quand un éclair a frappé et fait plonger l'environnement éclairé et bien trop bruyant de la tente laser dans un noir total et un silence de mort entrecoupé uniquement par l'appel paniqué de Thomas Produit via mon talkie-walkie, ou bien encore la complète tourmente que j'ai traversée avec Clemens Herkommer quand le laser a décidé de nous lâcher un vendredi à 21h et que nous avons dû décider de passer la nuit à le modifier pour le refaire fonctionner, nuit qui se termina par un départ en avion le lendemain suivi … du début d'un confinement général.

Je remercie Stelios Tzortzakis, Julien Labaune et Pascal Chabert pour avoir accepté d'être respectivement rapporteurs et président pour mon jury de thèse. J'ai tenté de rendre au plus plaisant la lecture de ce manuscrit, mais reste conscient de l'effort qu'ils ont dû fournir pour l'examiner en détail.

Je tiens aussi à remercier tous ceux que j'ai rencontrés lors des activités Doc'union et avec qui j'ai passé de nombreux bons moments. Merci à Cavallone pour nos nombreuses discussions sur le sens de nos vies n'aboutissant malheureusement et surtout heureusement à aucune réponse précise, et pour m'avoir démontré que même une planification parfaite (tâche pour laquelle je suis convaincu de te tenir toujours la dragée haute) ne vaut rien sans une bonne exécution (tâche où précisément tu me bats à plate couture). Merci à Ambra pour nos nombreux échanges et escapades. Moriremo tutti, peut-être, mais il reste beaucoup de choses à faire d'ici là. Merci à Pauline pour avoir toujours été partante pour mes meilleures et bien trop souvent mes pires idées d'activités. Après tous ces

échauffements, je pense que nous sommes enfin prêts pour la Grande Descente du RER B. Merci à Olga pour avoir été toujours l'exemple de la doctorante qui semble toujours pouvoir tout rendre possible. Je me suis souvent inspiré de ton tempérament quand je devais faire des choses qui me semblaient difficiles à réaliser.

Il me faut bien sûr aussi remercier les éminents membres de la Tour Noire sur lesquelles je me suis appuyé lors de ma thèse. Sammael, pour sa présence indéfectible et sa soif inépuisable de physique, bien que nombreux de ces points de vue ne « font pas rêver ». Grodur, pour ses trop nombreuses défections heureusement compensées par de notables et exceptionnelles apparitions, sources d'intarissables questionnements. Marto, dont l'appartenance et objectifs restent encore à définir mais qui a gagné ses lettres de noblesse lors des plus sombres heures du confinement. Merci à vous, car c'est surement grâce à vous que j'ai pu échapper et rester un traitre au désespoir.

Je veux aussi remercier mes amis de toujours, Laurent et Thomas. Ma bêtise ne me fait vous voir que bien trop rarement, mais nos rencontres m'ont toujours permis de faire un bilan et de mettre à plat le déroulement de ma vie qui me semble bien souvent chaotique et hasardeux. Il paraît que chaque année « tout va changer », mais j'ai plutôt l'impression qu'en conséquence rien ne change.

Et bien sûr, j'écris en dernier les remerciements auxquels j'ai pensé en premier et qui me tiennent le plus à cœur, ceux dédiés à ma famille. Merci à ma mère, Claudine, mon père, Gilbert, et mes deux sœurs Anne et Laure. Pour vous, mon quotidien doit être un peu un mystère que je ne partage pas beaucoup, mais je tiens à vous assurer que vous m'accompagnez constamment à travers celui-ci. Merci de me permettre d'avoir toujours un intemporel refuge où tout va pour le mieux dans lequel je peux m'échapper quand le besoin se fait sentir. C'est en pensant à vous que je finis d'écrire ces remerciements, et c'est grave à vous que je suis arrivé là où j'en suis… à écrire des remerciements.

Pierre Walch

Table of contents

Résumé

Mes travaux de thèse présentés dans ce manuscrit ont porté sur l'étude de la filamentation laser à haute cadence dans l'atmosphère pour le développement d'un paratonnerre laser. Ces travaux se sont conclus par l'expérience Laser Lightning Rod sur le Mont Säntis, illustrée en figure 1.

Figure 1 : Photo de l'expérience Laser Lightning Rod, lors de laquelle nous avons utilisé un laser pour guider des éclairs ascendants depuis la tour située au sommet du mont Säntis.

La filamentation laser est un phénomène physique insolite aux nombreuses applications. Quand une impulsion laser intense de durée femtoseconde se propage dans un gaz, elle donne lieu à la filamentation, un processus spectaculaire où une partie de l'énergie du faisceau se contracte pour former un long canal dans lequel l'intensité est maintenue à ~10^{13} W/cm^2. Ce régime de propagation autoguidée s'accompagne de la formation d'une colonne de plasma dans le sillage de l'impulsion laser, comme illustré en figure 2. Il a été montré récemment que cette colonne de plasma évoluait pour former un canal de gaz chaud sous-dense de longue durée de vie. Ce canal sous-dense permet d'envisager des applications telles que le guidage de décharges électriques, le contrôle d'écoulements hydrodynamiques sur des engins supersoniques ou le guidage de faisceaux laser énergétiques.

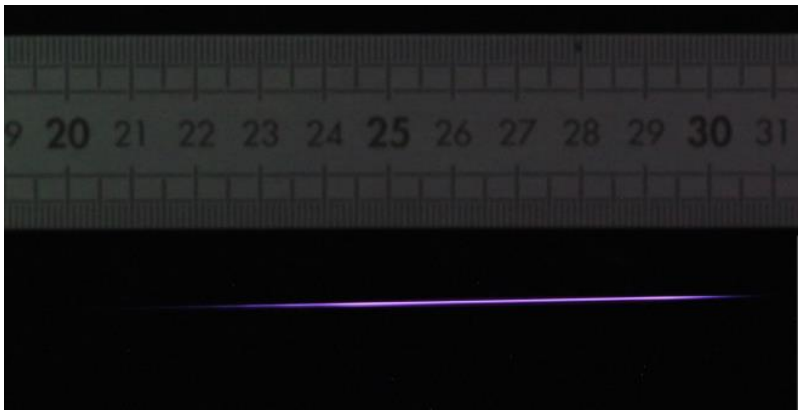

Figure 2 : Photo du premier filament observé lors de ma thèse, créé par une impulsion laser de 2.5 mJ d'énergie, d'une durée de 50 fs à la longueur d'onde de 800 nm. La lumière observée provient de la luminescence du plasma.

J'ai étudié plus particulièrement l'effet de la cadence du laser sur la filamentation et sur le canal sous-dense qui en résulte. J'ai observé que pour des cadences supérieures à 100 Hz chaque impulsion laser créé un canal sous-dense alors que celui créé précédemment est toujours présent. Il en résulte une accumulation du chauffage de plusieurs impulsions laser consécutives. Cet effet cumulatif, qui augmente avec la cadence du laser, donne lieu à la formation d'un canal sous-dense permanent et plus important que celui crée par un unique filament (comme présenté en figure 3). J'ai développé un modèle théorique permettant de décrire l'évolution de chaque canal sous-dense et comment leurs contributions résultent en l'apparition de cet effet cumulatif. La variation de densité induite par filamentation étant responsable de la réduction locale de la tension de claquage de l'air et donc du guidage de décharges électriques par laser, j'ai montré comment cet effet cumulatif pouvait produire un effet de guidage plus efficace à haute cadence. Afin d'expliquer certaines différences entre les mesures et les résultats simulés, j'ai étudié l'importance de la composition du gaz et mis en évidence une amélioration de l'effet de guidage dans l'air due à l'accumulation a haute cadence d'ions de longue durée de vie 0_2^-. Afin de préparer d'éventuelles applications en extérieur, j'ai caractérisé comment un flux d'air transversal pouvait amoindrir voire annuler de faibles effets de répétition et j'ai démontré l'importance de la géométrie de l'expérience en montrant qu'un effet cumulatif bien plus important était présent lorsque les filaments étaient créés verticalement.

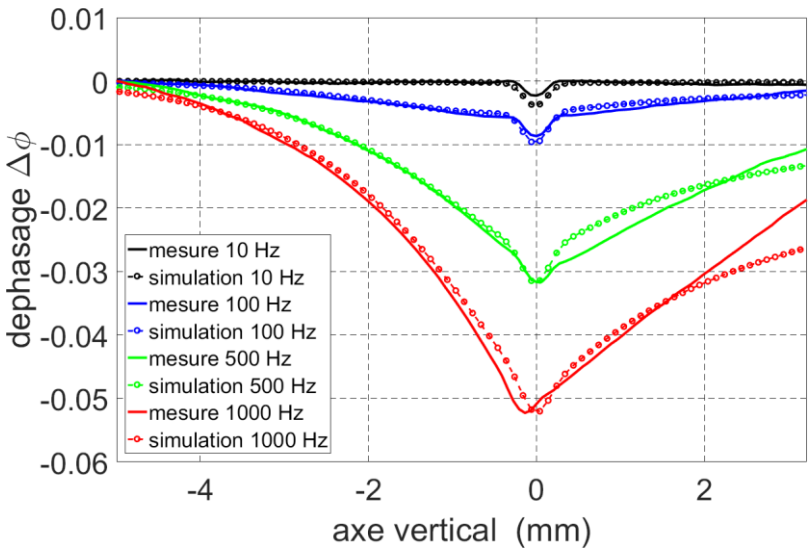

Figure 3 : Mesures du déphasage induit par la variation de densité générée par filamentation laser à différentes cadences. On observe pour des cadences ≥ 100 Hz un déphasage plus grand et présent sur une zone bien plus étendue qu'a 10 Hz, caractéristique d'un canal sous dense plus important.

Un autre aspect des effets de la cadence sur lequel je me suis penché est le guidage à haute cadence de décharges électriques successives dans le but de réaliser une colonne de plasma rectiligne conductrice quasi-continue. Ce travail visait à développer une antenne plasma émettrice dans la gamme radiofréquence. Afin d'arriver à ce but, j'ai tout d'abord étudié comment l'injection de courant supplémentaire dans la décharge guidée pouvait augmenter sa durée de vie. Grâce à l'utilisation d'une source de courant additionnelle, la durée de vie de notre décharge guidée a été augmentée de deux ordres de grandeur jusqu'à durer plusieurs millisecondes. Dans un second temps, j'ai étudié l'interaction entre deux décharges guidées successives séparée de 100 ms. J'ai ainsi observé que la première décharge guidée produisait un chauffage important qui empêchait le guidage

de la seconde décharge, comme présenté en figure 4. J'ai développé un modèle théorique pour expliquer ce phénomène et démontré une solution à ce problème en utilisant un flux d'air permettant d'annuler cet effet.

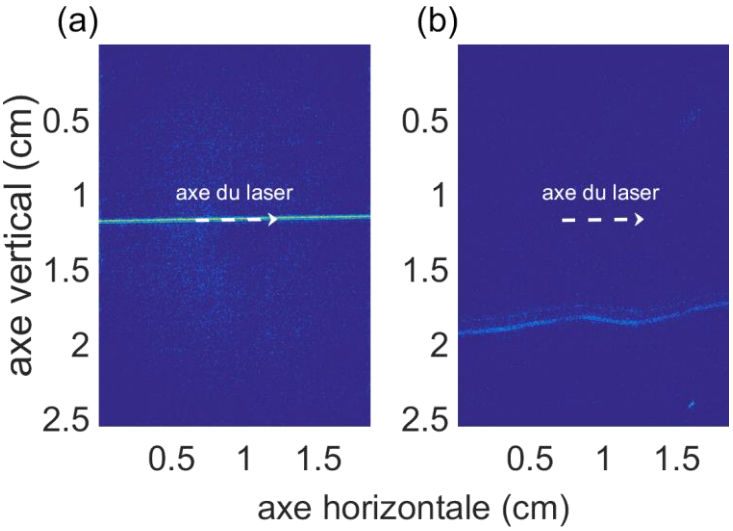

Figure 4 : Mesure par strioscopie du chemin emprunté par deux décharges guidées par laser consécutives réalisées à 10 Hz. La première décharge est guidée et suit le chemin du laser (a) alors que la seconde décharge ne l'est pas et suit un chemin aléatoire (b).

En raison de la large gamme d'énergie des lasers utilisés lors de ma thèse, j'ai observé des différences dans l'efficacité avec laquelle les filaments guident des décharges électriques. Afin d'expliquer ces différences, je me suis intéressé au régime dit de superfilamentation, montrant que focaliser fortement un laser à haute énergie conduit à un dépôt d'énergie accru et un canal sous-dense bien plus important que celui créé par le régime de filamentation régulier, comme présenté en figure 5. J'ai de plus caractérisé comment ce régime de filamentation conduisait à un meilleur guidage des décharges, ces dernières pouvant se propager sur une plus longue distance pour une tension équivalente.

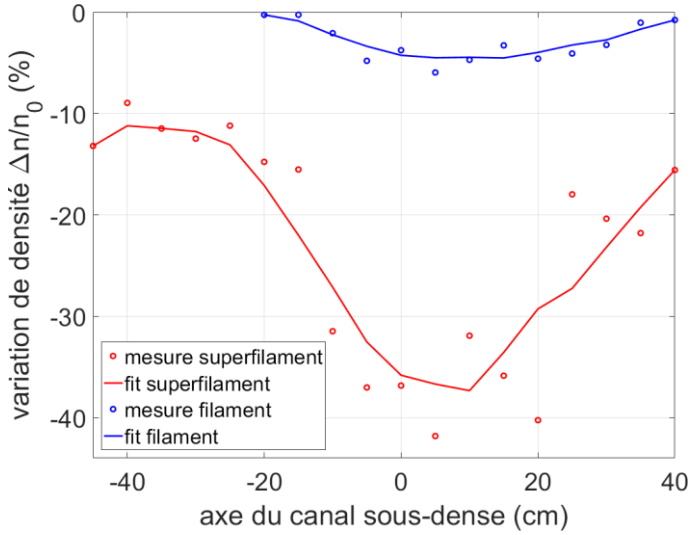

Figure 5 : Comparaison entre la variation de densité le long de l'axe du canal sous-dense résultant d'un superfilament (en rouge) et d'un filament standard (en bleu).

Dans le cadre du projet européen Laser Lightning Rod visant à développer un paratonnerre laser, deux importantes campagnes expérimentales ont été réalisées. La première portait sur la caractérisation de la filamentation à longue distance du laser kW développé lors de ce projet. J'ai caractérisé la répartition spatiale des filaments sur une distance de 140 m avec divers régimes de focalisation du laser, ainsi que leur capacité à guider des décharges électriques. L'observation de filaments créés à une distance de 115 m et s'étendant sur une zone de plus de 30 m a été d'un grand intérêt, car elle nous a permis de définir la configuration utilisée lors de la seconde campagne. Cette dernière visait à démontrer en conditions réelles la capacité des filaments laser à déclencher et guider des éclairs ascendants. Lors des 3 mois d'expérimentations, 16 éclairs ont été observés dont 4 en présence de filaments laser. En se basant sur la caractérisation de la propagation par interférométrie VHF ainsi que sur les vidéos prises par deux caméras ultra-rapides, j'ai montré que le précurseur ascendant de foudre avait été guidé par le laser sur 60 m en 4 occurrences, comme cela est présenté en figure 6. Une étude de la polarité des éclairs et de leur émission de rayons X a aussi mis en évidence un effet significatif lié à l'interaction de la foudre avec les filaments laser.

Figure 6 : Image capturée par une caméra rapide de la propagation d'un des éclairs observés en présence de filaments laser. Une photo prise du même angle de vue que la camera et montrant la trajectoire du laser y est superposée, mettant en évidence le phénomène de guidage.

Foreword

Laser filamentation is a truly fascinating phenomenon. Propagation of light makes us expect that any emitted light will diffract and its intensity will be reduced as it propagates. Moreover, this reduction of the intensity should be even faster for ultra-short laser pulses due to the group velocity dispersion. However, experiments using one of the first amplified femtosecond laser have shown quite the opposite [1]: as the laser was propagating through the air, the beam intensity was progressively increasing. This effect was called self-focusing, and was observed to be followed by another effect called self-guiding, where the laser beam keeps a high intensity while it propagates over long distance. This particular propagation regime is called filamentation, and was rapidly observed over ever-increasing distances from several tens of meters [2] up to kilometers [3], [4].

My thesis is focused on one of the main aspects of the laser filamentation that is the plasma generated in the wake of the laser pulse. As described in Chapter 1, the filament creates a long continuous plasma column. This plasma induces a heating of the medium resulting after the relaxation of the medium in an under-dense channel. Having a lower density, this channel can be used to guide electrical discharge at a voltage lower than the natural breakdown of air. This can have several applications, but the one we will focus on is the use of the laser filamentation to act as a lightning rod [5].

This under-dense channel having a slow evolution, one could imagine that a laser at high repetition rate would lead to an accumulation of the heating produced by multiple pulses. Such accumulation was observed shortly before the beginning of my thesis [6] but a characterization of this effect was required to understand the phenomenon. I present in Chapter 2 the work conducted on this topic, where I developed a density measurement setup allowing to characterize the under-dense channel created by filamentation at different repetition rates. For repetition rates higher than 100 Hz, a cumulative effect was observed leading to the apparition of a larger, permanent, under-dense channel. I developed a model describing the behavior of the under-dense channel during the transition from the single shot filamentation to the filamentation at high repetition rate. I tested the influence of the cumulative effect on the guiding of electrical discharges, showing that higher repetition rates lead to a more efficient guiding. Finally, I investigated the dependencies of this cumulative effect on parameters such as the gas composition, airflow, and verticality/horizontality of the setup.

In Chapter 3 is presented another study related to the repetition rate, devoted to the study of laser guided discharges at high repetition rate. In this case we investigated the possibility of creating a continuous plasma antenna using filament-guided discharges [7], [8]. The first approach that I had studied was to increase the lifetime of a singular discharge by injecting current into it, which successfully increased by several orders of magnitude the lifetime of the discharge. The second approach consisted in guiding consecutive discharges that would tend to create a continuous conductive channel. I observed in this regime an interaction between the consecutive discharges preventing the guiding effect of the subsequent filament. I developed a model of the discharge thermal expansion to describe this phenomenon, and the solution of using an airflow was proved to cancel this interaction.

While all filaments lead to the formation of a plasma, the wide range of lasers used during my thesis, with energy ranging from 0.7 mJ to more than 500 mJ, lead to the creation of different quality of plasma. In Chapter 4 is thus presented the investigation of the superfilamentation, a filamentation regime appearing when both a relatively strong focusing geometry and high laser energy are used [9]. I characterized the luminescence of the plasma as well as the created under-dence channel in this regime, both being more important than in regular filamentation. I then studied how this impact the guiding of an electrical discharge, showing that superfilament lead to longer guided discharges.

Equipped with all this knowledge, I finally present the two main experimental campaigns performed in the frame of the laser lightning rod project. The first campaign, presented in Chapter 5, was focused on the study of the filamentation produced by the J-range, 1 kHz repetition rate, laser system developed for this project. Using various diagnostics, I have characterized the spatial evolution of the filamentation over 140 m in different focusing configurations, as well as the created under-dense channel and its ability to guide electrical discharge. The second campaign that I present in Chapter 6 was a real scale experimental campaign aimed at guiding with our laser ascending lightning from the top of a tower on Mount Säntis in Switzerland. Analyzing the different data collected for the 16 lightning events recorded on the tower, I have shown that the ascending lightning precursor was guided by the laser over 60 m on 4 occurrences. Moreover, Study of the polarity of the lightning flashes and of their X-rays emission also demonstrated an interaction of the filaments with the lightning. These fascinating results are the first successful observations of a laser controlling the propagation of a lightning and will certainly be of major interest for the development of a laser lightning rod technology in the upcoming years.

Bibliography

[1] A. Braun, G. Korn, X. Liu, D. Du, J. Squier, et G. Mourou, « Self-channeling of high-peak-power femtosecond laser pulses in air », *Opt. Lett.*, vol. 20, nº 1, p. 73-75, janv. 1995, doi: 10.1364/OL.20.000073.

[2] E. T. J. Nibbering *et al.*, « Conical emission from self-guided femtosecond pulses in air », *Opt. Lett.*, vol. 21, nº 1, p. 62-64, janv. 1996, doi: 10.1364/OL.21.000062.

[3] G. Méchain *et al.*, « Long-range self-channeling of infrared laser pulses in air: a new propagation regime without ionization », *Appl. Phys. B*, vol. 79, nº 3, p. 379-382, août 2004, doi: 10.1007/s00340-004-1557-8.

[4] M. Durand *et al.*, « Kilometer range filamentation », *Opt. Express*, vol. 21, nº 22, p. 26836-26845, nov. 2013, doi: 10.1364/OE.21.026836.

[5] T. Produit *et al.*, « The laser lightning rod project », *Eur. Phys. J. Appl. Phys.*, vol. 93, nº 1, Art. nº 1, janv. 2021, doi: 10.1051/epjap/2020200243.

[6] A. Houard *et al.*, « Study of filamentation with a high power high repetition rate ps laser at 1.03 μm », *Opt. Express*, vol. 24, nº 7, p. 7437-7448, avr. 2016, doi: 10.1364/OE.24.007437.

[7] T. Dwyer, J. Greig, D. Murphy, J. Perin, R. Pechacek, et M. Raleigh, « On the feasibility of using an atmospheric discharge plasma as an RF antenna », *IEEE Trans. Antennas Propag.*, vol. 32, nº 2, p. 141-146, févr. 1984, doi: 10.1109/TAP.1984.1143275.

[8] F. Théberge, J.-F. Gravel, J.-C. Kieffer, F. Vidal, et M. Châteauneuf, « Broadband and long lifetime plasma-antenna in air initiated by laser-guided discharge », *Appl. Phys. Lett.*, vol. 111, nº 7, p. 073501, août 2017, doi: 10.1063/1.4985045.

[9] G. Point *et al.*, « Superfilamentation in Air », *Phys. Rev. Lett.*, vol. 112, nº 22, p. 223902, juin 2014, doi: 10.1103/PhysRevLett.112.223902.

Chapter 1

Description of the filamentation process, the propagation of electrical discharges, and the resulting filament guided discharges.

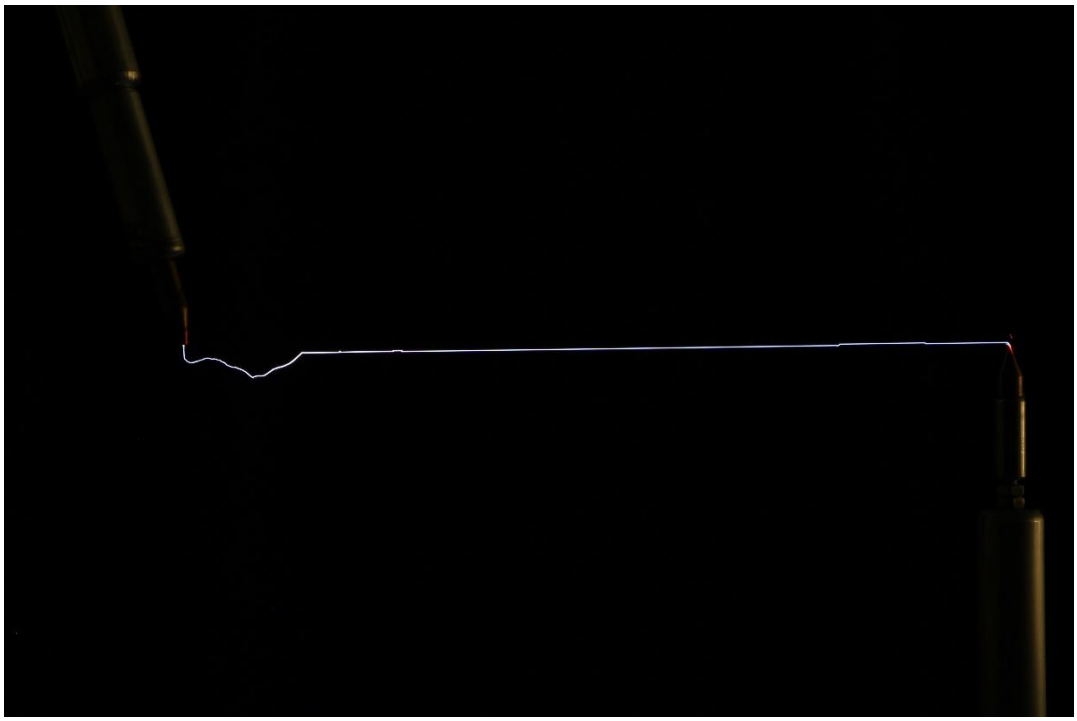

Figure 1: Picture of an electric discharge guided by laser filamentation over 1.4 m.

In this chapter, I will present the fundamental aspects of laser filamentation and electric discharge propagation that are needed to understand the experiments presented in this manuscript.

In the first part, I will focus on describing the propagation of a laser beam in air in the linear and nonlinear regime. In particular, I will explain how the nonlinear effects induce a self-focusing of the beam that will result in the creation of a long plasma column called filament. In a second part, I will present different physical models required to describe the electric discharges that we have encountered during our experiments. In a third part, I will finally analyse the interaction between the filament created by our laser and the electric discharges, to understand the guiding mechanism of discharges.

Table of contents

1 Laser filamentation

To describe the process of laser filamentation, which is a nonlinear propagation effect, I will first describe the propagation of a laser beam in the linear regime, and then use the perturbation theory to add the nonlinear terms.

1.1 Linear propagation of an electromagnetic wave in a transparent medium

In a transparent medium, the propagation of light can be described using the Maxwell's equations:

$$\vec{\nabla}.\vec{D} = \rho, \tag{1.1.1}$$

$$\vec{\nabla}.\vec{B} = 0, \tag{1.1.2}$$

$$\vec{\nabla} \wedge \vec{\mathrm{E}} = -\frac{\partial \vec{B}}{\partial t}, \tag{1.1.3}$$

$$\vec{\nabla} \wedge \vec{\mathrm{H}} = \vec{j} + \frac{\partial \vec{D}}{\partial t}, \tag{1.1.4}$$

with $\vec{D}$ the electric displacement field, $\vec{\mathrm{E}}$ the electric field, $\vec{B}$ the magnetic field, $\vec{H}$ the magnetizing field, ρ the charge density and $\vec{j}$ the electric current density.

The electric displacement field $\vec{D}$ and the magnetic field $\vec{B}$ in a medium can be written as:

$$\vec{D} = \varepsilon_0 \vec{E} + \vec{P}, \tag{1.1.5}$$

$$\vec{B} = \mu_0 \vec{H} + \vec{M}, \tag{1.1.6}$$

with $\vec{P}$ the polarization, $\vec{M}$ the magnetization field, ε_0 the permittivity of free space and μ_0 the permeability of free space.

As long as we stay in the linear regime and make the hypothesis of an isotropic medium, the polarisation $\vec{P}$ and the magnetization field $\vec{M}$ are proportional to the electric field $\vec{E}$ and the magnetizing field $\vec{H}$, respectively, and follow the equations:

$$\vec{P} = \varepsilon_0 \chi^{(1)} \vec{E}, \tag{1.1.7}$$

$$\vec{M} = \chi_m \vec{H}\,, \tag{1.1.8}$$

with $\chi^{(1)}$ the linear electric susceptibility of the medium and $\chi_m$the magnetic susceptibility of the medium (note that for a non-isotropic medium, both susceptibilities are no longer scalars but second order tensors).

We can then formulate the equations (1.1.5) and (1.1.6) as:

$$\vec{D} = \varepsilon_0 \varepsilon_m \vec{E}\,, \tag{1.1.9}$$

$$\vec{B} = \mu_0 \mu_m \vec{H}, \tag{1.1.10}$$

with ε_m the permittivity of the medium and μ_m the permeability of the medium, described as:

$$\varepsilon_m = 1 + \chi^{(1)}, \tag{1.1.11}$$

$$\mu_m = 1 + \chi_m. \tag{1.1.12}$$

We will now calculate the equation of propagation of a monochromatic plane wave in a non-magnetic medium ($\mu_m = 1$) without any accumulated charge ($\rho = 0$) and current ($\vec{j} = 0$). Given the monochromatic plane wave we are using, the equation (1.1.3) and (1.1.4) can be written as a function of the wave vector $\vec{\mathrm{k}}$:

$$i\vec{k} \wedge \vec{E} = i\omega\vec{B}, \tag{1.1.13}$$

$$\frac{i\vec{k} \wedge \vec{B}}{\mu_0\mu_m} = -i\omega\varepsilon_0\varepsilon_m\vec{E}. \tag{1.1.14}$$

To calculate the equation of propagation in the medium, we will use the following formula that is true for any vector $\vec{X}$:

$$\vec{\nabla} \wedge \left(\vec{\nabla} \wedge \vec{X}\right) = \overrightarrow{\text{grad}}\left(\vec{\nabla}.\vec{X}\right) - \vec{\Delta}\left(\vec{X}\right), \tag{1.1.15}$$

and apply it to the vector $\vec{E}$:

$$i\vec{k} \wedge \left(i\vec{k} \wedge \left(\vec{E}\right)\right) = \overrightarrow{\text{grad}}\left(\vec{\nabla}.\vec{E}\right) - \vec{\Delta}\left(\vec{E}\right). \tag{1.1.16}$$

Moreover, $i\vec{k} \wedge \vec{E} = i\omega\vec{B}$ and $\vec{\nabla}.\vec{E} = 0$ due to the absence of charge:

$$i\vec{k} \wedge \left(i\omega\vec{B}\right) = -i\vec{k} \wedge \left(i\vec{k} \wedge \vec{E}\right). \tag{1.1.17}$$

Using (1.1.14), we can write:

$$i\vec{k} \wedge \left(-i\omega\varepsilon_0\varepsilon_m\mu_0\mu_m\vec{E}\right) = -i\vec{k} \wedge \left(i\vec{k} \wedge \vec{E}\right). \tag{1.1.18}$$

By identification, we now have the following equation of propagation:

$$k^2 = v^2\omega^2, \tag{1.1.19}$$

with v the propagation speed of the wave written as:

$$v = \frac{1}{\sqrt{\varepsilon_0\varepsilon_m\mu_0\mu_m}} = \frac{c}{\sqrt{\varepsilon_m\mu_m}} = \frac{c}{\sqrt{\varepsilon_m}}. \tag{1.1.20}$$

Using this expression, we can calculate the optical index of the medium in the linear propagation regime:

$$n_0 = \frac{c}{v} = \sqrt{\varepsilon_m} = \sqrt{1 + \chi^{(1)}}. \tag{1.1.21}$$

1.2 Nonlinear propagation of an electromagnetic wave in a transparent medium

The previous description of the propagation of the wave was done in a linear regime. However, in the case of the propagation of high intensity laser pulses, this description is not sufficient and nonlinear effects should be taken into account. We now introduce the intensity of the laser field I, described as:

$$I = \frac{c\varepsilon_0 n_0}{2} < \left|\vec{E}\right|^2 >. \tag{1.2.1}$$

If the value of I is too high, the equation (1.1.7) is no longer valid and should be replaced by:

$$\vec{P} = \varepsilon_0(\chi^{(1)}\vec{E} + \chi^{(2)}\vec{E}^2 + \chi^{(3)}\vec{E}^3 + \cdots), \tag{1.2.2}$$

with $\chi^{(n)}$ the electric susceptibility of the order n. For a centrosymmetric medium, all the even terms are null ($\forall n \in N, \chi^{2n} = 0$), giving:

$$\vec{P} = \varepsilon_0(\chi^{(1)}\vec{E} + \chi^{(3)}\vec{E}^3 + \cdots). \tag{1.2.3}$$

If we take a first approximation considering terms up to the third order and a field $\vec{E} = \overrightarrow{E_0}\cos(\omega t)$ we can write:

$$\vec{P} = \varepsilon_0(\chi^{(1)}\vec{E} + \chi^{(3)}\overrightarrow{E_0}\left|\overrightarrow{E_0}\right|^2(\cos(\omega t)^3)$$

$$= \varepsilon_0(\chi^{(1)}\vec{E} + \chi^{(3)}\overrightarrow{E_0}\left|\overrightarrow{E_0}\right|^2\frac{1}{4}(3\cos(\omega t) + \cos(3\omega t))$$

$$\approx \varepsilon_0(\chi^{(1)}\vec{E} + \chi^{(3)}\overrightarrow{E_0}\left|\overrightarrow{E_0}\right|^2 \frac{1}{4}(3\cos(\omega t))$$

$$\rightarrow \vec{P} = \varepsilon_0(\chi^{(1)} + \frac{3}{4}\chi^{(3)}\left|\overrightarrow{E_0}\right|^2)\vec{E}. \quad (1.2.4)$$

Using the same steps of calculation as in the linear regime, we can retrieve the expression of the optical index in the nonlinear regime:

$$n = \sqrt{1 + \chi^{(1)} + \frac{3}{4}\chi^{(3)}\left|\overrightarrow{E_0}\right|^2} \approx n_0 + n_2 I, \quad (1.2.5)$$

with n_0 the linear refractive index and n_2 the nonlinear index described as:

$$n_2 = \frac{3\chi^{(3)}}{4\, {n_0}^2 c\varepsilon_0}. \quad (1.2.6)$$

With the equation (1.2.5), we see that the intensity of the electromagnetic wave will modify the optical index of the medium: this is what we call the Kerr effect. To give an order of magnitude, the value of n_2 of air is ~3.2×10^{-19} cm^2/W for a laser at 800 nm. This low value of n_2, compared to n_0, explains why a high intensity is required to observe a substantial difference in the propagation in air. As a comparison, the value of n_2 of fused silica is ~2.2×10^{-16} cm^2/W, providing a significant Kerr effect at lower peak power, of the order of several MW [1].

1.3 Self-focusing of intense laser beam

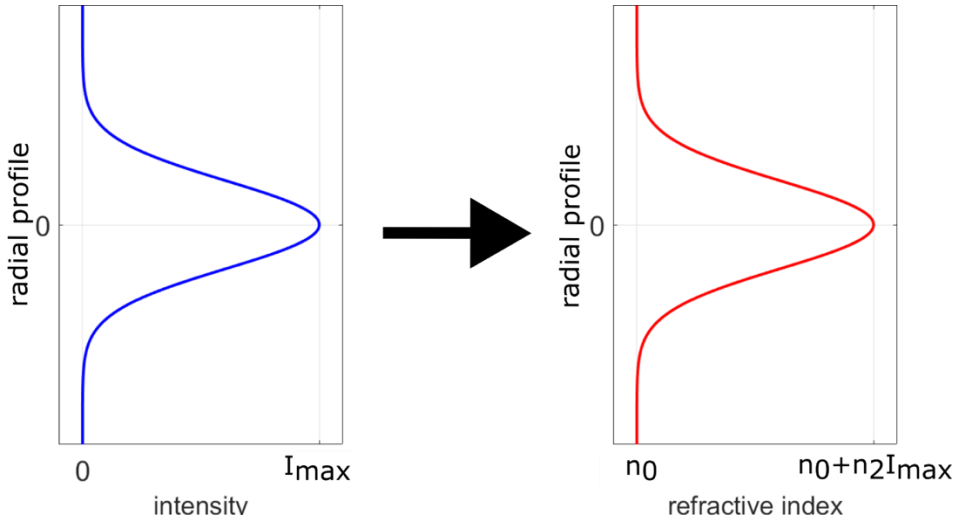

Figure 1.3.1: Schematic of the relation between the beam intensity profile and the profile of the refractive index of the medium.

One important consequence of the Kerr effect is the self-focusing of intense laser beams as they propagate. If we consider a typical laser beam, its radial intensity profile is non-constant and will be more intense at the center of the beam. Using equation (1.2.5), we can see that this intensity profile will result in an optical index profile with a higher value in the centre than at the edge of the beam, as described in figure 1.3.1. This index profile is similar to a lens; as such, the medium will behave as a converging lens for the beam as it propagates. This self-focusing effect has a snowball characteristic: as the pulse propagates, it is focused leading to a higher intensity, that then leads to a higher Kerr effect and thus a stronger focusing, etc. This phenomenon leads to a catastrophic collapse if not stopped from any other counteracting phenomenon.

This Kerr self-focusing effect should be compared to its linear counterpart, the diffraction. Due to the finite size of the laser source, the beam is subject to diffraction and will diverge. If we consider a Gaussian beam of a wavelength λ_0 and an initial diameter l_0, its diameter l after propagating over a distance z will be:

$$l = l_0 \sqrt{1 + \left(\frac{z}{L_r}\right)^2}, \tag{1.3.1}$$

with $L_r = \frac{\pi \times {l_0}^2}{\lambda_0}$ the Rayleigh length, characteristic length after which the beam diameter has increased by a ratio of $\sqrt{2}$.

We can then identify a limit between the competition of these two effects that is called the critical power for self-focusing P_{cr}. For a beam with a power lower than P_{cr}, the diffraction will dominate and the beam will continuously diverge. However, for a beam power higher than P_{cr}, the Kerr self-focusing will dominate diffraction and the beam will self-focus as it propagates. The expression of this critical power for a Gaussian beam at a wavelength λ_0 is given by [2]:

$$P_{cr} = \frac{3.77 \times {\lambda_0}^2}{8\pi \times n_0 \times n_2}. \tag{1.3.2}$$

Considering a beam with a power higher than P_{cr}, it will therefore self-focus in the snowballing effect described earlier and converge toward a point of infinite intensity (in theory). The distance of propagation L_c needed for a beam of power P_0 to reach this point is described by the semi-empirical formula derived by Marburger [3]:

$$L_c = \frac{0.367 \times L_r}{\sqrt{\left(\sqrt{\frac{P_0}{P_{cr}}} - 0.852\right)^2 - 0.0219}}. \tag{1.3.3}$$

The apparition of this singularity of infinite intensity, while predicted, is not physical and never observed. This is due to new processes induced by the increasing intensity that will hinder its apparition. These processes will be discussed in the next section.

1.4 Beam collapse and plasma creation

The main effect that will take place to hinder the collapse of the beam is the ionization of the medium by the laser field that happens at high intensity. This ionization is mainly due to two processes: multiphoton ionization and tunnel ionization.

Multiphoton ionization happens when the absorption of several photons is required for a bound electron to reach an energy state sufficient to escape from the barrier of Coulomb potential to become a free electron. The probability of multiphoton ionization p is given by:

$$p = \sigma_k \times I^k, \tag{1.4.1}$$

with σ_k the ionization cross section, I the laser intensity and k the order of the ionization. As an example, the order of ionization for the molecules O_2 and N_2 are respectively 8 and 11 for a wavelength of 800 nm.

Tunnel ionization is an effect appearing at even higher intensity. In these conditions, the laser electric field is high enough to lower the barrier of Coulomb potential, thus allowing a bound electron to cross it by tunnel effect.

Another process can be taken into account: the avalanche ionization. In this process, a free electron already present in the medium is accelerated by the laser electric field. Through this acceleration, the electron can gain kinetic energy and transfer it to a molecule by collision to liberate a new free electron. The two electrons will then repeat this cycle, creating each time more electrons. This process, while effective, need time on the order of picoseconds to create a significant number of free electrons. For laser pulses with femtosecond duration, it is therefore considered as negligible.

The presence of free electrons in the ionized medium will contribute to change its index. A simple model to apprehend this change is the free electron model. We consider a free electron detached from its parent ion, with no interaction with other electrons, in a medium where ions are stationary and without any effect of crystalline structure. In the presence of an external electric field $\vec{E} = \overrightarrow{E_0}\cos(\omega t)$, the spatial position $\vec{x}$ of the electron will follow the equation:

$$m_e \frac{d^2\vec{x}}{dt^2} = -e\overrightarrow{E_0}\cos(\omega t), \tag{1.4.2}$$

with $m_e$the electron mass and e the elementary charge. The solution of this equation reads:

$$\vec{x} = \frac{1}{\omega^2}\frac{e\vec{E}}{m_e}. \tag{1.4.3}$$

By definition, the linear polarization $\vec{P}$ is the average dipolar moment per unit volume:

$$\vec{P} = \frac{d\vec{p}}{dV} = -en_e\vec{x} = -\frac{e^2 n_e}{m_e\omega^2}\vec{E}, \tag{1.4.4}$$

with n_e the free electron density. Using equation (1.1.7) and (1.1.21), we can express the refractive index of the plasma of free electrons as

$$n_{plasma} = \sqrt{1 - \frac{e^2 n_e}{m_e\varepsilon_0}\frac{1}{\omega^2}} = \sqrt{1 - \frac{{\omega_p}^2}{\omega^2}} \approx 1 - \frac{1}{2}\frac{e^2 n_e}{m_e\varepsilon_0}\frac{1}{\omega^2} = 1 - \frac{1}{2}\frac{{\omega_p}^2}{\omega^2}, \tag{1.4.5}$$

with $\omega_p$the plasma frequency defined as

$$\omega_p = \sqrt{\frac{e^2 n_e}{m_e\varepsilon_0}}, \tag{1.4.6}$$

Another common way to express equation (1.4.5) is:

$$n_{plasma} = 1 - \frac{1}{2}\frac{n_e}{n_c}, \tag{1.4.7}$$

with n_c the critical electron density at which the plasma is reflective at the wavelength $\lambda = 2\pi\ c/\omega$, given by:

$$n_c = \frac{m_e\varepsilon_0}{e^2}\omega^2. \tag{1.4.8}$$

If again we take into consideration a typical laser beam, its radial intensity profile is non-constant and will be more intense at the center of the beam. The effects of ionisation being dependant on the intensity, they will be more important at the beam center, thus creating more electrons on the beam centre than on its edges. Using equation (1.4.7), we can see that this will lead to a reduction of the optical index due to the higher electron density at the centre of the beam. The plasma will thus act as a diverging lens. This effect, being increasingly more important as the intensity increases, will counteract the self-focusing and prevent the apparition of the singularity of infinite intensity.

1.5 The filamentation propagation regime

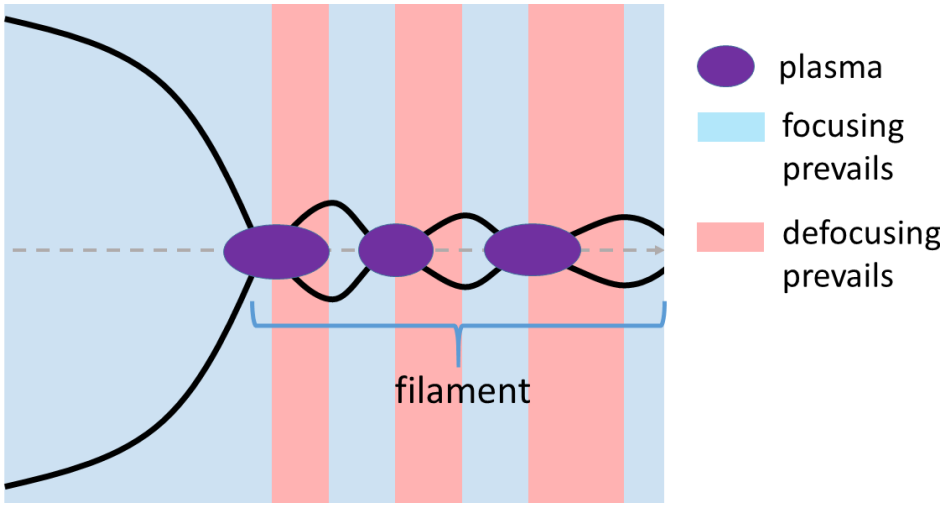

Figure 1.5.1: Scheme of the dynamic competition between the focusing and the defocusing in the filamentation regime.

Based on the previous section, we can see that during the propagation of a high power laser beam, a competition will be established between three effects: the diffraction, the Kerr self-focusing and the plasma defocusing. One important aspect of this competition is its equilibrium. While the initial competition between the Kerr self-focusing and the diffraction can be described by a power threshold, over which Kerr effect will dominate, the competition of these three effects is a dynamic process. A simplified way to understand it is as follows: in the initial stage, the beam intensity is too low to ionize the air and the self-focusing dominates, increasing progressively the intensity. At a certain point, the intensity is high enough to create a plasma, which induces plasma defocusing overcoming the Kerr self-focusing, thus decreasing the intensity. The intensity having decreased, the self-focusing will then take the lead, and refocus the beam a second time, etc... These cycles can be repeated over a long distance, as described in figure 1.5.1. It results in the formation of a thin light channel of high intensity that keeps a constant diameter of about 100 µm over a long distance, leaving in the wake of the pulse a long and weakly ionized plasma column: this propagation regime is called the filamentation regime [4].

Figure 1.5.2: Picture of the first filament observed during my thesis with a laser pulse of 2.5 mJ and a pulse duration of 50 fs @ 800 nm.

One should note that in reality, there is no alternation between zones with and without plasma and the competition reaches a quasi-equilibrium between the three effects with only slight evolutions

of the plasma densities. This result in a continuous plasma column, as seen in the picture presented in figure 1.5.2.

While numerical simulations have shown that filamentation is a complex dynamic competition, a very simplified model, where diffraction and plasma defocusing are continuously balanced by Kerr effect can be used to estimate the laser intensity in the filament, as described in [4]. For a Gaussian beam at a wavelength λ_0, this translates in the equality:

$$n_2 I - \frac{1}{2}\frac{n_e}{n_c} - \frac{(1.22\,\lambda_0)^2}{8\pi\, n_0\, {\omega_0}^2} = 0. \qquad (1.5.1)$$

As an example, if we take a laser pulse at 800 nm, with a pulse duration of 100 fs and a power of the order of the critical power, this equality gives the following values: a peak intensity of 1.6×10^{13}W/cm^2, a free electron density of 7×10^{15}cm^{-3}, and a filament diameter of 110 µm. All of these values are in good agreement with experimental measurements.

1.6 Multifilamentation

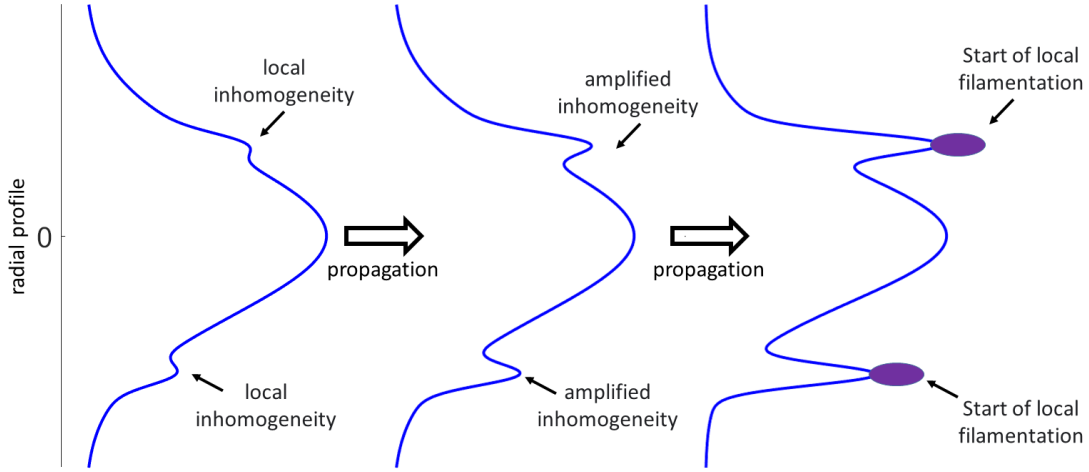

Figure 1.6.1: Scheme of the amplification of random local inhomogeneities as a laser beam of several critical powers propagates, leading to the creation of multiple filaments.

In the case of the propagation of a laser beam with a power largely exceeding the critical power P_{cr}, we can observe the creation of multiple filaments. Their creation can result from several effects, but the main phenomena is called the modulation instability [5]. This effect describes the amplification by the Kerr effect of the beam profile inhomogeneities during the beam propagation (see figure 1.6.1). Each of these inhomogeneities can result in a filament.

While this effect leads to a random distribution of multiple filaments when the inhomogeneities are produced by random noise, it is possible to control their creation by modulating the intensity or the phase of the initial beam profile, as an example by using an amplitude mask [6] or a phase mask. After their creation, each of these filaments can interact with each other, as they can attract, repel each other and even fuse together [7]–[9].

2 Electrical discharge propagation: Townsend discharge, streamer and leader

In this thesis, I will study the interaction between laser filaments and electrical discharges. Therefore, I will describe in this section the main model of discharge formation that we will encounter in our experiments.

2.1 Townsend discharges

The oldest model describing the formation of electrical discharge, which dates from the beginning of the 20th century, is called the Townsend discharge or Townsend avalanche. In this model, we consider the medium between two electrodes charged at a potential difference U and separated by a distance d, where a constant electric field E is generated by the electrodes. Initially, we neglect the phenomena of recombination and electronic attachment that may occur in the medium.

The few electrons naturally present in this medium, called seed electrons and coming mostly from ionization by cosmic radiation, will be accelerated by the electric field towards the cathode. They gradually gain kinetic energy before interacting with the molecules of the medium through collisions. If their acquired energy is sufficient to ionize, collision with a molecule will then result in two low-energy electrons, which will in turn be accelerated by the electric field. The number of free electrons therefore doubles at each cycle, resulting in an avalanche of electrons and a complete ionization of the medium, leading to the discharge.

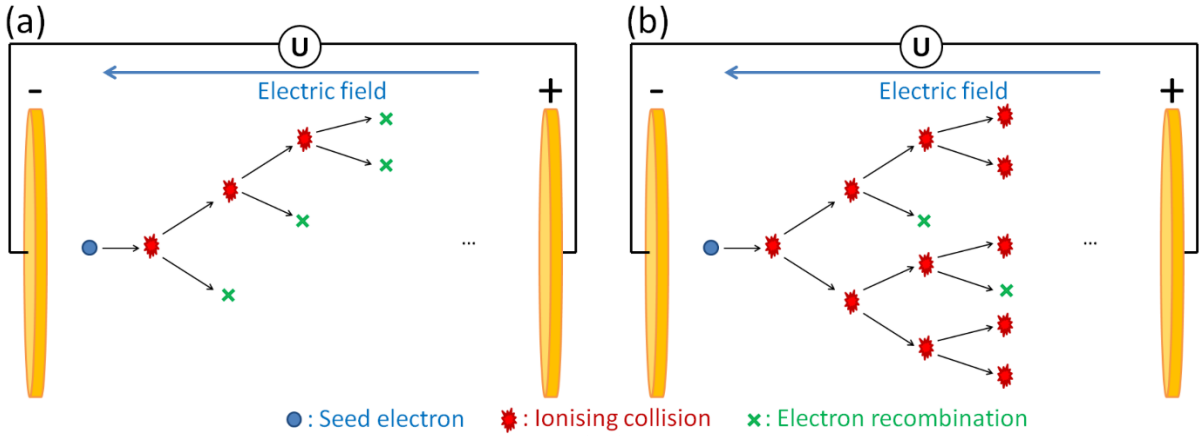

Figure 2.1.1: Scheme of a Townsend avalanche in the case of (a) dominant electron recombination/capture and (b) of dominant electron production.

If we now take into account the processes of recombination and electronic attachment, some of these electrons will disappear from the medium instead of carrying out ionization. To predict the evolution of the medium, we must then compare the number of electrons produced by avalanche per unit of length G to the number of recombined/captured electrons per unit of length P. If P is greater than G, nothing happens in the medium, since free electrons are disappearing faster that they are created (see figure 2.1.1 (a)). On the contrary, if G is larger than P, the number of free electrons increases during each cycle, leading to the discharge as presented in figure 2.1.1 (b).

From the Townsend avalanche model, we can derive an expression of the voltage necessary to initiate the discharge, called breakdown voltage. This expression is called the Paschen law. Again, we consider two charged plane electrodes separated by a distance d, inducing between them a constant electric field E. We make the hypothesis that the electrons accelerated by the electric field

create other electrons by collision as they progress through the gap with a linear efficiency α, and no recombination/capture occurs, giving us the following equation governing the electron density n_e:

$$\frac{dn_e}{dx} = \alpha \times n_e, \tag{2.1.1}$$

$$\rightarrow n_e = n_e(0) \times e^{\alpha x}. \tag{2.1.2}$$

The same collisions that increase the electron density increase at the same time the ion density n_i. The total quantity of ions arriving to the cathode is equal to the number of electrons created in the medium:

$$n_i(0) = n_e(0) \times (e^{\alpha d} - 1). \tag{2.1.3}$$

Furthermore, the number of electrons at the cathode is not zero and is equal to the number of electrons that are created by the ions hitting the cathode, with a proficiency coefficient γ. This gives us the relation:

$$n_e(0) = \gamma \times n_i(0) \tag{2.1.4}$$

Using equations (2.1.3) and (2.1.4), we now obtain an equality that must be verified to have a continuous current established between the electrodes:

$$e^{\alpha d} - 1 = \frac{1}{\gamma} \tag{2.1.5}$$

$$\rightarrow \alpha d = \ln\left(1 + \frac{1}{\gamma}\right). \tag{2.1.6}$$

We can then specify the expression of the linear efficiency of the creation of electrons α. If we consider σ the cross section of collision between the electrons and the atoms/molecules of the gas medium with density n_{gas}, the mean free path λ of the electrons is:

$$\lambda = \frac{1}{n_{gaz} \times \sigma}. \tag{2.1.7}$$

The proportion p of electrons with a free displacement distance l is then:

$$p = e^{-\frac{l}{\lambda}} = e^{-n_{gaz} \times \sigma \times l}. \tag{2.1.8}$$

Through acceleration over this distance l by the electric field E, a free electron will acquire a kinetic energy $\mathrm{l} \times e \times E$. The proportion p_i of electrons with an energy higher or equal to the ionization energy $E_{ionization}$ of the molecule is given by:

$$p_i = e^{-n_{gaz} \times \sigma \times \frac{E_{ionization}}{e \times E}}. \tag{2.1.9}$$

Using this expression, we can write α as

$$\alpha = n_{gaz} \times \sigma \times e^{-n_{gaz} \times \sigma \times \frac{E_{ionization}}{e \times E}}, \tag{2.1.10}$$

and rewrite the equation (2.1.6) as

$$d \times n_{gaz} \times \sigma \times e^{-n_{gaz} \times \sigma \times \frac{E_{ionization}}{e \times E}} = \ln\left(1 + \frac{1}{\gamma}\right). \tag{2.1.11}$$

We can introduce the voltage between the electrodes $U = d \times E$, and isolate it in equation (2.1.11), resulting in the general from of the Paschen law:

$$U = \frac{d \times n_{gaz} \times \sigma \times \frac{E_{ionization}}{e \times E}}{\ln(d \times n_{gaz} \times \sigma) - \ln\left(\ln\left(1 + \frac{1}{\gamma}\right)\right)}. \tag{2.1.12}$$

It is important to note that generally, the Paschen law is written as a function of the product $p \times d$, with p the gas pressure, but I choose to express it as a function of the product of $n_{gaz} \times d$ because all the measurements of this thesis were done at a constant pressure but with a varying gas density.

The limit for the breakdown ignition can be conceived as the condition where any electron from the cathode ionizes at least one atom during its propagation toward the anode over the distance d, which can be written as:

$$\alpha \times d \geq 1. \tag{2.1.13}$$

The lower limit $\alpha \times d = 1$, gives us the expression of the breakdown voltage U_{bd}:

$$U_{bd} = \frac{d \times n_{gaz} \times \sigma \times \frac{E_{ionization}}{e \times E}}{\ln\left(d \times n_{gaz} \times \sigma\right)}. \tag{2.1.14}$$

Once again, we can consider that recombination/capture occurs in the system with a linear efficiency depending on the gas density $\delta\left(n_{gaz}\right)$ (it depends on other parameters, but they remain constant in our experiments). This changes the equation (2.1.1) into

$$\frac{dn_e}{dx} = \alpha \times n_e - \delta \times n_e. \tag{2.1.15}$$

$$\rightarrow n_e = n_e(0) \times e^{\alpha \times x - \delta \times x}, \tag{2.1.16}$$

resulting in changing equation (2.1.12) into

$$U = \frac{d \times n_{gaz} \times \sigma \times \frac{E_{ionization}}{e \times E}}{\ln\left(d \times n_{gaz} \times \sigma\right) - \ln\left(\ln\left(1 + \frac{1}{\gamma}\right) + \delta \times d\right)}. \tag{2.1.17}$$

2.2 Streamer discharges

The previous model of the Townsend discharge is useful to get a first approach of discharge propagation. However, in the beginning of the 20th century, experimental observations such as the formation time of short discharges at atmospheric pressure, the weak influence of the cathode material (and thus of γ) or the lower breakdown field measured, have shown that this model cannot describe accurately discharge occurring at high pressure over long gaps. The validity of the Townsend discharge was established for values of pressure times gap length down to 0.13 atm.cm (100 mmHg.cm). In 1940, a new model of discharge was then described: the streamer discharge [10]. It can be summarized as follows:

We consider two electrodes charged at a potential difference U separated by a distance d in an asymmetrical configuration, creating an inhomogeneous electric field locally stronger near the cathode.

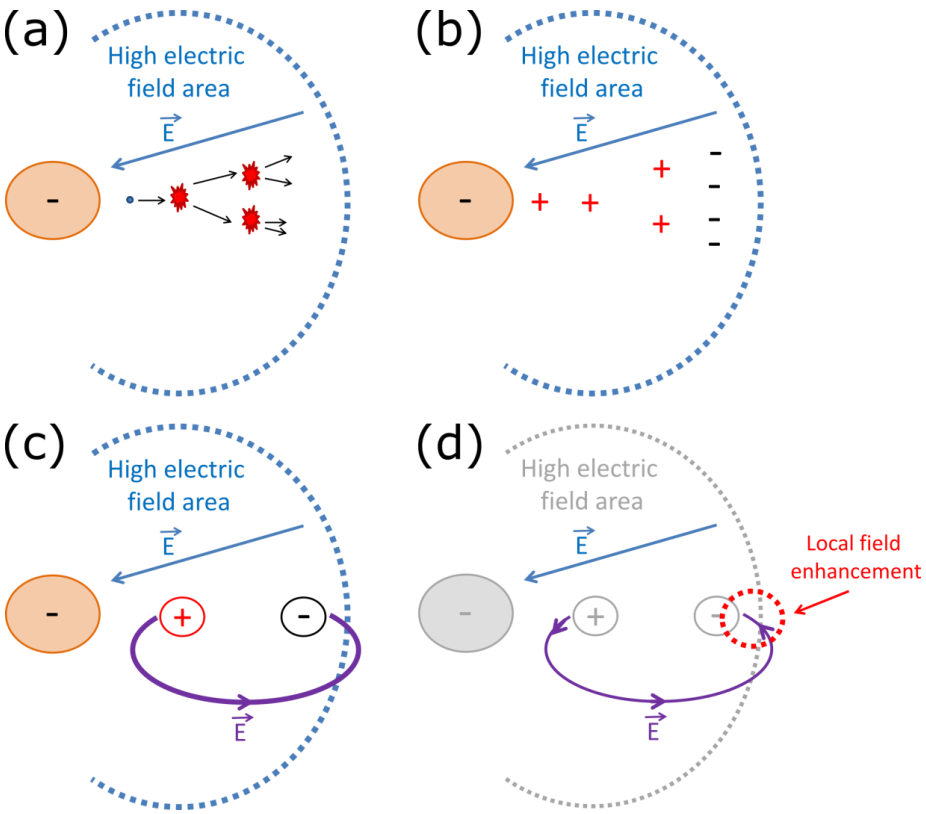

Figure 2.2.1: Different steps in the development of a streamer discharge. (a) It starts with an electron avalanche in the vicinity of the cathode. (b) The free electrons leave behind them positive ions as they propagate. (c) This space charge induces a secondary electric field. (d) It results in an enhanced electric field at the tip of the avalanche.

Similarly to the Townsend discharge, the seed electrons present in the medium due to photoionization will be accelerated under the effect of the electric field and will create an electronic avalanche. Due to the difference in the electrical mobility of ions and electrons (as an example, for an electric field of 5 $kV.cm^{-1}$, the electrical mobility of electrons is $\sim 7.1 \times 10^{-2}$ $cm^2.V^{-1}.s^{-1}$ while the ones of positive and negative ions are $\sim 2.2 \times 10^{-8}$ $cm^2.V^{-1}.s^{-1}$ and $\sim 2.4 \times 10^{-8}$ $cm^2.V^{-1}.s^{-1}$, respectively [11]), the ions can be considered as static and the electrons will leave them behind while they propagate. This creates a space charge that will induce a secondary electrical field. The space charge field disturbs the background electric field, creating a local enhancement of the electric field at the tip of the discharge, shielding the main electric field inside the discharge, and inducing an electrical field radial to the discharge channel. These processes are illustrated in figure 2.2.1.

Two scenarios are then possible:

- If the created space charge is too small to significantly distort the background electric field, the discharge avalanche will propagate until it is no longer possible to maintain sufficient ionization as the electric field becomes weaker and weaker as the distance from the cathode increases. In this case, the avalanche will be confined in the region of high electric field. This is called a corona discharge.
- If the space charge is important enough to significantly distort the background electric field, the enhanced electric field at the avalanche tip becomes important enough to maintain a significant ionization even in areas where the background electric field is low. Thus, the discharge will propagate further away than the prediction of Townsend model. Moreover, the radial electric field induced by the space charge will accelerate the free electrons produced by photoionization in the vicinity of the discharge channel and drain

them into the stem of the discharge, resulting in a characteristic finger-like structure. This type of discharge is called a steamer discharge and propagates in air at a speed of $10^5 - 10^7 m.s^{-1}$ [12].

It is however important to note that in a streamer discharge, the induced current is small and the plasma created has a low temperature. The electron recombination process inside the streamer thus remains efficient and the conductivity remains low. The competition between the background electric field that decreases as the streamer propagates away from the cathode, the induced electric field which also decreases along the propagation, and the electron recombination that stays efficient along all the propagation, will then arrest the propagation of the streamer after a certain distance. At atmospheric pressure, this distance is in the order of 10 cm.

This streamer discharge model is a model that can describe the propagation of a discharge between two electrodes and match the physical observations, such as a lower electric field threshold than the Townsend model predicted [13], [14], a dependence on photoionization [15], and a non dependence on the cathode material.

2.3 Streamer-leader discharges

To describe the development of meter-long electric sparks, a new model was developed: the streamer-leader discharge [16].

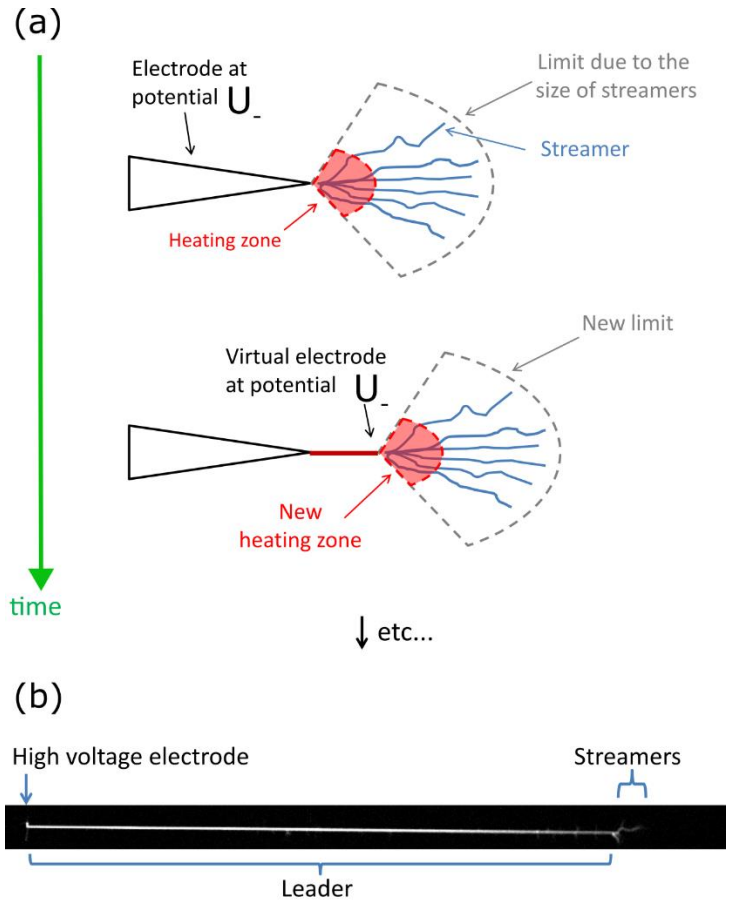

Figure 2.3.1: (a) Scheme of the cycle of propagation of a streamer-leader discharge. (b) Picture of a 1.4 m long guided streamer-leader discharge recorded by a high-speed camera, showing the leader part of the discharge with streamers emerging at its extremity.

We consider a similar setup as described previously, where streamers sporadically form near the cathode but cannot propagate far enough to reach the other electrode. If we consider the current induced by a single streamer, the resulting heating is not important enough to compensate the loss due to electron recombination, imposing a limit to its propagation distance. However, not one but numerous streamers appear in the high electric field region in the vicinity of the cathode. The addition of many streamer currents starting from the same point can locally induce a strong heating and create a highly conductive path that slowly expands into the gap. This channel of hot conductive plasma is called a leader. This propagation process and an example of such leader discharge are presented in figure 2.3.1.

Figure 2.3.2: Streamer-leader propagation of a discharge produced by our 300 kV Tesla generator, recorded with a high-speed camera at a speed of 400 000 frames/s. The stepping of the propagation is clearly visible (note that this stepping is also partially due to the oscillation of the background field), and the mean speed is measured to be in the range of $10^4 - 10^5$ m.s^{-1}, characteristic of a streamer-leader discharge.

Although leaders are generally associated with the propagation of lightning, they are characteristic of the development of any meter-long sparks. In the case of a lightning leader, each extension (called a step leader) is typically 10 to 50 meters in length. This process is several orders of magnitude slower than the propagation of streamers and has a characteristic speed in the order of $10^4 - 10^5$ m.s^{-1}. An example of leader process observed in our laboratory is the discharges propagation over 1 m obtained with our 300 kV Tesla Coil generator is presented in figure 2.3.2.

3 Guiding electrical discharges with lasers

The two subjects that were introduced in the previous sections, the laser filamentation and the propagation of electric discharge, can seem at first to be far apart from each other. However, if we combine the two, we can try to achieve one of the dreams of mankind: the control of lighting discharges. The idea to use a laser to control the path of lightning discharges was already proposed in the 1970's [17], [18].

3.1 Gas laser vs. femtosecond laser

At first, high energy gas lasers, such as CO_2 lasers, were considered to be used to control lightning as they are able to produce highly conductive plasma in air. The electrons of the gas are affected by the laser pulse and gain energy via inverse Bremsstrahlung. Then, they collide with the gas molecules and induce diverse effects such as excitation, dissociation and ionization. The newly

formed electron will then repeat the cycle and produce more electrons, similar to a cascade. Several cycles being necessary to reach a significant electron density, this process requires laser pulses with duration of several ns in air at atmospheric pressure. The cycles are repeated until the laser pulse is no longer present or that the electron density reaches a critical density (as defined in the equation (1.4.8)) at which the plasma is not transparent to the laser wavelength. For a CO_2 laser at a wavelength of 10.6 µm, the critical density is of the order of 10^{25} m^{-3}, which corresponds to an ionization rate of 40%. Moreover, the gas molecules are also heated via the collision of electrons to a temperature of several thousand degrees, reducing the rate of electron recombination and attachment and creating long-lived plasma.

However, this technique has two main drawbacks. The first is the high energy cost necessary to create the plasma, which was estimated to be of several hundreds of J per meter [19]. The second is the spatial distribution of the plasma. Rather than creating homogeneous plasmas, focused CO_2 lasers tend to create several plasma centres separated by a distance that will increase as one increases the focal distance [20]. The plasma channel was observed to be continuous only when it is not too long, but appear discontinuous for length greater than the meter scale. This discontinuity of the plasma channel hinders its polarization as one entity in an external field and does not permit using it as an efficient conductor.

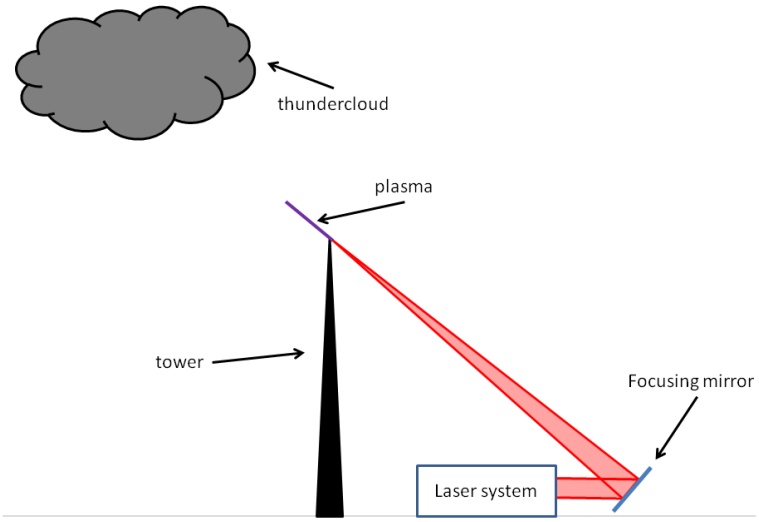

Figure 3.1: Schematic of the experiment aiming at triggering lightning conducted in 1995 on the seacoast of Japan [21].

An attempt to trigger and guide natural lightning with high power lasers was organized in 1995 [21]. This experiment located on the Japanese seacoast involved a 1 kJ, 50 ns CO_2 laser coupled to a 600 J, 50 ns Nd:glass laser focused to produce a 2 m long plasma starting at the top of a 50 m tall tower, as shown in figure 3.1. A Nd:YAG laser converted to the fourth harmonic was used to create weakly ionized plasma channels far above the tower to guide a leader towards thunderclouds. During this campaign, two successful attempts to attract lightning might have been observed and in these two cases, the lightning was synchronized with the laser pulses and an ascending leader left the tower. However, due to the small number of events and the impossibility to repeat the experiment, it is not clear if the observations were affected by the presence of the laser [22], so it remains uncertain if the experiments were successful or not.

In the late 90s, people suggested to use femtosecond laser to control lightning. As described in the first section of this chapter (“Laser filamentation”), these lasers can generate a high intensity over a long distance, creating of a thin column of plasma with a diameter in the range of 100 µm and an electron density in the range of 10^{22} to 10^{23} m^{-3} [23], [24]. This electron density is clamped and defined by the balance between the laser self-focusing and the plasma defocusing (note that the electron density can become higher in specific filamentation regime such as superfilamentation [9]).

It is important to note that in this type of plasma, while the intensity is high enough to induce inverse Bremsstralung, the pulse duration is too short to enable any collisional ionization. Thus, the temperature remains low and electron recombination and attachment stay efficient, reducing the plasma lifetime to only several ns. As a consequence, the plasma we call filament, while being able to be generated over several tens of meters, has a length limited by its lifetime to a few meters [25]. The filament could be considered as a plasma segment that exists only behind the laser pulse and travels with it at the speed of light.

Using femtosecond filamentation has several advantages compared to using long pulse lasers. While the femtosecond lasers have a more modest energy per pulse compared to the gas laser, the filamentation process is more efficient and the energy necessary to create a filament in air is in the order of 1 mJ at 800 nm [4] or 0.2 mJ at 248 nm [26]. Moreover, contrary to the discontinued channel created by high power gas laser, the plasma filament is continuous and homogeneous along the propagation of the laser. Furthermore, the presence of filaments at kilometric distances has been observed [27], [28].

3.2 Interaction between laser filamentation and electrical discharges

Thus, laser filamentation appears as a good tool to guide lightning [29], [30]. However, it is important to emphasize the difference between a filament interacting with a discharge compared to the plasma created by a high power laser and to understand what process enables the filaments to control discharge.

The first process would be to consider the plasma created by the filament as a conductor that will propagate the potential of the electrode near its location (as an example for the setup presented in figure 3.1, it extends the potential of the tower for an extra 2 m). However, it is necessary to take into account the time that the plasma would take to become equipotential, called the polarization time. If the plasma was a perfect conductor this time would be zero, but it is not the case for the weakly ionized plasma created by filament.

This polarization time τ_{pol} is related to the resistance R and the capacitance C of the filament. We consider a filament of length l and radius r, placed vertically between a charged cloud and the ground, with a cloud to ground voltage U and a voltage V along the filament. Due to the current continuity between the ground and the cloud, we have the equation:

$$C\frac{d(U-V)}{dt} = \frac{V}{R} \tag{3.2.1}$$

$$\rightarrow \frac{d(V)}{dt} = -\frac{V}{R \times C} = -\frac{V}{\tau_{pol}} \tag{3.2.2}$$

$$\rightarrow V = V_0 e^{-\frac{t}{\tau_{pol}}}. \tag{3.2.3}$$

The voltage along the filament decreases exponentially with a time constant equal to the polarization time. We can then express this polarization by considering the capacitance and resistance of the plasma:

- The capacitance can be considered as the capacitance of an ellipsoid with one axis length being $l/2$ and the other being negligible compared to $l/2$. This gives us the expression of the capacitance:

$$C = \frac{2 \times \pi \times l \times \varepsilon_0}{\ln\left(\frac{l}{r}\right)}. \tag{3.2.4}$$

- The resistance of the plasma can be expressed as:

$$R = \frac{1}{\sigma}\frac{l}{\pi \times r^2} = \frac{1}{e \times n_e \times \mu_e}\frac{l}{\pi \times r^2}\ , \tag{3.2.5}$$

with σ the plasma conductivity, n_e the electron density and $\mu_e$the electron mobility.

This gives us the expression for the polarization time:

$$\tau_{pol} = \frac{\varepsilon_0}{e \times n_e \times \mu_e}\frac{2 \times \left(\frac{l}{r}\right)^2}{\ln\left(\frac{l}{r}\right)}. \tag{3.2.6}$$

For the parameters characteristic of a filament, $n_e = 10^{22}$ m^{-3}, $l = 1$ m and $r = 100$ µm, the polarization time is of 2 µs. This time need to be compared to the lifetime of the plasma that is in the order of several ns. The contradiction is thus clear and the plasma created by the filament has a too short lifetime to become equipotential and act as a conductor.

The second process would be that the electrons present in the filament will act as seed electrons that will enhance the avalanche process happening during the discharge propagation. This could help in the initiation of the discharge propagation but it cannot explain the guiding effect of filament due to the relatively low speed at which discharges propagate over long distance. As an example, we look at the propagation of the 1 m long Tesla coil discharge presented in figure 2.3.2. The propagation speed of the discharge is in the order of $10^4 - 10^5$ m.s^{-1}, and the total propagation time is 15.8 µs. Again, this time is orders of magnitude greater than the plasma lifetime. The plasma is thus long gone during the propagation of the discharge and cannot explain the guiding effect of the filament.

The correct process that needs to be taken into account is the creation of an under-dense channel in the filament wake [31]. During the plasma recombination, the energy from the free electrons is transferred to rotational, vibrational and translational degrees of freedom of the molecules present in the medium and result in a heating of the medium that is confined to the volume initially occupied by the plasma filament [32]. This localized and quick deposition of energy leads to the propagation of an outward pressure wave. Then, pressure equilibrium is established over a µs timescale, while an under-dense channel with the same geometry than the filament appears [33]. This under-dense channel will slowly expand radially and has a lifetime of tens of ms. The reduction of density in this channel will decrease locally the breakdown voltage by increasing the electron mean free path. The free electrons will thus be accelerated over a longer distance in the channel and a lower electric field is necessary to produce the avalanche ionization. If we focus on the case of a Townsend discharge for relatively large values of the density time length $d \times n_{gaz}$ as described in equation (2.1.14), the ratio between the breakdown voltage and the gas density U_{bd}/n_{gaz} decreases as slowly (logarithmically) as $d \times n_{gaz}$ increases. Correspondingly, this means that for the typical values of d and $d \times n_{gaz}$ used in our experiments, the breakdown voltage is roughly proportional to the gas density [34].

Another aspect of the filament that could contribute to the guiding effect of discharge in air is the creation of long lived charged oxygen molecules by the attachment of free electrons to the oxygen molecules during the plasma recombination [35]. Theses electrons are loosely attached and will require an energy of 0.15 eV [36] to be ionized, as compared to the 13.6 eV and 15.6 eV required for electrons bound to oxygen and nitrogen, respectively. Therefore, they can be more easily set free by electrons collisions and as a consequence reduce the electric field required for the spark propagation. These attached electrons could live long enough to be present during the whole discharge propagation and therefore create a path with the same geometry as the filament and with a lower breakdown voltage that will guide the discharge.

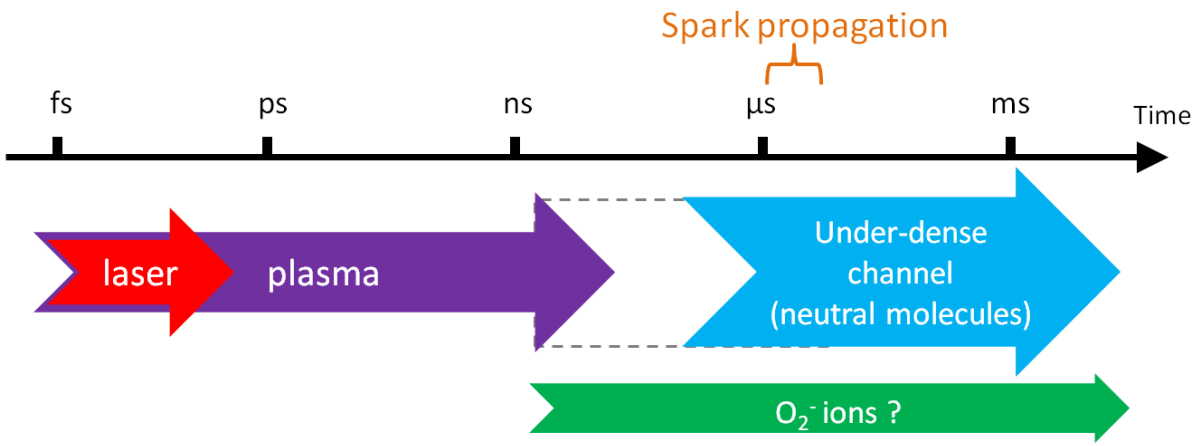

Figure 3.2: Comparison between the time scale of the different aspects of the filament and the measured time scale of the spark propagation of a 1 m, 300 kV discharge.

This discussion about the different filament contributions and their respective time scales compared to the spark propagation time of our 1 m long guided discharge is summarized in figure 3.2.

Bibliography

[1] Y. R. Shen, *Principles of nonlinear optics*, Wiley classics library ed. Hoboken, NJ: Wiley-Interscience, 2003.

[2] G. Fibich et A. L. Gaeta, « Critical power for self-focusing in bulk media and in hollow waveguides », *Opt. Lett.*, vol. 25, n° 5, p. 335-337, mars 2000, doi: 10.1364/OL.25.000335.

[3] J. H. Marburger, « Self-focusing: Theory », *Prog. Quantum Electron.*, vol. 4, p. 35-110, avr. 1975, doi: 10.1016/0079-6727(75)90003-8.

[4] A. Braun, G. Korn, X. Liu, D. Du, J. Squier, et G. Mourou, « Self-channeling of high-peak-power femtosecond laser pulses in air », *Opt. Lett.*, vol. 20, n° 1, p. 73-75, janv. 1995, doi: 10.1364/OL.20.000073.

[5] V. I. Bespalov et V. I. Talanov, « Filamentary Structure of Light Beams in Nonlinear Liquids », *Sov. J. Exp. Theor. Phys. Lett.*, vol. 3, p. 307, juin 1966.

[6] G. Méchain, A. Couairon, M. Franco, B. Prade, et A. Mysyrowicz, « Organizing Multiple Femtosecond Filaments in Air », *Phys. Rev. Lett.*, vol. 93, n° 3, p. 035003, juill. 2004, doi: 10.1103/PhysRevLett.93.035003.

[7] S. A. Hosseini *et al.*, « Competition of multiple filaments during the propagation of intense femtosecond laser pulses », *Phys. Rev. A*, vol. 70, n° 3, p. 033802, sept. 2004, doi: 10.1103/PhysRevA.70.033802.

[8] S. Henin *et al.*, « Saturation of the filament density of ultrashort intense laser pulses in air », *Appl. Phys. B*, vol. 100, p. 77, mars 2010, doi: 10.1007/s00340-010-3941-x.

[9] G. Point *et al.*, « Superfilamentation in Air », *Phys. Rev. Lett.*, vol. 112, n° 22, p. 223902, juin 2014, doi: 10.1103/PhysRevLett.112.223902.

[10] J. M. Meek, « A Theory of Spark Discharge », *Phys. Rev.*, vol. 57, n° 8, p. 722-728, avr. 1940, doi: 10.1103/PhysRev.57.722.

[11] Xin Miao Zhao, J.-C. Diels, Cai Yi Wang, et J. M. Elizondo, « Femtosecond ultraviolet laser pulse induced lightning discharges in gases », *IEEE J. Quantum Electron.*, vol. 31, n° 3, p. 599-612, mars 1995, doi: 10.1109/3.364418.

[12] E. Takahashi *et al.*, « Single-shot observation of growing streamers using an ultrafast camera », *J. Phys. Appl. Phys.*, vol. 44, n° 30, p. 302001, août 2011, doi: 10.1088/0022-3727/44/30/302001.

[13] H. J. White, « The Variation of Sparking Potential with Intense Ultraviolet Illumination », *Phys. Rev.*, vol. 48, n° 2, p. 113-117, juill. 1935, doi: 10.1103/PhysRev.48.113.

[14] R. R. Wilson, « Very Short Time Lag of Sparking », *Phys. Rev.*, vol. 50, n° 11, p. 1082-1088, déc. 1936, doi: 10.1103/PhysRev.50.1082.

[15] A. Cravath, « Photoelectric effect and spark mechanism », *Phys. Rev.*, vol. 47, p. 254, 1935.

[16] V. Cooray, « Basic Physics of Electrical Discharges », in *An Introduction to Lightning*, Dordrecht: Springer Netherlands, 2015, p. 7-27. doi: 10.1007/978-94-017-8938-7_2.

[17] L. M. Ball, « The Laser Lightning Rod System: Thunderstorm Domestication », *Appl. Opt.*, vol. 13, n° 10, p. 2292, oct. 1974, doi: 10.1364/AO.13.002292.

[18] D. W. Koopman et T. D. Wilkerson, « Channeling of an Ionizing Electrical Streamer by a Laser Beam », *J. Appl. Phys.*, vol. 42, n° 5, p. 1883-1886, avr. 1971, doi: 10.1063/1.1660462.

[19] V. V. Apollonov *et al.*, « Electric-discharge guiding by a continuous spark by focusing CO2-laser radiation with a conic mirror », *Quantum Electron.*, vol. 32, n° 2, p. 115, févr. 2002, doi: 10.1070/QE2002v032n02ABEH002140.

[20] E. M. Bazelyan et Y. P. Raĭzer, « The mechanism of lightning attraction and the problem of lightning initiation by lasers », *Phys.-Uspekhi*, vol. 43, n° 7, p. 701-716, juill. 2000, doi: 10.1070/PU2000v043n07ABEH000768.

[21] S. Uchida *et al.*, « Laser-triggered lightning in field experiments », *J. Opt. Technol.*, vol. 66, n° 3, p. 199, mars 1999, doi: 10.1364/JOT.66.000199.

[22] V. A. Rakov et M. A. Uman, *Lightning: physics and effects*. Cambridge: Cambridge University Press, 2007.
[23] A. Couairon et A. Mysyrowicz, « Femtosecond filamentation in transparent media », *Phys. Rep.*, vol. 441, nº 2-4, p. 47-189, mars 2007, doi: 10.1016/j.physrep.2006.12.005.
[24] S. L. Chin, *Femtosecond laser filamentation*, 1. Aufl. New York, NY Heidelberg: Springer, 2010.
[25] A. Couairon, « Filamentation length of powerful laser pulses », *Appl. Phys. B Lasers Opt.*, vol. 76, nº 7, p. 789-792, juill. 2003, doi: 10.1007/s00340-003-1217-4.
[26] S. Tzortzakis *et al.*, « Nonlinear propagation of subpicosecond ultraviolet laser pulses in air », *Opt. Lett.*, vol. 25, nº 17, p. 1270, sept. 2000, doi: 10.1364/OL.25.001270.
[27] M. Rodriguez *et al.*, « Kilometer-range nonlinear propagation of femtosecond laser pulses », *Phys. Rev. E*, vol. 69, nº 3, p. 036607, mars 2004, doi: 10.1103/PhysRevE.69.036607.
[28] M. Durand *et al.*, « Kilometer range filamentation », *Opt. Express*, vol. 21, nº 22, p. 26836-26845, nov. 2013, doi: 10.1364/OE.21.026836.
[29] J. P. Wolf, « Short-pulse lasers for weather control », *Rep. Prog. Phys.*, vol. 81, nº 2, p. 026001, févr. 2018, doi: 10.1088/1361-6633/aa8488.
[30] J. Kasparian et J.-P. Wolf, « On Lightning Control Using Lasers », in *Progress in Ultrafast Intense Laser Science*, vol. 98, K. Yamanouchi, A. Giulietti, et K. Ledingham, Éd. Berlin, Heidelberg: Springer Berlin Heidelberg, 2010, p. 109-122. doi: 10.1007/978-3-642-03825-9_6.
[31] G. Point, C. Milián, A. Couairon, A. Mysyrowicz, et A. Houard, « Generation of long-lived underdense channels using femtosecond filamentation in air », *J. Phys. B At. Mol. Opt. Phys.*, vol. 48, nº 9, p. 094009, mai 2015, doi: 10.1088/0953-4075/48/9/094009.
[32] Y.-H. Cheng, J. K. Wahlstrand, N. Jhajj, et H. M. Milchberg, « The effect of long timescale gas dynamics on femtosecond filamentation », *Opt. Express*, vol. 21, nº 4, p. 4740, févr. 2013, doi: 10.1364/OE.21.004740.
[33] S. Tzortzakis, B. Prade, M. Franco, A. Mysyrowicz, S. Hüller, et P. Mora, « Femtosecond laser-guided electric discharge in air », *Phys. Rev. E*, vol. 64, nº 5, p. 057401, oct. 2001, doi: 10.1103/PhysRevE.64.057401.
[34] J. P. Rajzer, J. P. Rajzer, et J. P. Rajzer, *Gas discharge physics*. Berlin Heidelberg: Springer, 1991.
[35] B. Zhou *et al.*, « Revival of femtosecond laser plasma filaments in air by a nanosecond laser », *Opt. Express*, vol. 17, nº 14, p. 11450, juill. 2009, doi: 10.1364/OE.17.011450.
[36] D. S. Burch, S. J. Smith, et L. M. Branscomb, « Photodetachment of O 2 − », *Phys. Rev.*, vol. 112, nº 1, p. 171-175, oct. 1958, doi: 10.1103/PhysRev.112.171.

Chapter 2

Laser filamentation at high repetition rate: Study of the cumulative air density depletion and its application to electric discharge triggering.

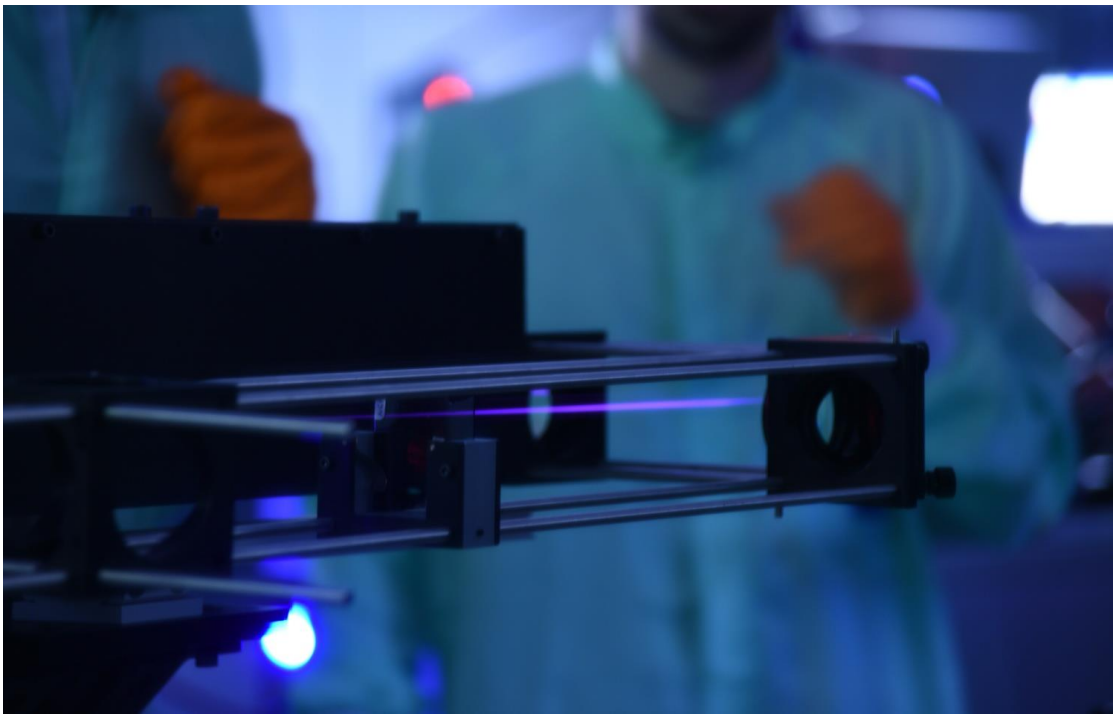

Figure 1: Picture of the density measurement setup characterizing a filament.

In this chapter, I will present our study on the influence of the laser repetition rate on the generation of low-density channels of air left in the path of femtosecond laser filament, and its consequence on their abilities to guide and trigger electric discharges [1]–[4]. Following the development of terawatt lasers operating at high repetition rate, growing attention is devoted to the study of the filament process and to the guiding of electric discharges at such high repetition rates [5]–[8].

I will first focus on the description of the density measurement setup that was developed to allow us to characterize the low-density channels. Then, a characterization of the filamentation process in the single shot regime, and the resulting low-density channel, will be presented. Next, a model will be developed based on the data of the single shot regime to infer the behaviour of the cumulative effects appearing at high repetition rate. Finally, experimental measurements will confirm the validity of our model and of our understanding of the cumulative effects. The dependencies of theses cumulative effects have on parameters such as the gas compositions, air flow, and verticality/horizontality of the setup, etc, will be discussed.

Table of contents C:\Users\Pierre Walch\Desktop\manuscrit\b - _Toc114958936

1 Density depletion measurement

1.1 Standard setup

The air density depletion resulting from energy deposition during filamentation is responsible for the guiding/triggering of electrical discharge. Its precise characterisation is therefore needed for many applications of filaments. To achieve this, an interferometric system measuring air density in the wake of the laser filament with fine temporal and spatial resolutions has been developed and thoroughly tested.

The system chosen for the task is a quadriwave lateral shearing interferometer developed by PHASICS. We will further refer to this interferometer as Phasics. Quadriwave lateral shearing interferometry, also known as modified Hartmann mask technique, stands out for its very high spatial resolution of few tens of µm [9]. When coupled to a pulsed probe laser with a short duration, the system achieves both high spatial and high temporal resolutions.

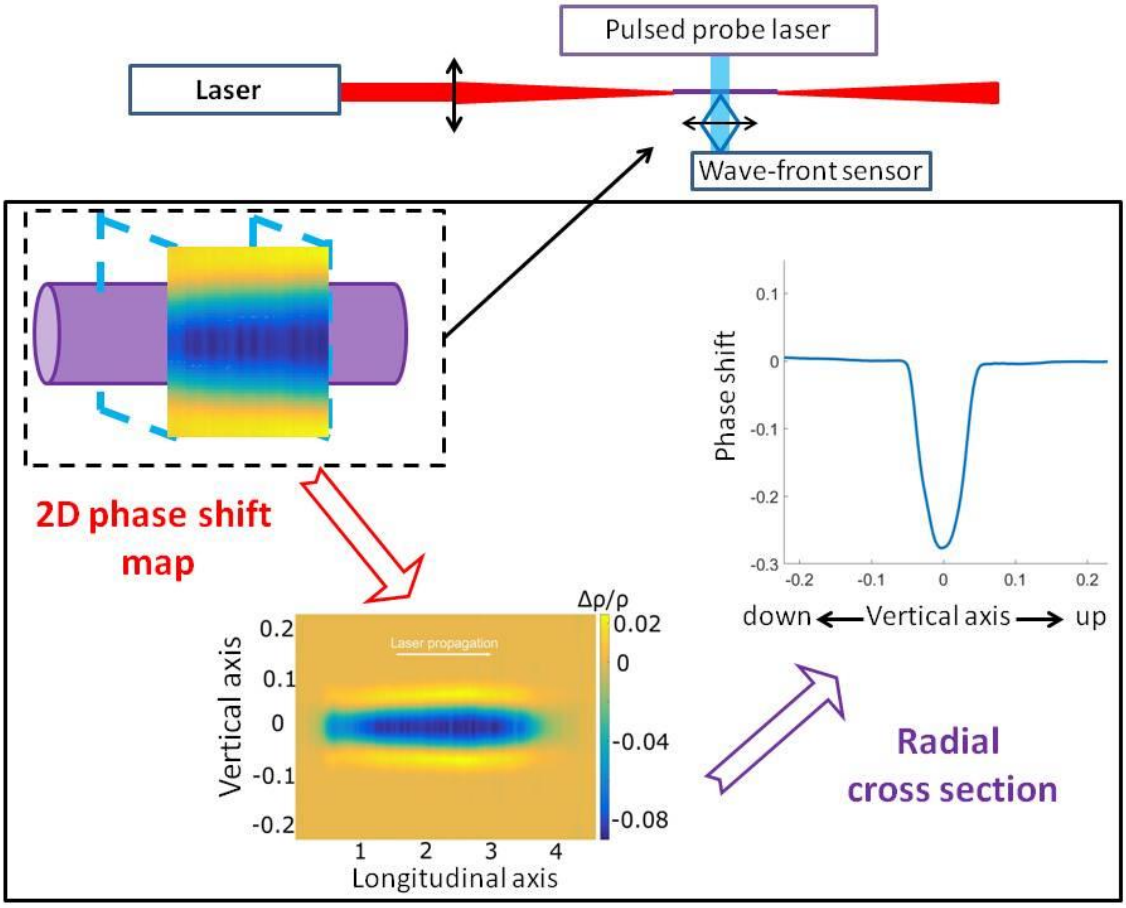

Figure 1.1.1: Typical setup and data processing steps to measure the density depletion created by filamentation.

The typical experimental setup and data processing steps of this measurement are presented in figure 1.1.1 The most straightforward setup consists of a femtosecond laser that is propagating through a lens to force the filamentation near the focus. A probe laser is then sent in the transverse direction through the filamentation zone and collected by the Phasics by passing through a lens that image the filamentation zone on its sensor. The Phasics measurement gives a 2D map of the phase shift induced by the filament on the probe beam. This phase shift can be due to a variation of gas density or to the presence of free electrons, but at long timescale (t > µs) the contribution of free

electrons is negligible [10]. With the data processing steps that will be presented afterward, we reconstruct a 3D map of the air density variation (providing some hypotheses on the symmetry of the channel). To ease the comparison of different sets of data, the radial cross section is usually plotted from the 3D map. By synchronizing the femtosecond laser and the probe laser and using a delay generator, it is possible to repeat these measurements at different times before and after the filamentation process, allowing a time resolved measurement of the air density variation.

1.2 Phasics: Quadriwave lateral shearing interferometer

The quadriwave lateral shearing interferometry is a technique to measure the absolute phase and intensity of a laser wavefront [9]. Its high sensitivity, and the possibility to characterize relatively large laser beams makes it particularly suitable to measure phase objects such as the low density channel produced by the filaments. An outline schematic of the system is presented in figure 1.2.1.

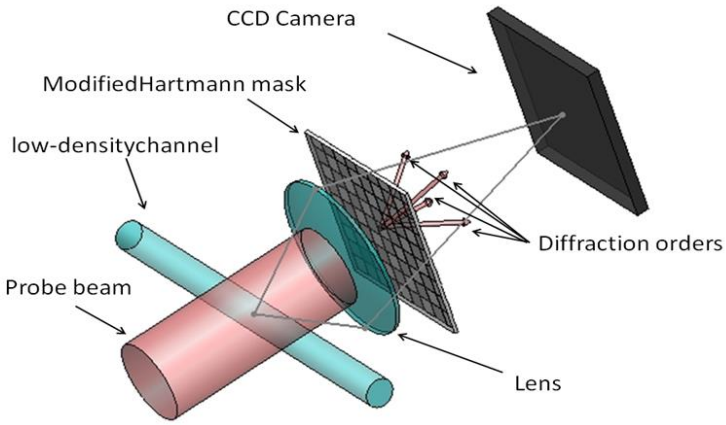

Figure 1.2.1: Outline schematic of a quadriwave lateral shearing interferometer.

The principle is the following:

While the probe beam propagates, it acquires a phase shift dependent on the environment it passes through and its wave front is distorted accordingly. Thus, this distortion of the wave front holds information about the crossed environment. To retrieve this information, the probe beam is sent through a bidimensional periodic optical grating of period *p* whose transmission is

$$T(x,y) = \cos\left(\frac{\pi\, x}{p}\right) \times \cos\left(\frac{\pi\, y}{p}\right),$$

and whose four diffraction orders correspond to four identical replicas of the entering wave front propagating in slightly different directions. Furthermore, a lens is used to conjugate the plane we want to probe with the plane of the CCD camera.

After propagating over a distance *z* between the grating and the CCD of the camera, the four replicas overlap and create an interference pattern of intensity *I* given by

$$I(x,y,z) = I_0\left(1 + \cos\left(\frac{2\pi\, x}{p} + \frac{2\pi}{p} z \frac{\partial \Delta\varphi}{\partial x}\right) + \cos\left(\frac{2\pi\, y}{p} + \frac{2\pi}{p} z \frac{\partial \Delta\varphi}{\partial y}\right)\right)$$
$$+ \frac{I_0}{2}\left(1 + \cos\left(\frac{2\pi\,(x+y)}{p} + \frac{2\pi}{p} z \frac{\partial \Delta\varphi}{\partial (x+y)}\right) + \cos\left(\frac{2\pi\,(x-y)}{p} + \frac{2\pi}{p} z \frac{\partial \Delta\varphi}{\partial (x-y)}\right)\right),$$

where $\Delta\varphi$ is the phase shift induced by the crossed environment (in this case the under-dense channel) and I_0 the intensity at the surface of the grating at z = 0. The phase gradient is then retrieved by means of a Fourier transform of the latter equation.

The whole 2D phase map is then obtained by integrating the phase gradient along the two following paths:

$$\Delta\varphi(x + dx, y + dy) = \Delta\varphi(x, y) + s\frac{\partial\Delta\varphi(x,y)}{\partial x} + s\frac{\partial\Delta\varphi(x+dx,y)}{\partial y},$$

$$\Delta\varphi(x + dx, y + dy) = \Delta\varphi(x, y) + s\frac{\partial\Delta\varphi(x,y+dy)}{\partial x} + s\frac{\partial\Delta\varphi(x,y)}{\partial y},$$

where *s* is a calibrated constant dependant of the grating spacing and the distance between the camera and the grating, but independent of the wavelength of the probe beam. By averaging the phase map acquired along the two paths, we avoid error propagation and considerably reduce the noise. An example of a measured 2D phase map is presented in figure 1.2.2.

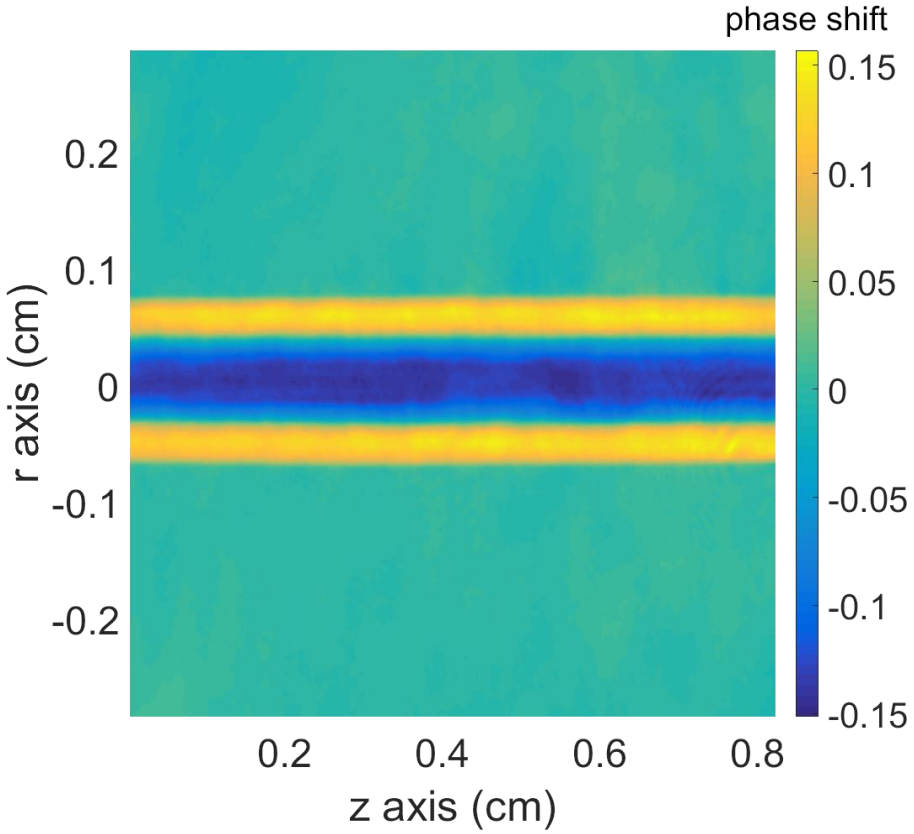

Figure 1.2.2: Example of a typically measured 2D phase map (unit: 2π rad) induced by a *fs* filament in air (from a 14 mJ, 50 fs, 800 nm laser pulse focused at NA=0.0078), r axis and z axis being respectively the vertical axis and the longitudinal axis (optical axis).

Based on these equations, it is easily understood that to retrieve an absolute phase shift value, the Phasics needs at least one point of known phase shift that will serve as the origin of the two paths of integration. The accuracy of the measurement is highly dependent on this origin point, thus it needs to be carefully chosen. Usually, this means that we need to have an unperturbed point with a phase shift of zero in the studied zone.

1.3 Data processing of the 2D phase map

To retrieve the 3D density map from the 2D phase map, additional steps are required. The first step is to link the measured phase shift with the density variation of the species in the medium that can affect this phase shift: electrons and neutrals. Since the phase shift measured by the Phasics is integrated through the path of propagation of the probe beam, it is linked to line-integrated densities

profiles. If the two species are present, their contribution can be discriminated by realising two phase shift measurements at two different wavelengths. The equation of the system is then

$$\int_{s1}^{s2}(n_e(s)-n_{e0})ds = \frac{\lambda_1\Delta\varphi(\lambda_1)-\lambda_2\Delta\varphi(\lambda_2)}{r_e({\lambda_2}^2-{\lambda_1}^2)},$$

$$\int_{s1}^{s2}(n_n(s)-n_{n0})ds = \frac{n_{n0}}{2\pi\beta}\frac{\lambda_2\Delta\varphi(\lambda_1)-\lambda_1\Delta\varphi(\lambda_2)}{\frac{\lambda_2}{\lambda_1}-\frac{\lambda_1}{\lambda_2}},$$

with n_e the perturbed electron density, $n_{e0} = 0$ the unperturbed electron density, n_n the perturbed neutral density, $n_0 = 2.47\times10^{25}$ m^{-3} the unperturbed neutral density, $r_e = 2.8\times10^{-15}$ m the classical electron radius and $\beta = 2.7 \times 10^{-4}$ the Gladstone-Dale constant [10].

If the phase shift measurement is made after a delay long enough to consider the filament electron density as negligible (typically t > 10 ns), the perturbed neutral density can be acquired with a measurement at a single wavelength and is given by

$$\int_{s1}^{s2}(n_n(s)-n_{n0})ds = \frac{n_{n0}}{2\pi\beta}\lambda\Delta\varphi(\lambda)\,.$$

Otherwise, if the measurement is made with a delay short enough to consider the perturbed neutral density as zero (and if no cumulative effects are observed [11]), the perturbed electron density can likewise be retrieved with a measurement at a single wavelength and is given by

$$\int_{s1}^{s2}(n_e(s)-n_{e0})ds = \frac{\Delta\varphi(\lambda)}{r_e\lambda}.$$

In the case where the two species are present, a measurement with two wavelengths is required to discern the variation coming from each of them.

The second step of the process consists in retrieving a 3D map of the density from the 2D map of the line integrated density of the relevant specie. Since the object of study is the remnant effect of the laser filament, a cylindrical symmetry for the zone is chosen (note that this hypothesis is not always valid for multiple filamentation regime). Through this property, it is possible to retrieve a 3D map from the 2D measurement with an inverse Abel transform. Thus, the density variation in cylindrical coordinates $\Delta n(r, z)$, with z the cylinder axis and r the radial axis, is given by

$$\Delta n(r,z) = -\frac{1}{\pi}\int_r^{+\infty}\frac{\partial\Delta n_{lim}}{\partial y}(y,z)\frac{dy}{\sqrt{y^2-r^2}}\,,$$

with $\Delta n_{lin}(y, z)$ the line integrated density in the 2D plan surface coordinates. An example of the neutral density variation in the cylindrical coordinate is presented in figure 1.3.1.

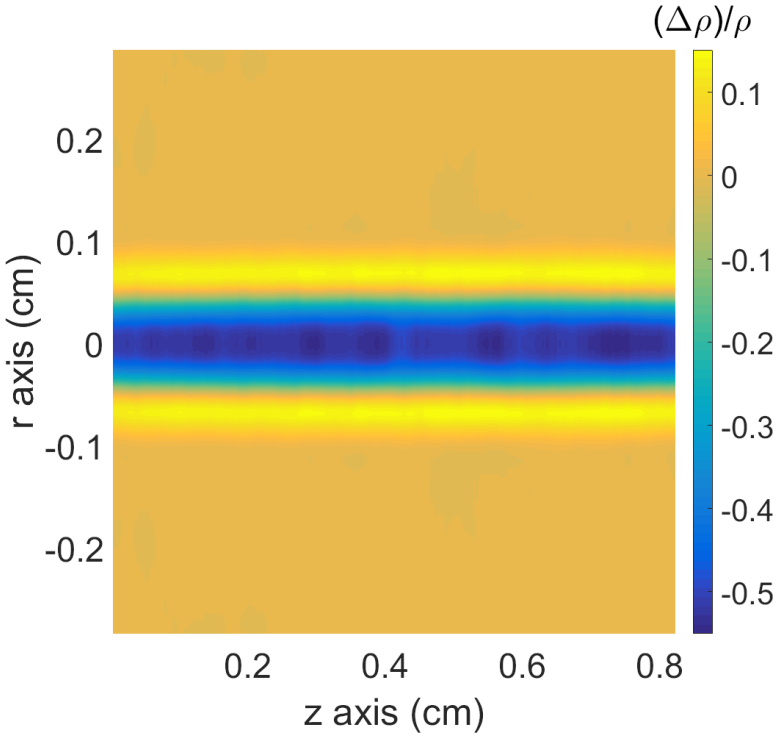

Figure 1.3.1: Relative variation of the neutral density (Δρ)/ρ in cylindrical coordinates, obtained from the 2D phase map presented in figure 1.2.2.

It is important to ensure the validity of the hypothesis of the cylindrical symmetry of the measurement. If the symmetry of the system is broken, as it can be in the case of filamentation at high repetition rate, the Abel inversion cannot be made and it is not possible to retrieve the density variation from one 2D phase map. If one wants to overcome this obstacle and retrieve the full 3D density variation map, a tomography setup is needed, where several 2D measurements are made at different angles around the filament to reconstruct the 3D map without using the Abel inversion.

2 Filamentation in single shot regime

A study of the filamentation process and of the resulting under-dense channel was done using the interferometry setup and data processing presented previously.

2.1 Experimental setup

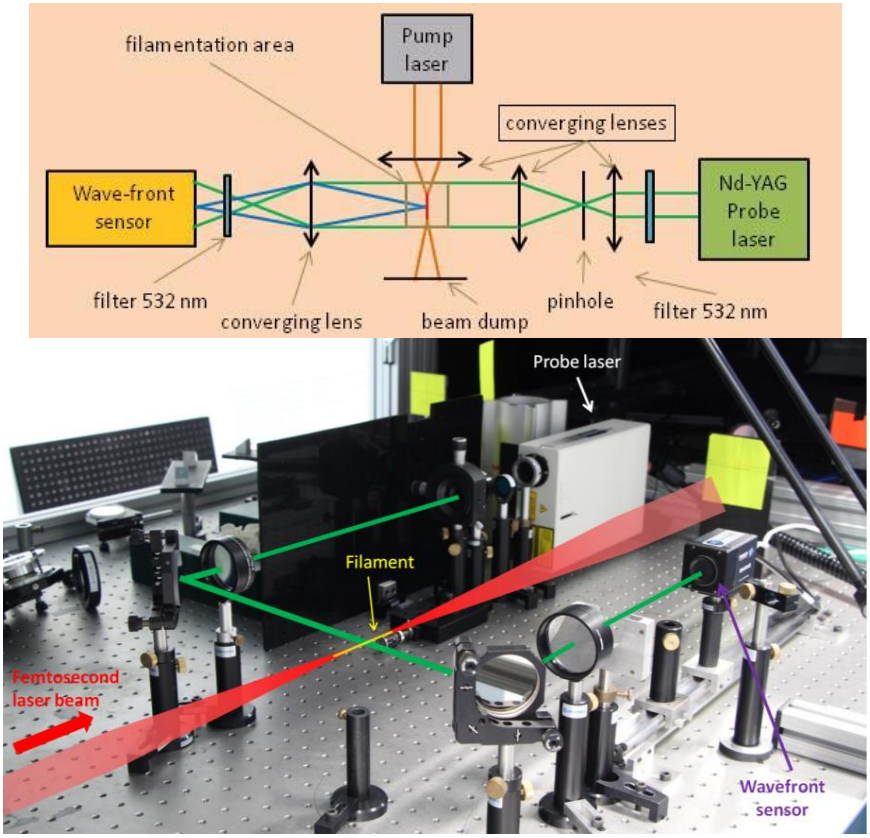

Figure 2.1.1: Schematics and photo of the experimental setup.

The experimental setup, presented in figure 2.1.1, consists of the following elements:

- A pump laser delivers pulses at 800 nm with duration of 50 fs and energy of 14 mJ, at a repetition rate of 1 Hz. These pulses are sent through a lens of a focal length of 500 mm and will undergo filamentation near the geometrical focus of the lens. The remaining pulse exiting the filamentation area is sent in a beam dump.
- A frequency-doubled Nd:YAG laser is used as the probe laser. It generates pulses with energy of 100 µJ and duration of 8 ns at 532 nm. To enhance the spatial quality of the beam and modify its size, the beam first passes through a telescope composed of a set of two converging lenses and a pinhole. The collimated beam then propagates through the filamentation area where it acquires the phase shift related to the density perturbation that we want to measure. Finally, it reaches the Phasics wavefront sensor by passing through a lens conjugating the plane of the study area and the CCD of the Phasics' camera. This probe beam is triggered by a delay generator synchronized with the clock of the pump laser.
- Two narrow band-pass filters at 532 nm are placed in front of the Phasics to reduce external noise.

2.2 Temporal evolution of the under-dense channel

To characterize the temporal evolution of the under-dense channel and to understand its behaviour over long timescales, measurements of the 2D phase shift were done at different delays. Cross sections of the density variation profile retrieved from these 2D maps are plotted in figure 2.2.1 for pump-probe delays ranging from 1 µs to 15 ms. In this range of delays, the perturbed electron density can be considered as negligible, and the induced phase shift is attributed to the perturbed neutral density [10].

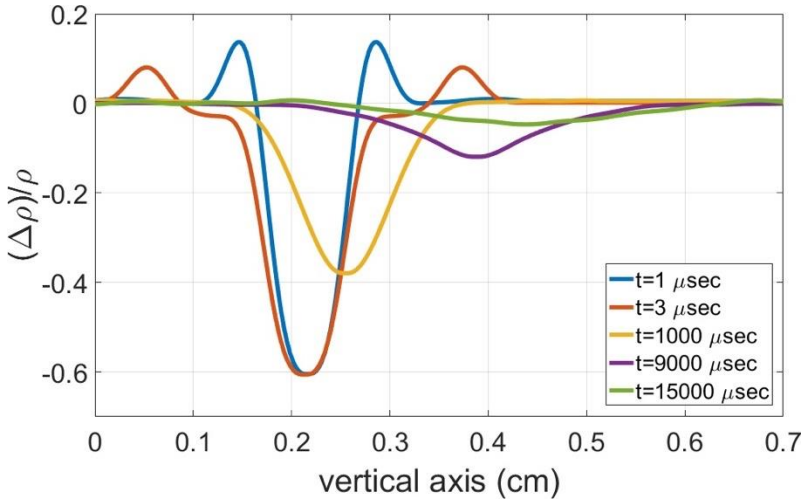

Figure 2.2.1: Profile of the density variation of the under-dense channel measured at different delays after its creation, ranging from 1 µs to 15 ms.

Two evolutions on different timescale can be observed: first, a fast evolution on a microsecond timescale, where the pressure equilibrium appearing after 1 µs results in the development of the density variation, while an over-dense wave propagates away from the channel; second, a slower evolution occurring over a ms timescale, where the under-dense channel decays by widening through thermal diffusion and moves up due to the buoyant force.

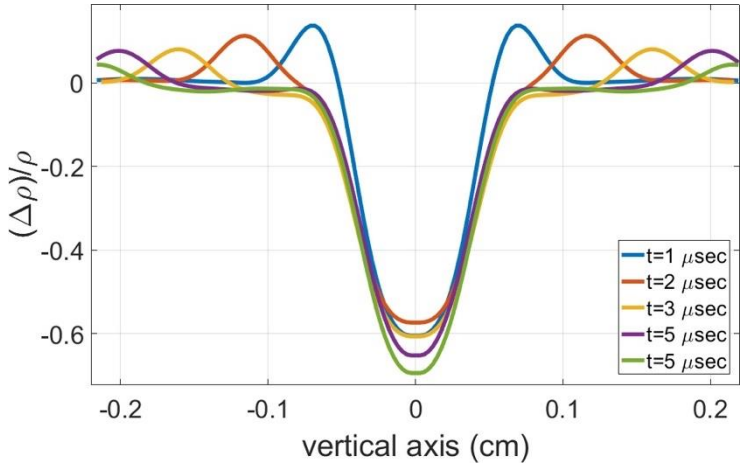

Figure 2.2.2: Profile of the density variation of the under-dense channel measured at different delays after its creation, ranging from 1 to 5 µs.

The µs evolution of the filament can be observed in more details in figure 2.2.2. The velocity of the over-dense wave is about 430 $m.s^{-1}$, thus being supersonic.

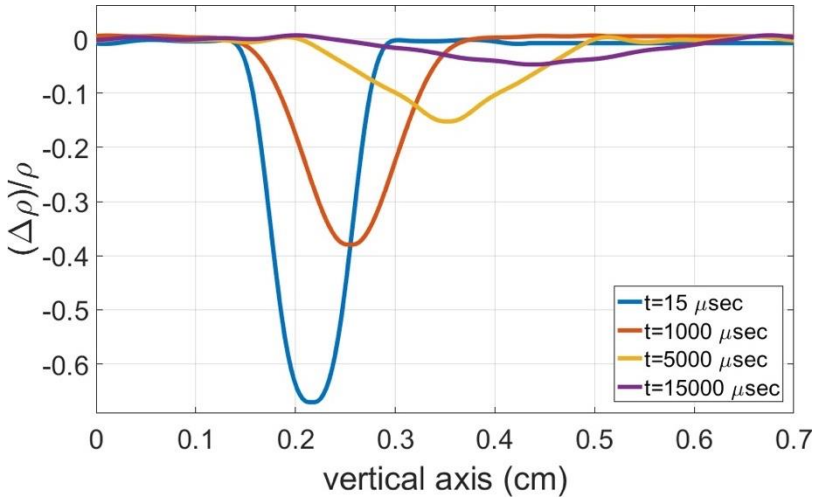

Figure 2.2.3: Profile of the density variation of the under-dense channel measured at different delays after its creation, ranging from 15 to 15000 µs.

In the same way, the millisecond evolution of the channel is represented in figure 2.2.3. The temporal evolution is clearly observable in this time range, and we can see that even after a delay of 15 ms the presence of the filament, although small, can be still seen via the Phasics measurement.

2.3 Spatial evolution of the under-dense channel

The previously presented measurements were made only on a small portion (length of 8 mm) of the under-dense channel, while a complete scan of the channel would be necessary to fully characterize the channel.

To characterize the whole channel length, we performed a series of measurements at several positions along the filamentation area. The magnification of the imaging system in front of the Phasics (see figure 2.1.1) is kept unchanged in order to preserve a high spatial resolution in the radial direction. Those measurements are then concatenated so as to reconstruct the entire channel

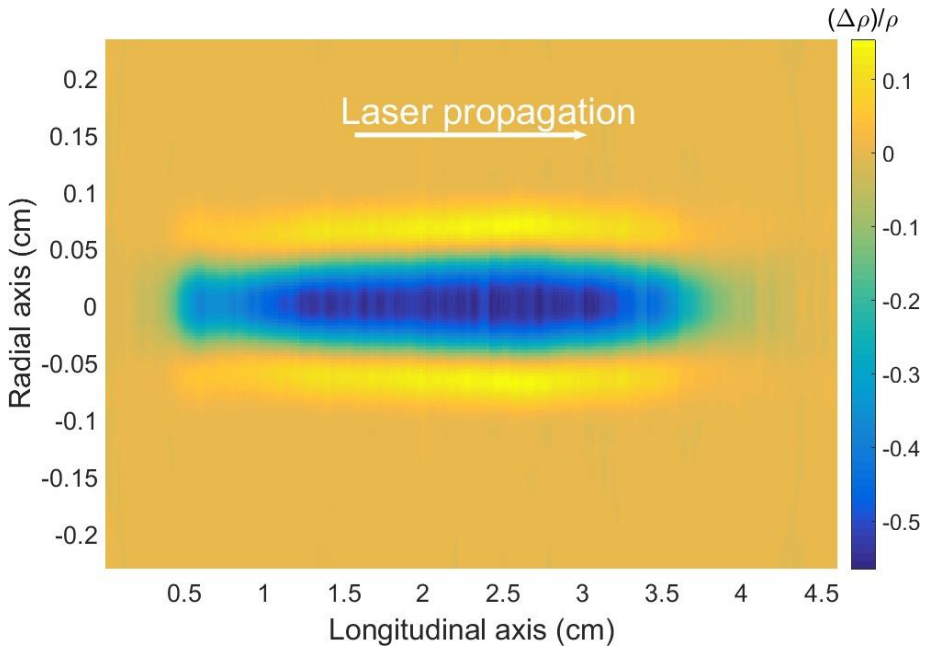

Figure 2.3.1: Longitudinal scan of the neutral density variation over the whole filament length. Measurements are performed 10 µs after the creation of the filament. The filament is produced by focusing a laser pulse of 14 mJ, 50 fs focused at NA=0.0078.

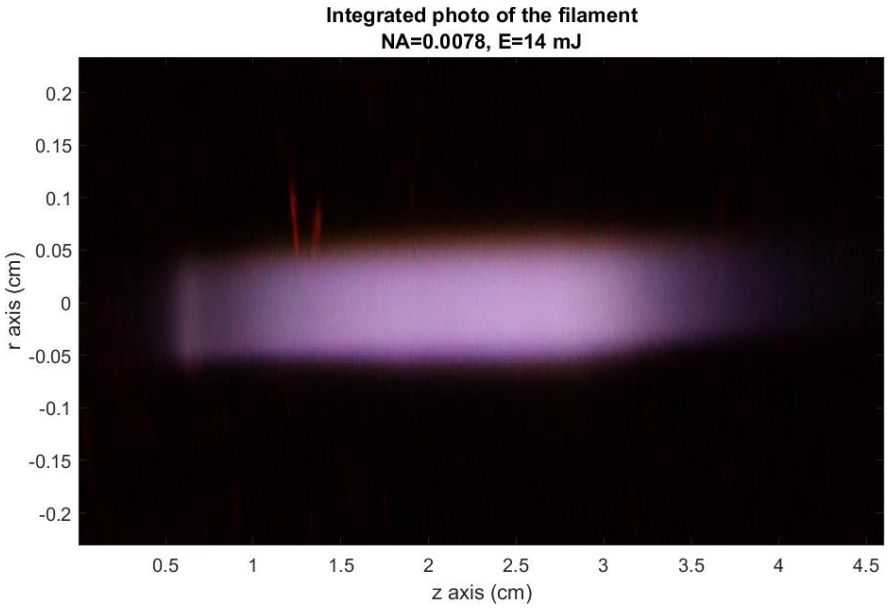

Figure 2.3.2: Picture of the luminescence of the 3 cm filament plasma characterized in Figure 2.3.1.

The result of a complete scan, measured at a delay of 10 µs after the creation of the filament, is presented in figure 2.3.1. An under dense channel more than 3 cm long can be seen in its entirety. Note that the size of the under-dense channel corresponds to the size of the luminescence of the filament plasma, presented in figure 2.3.2.

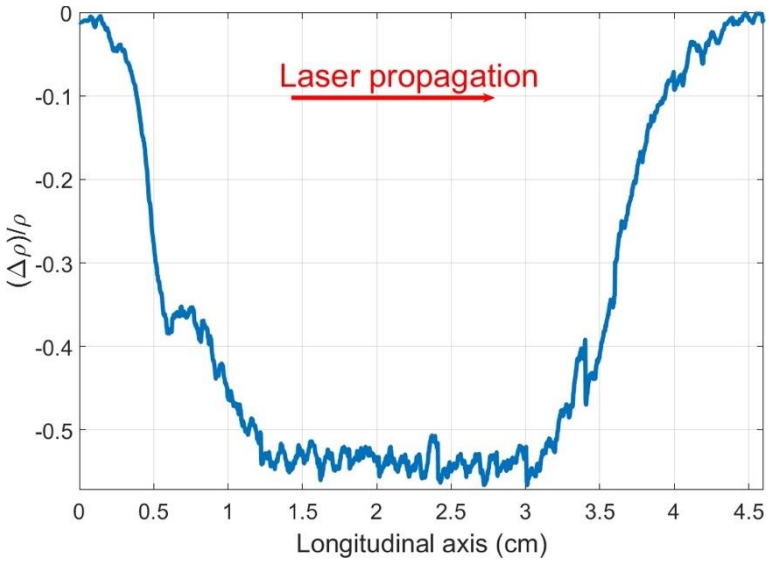

Figure 2.3.3: Profile of the neutral density variation measured along the filament axis.

One important observation, highlighted by the neutral density variation profile along the filament axis presented in figure 2.3.3, is that the center of the under-dense channel is homogeneous along its axis, whereas its two extremities are slightly dissymmetrical.

2.4 Propagation of the ionization front

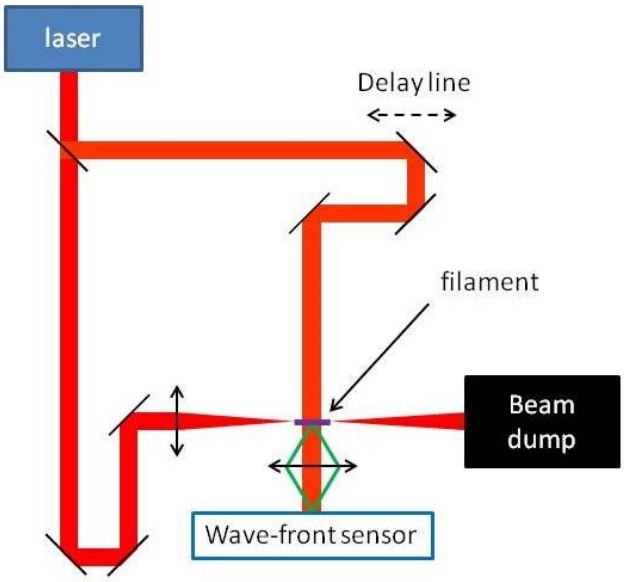

Figure 2.4.1: Experimental setup used to measure the electron density.

The time resolution of our interferometer setup is limited by the relatively long pulse duration of the probe laser (8 ns) and the electronic time jitter. In order to probe the filament at short times (< 1 ns) after its formation and with finer resolution (< 100 fs), we can use a portion of the fs laser as the probe beam. The pump-probe delay is then controlled with an optical delay line. The setup is shown in figure 2.4.1.

For sub-ns delays, the variation of neutral density can be considered as negligible, and the induced phase shift can be attributed to the electron density. Thus, the propagation of the ionization front of the filament can be observed by interferometry [12], [13].

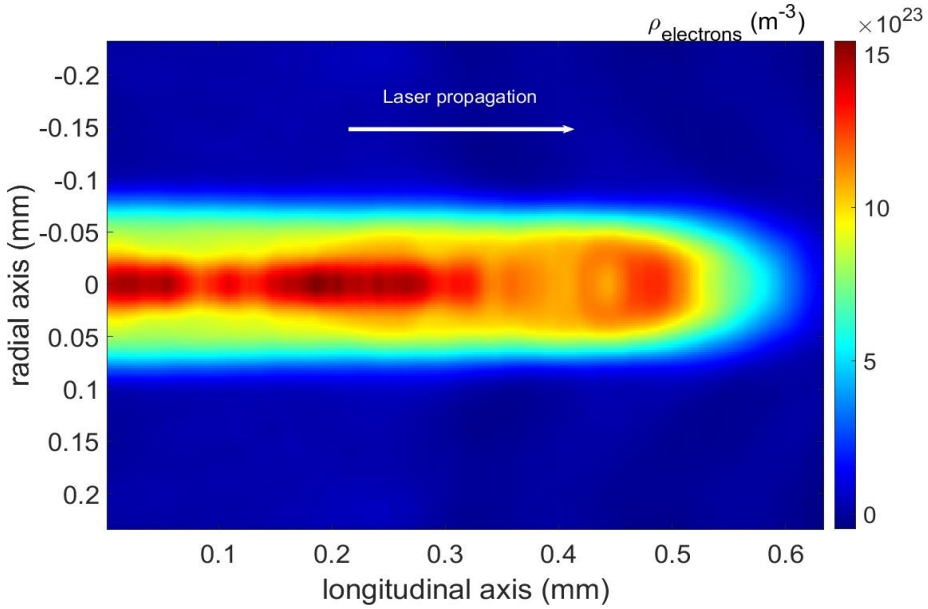

Figure 2.4.2: Electron density measured during the filamentation process.

An example of measurement is presented in figure 2.4.2. As expected, the ionization front propagates at the speed of light. The peak electron density is measured at 15×10^{23} m^{-3}, corresponding to an ionization rate of 6 %.

2.5 Model of the under-dense channel thermal evolution

To further understand the evolution of the under-dense channel, I developed a model of the under-dense channel thermal evolution. It was presented and published in [11].

In this model, we consider the air dynamics occurring after the under-dense channel has reached pressure equilibrium with ambient air at temperature T_{amb}. Its maximum depth and peak temperature slowly decay on a millisecond timescale because of thermal diffusion. The most homogeneous central part of the under-dense channel can be considered approximately invariant along the channel axis z. Its temporal evolution can then be modeled as

$$T(x,y,t) = T_{amb} + \Delta T(x,y,t),$$

$$\Delta T(x,y,t) = \Delta T_0 \times \frac{{R_0}^2}{(\sqrt{{R_0}^2+4\alpha t})^2} \times e^{-\frac{x^2+(y-v(t)\times t)^2}{(\sqrt{{R_0}^2+4\alpha t})^2}},$$

where α is the thermal diffusivity of air [14], T_{amb} the room temperature, R_0 and ΔT_0 are the radius and the peak temperature change of the initial Gaussian temperature distribution [15], x and y are the positions on the horizontal and vertical axes, centered on the channel axis z, v is the speed at which the channel moves upward. It consists of the buoyant force and a corrective term $v_{air\ flow}$ to take into account any additional air flow in the study zone.

$$v(t) = \left(1 - \frac{T_{amb}+\Delta T_0}{T_{amb}}\right) \times g \times t + v_{air\ flow},$$

where g is the acceleration of gravity.

As pressure equilibrium is maintained during the studied phase of the evolution, the relation between density and temperature change is

$$\frac{\Delta n}{n_{amb}} = -\frac{\Delta T}{T_{amb}},$$

where n_{amb} is the ambient air density.

This density variation is measured with the same setup as presented in figure 1.1.1. The recorded phase shift can be linked to the density variation by

$$\Delta\varphi = \frac{2\pi\beta}{\lambda}\int \frac{\Delta n(s)}{n_{amb}} ds.$$

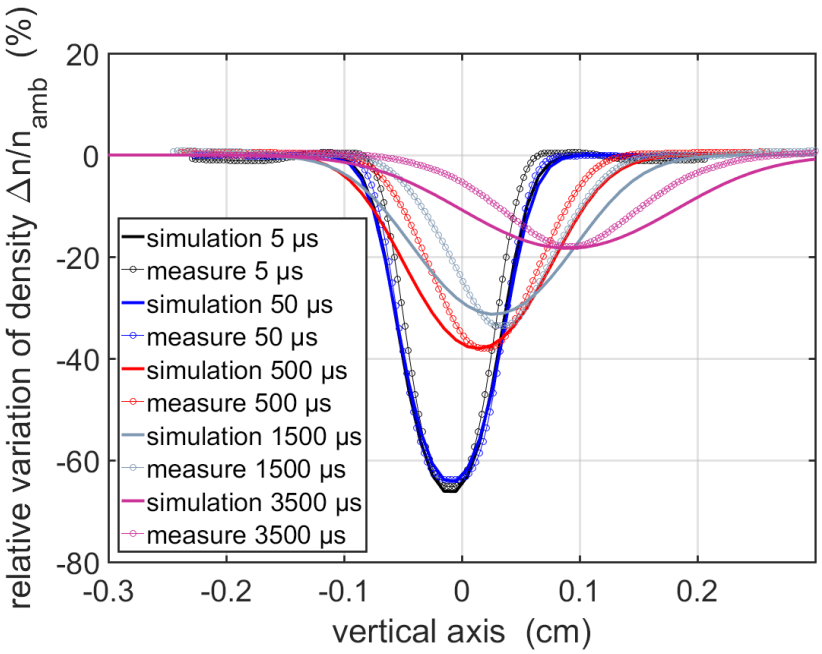

Figure 2.5.1: In circles: Measured temporal evolution of the density variation profile along the

vertical axis resulting from the filamentation of 14 mJ, 50 fs laser pulses focused at f/33. In Full line: simulated temporal evolution of the same profile with input parameters ΔT_0 = 700 K and R_0= 170 µm.

To test the validity of this air thermodynamics model, we compare its prediction with measurements of the under-dense channel resulting from the filamentation of a single 14 mJ, 50 fs laser pulse at 800 nm focused at f/33. This comparison is presented in figure 2.5.1 at times ranging between 5 µs and 3 500 µs with the input parameters ΔT_0 =700 K and R_0 = 170 µm. A satisfactory agreement is found between the simulation and the measurements. The temperature and radius variations are in the same range as in previous measurements [16].

3 Filamentation at high repetition rate

3.1 Cumulative effect explanation

As seen earlier (see figure 2.2.3), the under dense channel created after the filamentation process has a long lifetime of more than 10 ms. With such timescale, interaction between consecutive laser pulses appears for laser repetition rates higher than 100 Hz, resulting in an accumulation of heat in the medium that we call the cumulative effect.

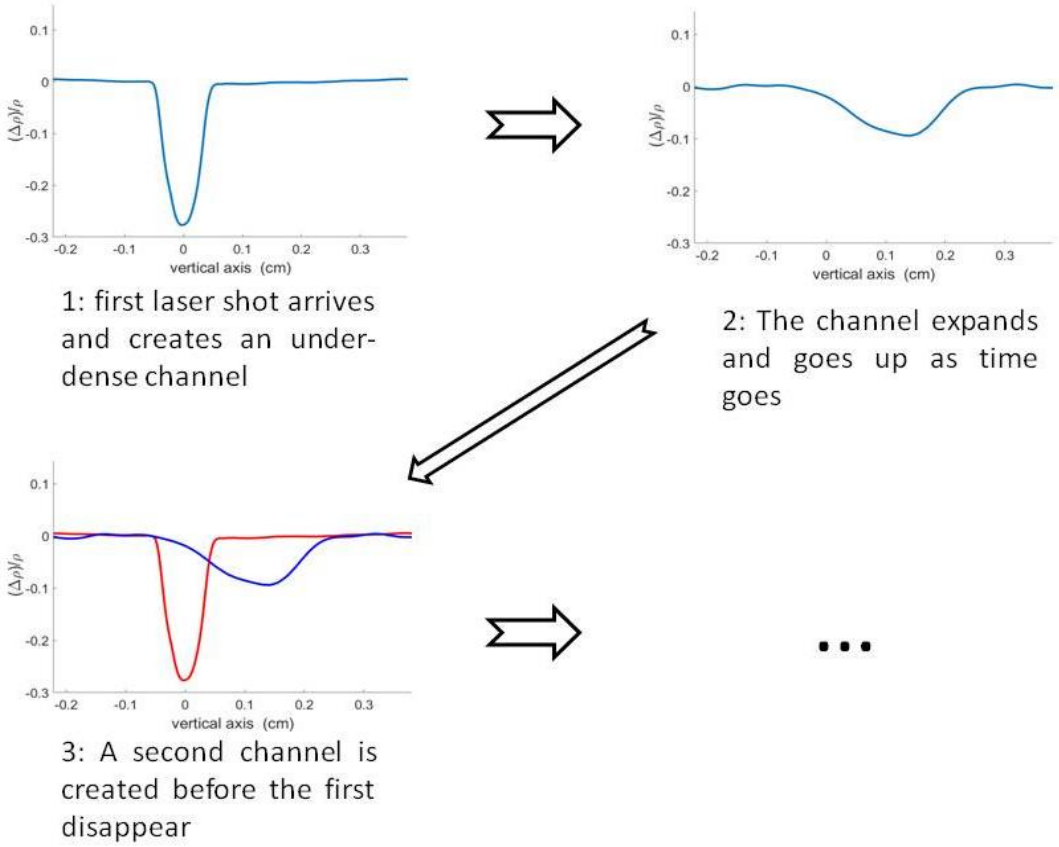

Figure 3.1.1: Simplified scheme explaining the cumulative effect resulting from the filamentation at high repetition rate.

The easiest way to describe the process leading to this cumulative effect is the following: first, an initial laser pulse propagates in the medium and undergoes filamentation, creating an under-dense channel. As presented earlier, the channel then expands and moves up with time. The delay between

each laser pulse being shorter than the lifetime of the under-dense channel, a second laser pulse passes through the medium and creates a second under-dense channel before the first one has disappeared. The two channels then evolve on their own, until a third laser pulse creates a third channel, etc. This cycle, represented in Figure 3.1.1, is repeated over and over.

To simulate this cumulative effect, the model described in Section 2)e) can be used. Considering a train of n pulses from a laser set at a repetition rate f, the total thermal variation $\Delta T_{cumul}(x, y, t)$ can be expressed as

$$\Delta T_{cumul}(x, y, t) = \sum_{i=0}^{n} \Delta T \left(x, y, t + \frac{i}{f}\right),$$

with ΔT, as used previously, being the thermal variation resulting from a single laser pulse.

This description of the cumulative effect can only be used for small temperature variations ($\Delta T < 300$ K). For higher temperature changes, effects such as the interaction of an incoming pulse with the previously formed channel should be taken into account.

3.2 Experimental setup

To quantify the under-dense channel at different repetition rates, the interferometer setup presented in figure 2.1.1 was used. However, the pump laser used to create filaments had an energy of 0.8 mJ per pulse, a duration of 35 fs with a tunable repetition rate ranging from 10 to 2500 Hz. The beam was focused at either f/33 or f/100 depending on the requirement of the measurement.

3.3 Under-dense channels created at repetition rates ranging from 10 to 2500 Hz

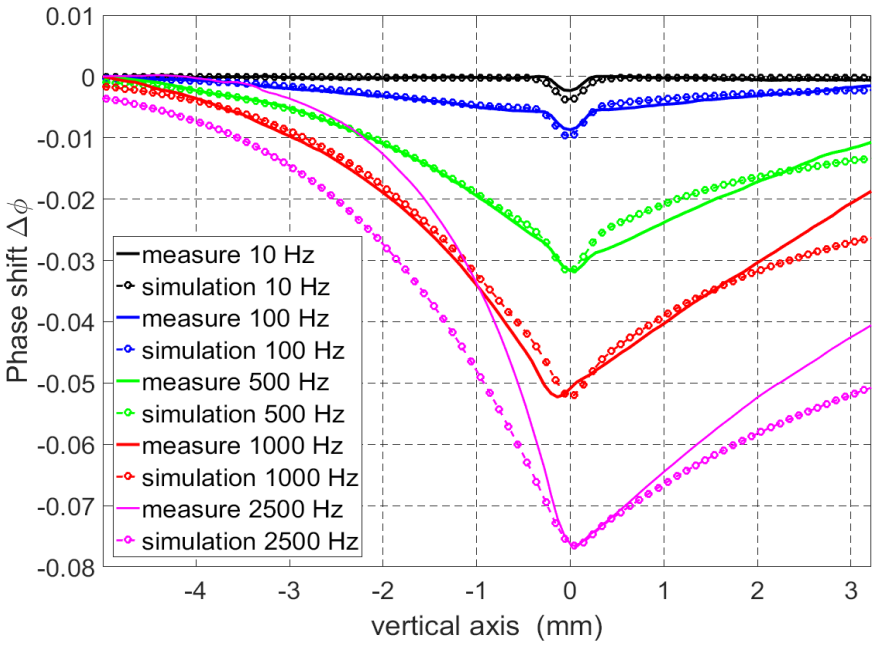

Figure 3.3.1. Phase shifts (2π rad) induced by the filamentation of 0.8 mJ, 35 fs laser pulses focused at f/100, measured 100 ms after the last laser pulse (full line) and corresponding simulations (circles), at various repetition rates ranging from 10 to 2500 Hz.

In Figure 3.3.1, the phase shifts induced by filamentation of the laser focused at f/100, measured at different repetition rates, are presented together with the simulated phase shift using the input parameters ΔT_0 = 18 K and R_0 = 170 mm. The delay between the last laser pulse and the observation time is set to 100 µs to ensure that the shockwave induced by the last laser pulse has exited the studied zone. A clear cumulative effect can be seen starting at 100 Hz and increasing at higher repetition rates. The simulated phase shifts show good agreement with the measurements. The

initial temperature variation of 18 K is small enough to neglect interaction between pulses and ensure the validity of the use of our model.

One important aspect of this cumulative effect is its longevity. At repetition rates higher than 100 Hz, the delay that separates each pulse is shorter than the lifetime of each individual under-dense channel. As a consequence, a permanent under-dense channel is formed during the whole laser operation. The channel then consists of two parts: one that evolves over a millisecond time scale due to the heating by the last laser shot, and a second one that is constant over time and is due to the accumulation of heating by all previous laser shots.

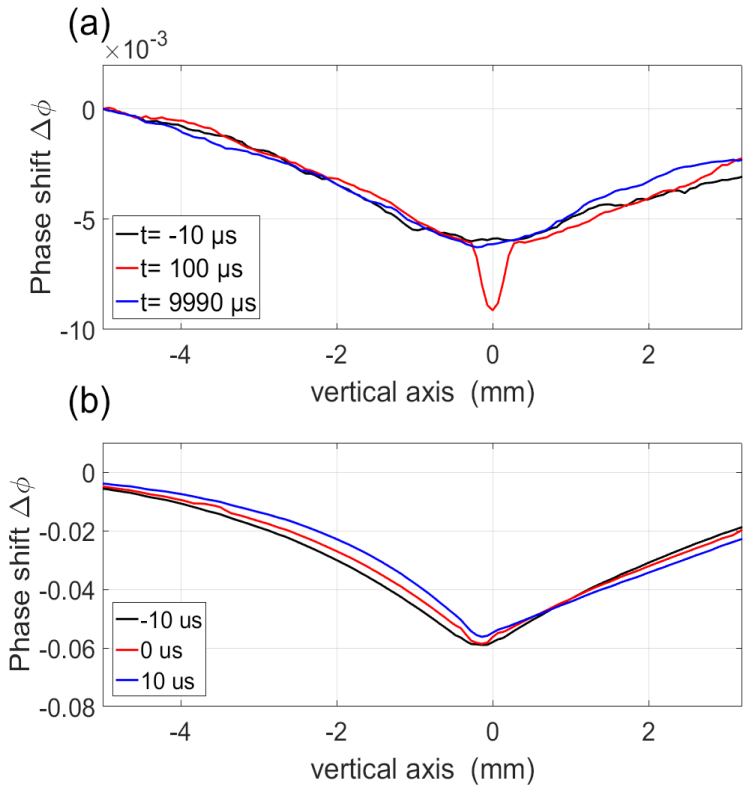

Figure 3.3.2: Phase shifts (2π rad) induced by the filamentation of a 0.8 mJ, 50 fs, 800 nm laser at a repetition rate of (a) 100 Hz and (b) 1000 Hz, measured at different delay from the last laser pulse.

This evolution of the two parts of the channel can be seen in Figure 3.3.2, where measurements of the phase shift at different delays from the last laser pulse for repetition rates of 100 Hz and 1000 Hz are presented. In Figure 3.3.2(a), the fast evolution that is generated by the last laser pulse can be seen on the measurement made at delay of 100 µs, but is not seen at the delay of 9990 µs because it has already fully merged within the accumulated heating. The second part is constant in the three measurements, proving its long lifetime. In Figure 3.3.2 (b), for the repetition rate of 1000 Hz the permanent part of the channel is so important that the fast-evolving part is difficult to distinguish.

3.4 THz transmission spectroscopy of the filament

One hypothesis needed for the validity of our measurement of the density variation is the absence of electrons at the µs timescale of our measurement. This hypothesis is indeed correct in the single shot regime due to the lifetime of the electrons being in the order of tenth of ns. However, it is not as straightforward in the high repetition rate regime, due the reduction of the air density resulting from all previous pulses filaments that may increase the electrons lifetime and due to the repletion rate that could lead to an accumulation of electrons even if only a small percentage of them stays present long enough.

To remove this uncertainty, measurements were done using THz waves to probing the electron density in the filamentation zone. The principle is as follow: The plasma created by the filament act as a high pass filter for electromagnetic waves with a cut of that is called by the plasma frequencyω_p, defined as:

$$\omega_p = \sqrt{\frac{n_e\, e^2}{m\, \varepsilon_0}},$$

where n_e is the electron density, e is the elementary electric charge, m is the effective mass of the electron and ε_0 the electric permittivity of free space. To ease the following discussion, we can rewrite the expression as a function of the ionisation rate $\tau_{ionisation}$:

$$\omega_p = \sqrt{\tau_{ionisation}} \times \sqrt{\frac{n_0\, e^2}{m\, \varepsilon_0}} = \sqrt{\tau_{ionisation}} \times 280 \text{ THz},$$

where n_o is the air neutral density.

By sending an electromagnetic wave with a broad spectrum through the filamentation zone, we can observe what spectral part of the wave is transmitted, thus we can observe the value of the plasma frequency. By sending the probing wave at different delay, we can measure the temporal evolution of the value of the plasma frequency. The plasma frequency being directly linked to the electron density, we can monitor the evolution of the electron density and confirm the non presence of electron over the μs timescale.

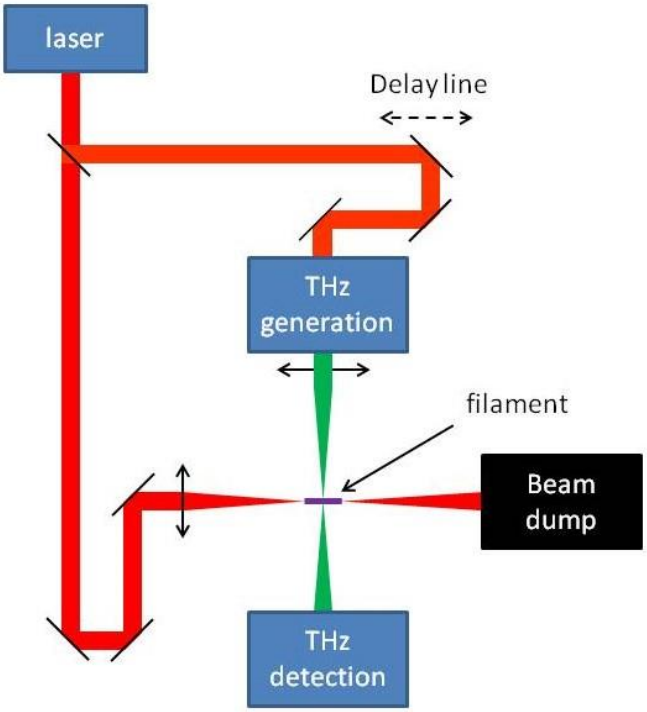

Figure 3.4.1: Experimental setup used to probe the filament by sending THz wave through it.

The experimental setup is presented in figure 3.4.1. The laser used for this experiment had an energy of 2.5 mJ per pulse, a duration of 35 fs and a repetition rate of 5000 Hz. The beam was sent through a beam splitter (R=67%, T=33%) so that a part is used to create the filament while another part is used to create the THz radiation, as described in [17], that is focused onto the filament and will act as a probe. The filament pump – THz probe delay is adjusted by means of a 15-cm long delay line. The part of THz radiation that is transmitted through the filament is then collected and detected

by electro-optic sampling in a ZnTe crystal. Fourier transform of the detected signal yields the transmitted THz spectrum.

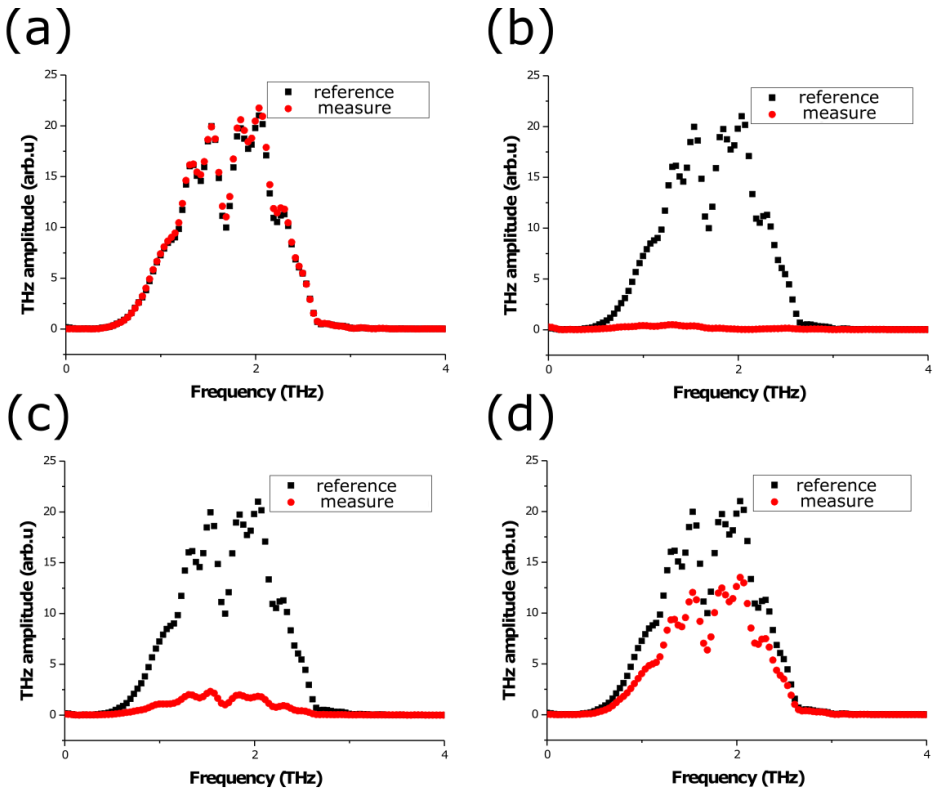

Figure 3.4.2: Comparison between the reference unperturbed THz spectrum and the THz spectrum measured at the delays (a) -16 ps, (b) 0 ps, (c) 133 ps, and (d) 246 ps relative to the last laser pulse.

Figure 3.4.2 shows the results of the measurements made at delays of (a) -16 ps, (b) 0 ps, (c) 133 ps, and (d) 246 ps relative to the last laser pulse and compare them to the unperturbed THz spectrum that is recorded than no filament are present. The unperturbed THz spectrum shows a signal from 0.7 to 2.6 THz, allowing us to probe a range of ionisation rate from 6.25×10^{-6} to 8.6×10^{-5}. If no perturbation of the THz signal is observed, that means that the ionization rate in the probed region is less than 6.25×10^{-6}. On the contrary, if no THz signal is measured, that means the ionisation rate if higher than 8.6×10^{-5}.

Both of these cases are observed at a delay of -16 ps and 0 ps, respectively. This means that the density of electrons measured just before a laser pulse, corresponding to what could have been possibly accumulated from all the previous pulses, is lower than 1.54×10^{20} e/m^3. It is however more difficult to have a clear answer to the evolution of the density of electron just after a laser pulse: At a delay 0, we know that the electron density is measured higher than 2.13×10^{21} e/m^3 because no THz are transmitted through the filaments plasma. For the other delays of 133 ps and 246 ps, a more important part of the signal is transmitted, showing a decrease of the electron density. Contrary to what we could have expected no clear cut off is observed, and the evolution of the transmission shows an increase of it for the entire spectrum. This behaviour can be explained by the limit of spatial resolution of our setup: Due to the diffraction limit the THz wave has a diameter of $1.22 \times \lambda \times N.A$, giving us values of 280 and 140 µm for 1 and 2 THz, respectively (Similar results were obtained by knife-edge measurements performed at the THZ focus). These values are similar to the transverse size of the filament itself (Sideview imaging of the plasma emission yields a vertical extent of 150 µm for a standard filament and of 350 µm with additional astigmatism onto the pump beam). The probing of the THz is thus not made at specific point of the filament but over its whole diameter. The electron density inside the filament being non homogeneous (as seen in figure 2.4.1), different parts

of the THz beam will encounter different electron density, thus will face a different cut off frequency. The sum of all these parts transmitted with a different cut off frequency could then lead to the signal measured in at the delays of 133 ps and 246 ps.

However, while this THz measurement failed to gives a clear evolution of the electron density after the filament, it gives us a clear confirmation that no electrons of significant number are accumulated at high repetition rate. The hypothesis of the absence of electrons at the µs timescale of the neutral density variation is thus confirmed.

3.5 Effect of the wind

Because the cumulative effects are related to air dynamics, they are sensitive to a change of air flow [15]. To quantify the latter effect, we measured the phase shift induced by the previously described laser filaments operating at repetition rates varying from 500 to 2500 Hz in the presence of a steady upward air flow of variable speed created by a fan blower.

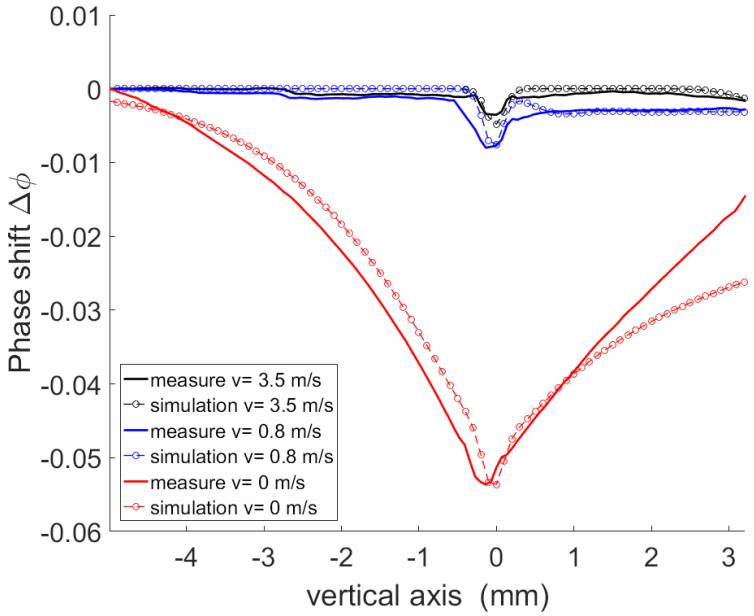

Figure 3.5.1: Phase shifts induced by the filamentation of 0.8 mJ, 35 fs laser pulses at a 1000 Hz repetition rate, focused at f/100. (a) Phase shifts measured (full line) and simulated (circles) with different air flows. Input parameters for simulations are ΔT_0 = 18 K and R_0 = 170 µm.

The results measured at 1000 Hz compared with the simulated phase shifts calculated with an appropriate value $v_{air\ flow}$ are shown in Figure 3.5.1. As $v_{air\ flow}$ increases, the cumulative effect is greatly reduced. At 1000 Hz, the cumulative effect has completely disappeared when the flow velocity exceeds $v_{air\ flow}$= 3.5 m.s^{-1}.

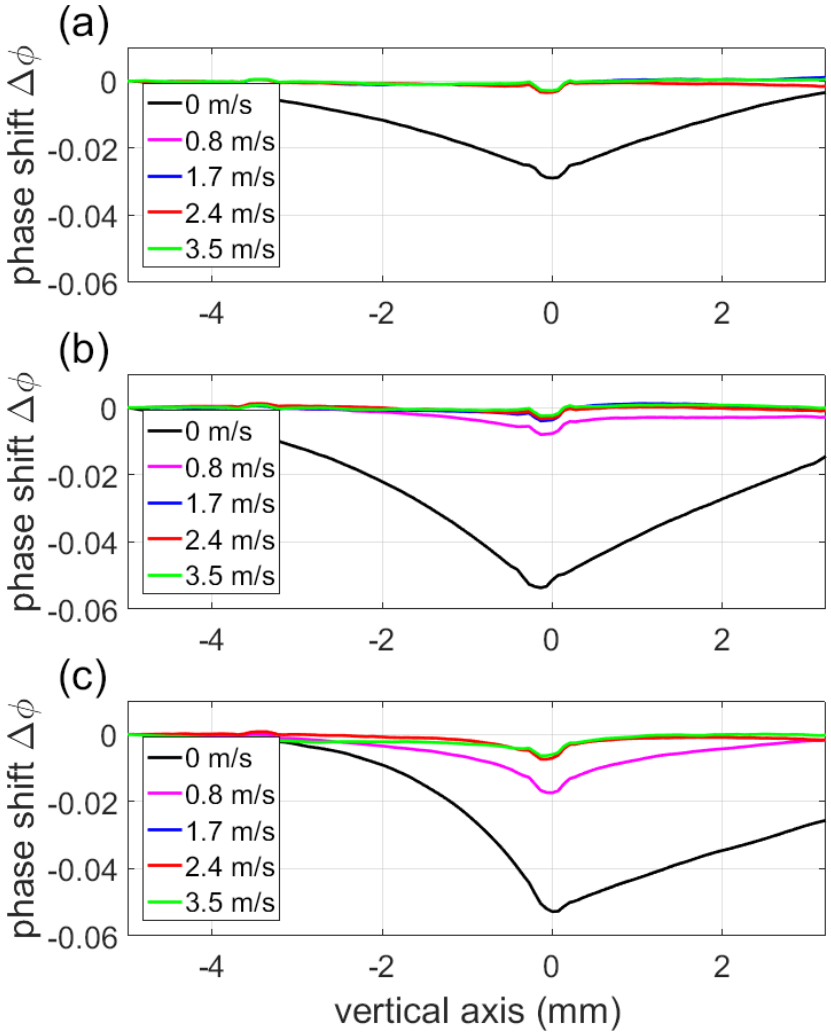

Figure 3.5.2: Measured phase shifts induced by the filamentation of 0.8 mJ, 35 fs laser pulses, focused at f/100, at a repetition rate of (a) 500 Hz, (b) 1000 Hz and (c) 2500 Hz, with different air flows.

The results of the experiment repeated at a repetition rate of 500 Hz, 1000 Hz and 2500 Hz, presented in Figure 3.5.2, shows that at 500 Hz the cumulative effect has already disappeared at $v_{air\ flow}$= 0.8 m.s^{-1}, while at 2500 Hz it is still visible and more important than at 1000 Hz. This showed that the air flow threshold that nullifies the cumulative effect decreases as the laser repetition rate is decreased.

3.6 Variation of the laser pointing

The cumulative effect appearing at high repetition rate results in an asymmetrical under-dense channel due to the buoyant force. This asymmetry of the density of the medium in which each laser pulse propagates results in a modification of the propagation path. A smaller density being seen by the top part of the laser beam compared to its lower part, it undergoes a downward deflection as it propagates through the region of the cumulative effect.

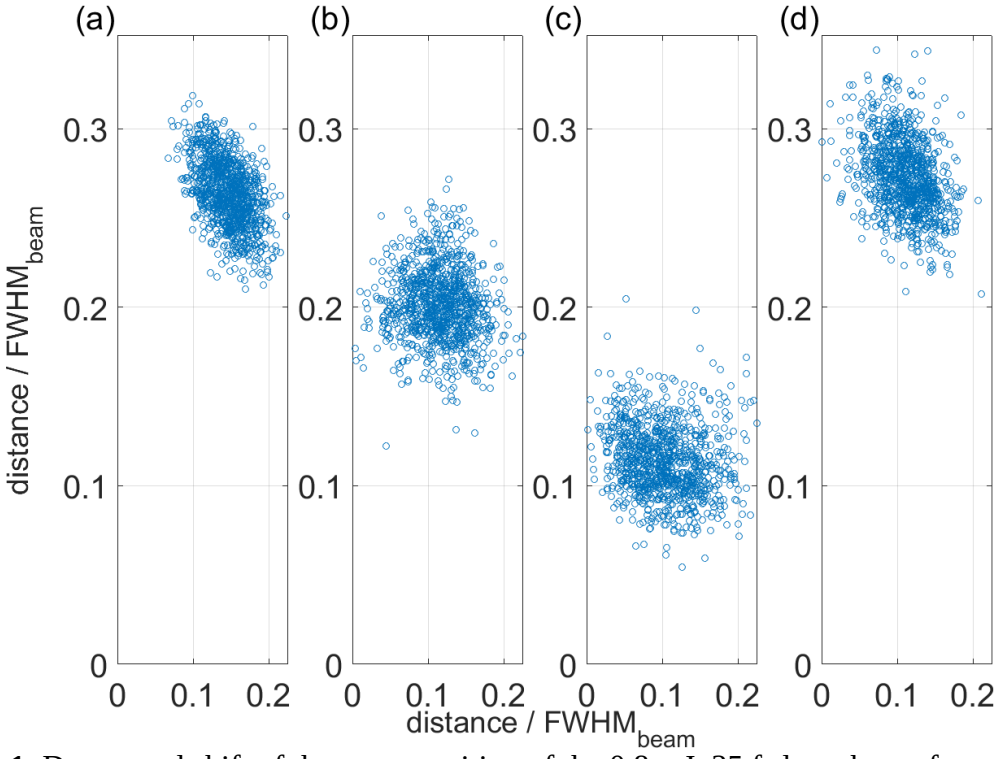

Figure 3.6.1: Downward shift of the mean position of the 0.8 mJ, 35 fs laser beam focused at f/100 measured 25 cm after the filamentary zone, measured without air flow at 10 Hz (a), 100 Hz (b), 1000 Hz (c), and at 1000 Hz with air flow (d).

The measurements of this downward shift are presented in Figure 3.6.1 for different repetition rates. The density variation and asymmetry both increasing with higher repetition rate, the downshift is expected to be more important at higher repetition rate. This is confirmed and clearly visible on the measurements. The use of an air flow being able to suppress the cumulative effect, it should nullify this beam wandering as confirmed by the measurement.

3.7 Reduction of the breakdown voltage at different repetition rates

The formation of an under-dense channel by the filament is the main mechanism responsible for the reduction of the breakdown voltage between two electrodes [16], [19], [20]. The density decrease in the channel lowers the breakdown voltage between two charged electrodes, forming a preferential path for the discharge. Other filament effects that can also influence the discharge propagation are the presence of long-lived free electrons [21] or electrons loosely attached to oxygen molecules that are generated during the plasma recombination [1], [22].

The filament cumulative effect leading to an enhanced under-dense channel, one can therefore expect it to further reduce the breakdown voltage between two electrodes. Since the part of the channel resulting from the cumulative effect is constant, one expects a reduction of the breakdown voltage that is constant over time. This removes the need of precise synchronization between the laser pulse and the high voltage increase that would lead to the breakdown [23].

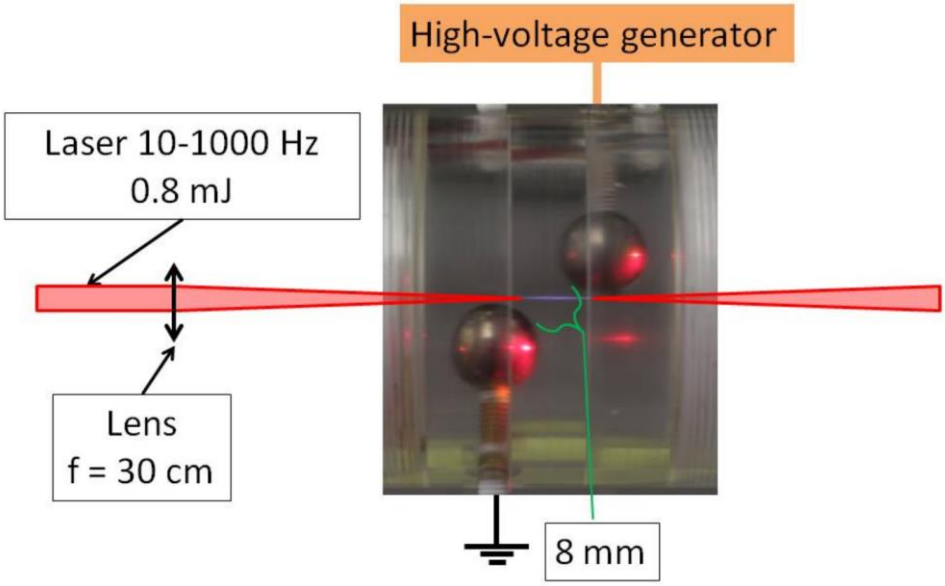

Figure 3.7.1: Experimental setup used to measure the reduction of the breakdown voltage induced by filamentation at different repetition rates.

We investigated this concept by triggering spark discharges with a system composed of a high-voltage pulsed generator and two spherical electrodes placed in the vicinity of the filament, as depicted in Fig. 3.7.1. These measurements were repeated in air and pure nitrogen to be able to distinguish the effect of the under-dense channel from the possible contribution of electrons loosely attached to oxygen molecules [22].

The high-voltage generator could deliver single-shot voltage pulses with 5 ns duration and a maximum amplitude of 30 kV. Each voltage value was measured with a precision of 2%. The breakdown voltage U_{BD} was defined as the voltage for which a breakdown probability of 100 % was obtained over 10 shots. The applied voltage pulse could be delayed or advanced with respect to the laser pulse.

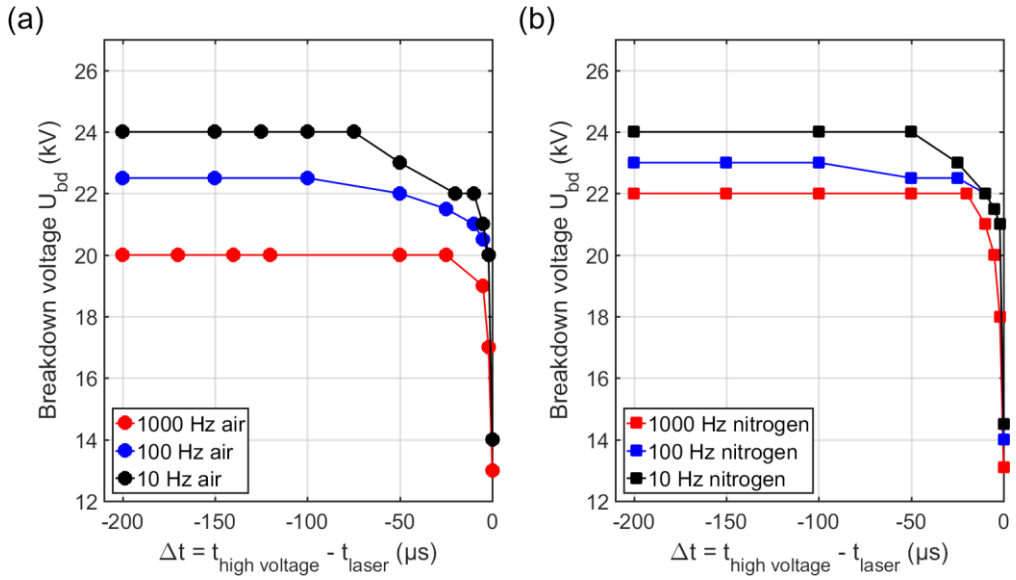

Figure 3.7.2: Breakdown voltage measured with 0.8 mJ, 35 fs laser pulses focused at f/100, as a function of the delay between the high voltage pulse and the last laser pulse, at different laser repetition rates. (a) Measurements made in ambient air. (b) Same measurements made in pure nitrogen. In both cases, the natural breakdown without laser is 29 kV.

Figure 3.7.2 presents the measured breakdown voltage as a function of the delay between the high voltage pulse and the last laser pulse at different repetition rates ranging from 10 Hz to 1000 Hz. The evolution of the breakdown voltage can be split in two parts: the first one, evolving over a µs timescale, is linked to the quick evolution of the under-dense region. The second one, produced by the cumulative effect, is quasi-constant over the studied timescale of 200 ms. As expected, this second part leads to a reduced breakdown voltage as the repetition rate of the laser is increased.

Repetition rate (Hz)	Expected U_{BD} (kV)	Measured U_{BD} in air (kV)	Measured U_{BD} in nitrogen (kV)
10	24	24.0	24.0
100	23.4	22.5	23.0
1000	21.9	20.0	22.0

Table 3.7.1: Table comparing the expected breakdown voltage with the measurements made in air and in pure nitrogen, at a delay of -100 µs for the different laser repetition rates.

Using the air dynamics model we calculated the density variation and the theoretical breakdown voltage U_{BD} for each repetition rate and compared it with the measurements. These values are presented in Table 3.7.I. We note that the measurements made in pure nitrogen match well the theoretical values for the reduced breakdown voltage. However, the measured breakdown fields in air are lower than the expected values for 100 Hz and 1 kHz. Considering that ionization and laser energy deposition in the filament are almost the same in air and in nitrogen [24], the same breakdown field should be observed if the filament hydrodynamic was the only guiding mechanism.

We attribute this discrepancy to the presence of long-lived O_2- ions at high laser repetition rate. These ions provide a reserve of easily detached electrons that facilitate the electrical breakdown. Due to their long lifetime, they can be accumulated at high repetition rate and contribute to the cumulative effect by reducing even further the breakdown voltage [22].

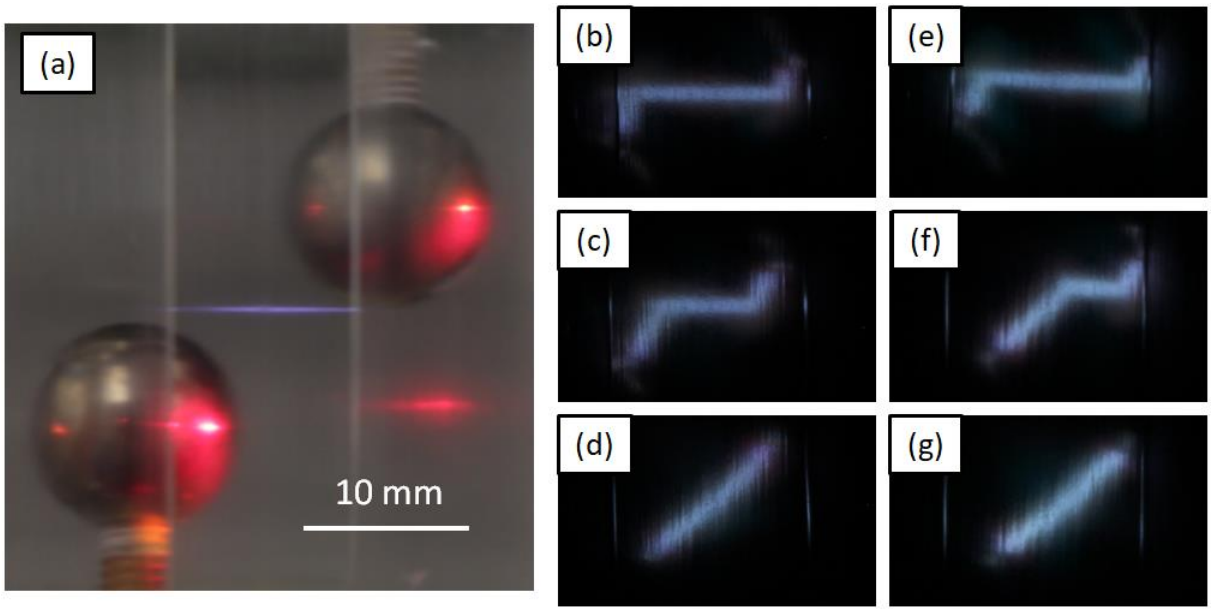

Figure 3.7.3: Pictures of the filament region showing the plasma luminescence and the two electrodes (a). Pictures of the discharge in air for three different triggering delays between the high

voltage pulse and the femtosecond laser pulse: -2 µs (b), -25 µs (c) and -100 µs (d). Pictures of the discharge in pure nitrogen for the same triggering times: -2 µs (e), -25 µs (f) and -100 µs (g).

Figure 3.7.3 (a) presents a still picture of the filament region and in figures 3.7.3 (b-g) pictures of the discharge path are presented for three different delays between the laser and the high-voltage pulse, made with a laser repetition rate of 1 kHz. At a delay of -2 µs, the discharge is clearly guided along the laser path. As the delay increases, the distance over which the discharge follows the laser path is reduced. At short delays, the discharges are indeed still affected by the spatial perturbation made by the last laser pulse. At longer delays, the only remaining perturbation is the one resulting from the cumulative effect. The latter, being spatially wider than the distance between the electrodes, helps the triggering of the discharge without imposing a specific path. The discharge path is then determined by the electric field lines imposed by our setup, as it is the case in regular discharges. The similarity of the discharges paths when they are realized in air or in nitrogen shows that the accumulation of both the heating and the O_2- ions occurs on similar spatial scale.

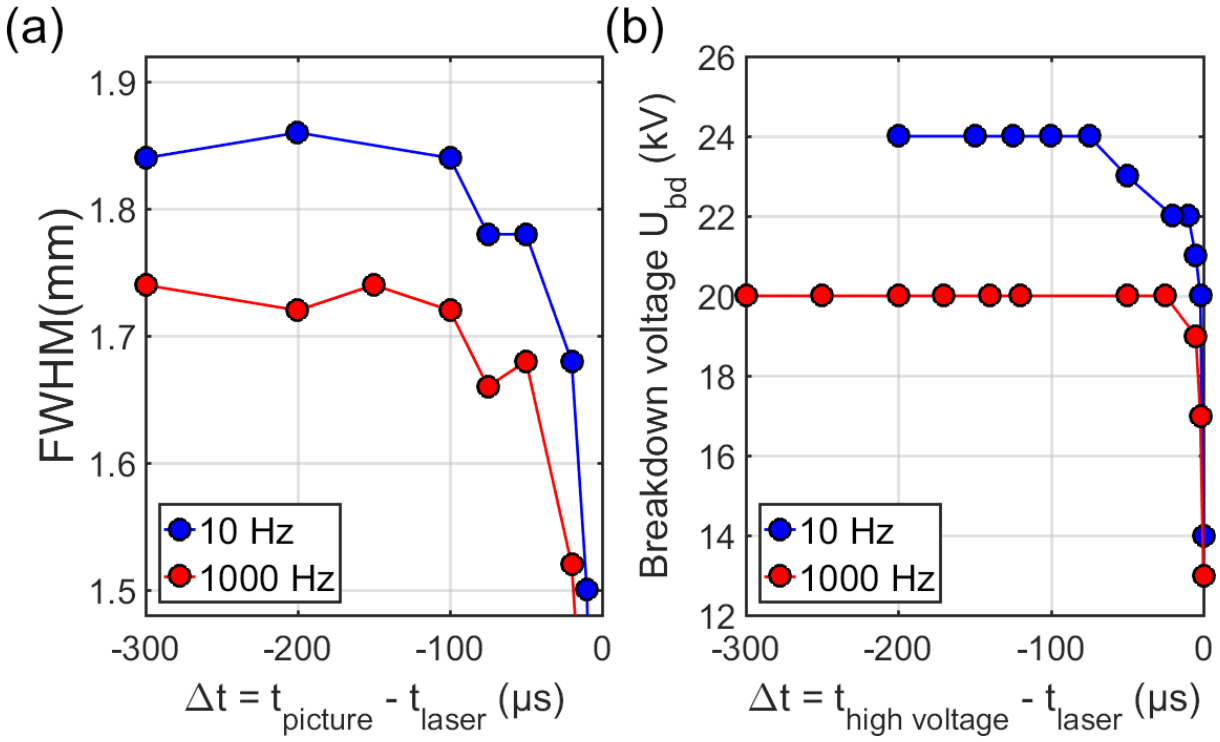

Figure 3.7.4: Evolution of (a) the discharge FWHM and (b) the breakdown voltage inducing by a 0.8 mJ, 35 fs laser pulses focused at f/100 and at a repetition rate of 1000 Hz, as a function of the delay between the high voltage pulse and the last laser pulse.

The evolution of the width of the discharge path as a function of the delay between the high voltage pulse and the last laser pulse can be retrieved from these same pictures. This evolution is plotted in figure 3.7.4 for a repetition of 1000 Hz and compared to the evolution of the corresponding breakdown voltage reduction. A clear similarity can be seen in the two evolutions.

At these short delays, the discharge path being determined by the spatial perturbation made by the last laser pulse, the width of the discharge can be seen as the width of the under-dense channel created by the laser pulse. Thus, the reduction of the breakdown voltage at short timescale seems to follow the evolution of the width of the last created under-dense channel. This hypothesis is consistent with the width of the laser path being constant over long timescales: at such delay, the last created

under-dense channel already merged with the channel resulting from the cumulative effect. This channel being constant in time, the discharge width remains constant.

3.8 Difference between horizontal and vertical filamentation

One interesting point to consider while studying the cumulative effect is its dependence to the laser direction since the buoyant force moves each under-dense channel upward. When the laser propagates horizontally, the buoyant force moves each under dense channel away from the laser path, resulting in a cumulative channel with the typical asymmetric shape discussed in this chapter. In this case, all the consecutive channels contribute (provided the repetition rate exceeds 100 Hz) but they don't fully overlap because they are not aligned. By contrast, when the laser propagates vertically, the buoyant force moves each channel in the same direction as the laser path. In this case, each under-dense channel keeps the same alignment and overlap with the previous ones, resulting in a cumulative channel that has a smaller radius, but is longer and has a greater density variation.

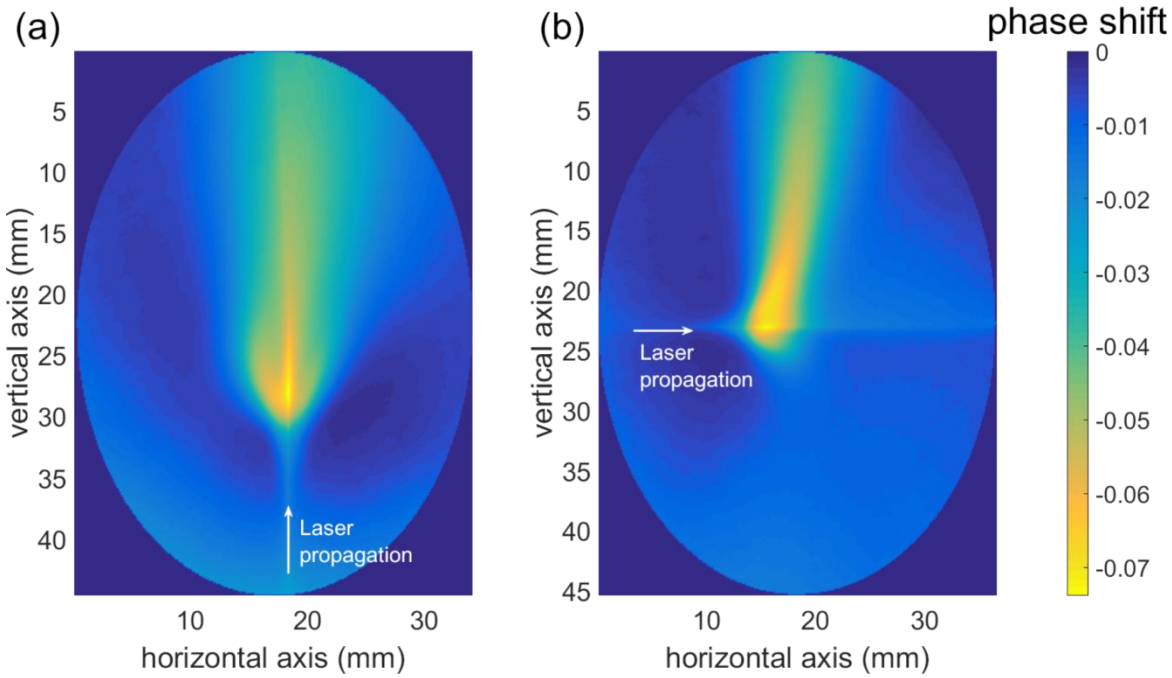

Figure 3.8.1: Measured phase shift induced in the case of (a) a laser propagating vertically and (b) a laser propagating horizontally.

To study this effect, we used a 1 kHz laser creating 0.8 mJ, 35 fs pulses that were focused at f/200. We measured the phase shift induced by the under-dense channel 100 µs after the last laser pulse for both cases of the laser propagating horizontally and vertically. The result, presented in figure 3.8.1, confirms our expectancies. In the case of the laser propagating horizontally, a significant heating is seen away from the filament axis, while the heated zone stays on the filament axis in the case of the laser propagating vertically.

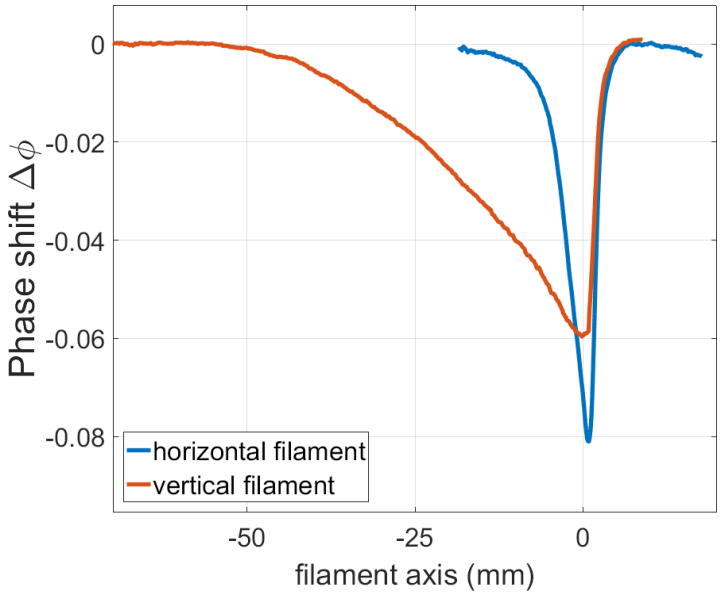

Figure 3.8.2: Measured phase shift induced along the filament axis in the case of a laser propagating vertically and a laser propagating horizontally.

By looking at the measured phase shift along the filament axis in both configurations, as presented in Figure 3.8.2, we see that the phase shift, and thus the density reduction, is important over a longer distance in the case of the vertical filament.

The under-dense channel being responsible for the reduction of the air breakdown voltage, a longer and more important channel should lead to a greater reduction of the breakdown voltage over a longer distance. To verify this hypothesis, we used the same laser focused at f/100 and added to the setup two flat electrodes separated by a distance of 1 cm and pierced in their center to let the filament pass through. We measured the breakdown voltage between them in the presence of the filament while moving the electrodes along the laser path, allowing us to quantify the spatial evolution of the breakdown voltage reduction. These measurements were repeated for both the case of a horizontal and vertical filament.

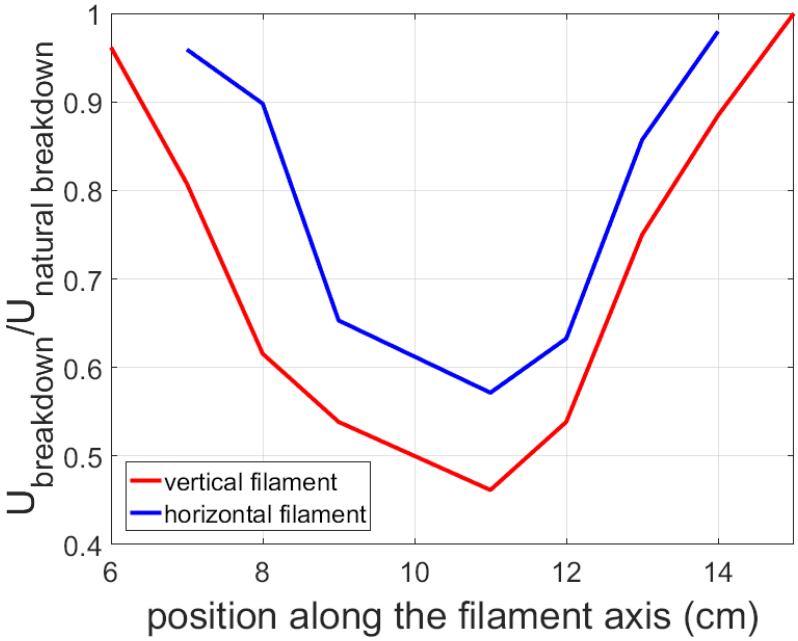

Figure 3.8.3: Measured reduction of the breakdown voltage at different positions along the filament axis for both a vertical and horizontal axis.

The results, presented in Figure 3.8.3, show that the reduction of the breakdown voltage is indeed larger in the case of a vertical filament and occur over a longer distance. The maximum reduction reaches 54 % for the vertical filament and only 43 % for the horizontal filament. The full widths at half maximum of the spatial evolution of the breakdown voltage reduction are 5.2 cm and 4 cm for the vertical and horizontal filament, respectively. If we consider the integrated breakdown reduction over the whole filament, we have an increase of 63 % of the breakdown reduction in the case of a vertical filament.

We can try to understand this phenomenon by using a similar model of the thermal evolution of each consecutive under-dense channel as described in the section 2.5.

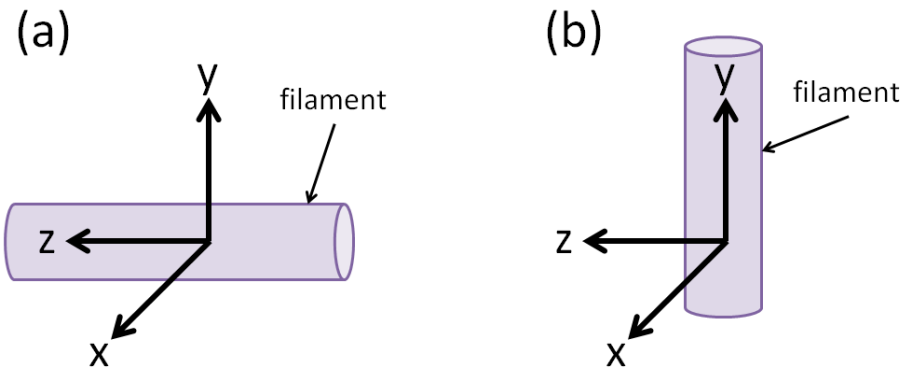

Figure 3.8.4: Position of the filament according to the axis used in the simulation, in the case of (a) a horizontal filament and (b) a vertical filament.

Using the axes frame shown in figure 3.8.4, we can express the temperature variation in the case of a horizontal filament $\Delta T_{\text{horizontal}}$ and in the case of a vertical filament $\Delta T_{\text{vertical}}$ as:

$$\Delta T_{horizontal}(x,y,z,t) = \Delta T_0 \times \frac{{R_0}^2}{(\sqrt{{R_0}^2+4\alpha t})^2} \times e^{-\frac{x^2+(y-v(t)\times t)^2}{(\sqrt{{R_0}^2+4\alpha t})^2}} \times e^{-\frac{z^2}{(\sqrt{{L_0}^2+4\alpha t})^2}},$$

$$\Delta T_{vertical}(x,y,z,t) = \Delta T_0 \times \frac{{R_0}^2}{(\sqrt{{R_0}^2+4\alpha t})^2} \times e^{-\frac{x^2+y^2}{(\sqrt{{R_0}^2+4\alpha t})^2}} \times e^{-\frac{(z-v(t)\times t)^2}{(\sqrt{{L_0}^2+4\alpha t})^2}},$$

where α is the thermal diffusivity of air [14], ΔT_0 the peak temperature change of the initial Gaussian temperature distribution, R_0 the initial filament radius, L_0 its initial length and $v(t)$ the speed at which the channel move upward, as described in the section 2.5.

From these expressions, we can calculate the phase shift integrated along the *x* axis, as will be measured by our setup, when creating filament at a repetition rate *f* for both the horizontal and vertical configuration:

$$\Delta\varphi_{horizontal/vertical}(y,z,t) = -\frac{2\pi\beta}{\lambda}\int \sum_{i=0}^{\infty} \frac{\Delta T_{horizontal/vertical}(x,y,z,t+\frac{i}{f})}{T_{amb}} dx.$$

where T_{amb} is the air room temperature, $\beta = 2.7 \times 10^{-4}$ the Gladstone-Dale constant, and λ the wavelength of the probe laser.

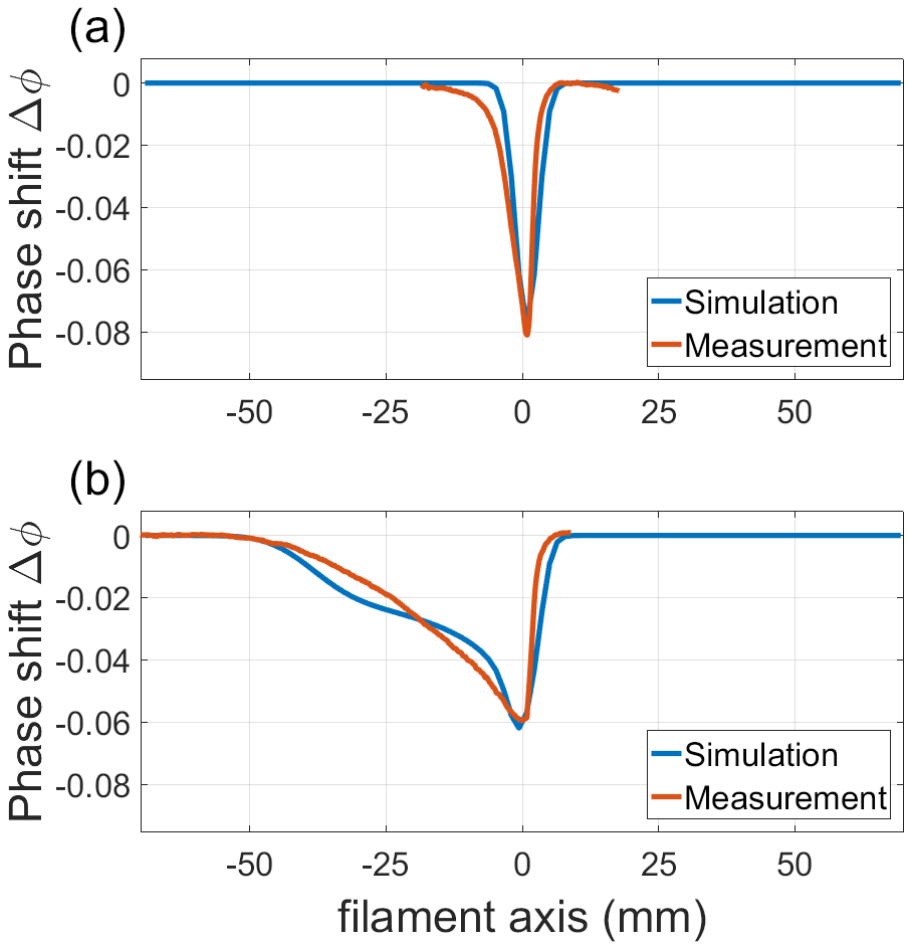

Figure 3.8.5: Comparison between the measured and simulated phase shift along the filament axis for both an (a) horizontal and (b) a vertical filament, measured at 1000 Hz.

We can then plot the evolution of the integrated phase shift along the filament axis for both horizontal and vertical setups. The results, presented in figure 3.8.5, show a good agreement between the simulation and the measurements. The values used for both L_0 and R_0 are retrieved from the experimental measurements, and the value of ΔT_0 is chosen as 250 K to best fit our measurement.

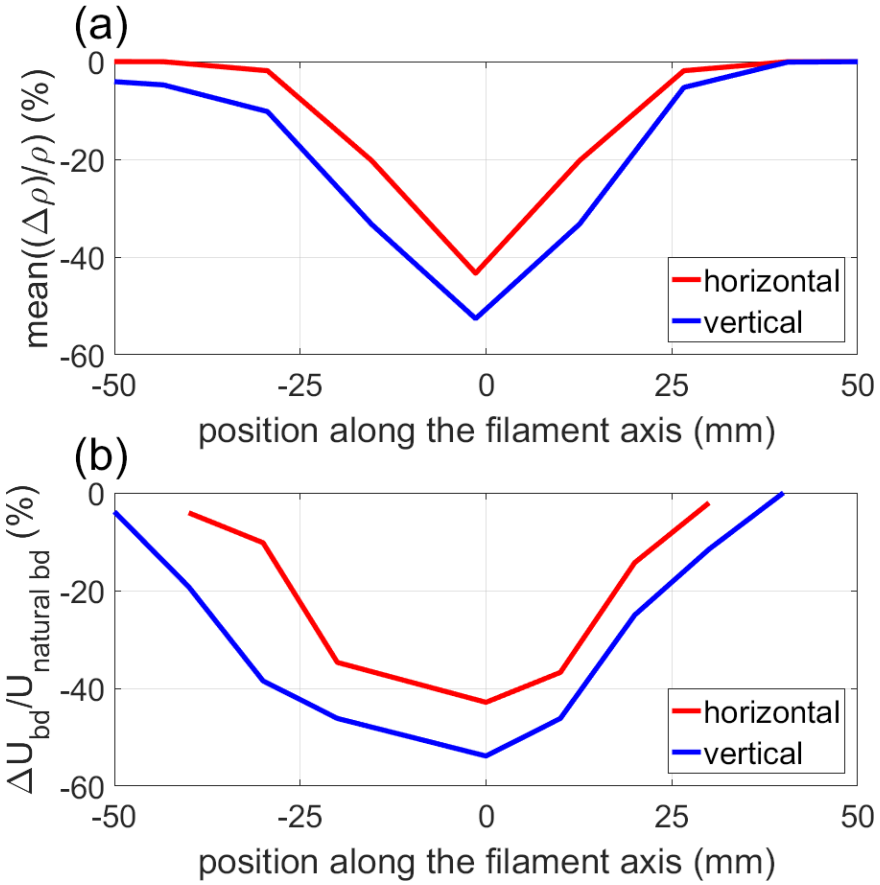

Figure 3.8.6: Comparison between (a) the mean of the simulated density variation between the two electrodes and (b) the measured reduction of the breakdown voltage, at different position along the filament axis for both a vertical (blue) and horizontal (red) filament, measured at a laser repetition rate of 1000 Hz.

Using this model, we can also use the simulated under-dense channels to quantify the reduction of the breakdown voltage between the two electrodes. From the simulation, we can retrieve the mean value of the density variation $\frac{\Delta n}{n_{amb}}$ between the two electrodes at the different positions along the filament axis and compare it to the reduction of the breakdown voltage $\frac{\Delta U_{bd}}{U_{natural\,bd}}$ measured at these same positions. The results, presented in figure 3.8.6, show a good match between the simulation and the measurement. If again we calculate the increase in the integrated reduction of density, we have an increase of 55.9% for the vertical filament compared to the horizontal one. This value is similar to the increase of 63% that was observed in the measurement of the breakdown reduction in the case of a vertical filament compared to the horizontal one.

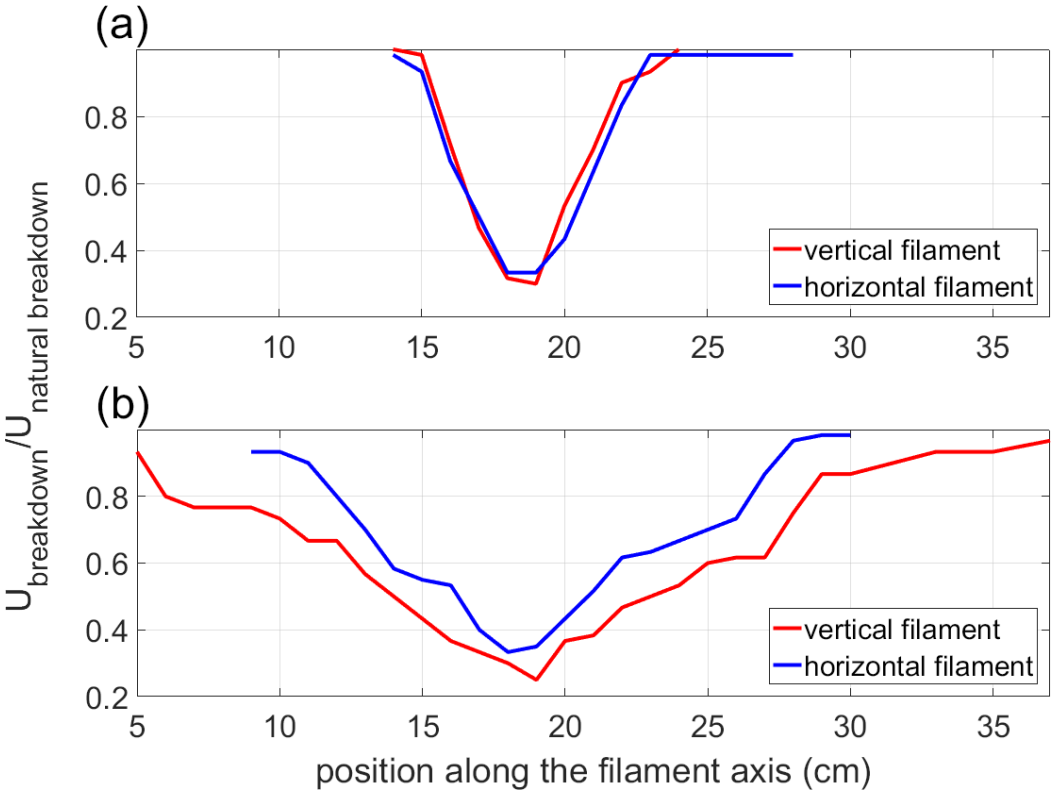

Figure 3.8.7: Measured reduction of the breakdown voltage at different position along the filament axis for both a vertical and horizontal axis, measured at (a) 1 Hz and (b) 100 Hz.

To confirm our understanding of this effect, we made a new series of measurements using the 14 mJ laser that was operated at repetition rates of 1 Hz and 100 Hz. The beam was focused at f/100. The results are presented in Figure 3.8.7. No differences are observed between the vertical and horizontal configuration for a repetition rate of 1 Hz. This is consistent with our explanation, because no cumulative effect that would create a difference between the two configurations is present as this low repetition rate. On the contrary, at a repetition rate of 100 Hz - at which the cumulative effect appears - the breakdown voltage reduction is larger and more extended in the case of the vertical filament.

Based on all of these measurements, we can conclude that cumulative filaments lead to a more important effect when the filaments are created in the vertical direction, as compared to the horizontal direction. This is an important observation and could play a major in the efficiency of a lot of real life application of filament such as the laser lightning rod [6] or the laser cloud clearing[25].

3.9 Particular cumulative effect appearing by strongly focusing a high energy laser

A peculiar cumulative effect was observed when strongly focusing the 14 mJ 50 fs laser at f/20. This effect was not observed when the repetition rate of the laser was 1 or 10 Hz, but appeared at the repetition rate of 100 Hz, thus calling it a cumulative effect. Furthermore, it was not observed when using our 0.8 mJ 50 fs laser, similarly focused, for all tested repetition rates ranging from 10 Hz to 2500 Hz. Thus a high energy per pulse or intensity seems to be required.

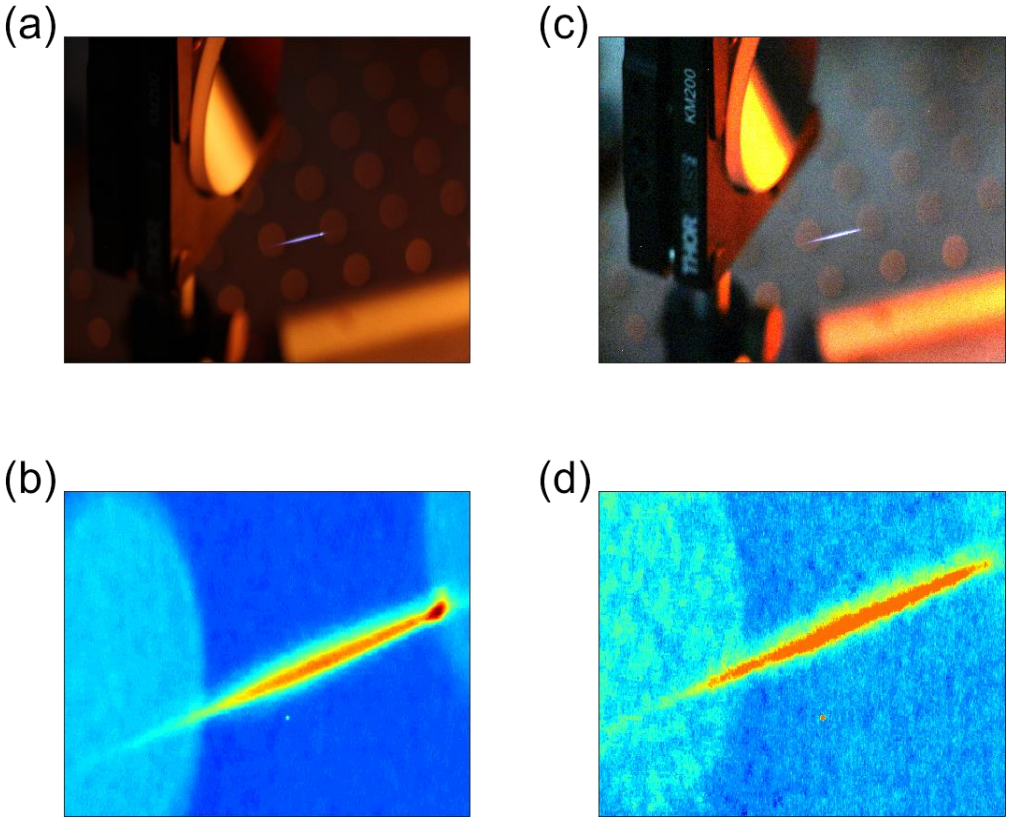

Figure 3.9.1: Real colour picture of the light emitted by the filament taken by (a) integrating during 1 s with the laser set at 100 Hz and (c) integrating during 10 s with the laser set at 10 Hz. (b) and (d) are the corresponding picture of the filament region only of (a) and (b) by converting them in false color. In all the pictures, the laser propagates from right to left.

Figure 3.9.1 (a) and (c) presents pictures from the light emitted by the filament for a repetition rate of 100 and 10 Hz. In both pictures, the integration time is set respectively to 1 s and 10 s to accumulate the light from 100 consecutive filaments. The important difference between the two pictures, highlighted in figure 3.9.1 (b) and (d), is the apparition at 100 Hz of a sphere at the end of the filament. Moreover, the filament at 100 Hz, while it starts at the same position as the one at 10 Hz, stops prematurely and does not go further than the position of the sphere.

To investigate this effect, we probed the electron density of the plasma by using the technique presented in Section 2.d. By adapting the setup presented earlier in figure 2.1.1, we measured the propagation of the ionization front of the filament for both repetition rates.

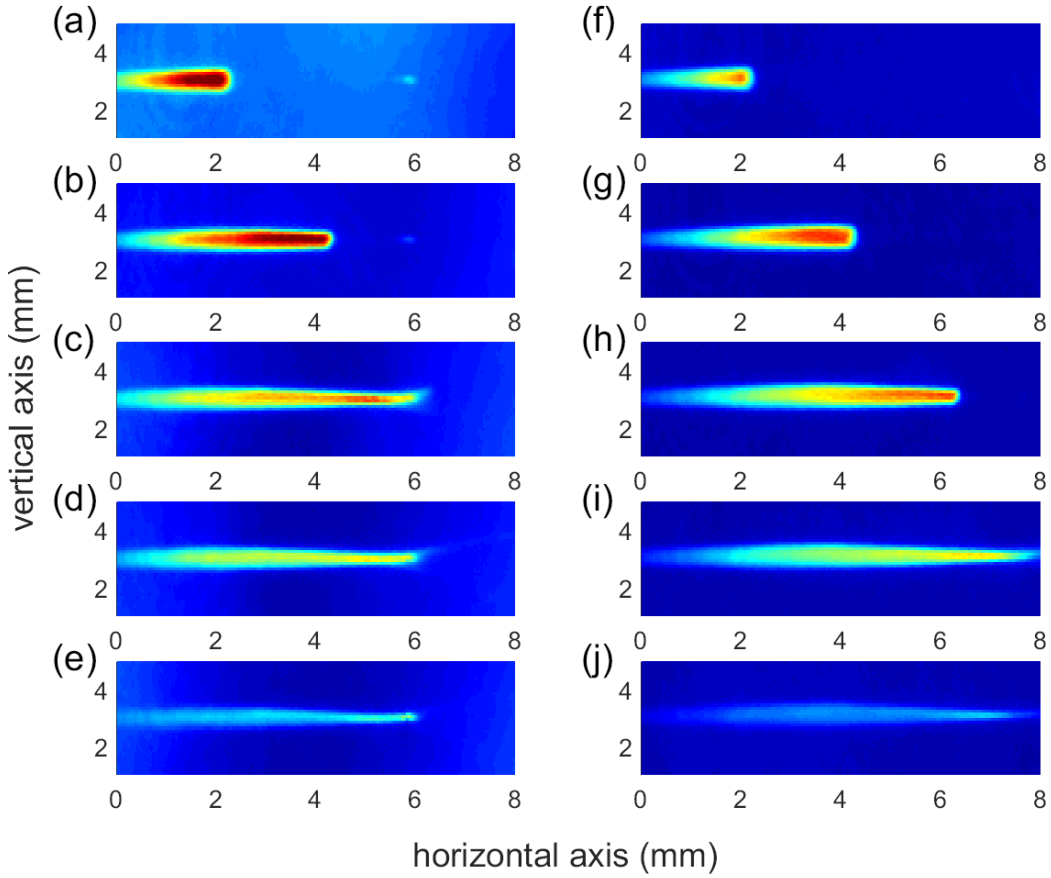

Figure 3.9.2: 2D maps of the phase shift measured by interferometry at a delay of (a and f) 5.8 ps, (b and g) 12.8 ps, (c and h) 19.8 ps, (d and i) 26.8 ps, and (e and j) 33.8 ps after the beginning of the filamentation, using a 14 mJ, 50 fs, 800 nm laser at a repetition rate of 100 Hz and 10 Hz, respectively.

The results, presented in figure 3.9.2, show a similar behaviour: For the repetition rate of 10 Hz, the ionization front of the filament propagates at the speed of light over a distance of 8 mm. Meanwhile, at 100 Hz, the ionization front propagates at the speed of light, starts at the same position, but it only propagates over 6 mm. It stops at the position 5.9 mm of the horizontal axis, where a signal coming from the sphere described earlier is observed. This signal is present even before the filamentation process of the current laser pulses starts, which means that it stays present between consecutive pulses. This behaviour and the fact that it is only observed at high repetition rate are characteristics of cumulative effects.

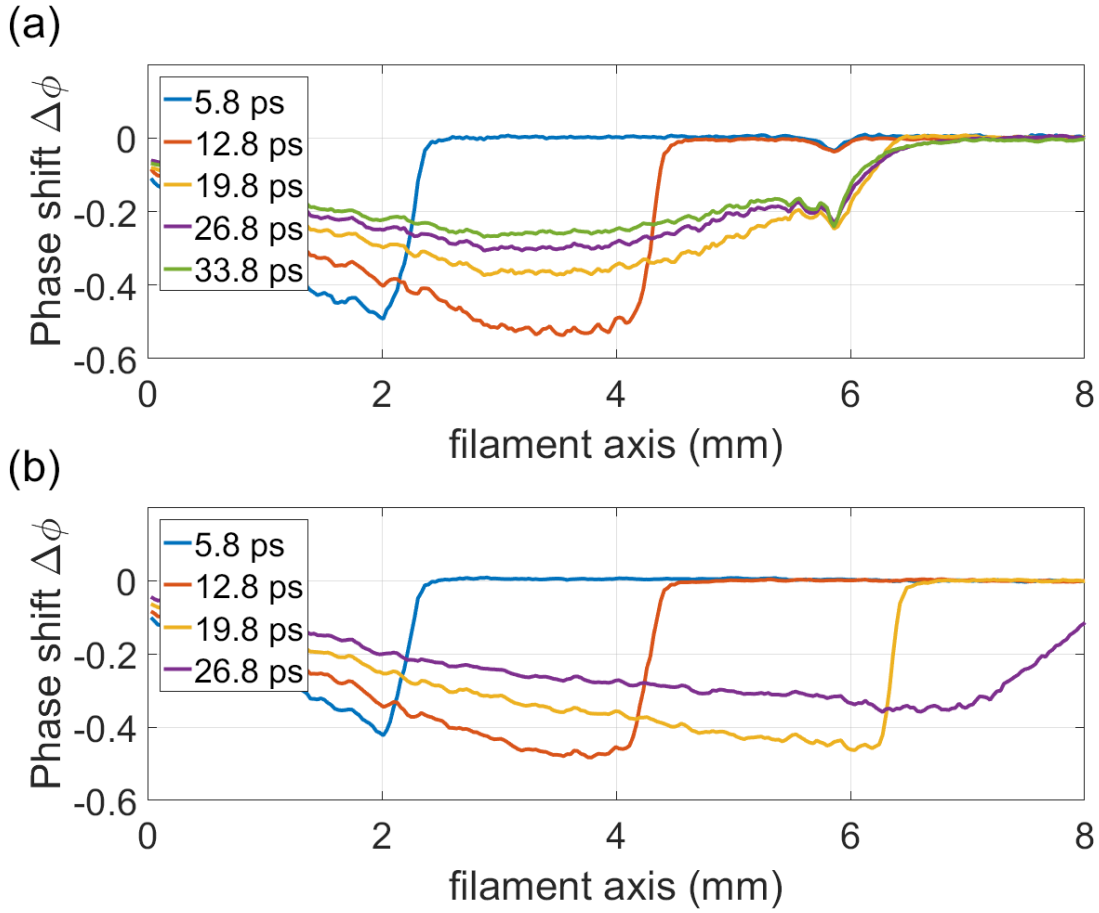

Figure 3.9.3: Measured phase shift along the filamentation axis measured at delays of 5.8 ps (in blue), 12.8 (in red), 19.8 ps (in yellow), 26.8 ps (in violet) and 33.8 ps (in green) measured at a repletion rate of (a) 100 Hz and (b) 10 Hz.

In figure 3.9.3 are presented the phase shifts measured along the filament axis at different delays during the propagation of the ionization front. Here we can clearly see that the ionization front does not propagate any further than the position of the sphere. This leaves us the question of the nature of the sphere. The interferometry technique used in this technique only using a single colour, it does not allow us to distinguish between a variation in the electron of density and a variation of the neutral density. The sphere being present over the timescale of the pulse to pulse period of 10 ms, one would think that it consists of a variation of neutral density, the electron lifetime being several orders of magnitude shorter than this. However, a neutral density variation would not completely stop the propagation of the ionization front. Such behaviour seems more like the ones observed in the presence of electron. It is important to note that due to the wavelength of our laser at 800 nm, no "plasma mirror" effect can be observed in ambient air: the highest plasma frequency achievable is of 283 THz for a fully ionised air, which is still lower than the frequency of our laser. The presence of electrons could however create a region of negative refractive index and thus increase the divergence of the beam, therefore stopping the filamentation process.

Although it is not possible to conclude about the nature of the sphere with the present measurements, we can attribute it to a cumulative effect appearing while strongly focusing a high energy laser. Further measurements, such as THz probing or dual colour interferometry, will be necessary.

4 Conclusion

In this chapter, I have shown that at high repetition rates, filamentation induces a cumulative effect resulting in the apparition of a constant over time under-dense channel with a depth and width more important than the ones created by a single filament. This cumulative effect was characterized and a model capable of simulating the effect of the repetition rates was developed. I have measured and described how this cumulative effect induced a greater reduction of the breakdown voltage of a filament guided electrical discharge. Other important aspects for real life application of the cumulative effect, such as its dependency to external air flow or to the experimental setup geometry were characterized.

I am convinced that this will be a topic of interest in the following years. With the advancement of laser technology, repetition rate and average power of laser system will continue to increase, leading to ever more important cumulative effect. Furthermore, the peculiar characteristic of the cumulative effect would play an important role for field application where an important and constant over time effect is required, such as the laser lightning rod [6] or the laser cloud clearing[25]

Bibliography

[1] Xin Miao Zhao, J.-C. Diels, Cai Yi Wang, et J. M. Elizondo, « Femtosecond ultraviolet laser pulse induced lightning discharges in gases », *IEEE J. Quantum Electron.*, vol. 31, nº 3, p. 599-612, mars 1995, doi: 10.1109/3.364418.

[2] O. G. Kosareva *et al.*, « Remote triggering of air-gap discharge by a femtosecond laser filament and postfilament at distances up to 80 m », *Appl. Phys. Lett.*, vol. 119, nº 4, p. 041103, juill. 2021, doi: 10.1063/5.0057544.

[3] D. Comtois *et al.*, « Triggering and guiding leader discharges using a plasma channel created by an ultrashort laser pulse », *Appl. Phys. Lett.*, vol. 76, nº 7, p. 819-821, févr. 2000, doi: 10.1063/1.125595.

[4] A. A. Ionin *et al.*, « Triggering and guiding electric discharge by a train of ultraviolet picosecond pulses combined with a long ultraviolet pulse », *Appl. Phys. Lett.*, vol. 100, nº 10, p. 104105, mars 2012, doi: 10.1063/1.3691918.

[5] A. Houard *et al.*, « Study of filamentation with a high power high repetition rate ps laser at 1.03 µm », *Opt. Express*, vol. 24, nº 7, p. 7437-7448, avr. 2016, doi: 10.1364/OE.24.007437.

[6] T. Produit *et al.*, « The laser lightning rod project », *Eur. Phys. J. Appl. Phys.*, vol. 93, nº 1, Art. nº 1, janv. 2021, doi: 10.1051/epjap/2020200243.

[7] A. D. Koulouklidis *et al.*, « Impact of gas dynamics on laser filamentation THz sources at high repetition rates », *Opt. Lett.*, vol. 45, nº 24, p. 6835-6838, déc. 2020, doi: 10.1364/OL.413538.

[8] A. Higginson *et al.*, « Wake dynamics of air filaments generated by high-energy picosecond laser pulses at 1 kHz repetition rate », *Opt. Lett.*, vol. 46, nº 21, p. 5449-5452, nov. 2021, doi: 10.1364/OL.439232.

[9] J.-C. Chanteloup, « Multiple-wave lateral shearing interferometry for wave-front sensing », *Appl. Opt.*, vol. 44, nº 9, p. 1559, mars 2005, doi: 10.1364/AO.44.001559.

[10] G. Point *et al.*, « Two-color interferometer for the study of laser filamentation triggered electric discharges in air », *Rev. Sci. Instrum.*, vol. 85, nº 12, p. 123101, déc. 2014, doi: 10.1063/1.4902533.

[11] P. Walch, B. Mahieu, L. Arantchouk, Y.-B. André, A. Mysyrowicz, et A. Houard, « Cumulative air density depletion during high repetition rate filamentation of femtosecond laser pulses: Application to electric discharge triggering », *Appl. Phys. Lett.*, vol. 119, nº 26, p. 264101, déc. 2021, doi: 10.1063/5.0077635.

[12] D. G. Papazoglou et S. Tzortzakis, « In-line holography for the characterization of ultrafast laser filamentation in transparent media », *Appl. Phys. Lett.*, vol. 93, nº 4, p. 041120, juill. 2008, doi: 10.1063/1.2968190.

[13] M. Centurion, Y. Pu, Z. Liu, D. Psaltis, et T. W. Hänsch, « Holographic recording of laser-induced plasma », *Opt. Lett.*, vol. 29, nº 7, p. 772, avr. 2004, doi: 10.1364/OL.29.000772.

[14] « E. ToolBox, “Air - thermal diffusivity” », 2008. https://www.engineeringtoolbox.com/air-thermal-diffusivity-d_2011.html

[15] J. K. Wahlstrand, N. Jhajj, et H. M. Milchberg, « Controlling femtosecond filament propagation using externally driven gas motion », *Opt. Lett.*, vol. 44, nº 2, p. 199, janv. 2019, doi: 10.1364/OL.44.000199.

[16] G. Point, C. Milián, A. Couairon, A. Mysyrowicz, et A. Houard, « Generation of long-lived underdense channels using femtosecond filamentation in air », *J. Phys. B At. Mol. Opt. Phys.*, vol. 48, nº 9, p. 094009, mai 2015, doi: 10.1088/0953-4075/48/9/094009.

[17] K. Y. Kim, J. H. Glownia, A. J. Taylor, et G. Rodriguez, « Terahertz emission from ultrafast ionizing air in symmetry-broken laser fields », *Opt. Express*, vol. 15, nº 8, p. 4577-4584, avr. 2007, doi: 10.1364/OE.15.004577.

[18] T. Bartel, P. Gaal, K. Reimann, M. Woerner, et T. Elsaesser, « Generation of single-cycle THz transients with high electric-field amplitudes », *Opt. Lett.*, vol. 30, nº 20, p. 2805, 2005, doi: 10.1364/OL.30.002805.

[19] F. Vidal *et al.*, « Modeling the triggering of streamers in air by ultrashort laser pulses », *IEEE Trans. Plasma Sci.*, vol. 28, nº 2, p. 418-433, avr. 2000, doi: 10.1109/27.848101.
[20] S. Tzortzakis, B. Prade, M. Franco, A. Mysyrowicz, S. Hüller, et P. Mora, « Femtosecond laser-guided electric discharge in air », *Phys. Rev. E*, vol. 64, nº 5, p. 057401, oct. 2001, doi: 10.1103/PhysRevE.64.057401.
[21] E. Schubert, D. Mongin, J. Kasparian, et J.-P. Wolf, « Remote electrical arc suppression by laser filamentation », *Opt. Express*, vol. 23, nº 22, p. 28640, nov. 2015, doi: 10.1364/OE.23.028640.
[22] B. Zhou *et al.*, « Revival of femtosecond laser plasma filaments in air by a nanosecond l aser », *Opt. Express*, vol. 17, nº 14, p. 11450, juill. 2009, doi: 10.1364/OE.17.011450.
[23] L. Arantchouk *et al.*, « Large scale Tesla coil guided discharges initiated by femtosecond laser filamentation in air », *J. Appl. Phys.*, vol. 116, nº 1, p. 013303, juill. 2014, doi: 10.1063/1.4886582.
[24] A. Couairon et A. Mysyrowicz, « Femtosecond filamentation in transparent media », *Phys. Rep.*, vol. 441, nº 2-4, p. 47-189, mars 2007, doi: 10.1016/j.physrep.2006.12.005.
[25] G. Schimmel, T. Produit, D. Mongin, J. Kasparian, et J.-P. Wolf, « Free space laser telecommunication through fog », *Optica*, vol. 5, nº 10, p. 1338-1341, oct. 2018, doi: 10.1364/OPTICA.5.001338.

Chapter 3

Study of the feasibility of a plasma antenna using meter-long long-lived guided discharges at high repetition rate.

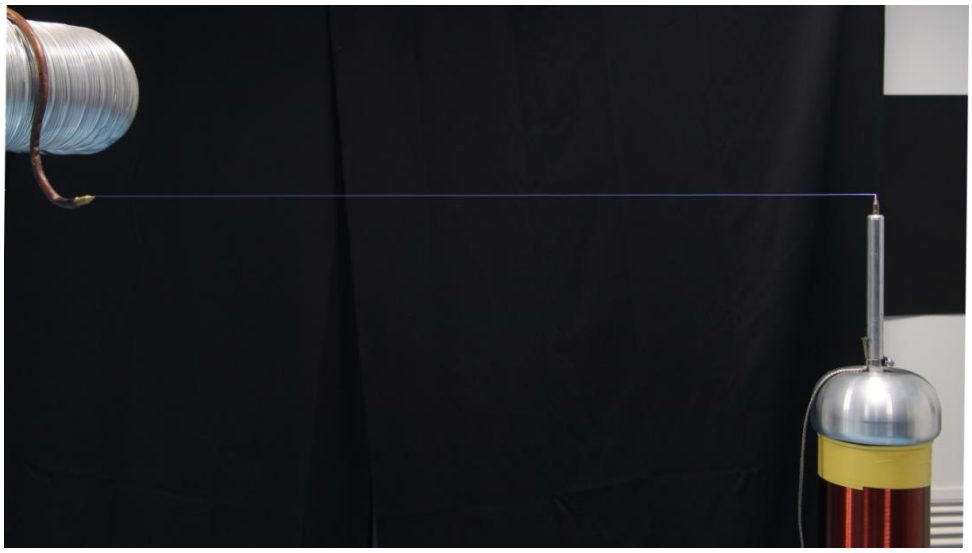

Figure 1: Picture of a 80 cm guided discharge.

In this chapter, I will investigate the feasibility of creating a continuous plasma antenna using filament guided discharges [1], [2]. Previous experiments were conducted and successful coupling between a radiofrequency signal and a guided discharge was observed [3]. This coupling was however limited to a short timescale in the order of hundreds of ns due to the short discharge lifetime.

I will present the experiments we carried out to overcome this limitation, based on two different approaches: the first is to increase the discharge lifetime by injecting additional current into it; the second is to create consecutive guided discharges at a repetition rate of 10 Hz. With a sufficiently long discharge lifetime and a high repetition rate, the consecutive guided discharges will tend to a permanent conductive channel that could act as an emission/reception antenna.

Table of contents

1 Context

In the frame of a contract from the French DGA, the F-ILM group has been working for about ten years on the development of a plasma antenna created by laser filamentation in air [3]. Such a "virtual" antenna would be able to emit in the radiofrequency range. Advantages of plasma antennas include fast turn-on and turn-off times, stealth features (a low radar cross-section when de-energized) and reconfigurable shape. The plasma column created by the filament has a lifetime too short to act as a linear conductor, therefore an electric discharge is used to energize the filament path creating a discharge with higher conductivity. Brelet *et al.* demonstrated that this guided discharge can act as a linear emitting antenna, when a signal at 100 MHz is coupled in it [3]. But the duration of the emission was limited to a few 100 ns due to the duration of the discharge.

2 Long lived guided discharge

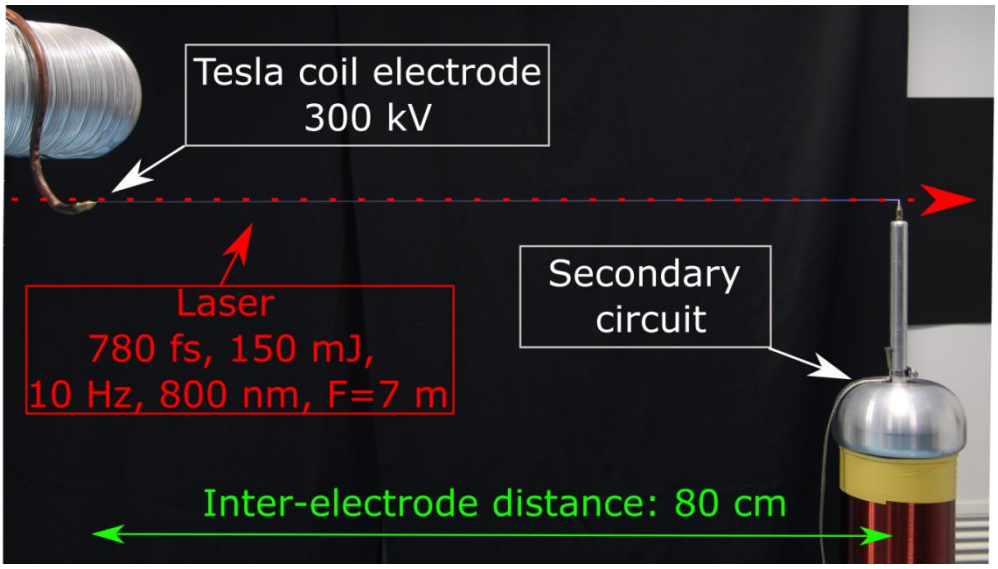

Figure 2.1: Experimental setup used to create 80 cm guided discharges and to increase the discharges lifetime by injecting current using a secondary circuit.

The first step to reach the goal of a continuous antenna is to increase the lifetime of our guided discharge. To do this, we used a 150 mJ 780 fs laser at 800 nm that was focused through a 7 m lens. The focal point was placed so that the filaments are present and guide an electrical discharge between two electrodes separated by 80 cm. The electrical discharge was created by a Tesla generator delivering 300 kV high voltage pulses synchronized with the laser pulse. Once this discharge is established, a secondary circuit was used to inject current into the discharge to increase its lifetime. A picture of the experimental setup is presented in figure 2.1.

2.1 Electrical setup

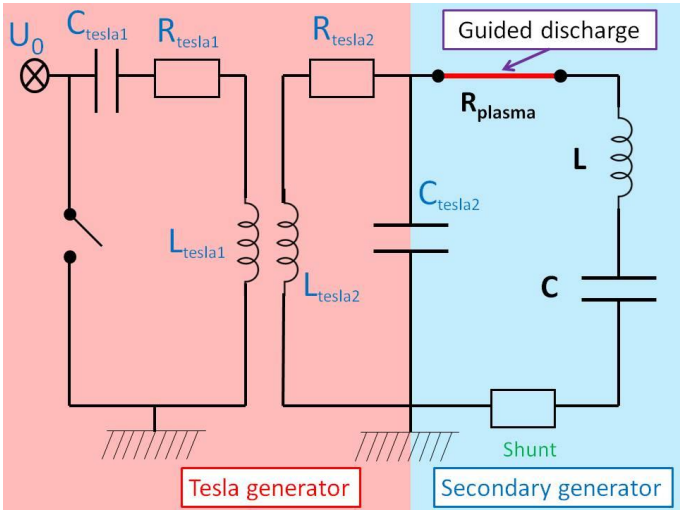

Figure 2.1.1: Electrical setup used to create long lived 80 cm long guided discharges. The Tesla generator (in red) produces the initial high voltage pulse creating the guided discharge, while the secondary circuit (in blue) injects a long lived current that increases the discharge lifetime.

The electrical setup used in our experiment, presented in figure 2.1.1, consists of two parts:

- The first part is the Tesla generator creating a 300 kV oscillating high voltage pulse. The oscillation can be described as two damped sinusoidal oscillations, with a carrier frequency at 100 kHz, as presented in figure 2.1.2. The high voltage pulse is synchronized with the laser pulse so that a negative maximum of voltage is observed at the electrode when the filaments are created. This will result in the propagation of a guided leader starting from the Tesla electrode that will bridge the 80 cm gap and reach the ground electrode.

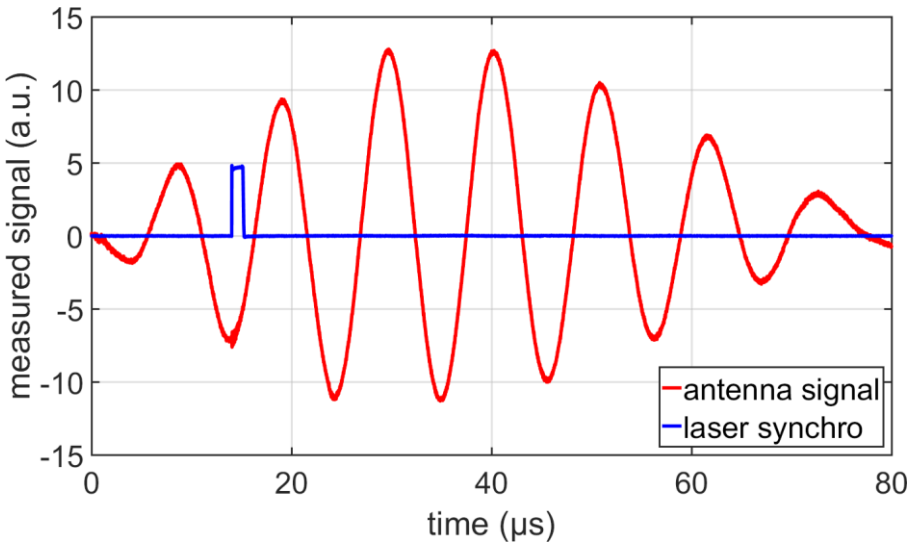

Figure 2.1.2: Plot of the oscilloscope measurement showing (in blue) the signal of synchronization of the laser pulse, and the signal of the antenna measuring the voltage at the high voltage electrode of the Tesla generator (in red).

- The second part is the secondary generator. This secondary generator consists of an RLC circuit whose capacitor is charged beforehand at a voltage of 20 kV. The value of this capacitor C can be changed to 350, 540 or 720 nF, changing the amount of current available to be injected into the discharge. The voltage of this circuit is not sufficient to create by itself discharge guided by the filament over 80 cm. However, the increased conductivity due to the

heating of both the filaments and the Tesla discharge is enough to enable the breakdown of this circuit.

This setup allowed us to create the desired discharge over 80 cm with a lifetime that was up to the ms timescale [4].

2.2 Current measurement

The first characterization of our system was done by measuring the current flowing in the discharge by adding a shunt to our circuit, as presented in figure 2.1.1. This measurement was done for all three values of capacitance 350, 540 and 720 nF.

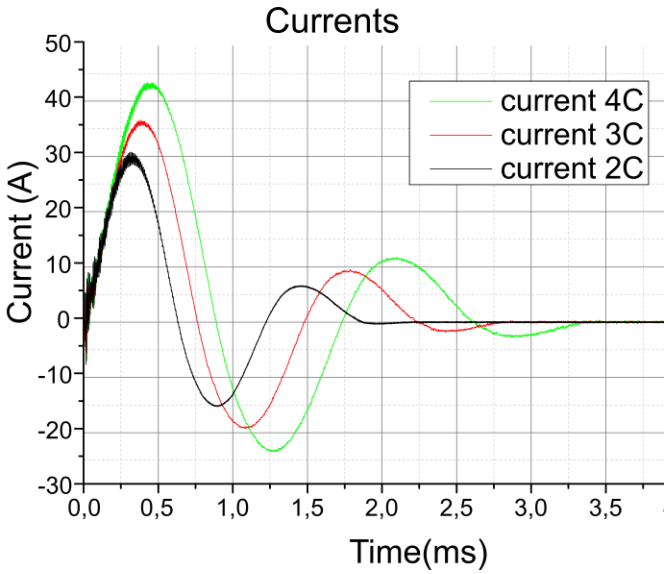

Figure 2.2.1: Current in the high voltage discharge measured for the three values of capacitance C = 350 nF (labelled as 2C, in black), C = 540 nF (labelled as 3C, in red) and C = 720 nF (labelled as 4C, in green).

The result, presented in figure 2.2.1, shows a current being present in all three cases during several ms. This is several orders of magnitude longer than the current of the Tesla discharge alone, the latter only lasting several µs. Moreover, we note that a higher value of capacitance leads to a longer current with greater amplitude.

The circuit being involved in the long discharge being an RLC circuit, its current *i* follows the equation:

$$L\frac{\partial^2 i}{\partial t^2} + R\frac{\partial i}{\partial t} + \frac{i}{C} = 0,$$

with *L*, *R* and *C* being respectively the circuit inductance, resistance and capacitance. Note that the value of R mainly comes from the resistance of the plasma channel, while the other parameters are dominated by the electric component of the circuit and not the discharge. Thus, the value of R is not known beforehand and will need to be retrieved from the measurement.

If we assume the values R, L and C as constant over the discharge lifetime, we can solve the equation and find the expression of the current *i*:

$$i(t) = I_0 \times \sin(\omega\, t) \times e^{-\frac{t}{\tau}},$$

$$\text{with } \omega = \sqrt{\frac{1}{LC} - \frac{R^2}{4L^2}}, \text{ and } \tau = \frac{2L}{R}.$$

The hypothesis of a discharge with a constant resistance value may be counter-intuitive at first, but gives a good match with our experimental observation and similar results were presented in [5].

C (nF)	I_0 (A)	ω (kHz)	R (Ohm)
350	30	579	239,5
540	36	703	175
720	43	830	147

Table 2.2.1: Values of I_0, ω and R retrieved from the fitting of the current evolution for the three values of capacitance C = 350, 540 and 720 nF.

To retrieve the value of R of the discharge, we fit the measurements of current (see Fig. 2.2.1) to the expression of *i(t)* given hereabove. This is repeated for all three values of capacitance. The results, presented in table 2.2.1, show that the resistance decreases from R = 240 Ohm with C = 350 nF to R = 147 Ohm with C = 720 nF, while the maximum current increases from 30 A to 43 A, respectively. This decrease of the resistance was expected: an increase of the value of C leads to a higher current, thus a stronger Joule heating of the medium, resulting in a lower resistance.

The use of the secondary circuit allowed us to increase the current duration of the discharge up to several ms. An increase in the value of the capacitance of the circuit allowed us to increase even further the current duration, up to more than 3 ms with the maximum capacitance of 720 nF.

2.3 Schlieren imaging

The electric discharge has an optical index different from the regular air in its surrounding due to the lower gas density and the presence of free electrons. It can therefore be characterized using the Schlieren imaging technique.

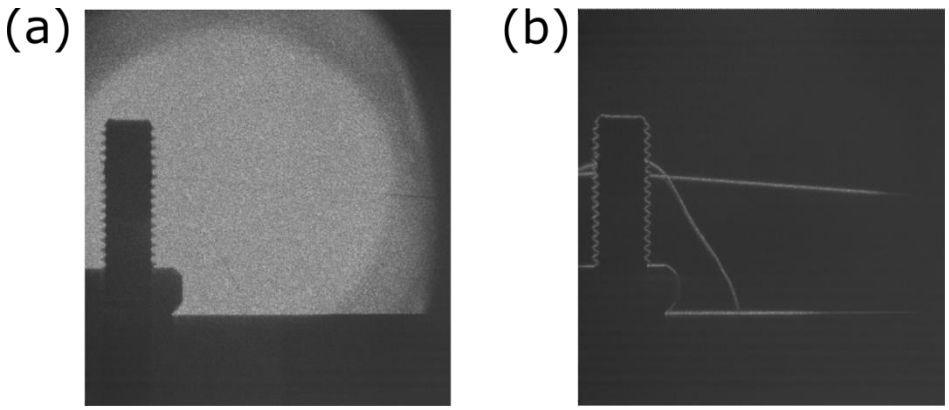

Figure 2.3.1: Example of the Schlieren imaging of a hair (a) without passing through the spatial filter and (b) by passing though the spatial filter.

This technique uses a collimated light source that is sent through the object that we want to characterize. The gradients of refractive index, caused in our case by the variation of gas density due to the discharge, distort the collimated light beam and create a spatial variation of the light. By sending the light beam through a lens and using a spatial filter placed at the Fourier plane of the lens, we can remove the unperturbed portion of the light and send the remaining distorted light on a

camera to visualize it. An example of the Schlieren imaging of a hair and the effect of the spatial filter, highlighting the index variation, can be seen in figure 2.3.1.

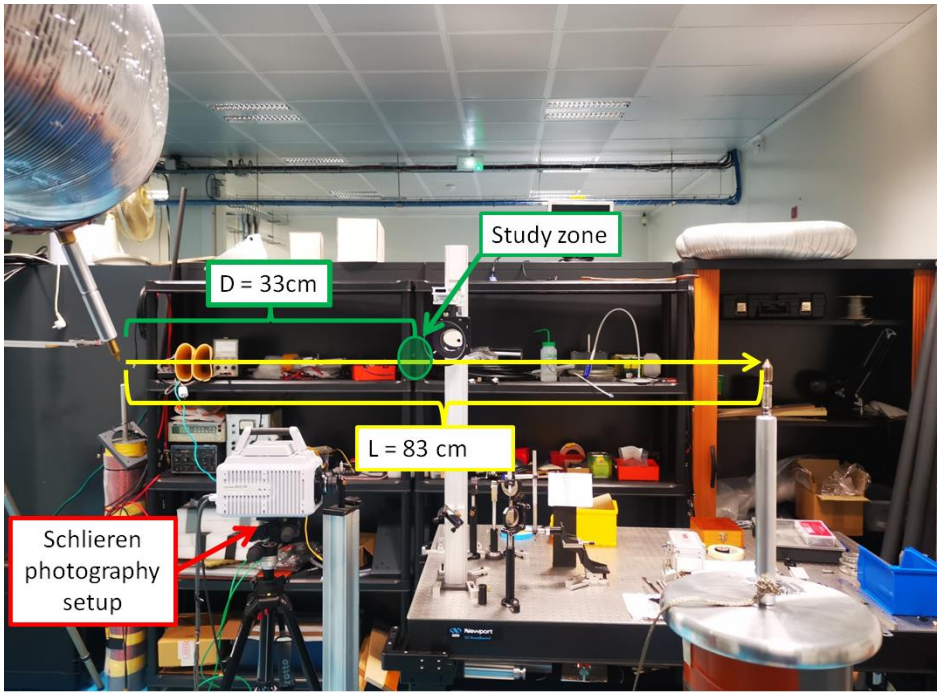

Figure 2.3.2: Experimental setup of the Schlieren imaging system.

The experimental setup, presented in figure 2.3.2, consists of a probe laser pulse at 640 nm with a duration of 1 µs collimated to study a zone of 3 cm diameter. This laser was sent perpendicularly through the discharge at a distance D = 33 cm from the Tesla electrode to avoid any point effect due to the electrode. A high-speed camera, model Fastcam SA-X2 from Photron, set at a frequency of 40 000 images/s was used to record the images. The probe laser was synchronized with the high-speed camera. A narrow band filter, centred at 640 nm, was placed in front of the camera to reduce the perturbation due to the light emitted by the discharge.

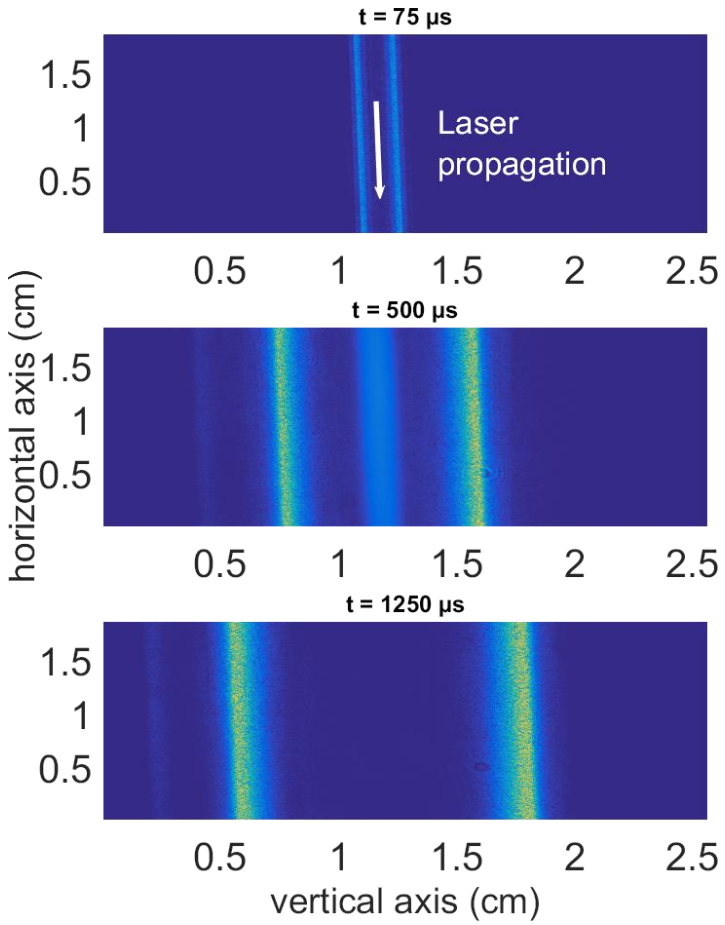

Figure 2.3.3: Schlieren images captured at delays of 75, 500 and 1250 µs after the beginning of the discharge. The temporal evolution of the edge of the discharge can be observed (in yellow). Light emitted from the discharge can also be observed in the central part of the image captured at a delay of 500 µs.

Images recorded at different delays after the beginning of the discharge are shown in figure 2.3.3. From these measurements, the position of the edge of the discharge channel can be easily distinguished. Indeed, the Schlieren imaging is sensible to the gradient of the refractive index, corresponding in this case to a gradient of temperature (or gas density) that is maximal on the lateral boundaries of the discharge. By monitoring the position of the edge of the discharge channel, we can measure the temporal evolution of the discharge radius.

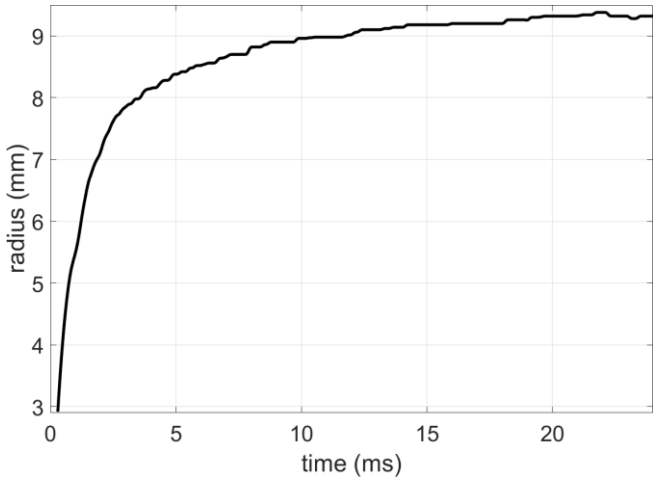

Figure 2.3.4: Measured temporal evolution of the discharge radius for a capacitance in the secondary circuit of C = 720 nF.

The measured temporal evolution of the discharge radius for a capacitance of 720 nF in the secondary circuit is presented in figure 2.3.4. A rapid expansion can be observed during the first 3 ms, followed by a much slower expansion until the radius reaches a plateau near 9 mm after 15 ms. The duration of the quick expansion of the discharge can be linked to the duration of the current, as seen in figure 2.2.1.

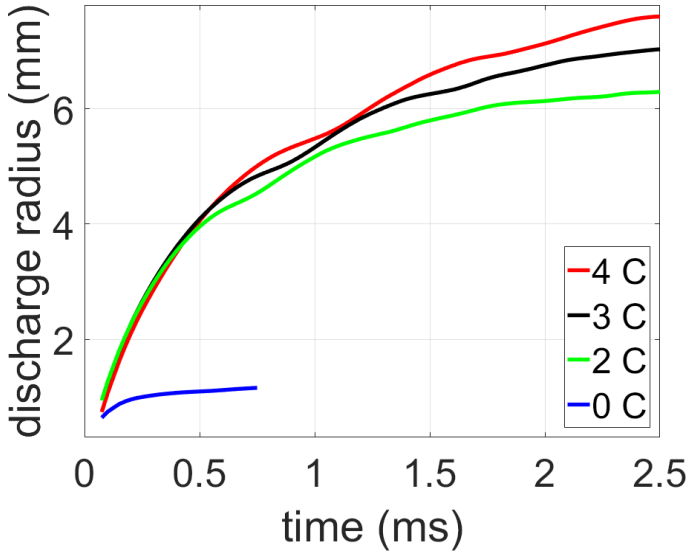

Figure 2.3.5: Measured temporal evolution of the discharge radius for capacitance values in the secondary circuit of C = 720 nF (labelled as 4C, in red), C = 540 nF (labelled as 3C, in black), C = 350 nF (labelled as 2C, in green), and for no capacitance (labelled as 0C, in blue).

This measurement was repeated for three values of capacitance 350, 540 and 720 nF and without any capacitance (Tesla generator only). The results, presented in figure 2.3.5, show a clear distinction between the evolutions of the discharges produced with the secondary circuit (2 to 4 C) and without it (0 C). When the secondary circuit is used, the diameter grows up to a plateau at a value greater than 6 mm that is reached after more than 2.5 ms, while it saturates at 1 mm after only 200 µs when the secondary circuit is not used. One other important observation is the slight modulations of the expansion rate that are observed in all three discharges using the secondary circuit.

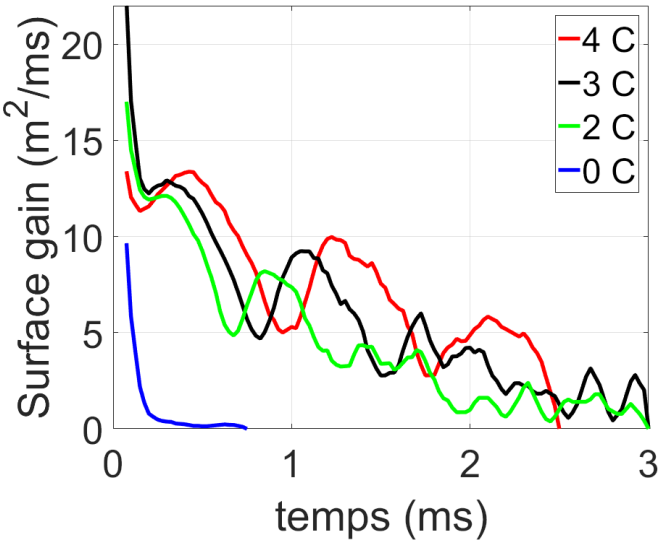

Figure 2.3.6: Measured surface gain of the cross section of the discharge $2\pi r\frac{\partial r}{\partial t}$ for capacitance values in the secondary circuit of C = 720 nF (labelled as 4C, in red), C = 540 nF (labelled as 3C, in black), C = 350 nF (labelled as 2C, in green), and for no capacitance (labelled as 0C, in blue).

Theses modulations are more easily observed by looking at the evolution of the surface gain of the cross section of the discharge $2\pi r\frac{\partial r}{\partial t}$, as shown in figure 2.3.6. We observe that these modulations have a larger amplitude and a larger period when the capacitance value C is increased. This behaviour is analogous to the evolution of the current of discharges. It is quite normal to find a similar behaviour in these two measurements because the evolution of the discharge radius results from the thermal expansion of the heated air, and this heating is produced by the Joule effect, proportional to the square of the current.

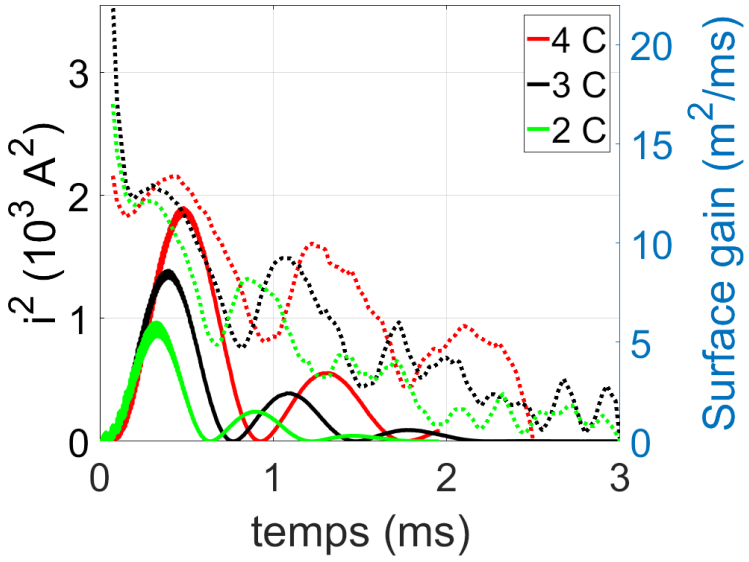

Figure 2.3.7: Comparison between the temporal evolution of the surface gain of the cross section of the discharge $2\pi r\frac{\partial r}{\partial t}$ (dashed lines) and the temporal evolution of the square of the current (continuous lines), for capacitance values in the secondary circuit of C = 720 nF (labelled as 4C, in red), C = 540 nF (labelled as 3C, in black), C = 350 nF (labelled as 2C, in green), and for no capacitance (labelled as 0C, in blue).

The comparison between the temporal evolution of the surface gain of the cross section of the discharge $2\pi r\frac{\partial r}{\partial t}$ and the temporal evolution of the square of the current is presented in figure 2.4.7. The temporal modulation of the surface gain and of the current are synchronized. The synchronization is, as explained earlier, due to the direct dependency of the expansion speed on the Joule heating. However, a delay of 57 µs between the surface gain and the current can be observed on the first oscillation, while the following ones are synchronized. This initial delay is attributed to the variation of the discharge resistance occurring at the beginning of the discharge, when the temperature is the highest. The variation of R leads to a shifting of the temporal maximum of the joule heating RI^2 compared to I^2.

2.4 Model of the discharge thermal expansion

To investigate the evolution of the electrical discharge, a model was developed to simulate the thermal expansion of the discharge channel. The model is based on the Elenbaas-Heller equation, which describes the temperature distribution of a steady state discharge in a cylindrical volume and with an axial symmetry:

$$\frac{1}{r}\frac{\partial}{\partial r}\left(r\lambda\frac{\partial T}{\partial r}\right)+\sigma E^2-Q_r=0,$$

where r is the radius, T the temperature, λ and σ the thermal conductivity and electrical conductivity, E the electrical field strength and Q_r the volumetric power of radiation losses.

In our case, the discharge is not in a steady state and evolves as the current changes. However, we can retrieve from this equation the term involved in the energy balance. To simplify the calculation, we will consider that the temperature distribution remains gaussian with time and we will confirm experimentally this hypothesis later on. Thus, the discharge is assumed to be a cylinder with a gaussian radial profile of temperature and by neglecting the point effect of the electrodes, this profile is assumed invariant over the discharge length.

Then, we will simulate the evolution of the discharge temperature and radius of the discharge by simulating the enthalpy evolution of the system. The energy balance is calculated at the FWHM position of the Gaussian, that we will call the discharge radius, using terms based on the Elenbaas-Heller equation. This equation being volumetric, we first need to integrate this term over the discharge volume, which gives:

- For the thermal conductivity loss, using the Green-Ostrogradsky's theorem and the invariance of our system:

$$P_{\text{thermal conductivity}}=\iiint\frac{1}{r}\frac{\partial}{\partial r}\left(r\lambda\frac{\partial T}{\partial r}\right)dV=\oiint\lambda\frac{\partial T}{\partial r}dS=\lambda\times\frac{\partial T}{\partial r}\times S,$$

  with λ the thermal conductivity of air and S the surface of the discharge.

- For the electric gain, using the value of resistance R_{ohm} and current i retrieved from our measurements:

$$P_{\text{electric gain}}=\iiint\sigma E^2dV=R_{ohm}i^2,$$

- For the radiation losses, using the expression of the radiation of a grey body:

$$P_{\text{radiative}}=\iiint Q_r dV=S\times\varepsilon\times\sigma_b\times{T_{FWHM}}^4,$$

  with ε the blackness coefficient, σ_b the Stefan-Boltzmann constant and T_{FWHM} the temperature at the FWHM position.

All the radiation constants and transport properties are interpolated from the values of the tables from [6], [7] and input in the code to be estimated at each time steps.

We then use these three terms to calculate the evolution of the enthalpy of the system, which reads:

$$\Delta T(t)\times c_p\times\pi\times L\times R(t)^2\times\rho(t)$$

$$= \Delta T(t_0) \times c_p \times \pi \times L \times R(t_0)^2 \times \rho(t_0) - \int_{t_0}^{t} (P_{\text{radiative}}(t) + P_{\text{thermal conductivity}}(t))\, dt + \int_{t_0}^{t} P_{\text{electric gain}}(t) dt + P \times \pi \times L \times (R(t)^2 - R(t_0)^2),$$

with ΔT the temperature variation at the FWHM position, c_p the isobaric specific heat, L the length of the discharge (in our case, 80 cm), ρ the air density, and R the FHWM position.

Moreover, the radial expansion of the channel is calculated from the thermal expansion of air:

$$R(t + dt) = R(t) + \frac{4 \times \alpha(\Delta T(t))}{2 \times R(t)} \times dt,$$

with α the thermal diffusivity.

The simulation will start 0.3 ms after the beginning of the discharge to avoid taking into account the initial evolution resulting from the Telsa discharge, since our model only considers the contribution of the secondary circuit.

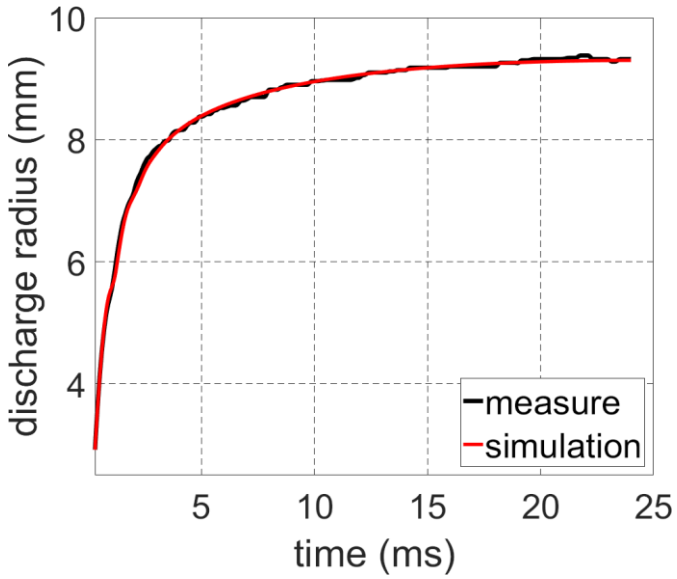

Figure 2.4.1: Comparison between the measured and simulated temporal evolution of the radius of the discharge for a capacitance value in the secondary circuit of C = 720 nF.

Using this model, we calculate the evolution of the discharge radius over 25 ms using as an input the measured evolution of the current for capacitance value in the secondary circuit of C = 720 nF. The comparison between the simulation and the measurement is presented in Figure 2.4.1. The plot shows a near perfect match between the measurement and the simulation.

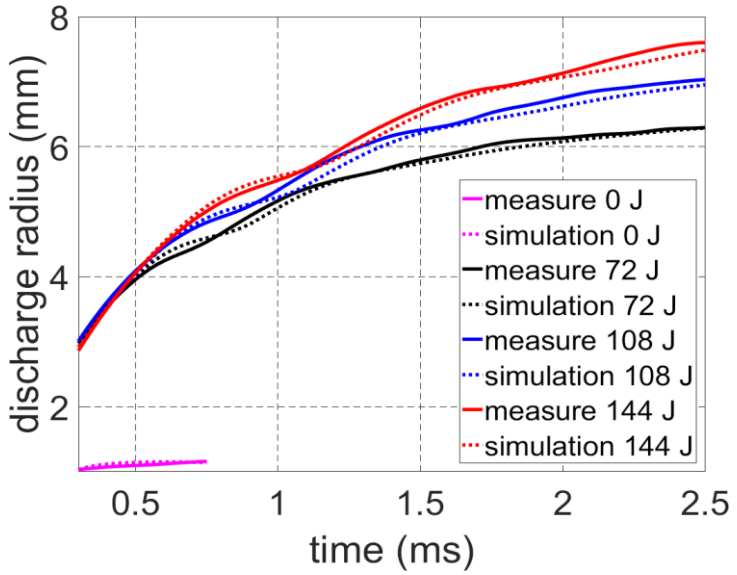

Figure 2.4.2: Comparison between the measured and simulated radius of the temporal evolution of the discharge for capacitance values in the secondary circuit of C = 720 nF (labelled as 4C, in red), C = 540 nF (labelled as 3C, in blue), C = 350 nF (labelled as 2C, in black), and for no capacitance (labelled as 0C, in violet).

To further test the validity of our model, we simulated the evolution of the discharge over 2.5 ms for all previously measured values of capacitance in the secondary circuit C = 720 nF, C = 540 nF, C = 350 nF, and for no capacitance. The comparisons between the simulations and measurements are presented in figure 2.4.2. The plots show a good match between the simulations and the measurements. The slight difference observed in the evolution is mainly attributed to the limit of the validity of the hypothesis of the constant resistance of the discharge, because a variation of the discharge resistance may plausibly happen at the beginning of the discharge, when the temperature is at its highest.

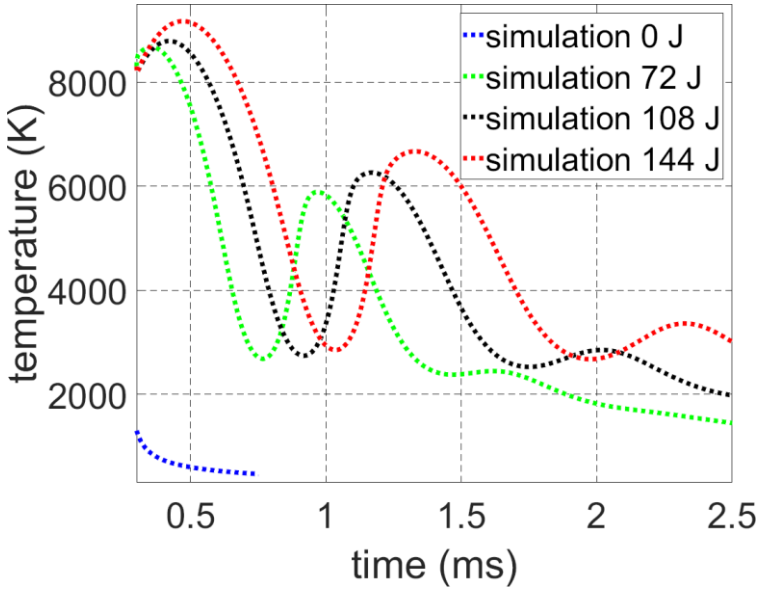

Figure 2.4.3: Simulation of the temporal evolution of temperature at the discharge center for capacitance values in the secondary circuit of C = 720 nF (labelled as 4C, in red), C = 540 nF (labelled as 3C, in black), C = 350 nF (labelled as 2C, in green), and for no capacitance (labelled as 0C, in blue).

Using this model, we can also simulate the temporal evolution of the temperature at the center of the discharge for the different tested values of capacitance in the secondary circuit. The results, presented in Figure 2.4.3, show a clear distinction between the temperature evolution for discharges using the secondary circuit and the ones without: without the secondary circuit, the temperature goes back to the room temperature in less than a 1 ms, while the use of the secondary circuit increases both the maximum of temperature and the time during which the discharge temperature stays high.

This is a really important step toward creating a plasma antenna that stays conductive over a long period of time. However, one should keep in mind that the conductivity of the discharge is very small for a temperature of the order of several thousands Kelvin. Thus, even with the use of the secondary circuit with 4C, the conductivity remains relevant for not more than ~1.5 ms. This is orders of magnitude higher compared to the previous limit of about 50 µs for a non prolonged discharge and a step in the right direction, but still too short to reach our goal of a discharge conductive for 10 ms.

2.5 Spectroscopy measurement

To further characterize our discharge and validate our model, we performed a spectroscopic measurement of the light emitted by the discharge with a capacitance value in the secondary circuit of 720 nF, using a spectrometer Acton SP2756 from Princeton Instruments. This measurement was repeated at two different time intervals, during the first millisecond and during the second millisecond after the beginning of the discharge. The results were fitted using the SPECAIR program [8] to estimate the value of the discharge during these two time intervals.

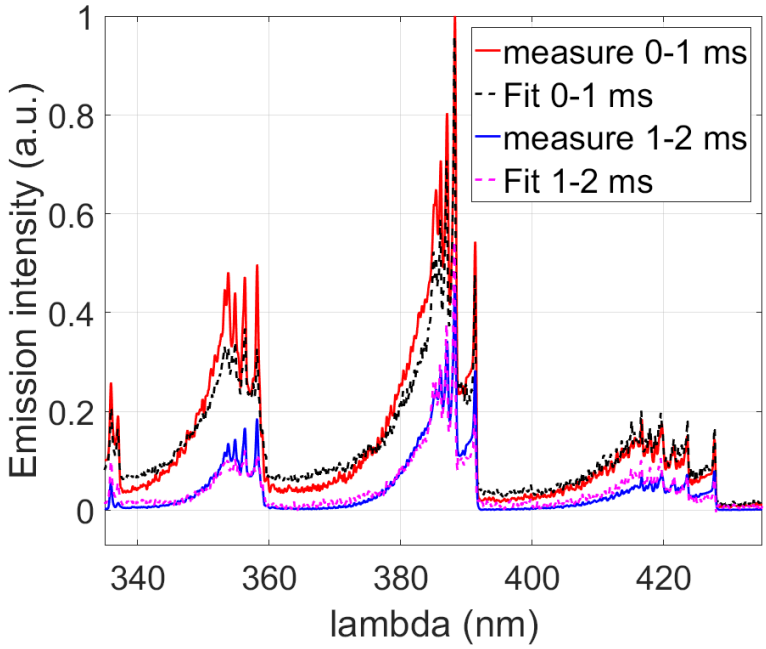

Figure 2.5.1: Measured and fitted emission spectrum of the discharge, for the first and second ms after the beginning of the discharge, for a capacitance value in the secondary circuit of 720 nF.

The measured emission spectrum of the discharge and the corresponding fitting are presented in figure 2.5.1. The values of temperature retrieved from the fitting are 7350 K and 5500 K for the first and second ms, respectively.

These values should be compared not to the mean value of the simulated temperature but to $\sqrt[4]{< \Delta T^4 >}$, to take into account the fact that the discharge emission is not constant over time. For the time periods from 0.3 to 1 ms and from 1 ms to 2 ms, $\sqrt[4]{< \Delta T^4 >}$ = 7830 K and 5420 K, respectively. These values are very close to the one retrieved from the emission spectrum, adding another proof of the validity of our model.

2.6 Transverse interferometry of the discharge

The Schlieren imaging allowed us to characterize the temporal evolution of the radius of the discharge but does not enable to retrieve the radial profile of the discharge temperature. Therefore, we used the interferometer setup described in the chapter "Laser filamentation at high repetition rate" to measure the 2D map of the air density depletion in the discharge at different time delays.

The use of this technique is not valid to get a quantitative value of the air density variation, because the current system cannot distinguish the contribution of the free electrons density and the one of air density in the measured variation of index. It will however give us insight about the radial profile of the density variation.

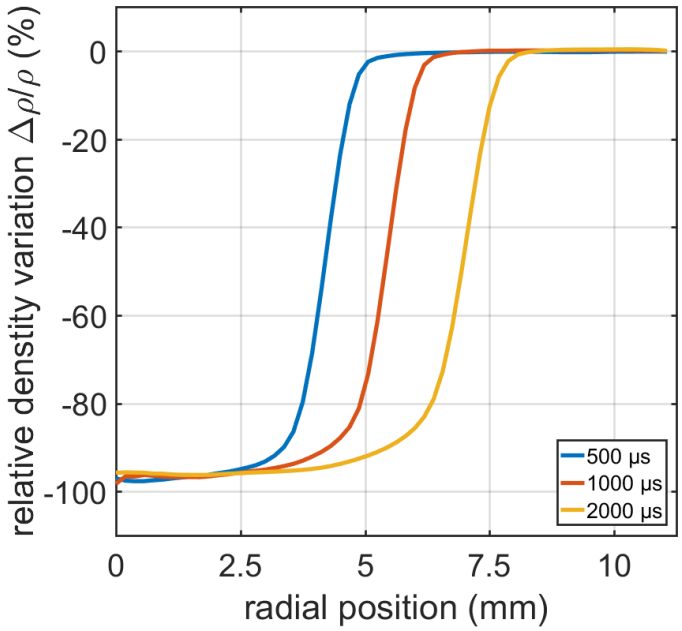

Figure 2.6.1: Measured radial profiles of the air density variation in the discharge for a capacitance value in the secondary circuit of 720 nF, measured at a delay of 500 µs (in blue), 1000 µs (in orange) and 2000 µs (in blue) after the beginning of the discharge. Note that the quantitative values of the density variation are not valid due to the presence of electron disturbing the measurement.

The measured radial profiles are presented in figure 2.6.1. From the profiles of the density, which is inverted compared to the temperature profile (the discharge being at the pressure equilibrium, $\rho \times T = cst$), we can confirm the validity of the hypothesis of the Gaussian radial profile of the temperature.

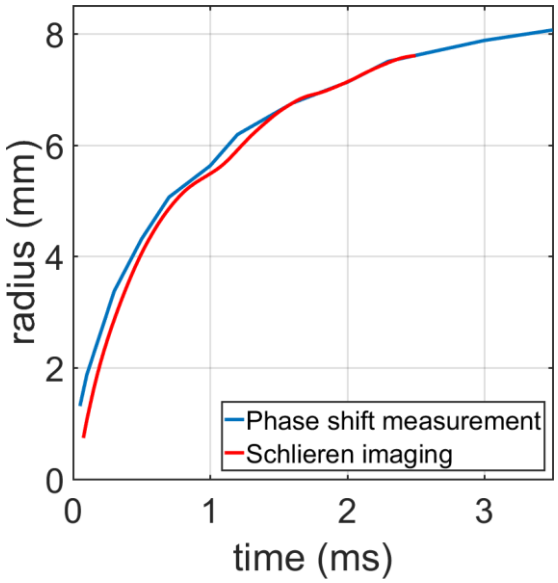

Figure 2.6.2: Comparison between the temporal evolution of the discharge radius measured by Schlieren imaging (in red) and by phase shift measurement (in blue) for C = 720 nF.

Furthermore, this measurement gives us a second measure of the temporal evolution of the discharge radius (we consider the radius as the FWHM position of the density profile). The comparison between this measurement and the one from the Schlieren imaging is presented in figure 2.6.2. A good agreement between the two measurements is observed, consolidating again the validity of the previous hypothesis.

3 Interaction between consecutive guided discharges at 10 Hz

While the previous part of this chapter focused on the increase of the lifetime of a single guided discharge, the present one will focus on the study of the second aspect needed to create a continuous conductive antenna: the guiding of consecutive discharges. Due to the limitation of our experimental setup (especially the TW laser system), the maximum repetition rate at which we can chain consecutive discharges is 10 Hz. This repetition rate is at least one order of magnitude lower than the repetition rate that will be needed to create a continuous conductive antenna (at least 100 Hz), but the study of this regime will allow us to make a first step in the study of the feasibility to produce consecutive laser guided discharges.

3.1 Schlieren imaging of consecutive discharges

To attest the guiding of the discharges, we will use the same Schlieren imaging setup described previously to characterize and record the discharge channel.

We will study two types of consecutive discharges:

- The first type is a series of two “short discharges” created by the Tesla generator only. Both of these discharges will result in a weak heating of the medium and a slow evolving channel.
- The second type is a first “long discharge” created by both the Tesla and the secondary circuit, followed by a discharge created by the Tesla generator only. The first discharge will result in a strong heating of the medium with a fast evolution. It can then hinder the guiding of the second discharge.

It would be interesting to study the sequence of two discharges created by both the Tesla generator and the secondary circuit, but the limitation of our current charging circuit did not allow us to charge the secondary circuit in less than 100 ms.

3.1.1 Sequence of two short discharges

By using Schlieren imaging, we will assess the guiding of consecutive discharges and compare the evolution of successive discharges. If both discharges are confirmed as guided and with a similar evolution, this should ensure the possibility to chain an unlimited number of discharges.

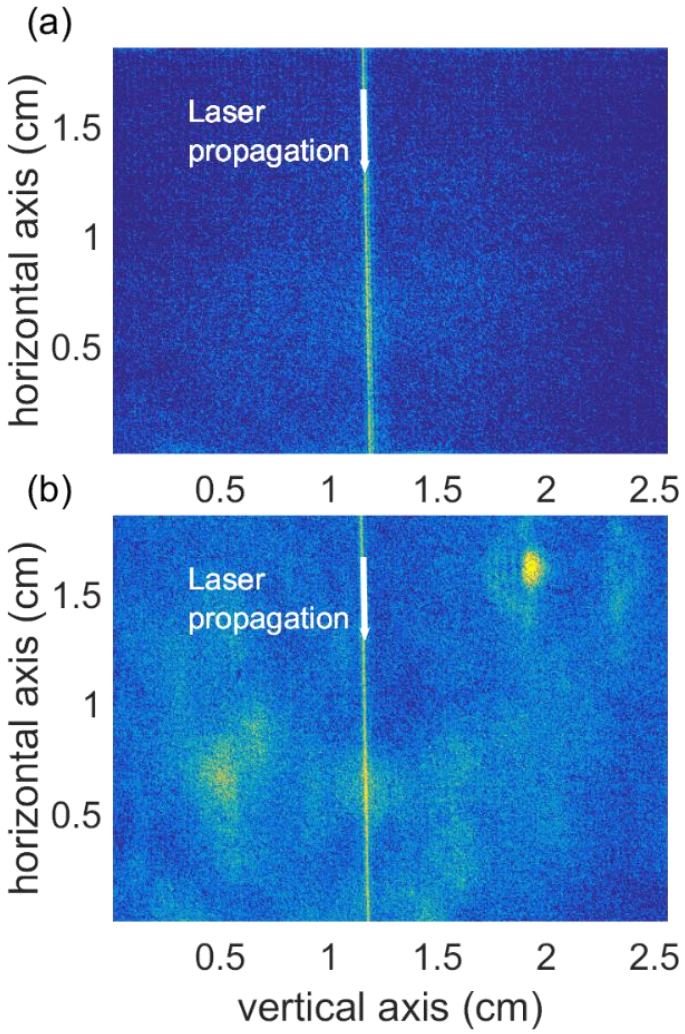

Figure 3.1.1.1: Schlieren imaging of two consecutive "short discharges" separated by 100 ms.

The first Schlieren images of the two consecutive "short discharges" are presented in figure 3.1.1.1. We can see that both discharges are straight and follow the laser path, which is typical of laser guided discharges. We can see on the second image (figure 3.1.1.1 (b)) a background noise resulting from the heating produced by the first discharge, but this effect does not prevent the second discharge to be guided.

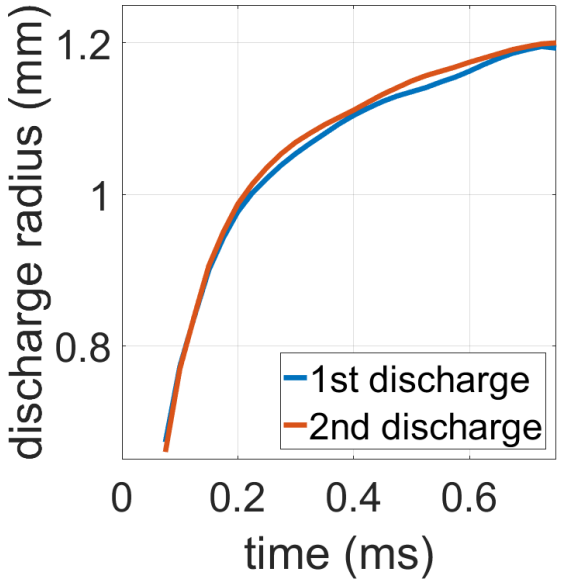

Figure 3.1.1.2: Temporal evolution of the radius of the two consecutive short discharges separated by 100 ms.

From the Schlieren images, we retrieve the temporal evolution of the radius of the discharges. The results, presented in figure 3.1.1.2, show that the evolutions of both discharge radii are similar, with a slight difference in the order of the uncertainty of the measurement.

We can therefore conclude that consecutive short laser guided discharges can be generated at 10 Hz.

3.1.2 Sequence of a long discharge followed by a short discharge

After studying the succession of two short discharges, the next step will be to study the generation of a long discharge followed by a short discharge.

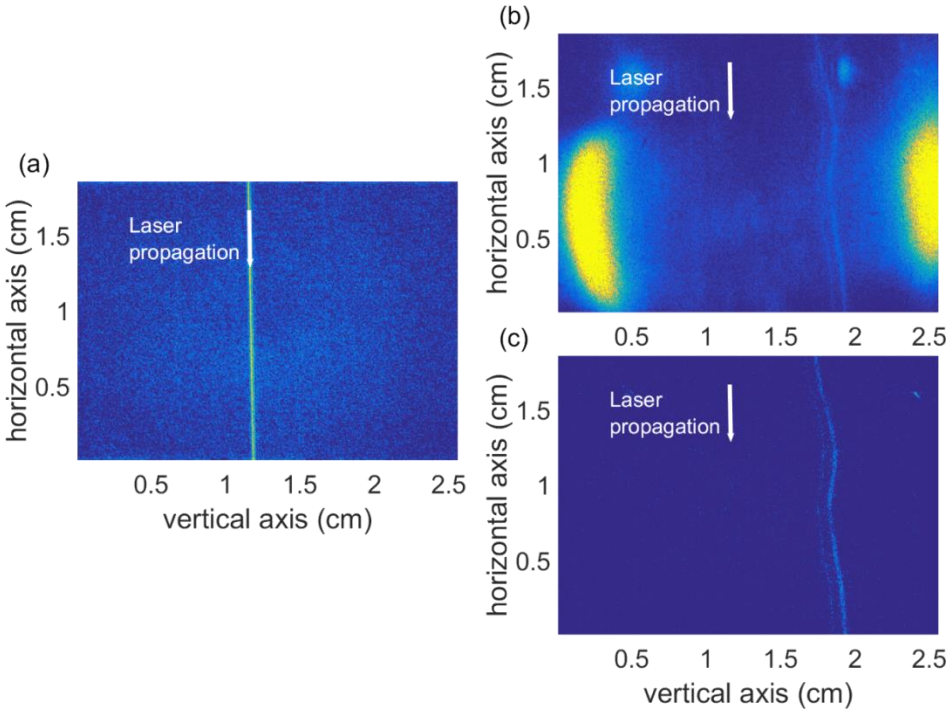

Figure 3.1.2.1: Schlieren imaging of two consecutive discharges separated by 100 ms. (a) image of the first long discharge, (b) image of the second short discharge, and (c) image of the second short discharge with the background substracted to distinguish the discharge path.

The first Schlieren images of each consecutive discharge are presented in figure 3.1.2.1. The first long discharge is straight and follows the laser path. However, the second discharge is curved and does not follow the laser path, thus is not guided. In figure 3.1.2.1 (b), we see a strong background noise due to the important heating of the first long discharge. By removing this background noise, as seen in figure 3.1.2.1 (c), we see more clearly the discharge path. It is interesting to note that the discharge path seems to follow the shape of the big yellow area in the background noise.

This test was repeated 5 times and the second discharges were never guided and always failed to reach the second electrode. It is however important to note that even if the discharges were not guided by the laser, they were always visible on the Schlieren image and stayed in the 2 cm wide heated channel remaining from the first discharge.

This was repeated for all three values of capacitance in the secondary circuit 720 nF, 540 nF, and 350 nF. In all these cases, the second discharge was never observed as guided and never reached the second electrode.

3.2 Perturbation of the guiding effect

As described previously, it is important to try to understand why the first long discharge seems to interact with the second discharge and prevent its guiding.

To explain this, we first need to characterize the under dense channel that is responsible for the guiding effect. To do so, we use again the interferometric setup previously described in chapter "Laser filamentation at high repetition rate" [9].

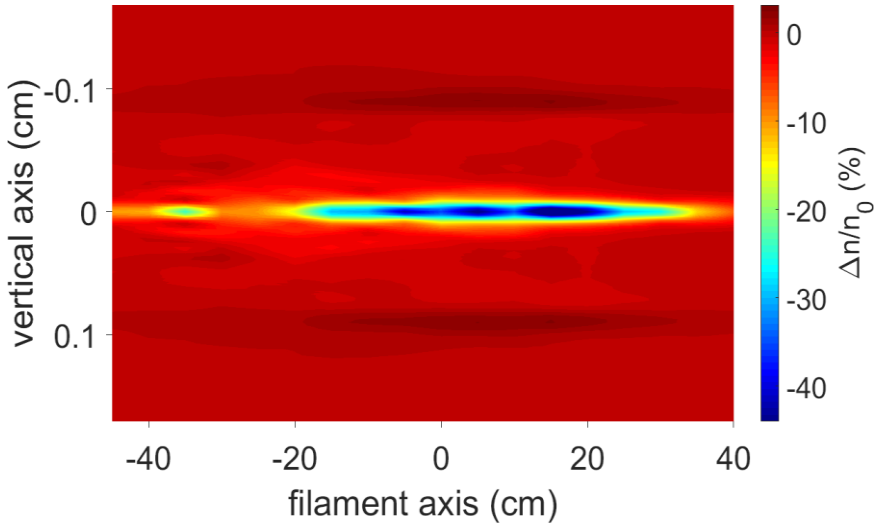

Figure 3.2.1: Measurement of the density variation of the under-dense channel responsible for the guiding of the discharge, created by a 150 mJ, 780 fs, 800 nm laser pulse focused at 7 m. This measurement was done 10 µs after the laser pulse.

The result, presented in figure 3.2.1, shows the 2D map of the under-dense channel created between the two electrodes. From the density variation, we calculate the corresponding temperature variation in the channel. The first observation is that the channel is not homogeneous along the electrode gap. The maximum elevation of temperature measured in the channel is of 208 K, and the mean value along the 80 cm is 89 K.

These values should be compared with the value of the temperature variation in the discharge channel that remains 100 ms after the first discharge. Using the model previously described, we can run the simulation for a period of 100 ms and have an estimation of this value.

In the case where the first discharge is short (without the secondary circuit), the remaining temperature variation in the discharge channel is of 61 K. This value is smaller than the heating due to the filamentation power. Thus, the filament effect is still stronger than the discharge perturbation and the guiding is possible.

In the case where the first discharge is long (with a capacitance in the secondary circuit of 720 nF), the remaining temperature variation in the discharge channel is of 248 K. This time, the value is greater than the heating due to the laser filamentation. Thus, the remaining perturbation of the first discharge is greater than the filament heating and prevents the guiding effect. The same conclusion is obtained for the capacitance values in the secondary circuit of 540 nF and 350 nF.

This effect being due to thermal variation of the air, it is affected by any air flow that could refresh the air between the consecutive discharges. Using an air blower to create an air flow of 8 $m.s^{-1}$ in the region between the electrodes, we successfully achieved to guide a second discharge following a long initial discharge.

4 Conclusion

In this chapter, I described how we achieved two important milestones in the development of a plasma antenna with a guided discharge:

- We increased the lifetime of our 80-cm long guided discharge from 50 µs up to 3 ms by adding a secondary circuit that injects current to the guided discharge initially created by a Tesla generator.
- We successfully managed to guide a second discharge 100 ms after a first long lived discharge. We faced some issues due to the interaction between the consecutive discharges preventing the guiding of the second discharge, described how this interaction works and overcome them with the simple solution of using an air blower to cancel the interaction.

The next steps of this study, that is currently ongoing, will consist in upgrading our electrical setup to allow a charge of the secondary circuit in less than 100 ms to assess the feasibility of guiding many consecutives long lived discharges.

Then, the next important milestone would be to increase the repetition rate at which we create the guided discharge up to 100 Hz. The lifetime of long-lived discharge being of 3 ms, by creating them at 100 Hz we will be close to a continuous discharge that could act as a permanent plasma antenna.

Bibliography

[1] T. Dwyer, J. Greig, D. Murphy, J. Perin, R. Pechacek, et M. Raleigh, « On the feasibility of using an atmospheric discharge plasma as an RF antenna », *IEEE Trans. Antennas Propag.*, vol. 32, nº 2, p. 141-146, févr. 1984, doi: 10.1109/TAP.1984.1143275.

[2] F. Théberge, J.-F. Gravel, J.-C. Kieffer, F. Vidal, et M. Châteauneuf, « Broadband and long lifetime plasma-antenna in air initiated by laser-guided discharge », *Appl. Phys. Lett.*, vol. 111, nº 7, p. 073501, août 2017, doi: 10.1063/1.4985045.

[3] Y. Brelet *et al.*, « Radiofrequency plasma antenna generated by femtosecond laser filaments in air », *Appl. Phys. Lett.*, vol. 101, nº 26, p. 264106, déc. 2012, doi: 10.1063/1.4773492.

[4] L. Arantchouk *et al.*, « Large scale Tesla coil guided discharges initiated by femtosecond laser filamentation in air », *J. Appl. Phys.*, vol. 116, nº 1, p. 013303, juill. 2014, doi: 10.1063/1.4886582.

[5] P. Castera et P.-Q. Elias, « Resistance Models Applied to the Return Stroke Phase of Negative Pulsed Surface Discharges in Air », *IEEE Trans. Plasma Sci.*, vol. 42, nº 7, p. 1922-1931, juill. 2014, doi: 10.1109/TPS.2014.2324637.

[6] G. S. Romanov, Yu. A. Stankevich, L. K. Stanchits, et K. L. Stepanov, « Thermodynamic and optical properties of gases in a wide range of parameters », *Int. J. Heat Mass Transf.*, vol. 38, nº 3, p. 545-556, févr. 1995, doi: 10.1016/0017-9310(94)00173-S.

[7] I. Sokolova, « Coefficients of air transfer in the range of temperatures from 3000 to 25 000° K and pressures 0.1, 1, 10, and 100 atm », *J Appl Mech Tech Phys*, nº 2, p. 80-90, 1973.

[8] C. Laux, « Radiation and nonequilibrium collisional-radiative models », *Von Karman Inst. Lect. Ser. Phys.-Chem. Model. High Enthalpy Plasma Flows*, p. 2002-2007, janv. 2000.

[9] P. Walch, B. Mahieu, L. Arantchouk, Y.-B. André, A. Mysyrowicz, et A. Houard, « Cumulative air density depletion during high repetition rate filamentation of femtosecond laser pulses: Application to electric discharge triggering », *Appl. Phys. Lett.*, vol. 119, nº 26, p. 264101, déc. 2021, doi: 10.1063/5.0077635.

Chapter 4

Study of the superfilamentation regime: transition from filaments to superfilament and consequence on the guiding of electrical discharges.

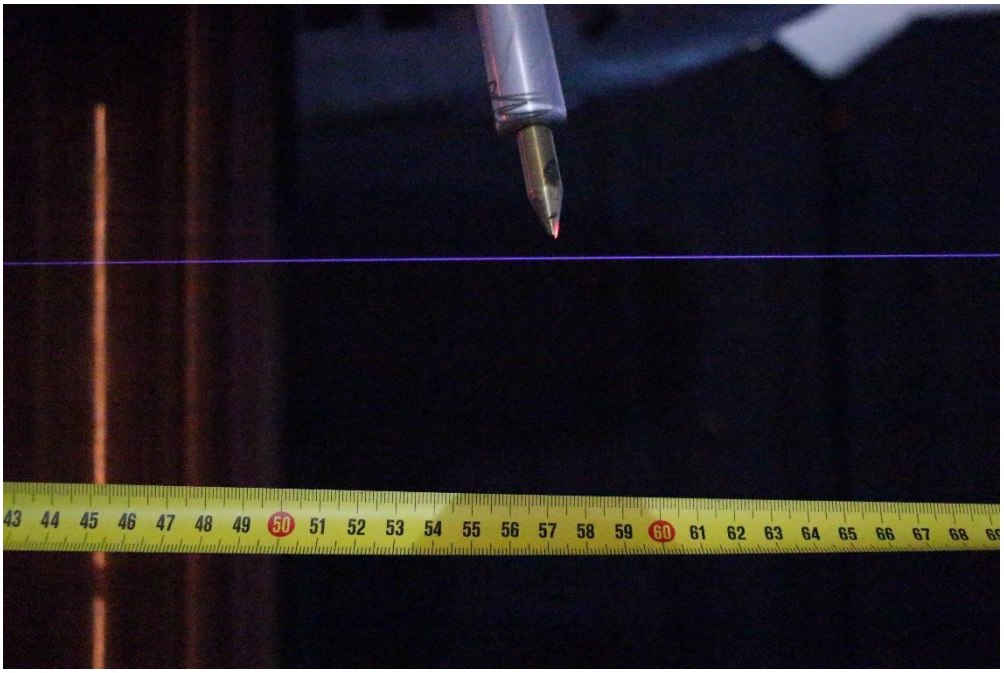

Figure 1: Picture of the filament present in the vicinity of the high voltage electrode of the Tesla generator.

In this chapter, I will present the investigation of a specific filamentation regime, called superfilamentation, appearing when both a strong focusing geometry and high laser energy are involved [1].

First, I will focus on the study of the luminescence of the plasma filament and on the neutral density variation induced by the filament. I will compare filaments produced with high and low energy pulses to showcase the transition from a regime of weakly ionized plasma to a regime with a higher plasma density that we call superfilament [2], [3].

In a second time, I will analyse how this transition from multiple filaments to superfilament affects the guiding of electrical discharges. I will characterize, for both filamentation regimes, the maximal discharge length for a set voltage, the discharge speed and the discharge path.

Table of contents

1 Context

Most studies of the filamentation process have been focused on the characterization of single filaments or the interaction between pairs of filaments. Such binary interaction leads to the fusion, repulsion, energy redistribution or spiral motion of the filaments, depending on their relative optical phase [4]–[6].

In this chapter, we will characterize a new filamentation regime that is called the superfilament regime, where a dense bundle of filament, which can no longer be described by binary interactions, will merge to create the so-called superfilament [1]. This regime is obtained by focusing a high energy femtosecond laser pulse in air.

In the focal region, a reorganization of the interacting filament bundle takes place. It results in the apparition of a structure similar to standard filaments, but carrying a significantly higher intensity than standard filaments and persisting over several tens of centimetres. The plasma produced and its resulting heating of the medium are expected to be one order of magnitude denser than regular filaments [1]. As a consequence, this specific filamentation regime can play a crucial role in the triggering and guiding of high voltage discharges over long distances [7].

2 Filamentation regimes: from regular filament to superfilament

2.1 Measurement of the plasma luminescence

The first characterization was made by measuring the light emitted by luminescence of the plasma created in the two filamentation regimes.

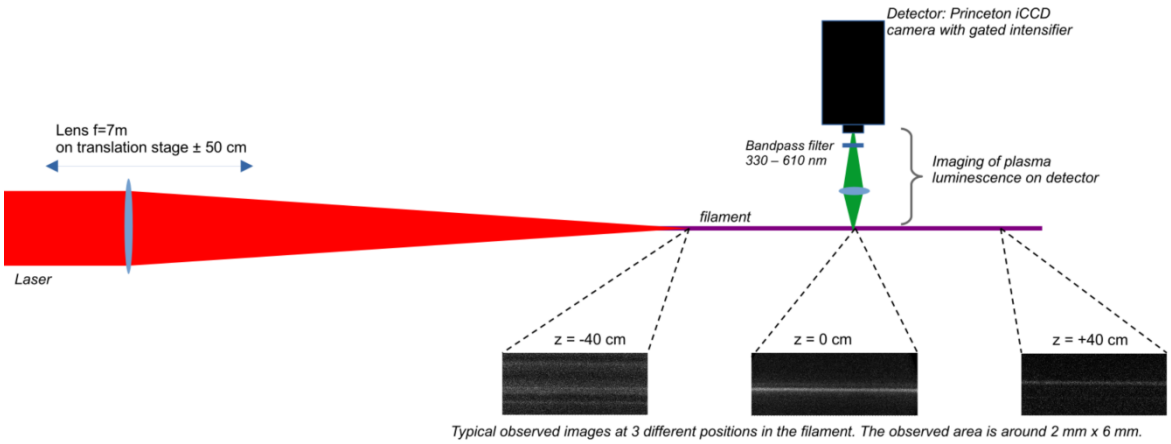

Figure 2.1.1: Experimental setup used to measure the plasma luminescence.

The experimental setup, presented in figure 2.1.1, consists of a pump laser focused by a lens of 7 m focal length to create the filaments and a time-gated intensified camera (Princeton iCCD) used to collect the light emitted by the filaments in the transverse direction. The pump laser has a maximum energy of 150 mJ and a minimum pulse duration of 780 fs. The iCCD detector is set at a fixed position, but the lens focusing the pump laser is moved by steps of 5 cm in the longitudinal direction, allowing to measure the light emitted at different positions along the filament axis. The detector has a gate time of 5 ns and is synchronized with the laser, with a ~1 ns jitter.

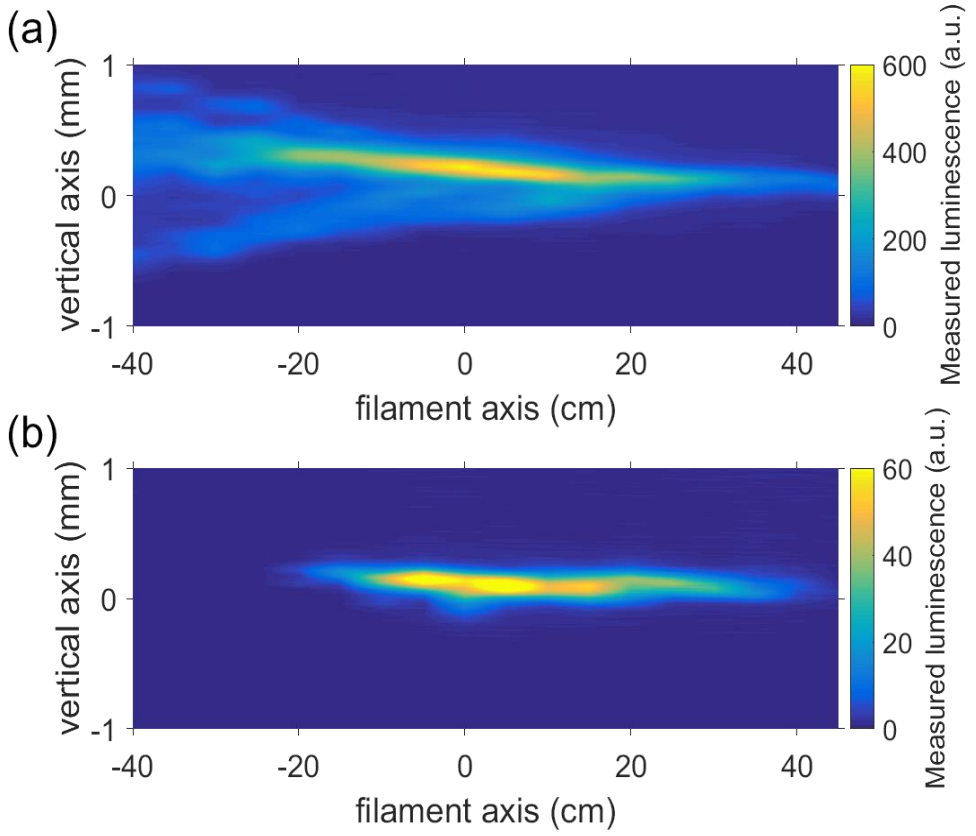

Figure 2.1.2: Picture of the luminescence of the plasma measured for an energy of (a) 150 mJ and (b) 20 mJ, for a pulse duration of 780 fs. The laser propagates from the negative to the positive values of the filament axis, and the lens focal plane is at z = 10 cm.

This measurement was done for two different laser pulse energies: 20 mJ and 150 mJ. These values are expected to correspond to the regular filamentation regime and superfilamentation regime, respectively. For these measurements, the pulse duration was set at 780 fs because it is the value commonly used during our experiment of guiding discharge.

The results, presented in figure 2.1.2, show a clear difference between the two regimes. The regime of superfilamentation presented in figure 2.1.2 (a) shows a maximum signal 7.5 times more important than for the regime of regular filamentation presented in figure 2.1.2 (b). This difference in luminescence is linked to a difference in the deposited energy, as it will be confirmed by additional measurement later in this chapter. Signal is measured over 60 cm in the regular filamentation regime, while it is measured over a whole length of 85 cm for the superfilamentation regime. It is important to note that the increase of length is not occurring in a symmetrical manner, but rather in the direction toward the laser, so further upstream the laser propagation.

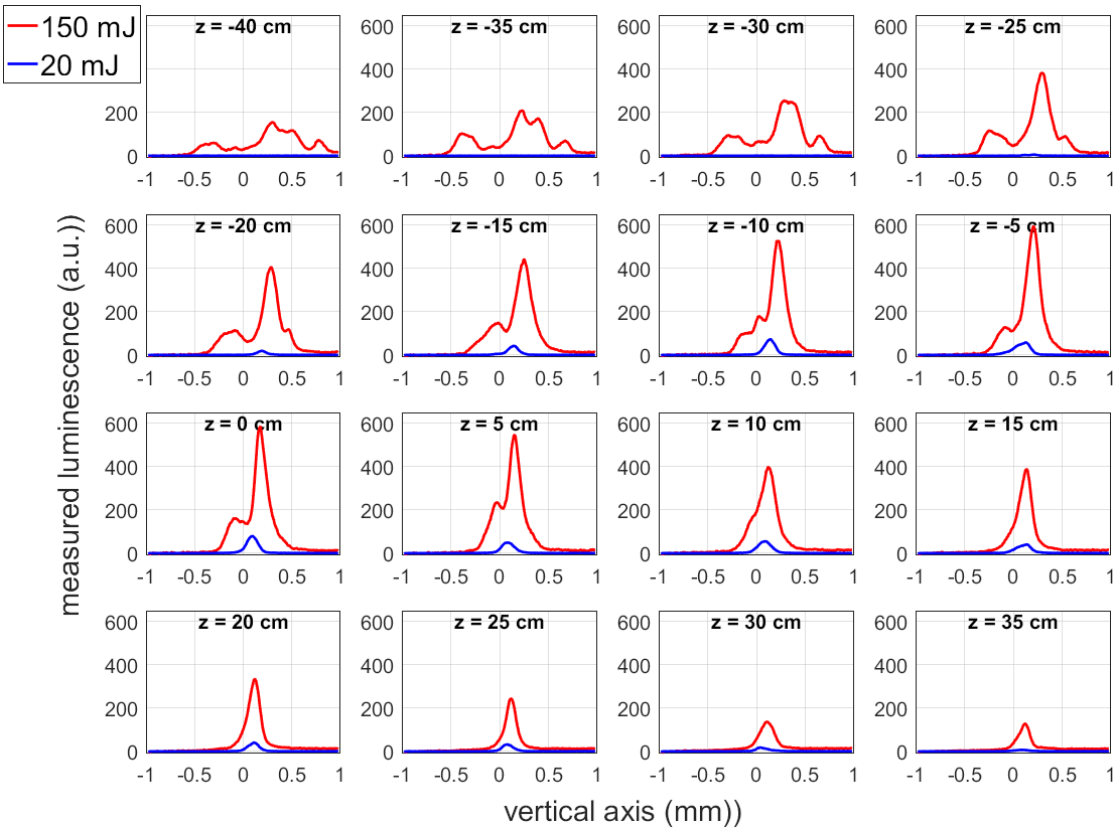

Figure 2.1.3: Plot of the luminescence profile along the vertical axis measured at different positions along the filament axis z, for an energy of 150 mJ (in red) and an energy of 20 mJ (in blue). The pulse duration is 780 fs.

Moreover, another distinction can be observed by looking at the profiles of the luminescence at different positions along the filament axis, as presented in figure 2.1.3. The regular filamentation shows profiles with a single peak, characteristic of a single filament. On the contrary the superfilamentation regime starts with profiles with several peaks, characteristic of the presence of multifilaments [8], and then evolves in profiles consisting of two peaks and finish with a single one. These later peaks show a much higher value of measured luminescence, and are attributed to what we expect to be the superfilaments.

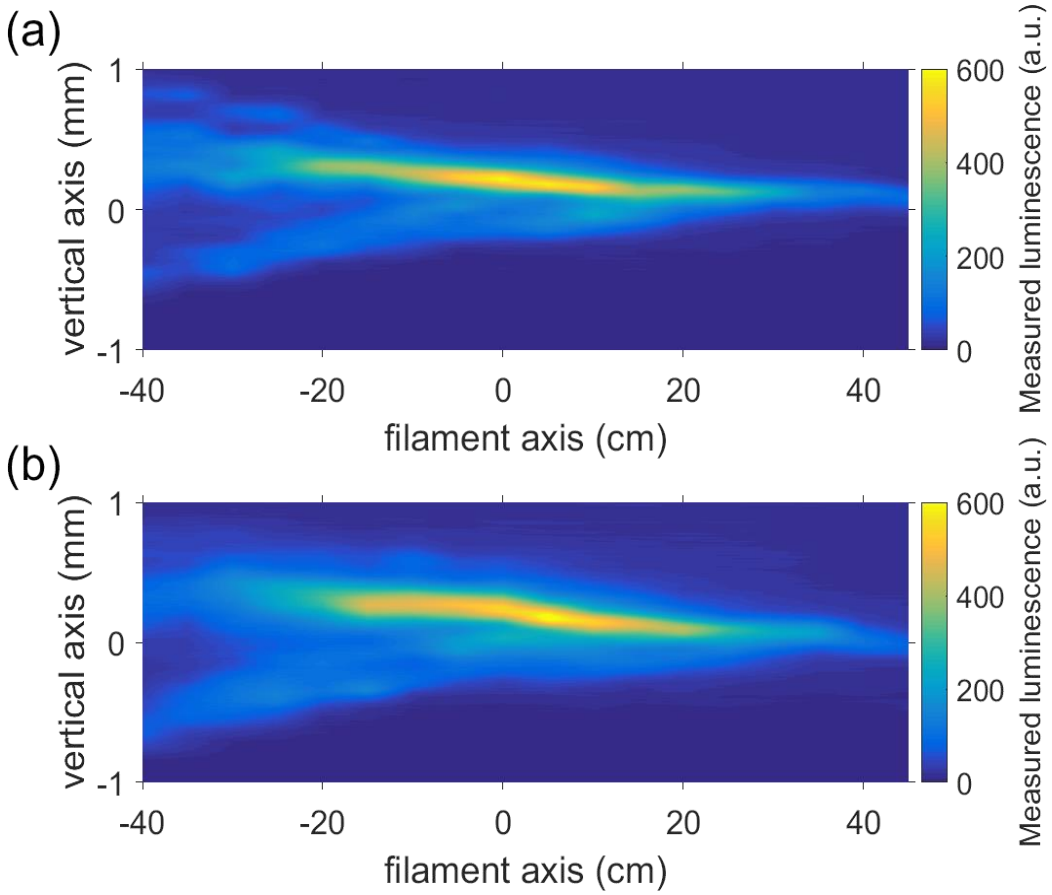

Figure 2.1.4: Picture of the luminescence from the plasma measured for an energy of 150 mJ, for a pulse duration of 780 fs (a) and 50 fs (b). The laser propagates from the negative to the positive values of the filament axis, and the lens focal plane is at z = 10 cm.

To characterize the effect of the pulse duration on our measurement, it was repeated for a set energy of 150 mJ for the two pulse durations of 50 fs and 780 fs. The results, presented in figure 2.1.4, show no significant differences between the measurements at the two pulse durations. This confirms that the observations based on the measurements made at a pulse duration of 780 fs that will be later presented in this chapter would be similar for shorter pulse durations.

2.2 Measurement of the induced density variation

The superfilament carrying a significantly higher intensity and depositing more energy in the medium, it should lead to a higher heating and thus a higher density variation.

To confirm this, the density variation setup presented in the previous chapter “Laser filamentation at high repetition rate: Study of the cumulative air density depletion and its application to electric discharge triggering” was used to characterize the under-dense channel created in the superfilament regime [9]. The filaments were created, in the same way as previously, by focusing a pump laser through a lens of a focal length of 7 m. The pump laser has a repetition rate of 10 Hz, thus no cumulative effect is expected. The phase shift induced on a probe laser passing through the filamentation zone is measured at several positions along the filament axis, allowing to characterize the under-dense channel over the whole study zone.

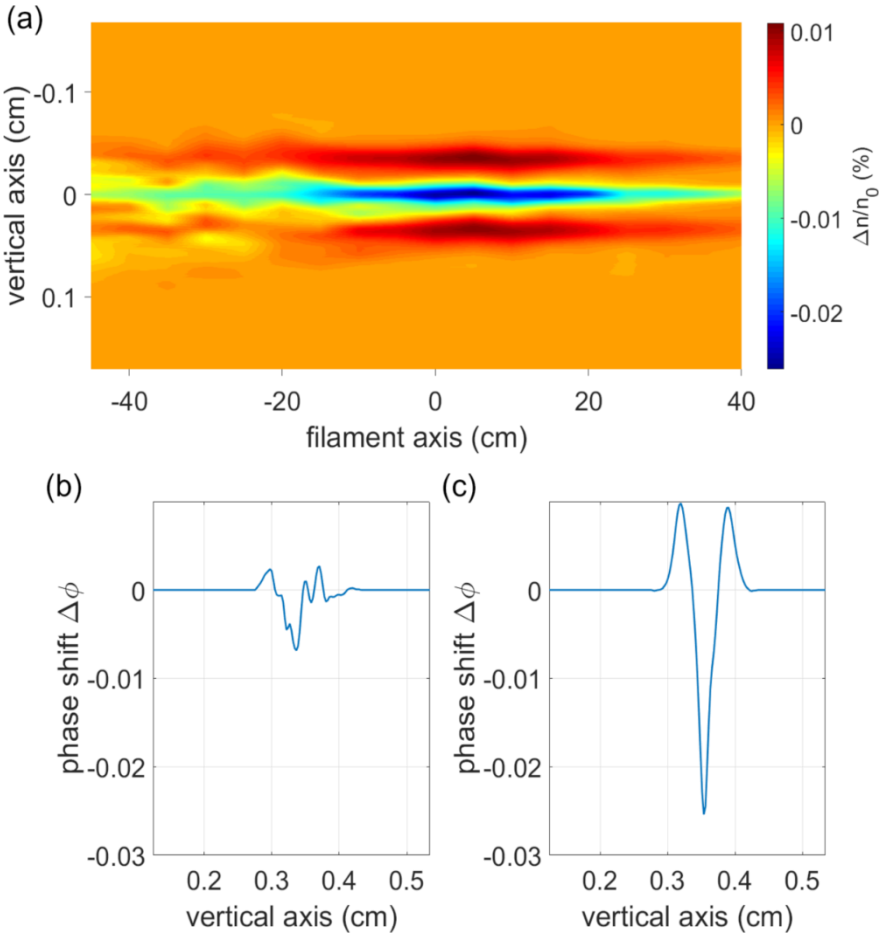

Figure 2.2.1: (a) Phase shift induced by the under-dense channel created by the filamentation of the 150 mJ, 780 fs pump laser, measured 1 µs after the laser pulse. Profiles of the phase shift measured at the position -40 cm (b) and 0 cm (c) along the filament axis. The laser propagates from the negative to the positive values of the filament axis, and the lens focal plan is at z = 10 cm.

The result of the characterization of the under-dense channel created in the superfilament regime, by using a pump energy of 150 mJ, is presented in figure 2.2.1. Similar features that were already observed on the filament luminescence is again observed in the phase shift measurement: as seen in figure 2.2.1 (a), the phase shift starts with a profile showing several relatively weak peaks and then evolves as we approach the focal plane in a profile with a single important peak, as observed in figure 2.1.1 (c). This highlights the transition from the multi-filamentation regime, characterized by the presence of several filaments, to the regime of superfilament.

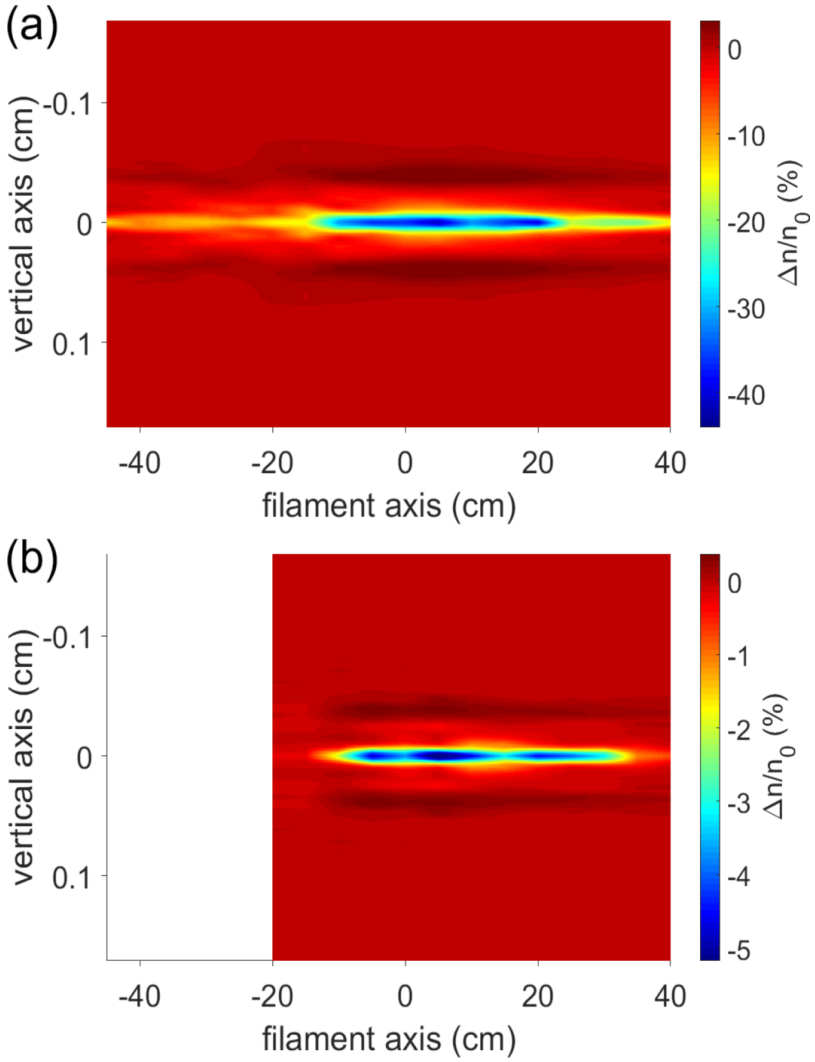

Figure 2.2.2: Neutral density variation induced by the filamentation of a 780 fs laser pulse with an energy of 150 mJ (a) and 20 mJ (b), measured 1 µs after the laser pulse. The laser propagates from the negative to the positive values of the filament axis, and the focal plane of the 7 m lens is at z =10 cm.

The same measurement was done for a pump energy of 20 mJ, and the comparison of the density variation retrieved from both measurements is presented in figure 2.2.2. A much more important signal is measured in the superfilamentation regime, with a maximum density variation of -41.8% to compare to the -5.6% in the regular filament regime. This difference in magnitude is easily seen in the profiles presented in figure 2.2.3.

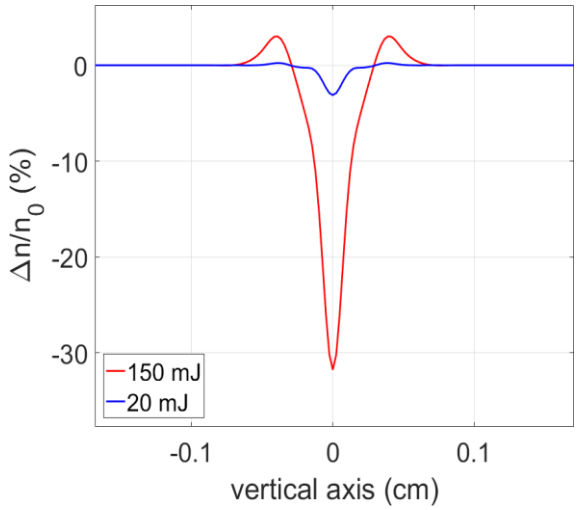

Figure 2.2.3: Profile of the density variation induced by the filamentation of the 780 fs pump laser set at 150 mJ (in red) and 20 mJ (in blue), measured at the 0 cm position of the filament axis, 1 µs after the last laser pulse.

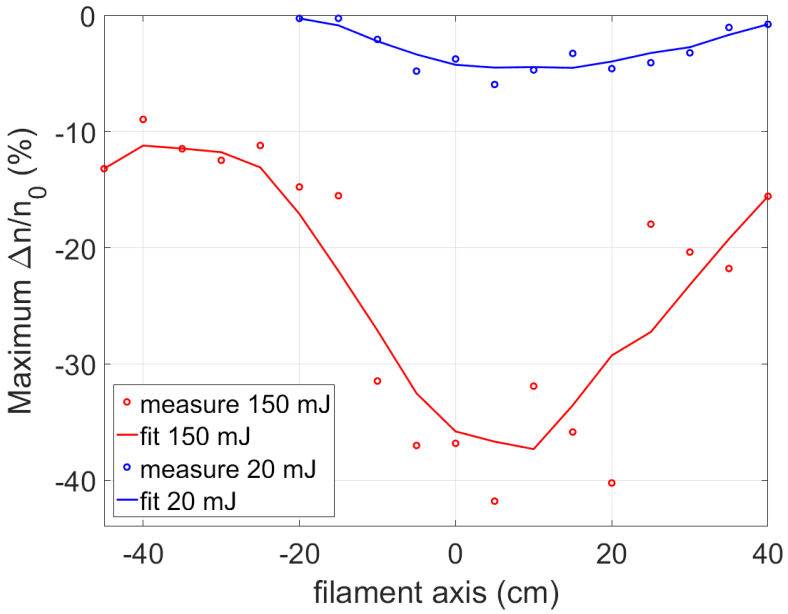

Figure 2.2.4: Evolution along the filament axis of the maximum of the density variation induced by the filaments created with a pump energy of 150 mJ (in red) and 20 mJ (in blue). The laser propagates from the negative to the positive values of the filament axis, and the focal plan of the 7 m lens is at z = 10 cm.

From the 2D measurement we retrieved the spatial evolution of the maximum of the density variation along the filament axis for both filamentation regimes. The results, presented in figure 2.2.4, show a clear length difference, as observed in the luminescence. Signal is observed over 60 cm for the regular filament, while it is observed over the whole 85 cm of the study zone in the superfilamentation regime.

Moreover, we can retrieve from the measurements the radius of the under-dense channel (see Figure 2.2.3) and the temperature in the underdense channel. We can then calculate the energy $E_{heating}$ necessary to heat the volume of air of this channel to this temperature using the formula:

$$E_{heating} = c_V \times \pi \times r^2 \times L \times \Delta T,$$

with c_v the air volumetric heat capacity, r the half-height radius of the under-dense channel, L its length and ΔT its mean temperature variation. For ease of calculation, ΔT is taken as half the value of the mean of the maximum temperature variation at each position.

The results give an estimated deposited energy of 61 mJ and 5.9 mJ in the case of the superfilamentation regime and regular filamentation regime, respectively. These values should be compared to the measured deposited energy in the medium by measuring the laser energy with a power meter before and after the filamentation area. The measurements give values of 79.2 mJ and 9.6 mJ for the two regimes. The calculated and measured values are in good agreement. The slight differences are mainly attributed in the case of the regular filamentation regime to the power meter precision of several mJ (the power meter is typically used to measure value of several hundreds of mJ) and in the case of the superfilamentation regime to an underestimation of the value of $E_{heating}$ due to the fact that not all the heated areas could be considered because they were outside the range of our study zone. A part of the deposited energy is also radiated by the plasma or transferred to the surrounding medium through the emission of a shockwave.

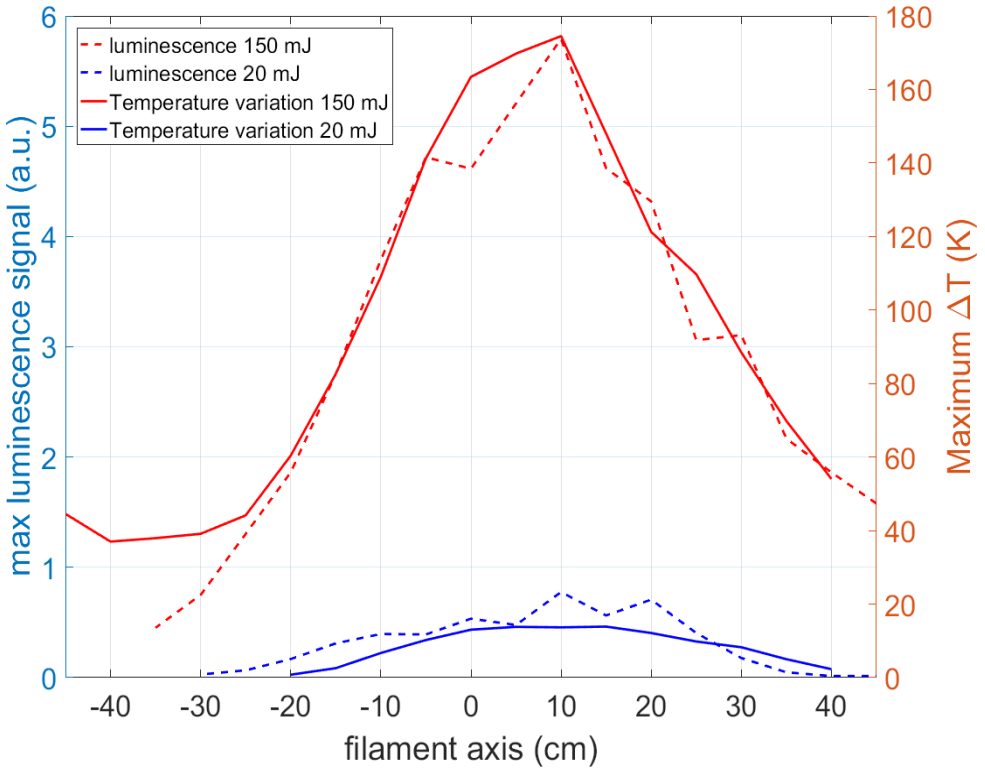

Figure 2.2.5: Comparison between the evolution along the filament axis of the maximum of the temperature variation and the luminescence, induced by the filaments created for a pump energy of 150 mJ (in red) and 20 mJ (in blue). The laser propagates from the negative to the positive values of the filament axis, and the focal plane of the 7 m lens is at z = 10 cm.

The measurement of the luminescence and the density variation showing similar features, a link between the two can be presumed. A simplified way to conceptualize it is the following: both effects come from the free electrons that are detached from the medium by the high field ionization occurring in the filament. Then, these free electrons recombine with their parent ions emitting a part of their excessive energy in the form of luminescence, while another part is transferred to the ions in the form of kinetic energy, thus leading to an elevation of the temperature of the medium. An increase of the number of free electrons during the filamentation would lead to increase both the luminescence and the temperature. These two values should then stay proportional to each other. Note that this interpretation is simplified and does not consider any saturation that could occur at high electron

density or temperature variation. Such simplification is reasonable in the present case, the ionisation rate being in the range of several % and the temperature variation being in the range of the hundreds of K.

The comparison between the maximum of the temperature variation and the maximum of the luminescence, measured at different positions along the filament axis both in the regular filamentation and superfilamentation regimes, is presented in figure 2.2.5. The results indeed show a constant proportionality of the two measurements in both regimes, validating the interpretation described above. This can allow us to simplify the characterization of filamentation regime in future experiments, the measurement of the luminescence being directly related to the temperature variation while being way quicker and simpler to perform.

2.3 Astigmatism: difference between side- and top-view measurements

The filamentation growth being closely related to the transverse intensity profile and to the spatial phase of the laser beam, it is affected by any possible aberration, such as astigmatism [10, 11]. This astigmatism was characterized by measuring the beam transverse size in both the horizontal and vertical directions using a laser beam profiler (BEAMAGE-4M CMOS camera from GENTEC-EO).

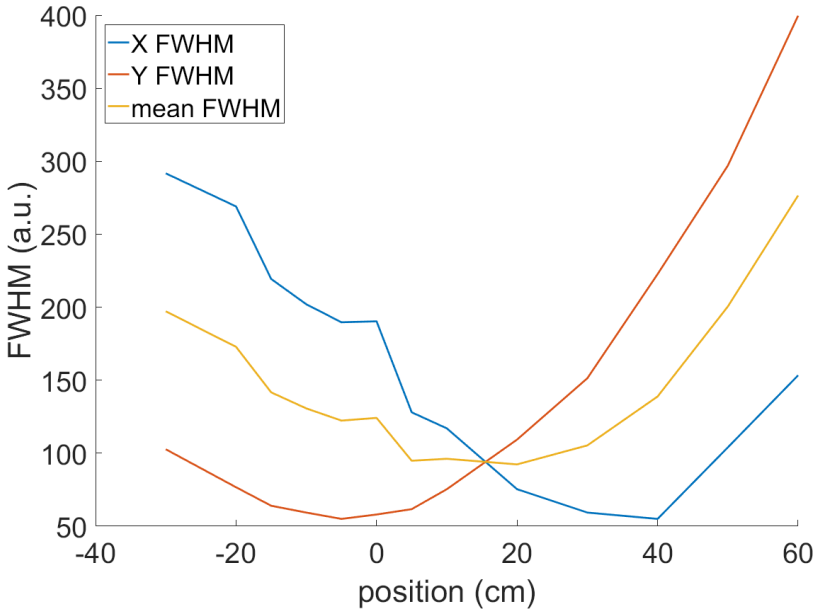

Figure 2.3.1: Plot of the evolution of the measured beam FWHM in the y direction (vertical direction), x direction (horizontal direction) and corresponding averaged FWHM.

The results, presented in figure 2.3.1, show the presence of two different focal points for the x and y directions, separated by 40 cm, which is typical of a 0° astigmatism. The presence of this astigmatism will affect the spatial distribution of filaments in each direction.

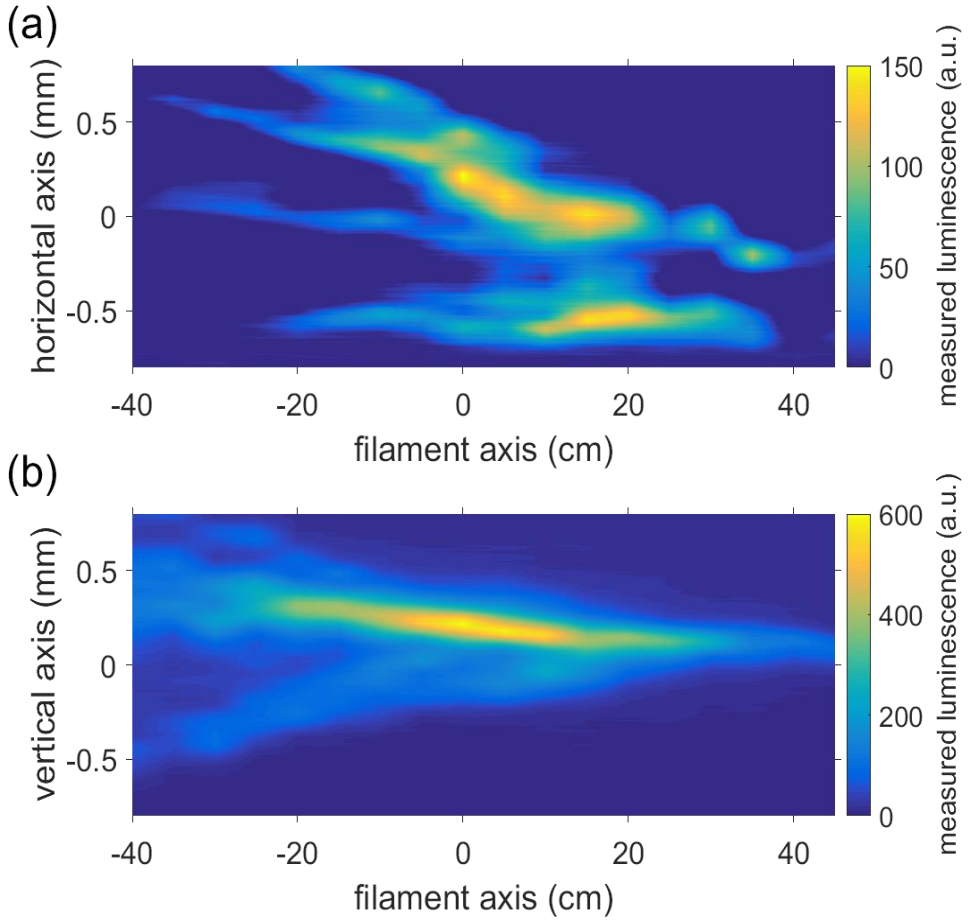

Figure 2.3.2: Picture of the luminescence from the plasma measured for an energy of 150 mJ, pulse duration 780 fs, taken from the top (a) and from the side (b). The picture is averaged over 50 laser pulses.

To characterize this effect, we performed measurement of the plasma luminescence using the same setup as described in figure 2.1.1. The latter was slightly modified so that the camera collects the light emitted in the vertical direction, allowing us to reconstruct the spatial distribution of filaments in the horizontal plane. The comparison between the filaments distribution in the horizontal plane and in the vertical plane is presented in figure 2.3.2. Contrary to the vertical distribution, where only one superfilament seems distinguishable, a structure with two superfilaments can be seen in the horizontal plane. The presence of these two superfilaments will affect the conductive behaviour of the filamentation, this effect being explained more in details later in this chapter.

2.4 Shot to shot variation

In our measurement, the spatial distribution of the luminescence is reconstructed from several measurements made consecutively at different positions along the laser propagation. At each position, the luminescence signal was averaged over 50 shots. One can then think that the discontinuity observed in top-view measurements (figure 2.3.2(a)) could be due to the shot-to-shot variations of the transverse position of filaments. This could lead to the identification of two distinct superfilaments, while only one would be present at each laser shot, with its position changing from left to right from shot to shot.

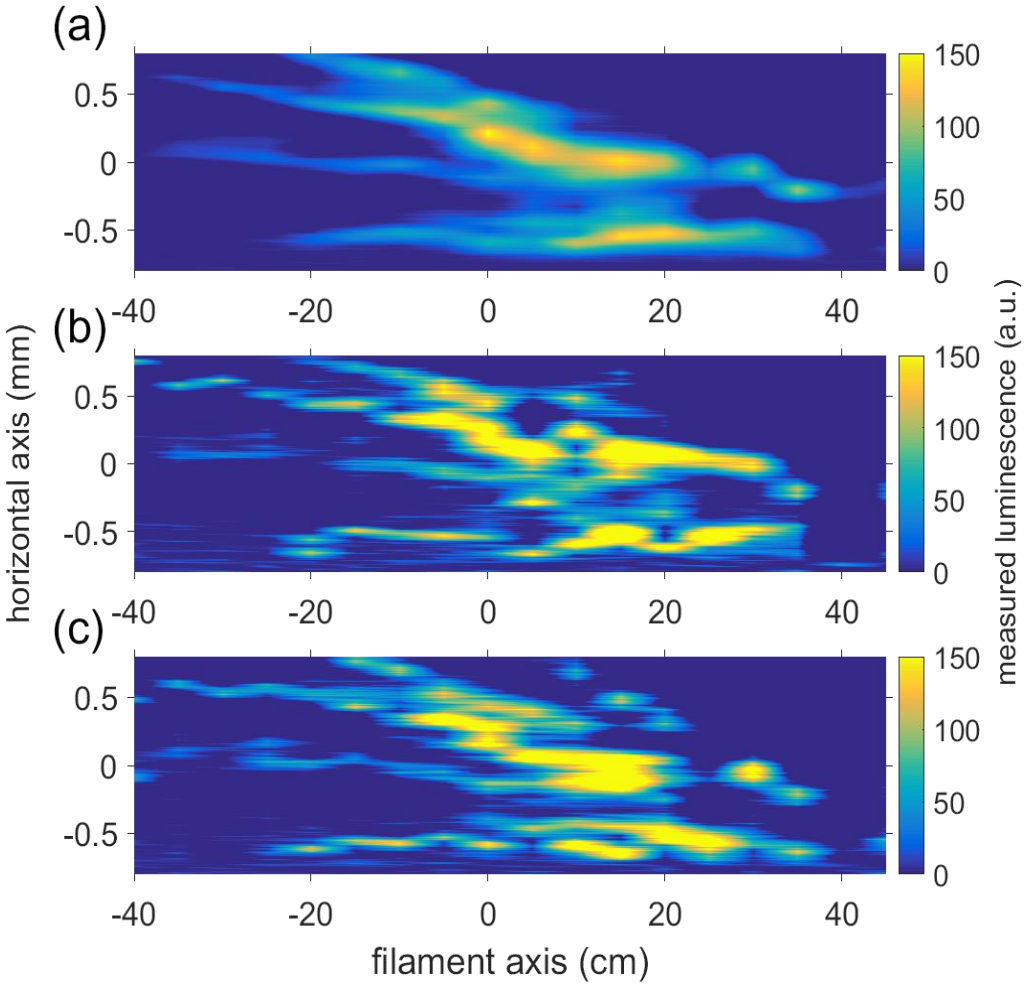

Figure 2.4.1: Picture of the luminescence from the plasma measured for an energy of 150 mJ, pulse duration 780 fs, taken from the top. (a) is averaged over 50 laser pulses, while (b) and (c) are from two different single shots.

To ensure the validity of our observation, we repeated the whole process by measuring the plasma luminescence induced by 50 laser pulses at each position along the filament. We then reconstructed the whole spatial distribution and compared the results based on two different single shots and on the average of the 50 pulses. The results, presented in figure 2.4.1, indicate a slight variation from shot to shot, but not large enough to invalidate the reconstruction of the whole 2D map from several measurement.

3 Consequence on guided discharges

In the last part, we saw that the two filamentation regimes lead to very different under-dense channels. The one resulting from the superfilamentation is deeper and longer than the one resulting from regular filamentation. The under-dense channel being the main cause affecting the guiding of discharges, a strong difference should be observed for each filamentation regime.

3.1 Discharge length for the two filamentation regimes

We first characterized the maximum length of a high voltage streamer discharge guided by the two filamentation regimes, by recording its propagation with a high speed camera.

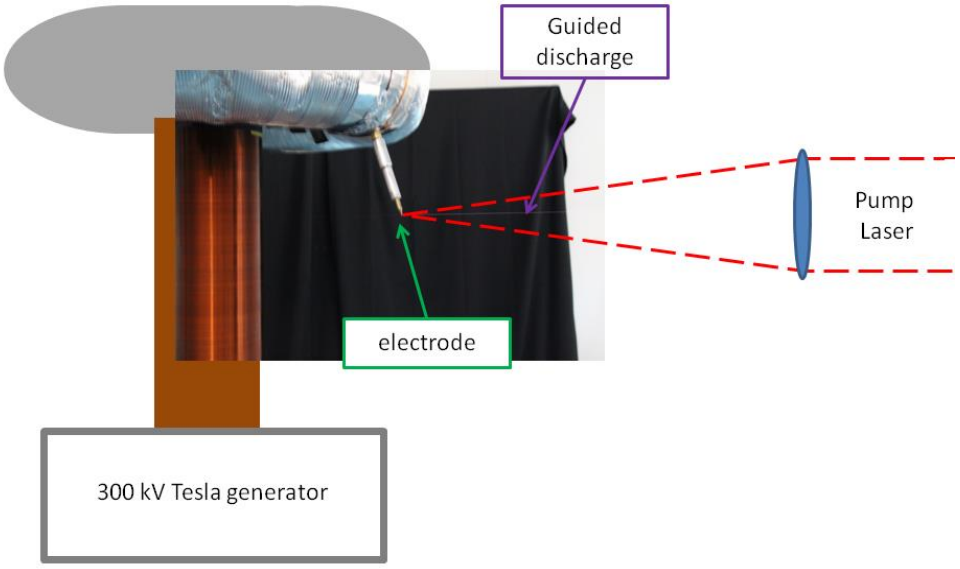

Figure 3.1.1: Experimental setup used to measure the length of the guided discharge as a function of the pump energy of the laser.

The experimental setup, presented in figure 3.1.1, consists of a laser pulse focused through a lens of focal length 7 m that will be used to create the filaments, and a 300 kV high voltage Tesla generator. The lens longitudinal position is adjusted so that its focal point is near the tip of the high voltage electrode. The Tesla generator is triggered by the laser clock system with a delay set so that the laser pulse is synchronized with one of the maximum of the oscillating voltage of the Tesla generator, as shown in figure 3.1.2. Triggered by the same signal, a high speed camera with a frame rate of 200 000 frames/s is used to record the propagation of the discharges in air. Note that only one electrode is used in this setup and no ground electrode is present.

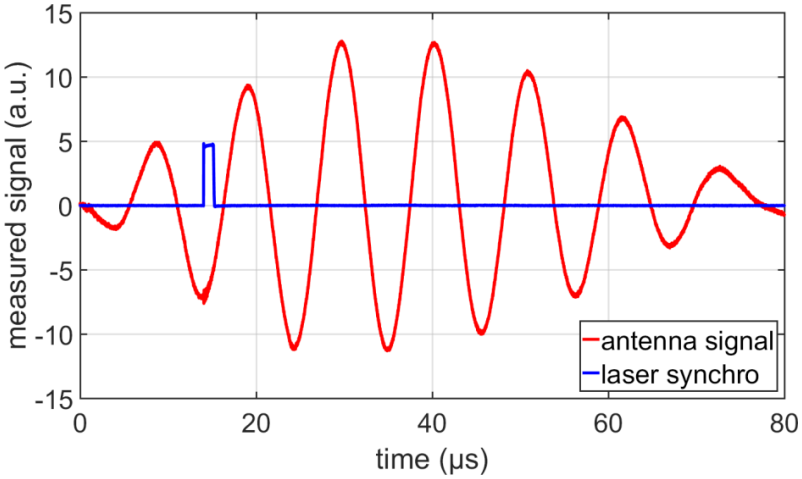

Figure 3.1.2: Plot of the oscilloscope measurement showing the signal of synchronisation of the laser pulse (in blue), and the signal of the antenna measuring the voltage at the high voltage electrode of the Tesla generator (in red).

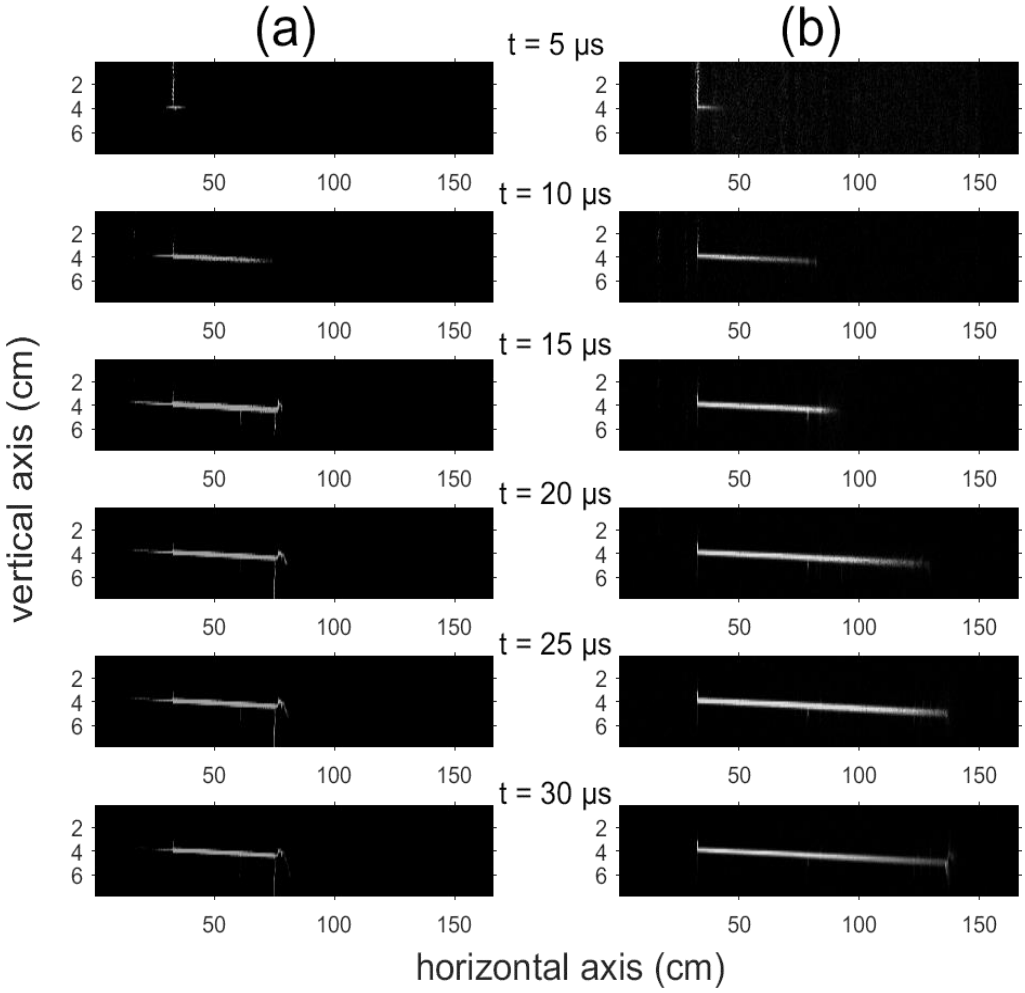

Figure 3.1.3: High speed camera frames showing the propagation of the electrical discharge guided by filaments created by a pump laser set at energy of 20 mJ (a) and 150 mJ (b), corresponding to the regular filamentation and superfilamentation regime, respectively. The high voltage electrode is located at the 32 cm position of the horizontal axis. The laser propagates from the left to the right of the frames.

The propagation of the electrical discharge was recorded in both cases of the regular filamentation and superfilamentation regime by setting the energy of the pump laser at 20 mJ and 150 mJ, respectively. The results, presented in figure 3.1.3, show a clear difference in the discharge length between the two regimes. In the case of the regular filamentation, the discharge covers a distance of 49 cm, while it goes up to 106 cm in the superfilamentation regime. This difference of a factor 2 is significant, but can be explained by the density variation measured previously.

If we look at the propagation of the discharge, it propagates as far as possible until the mean electric field integrated over the discharge path becomes lower than an electric field threshold that will be called E_{lim}, threshold that is mainly determined here by the setup geometry and the discharge type[1]. The distance of propagation being on the order of several tens of cm - one order of magnitude greater than the radius of curvature of the electrode - we can neglect the peak effect of the electrode and define the mean value of the electrode field as $E_{lim} = U/L_{lim}$, where U is the Tesla generator peak voltage (300 kV) and L_{lim} the maximum distance over which the discharge can propagate.

Since the filament modifies the air density, we should also consider its effect. The limit is thus not only determined by E_{lim} but by the ratio E_{lim}/n_{mean} [12], where n_{mean} is the mean air density over

[1] For the propagation of positive streamers, a background electric field of about 500 kV/m is required and, for negative streamers the required field is about 1 MV/m to 2 MV/m. The electric field changing sign during the propagation in our experiment, the value is not fully determined but lies most probably between these two values.

the discharge path. Using the previous explanation, we can write the limit value as $U/(L_{lim}*n_{mean})$. The value of U being constant in our experiment as well as the discharge type and the setup, the product $L_{lim}*n_{mean}$ should remain constant. The two different filamentation regimes resulting in a different under-dense channel and thus a different n_{mean}, it is then expected to have a different length of discharge L_{lim}.

To ease the comparison that will be presented in this paragraph, we now consider a system of unit, where the normal air density (2.47×10^{25} m^{-3}) is considered to be dimensionless and has a value 1, while the distances are counted in cm. By using the value measured in the superfilamentation regime, the product $L_{lim}*n_{mean}$ give us a value of 48.7, while it has a value of 51.4 in the regular filamentation regime. These two values are quite similar and agree with the previous explanation. The slight difference between the two can be quite easily explained by the oversimplification of our model where the spatial variation of the field is not taken into account, and no effect other than the density variation is considered.

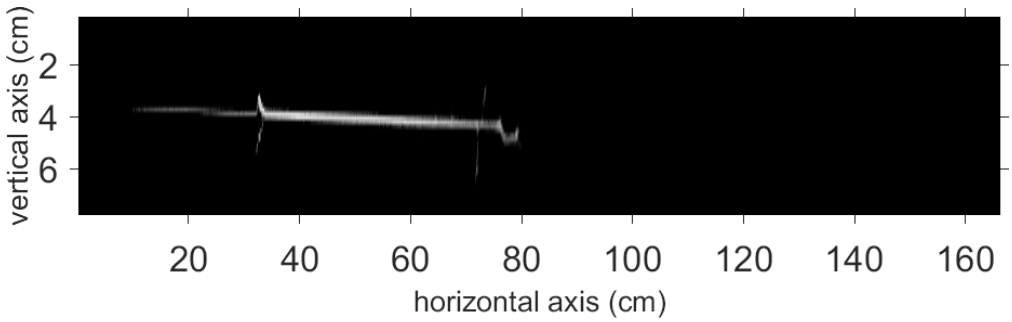

Figure 3.1.4: High-speed camera frame showing the propagation of the electrical discharge guided by filament created by a laser pulse with an energy of 20 mJ, taken 30 μs after the laser pulse. The discharge propagates in two opposite directions (upstream and downstream of the laser propagation) in regard to the high voltage electrode, located at the 32 cm position of the horizontal axis. The laser propagates from the left to the right of the frame.

An interesting point observed in the discharge propagation is that it goes along the filament axis in the two opposite directions starting from the high voltage electrode, as displayed in figure 3.1.4. This shows that a conducting path is present in both directions. This is consistent with the previous observation, showing the presence of a density variation still present after the lens focal point, thus after the electrode (see figure 2.2.2).

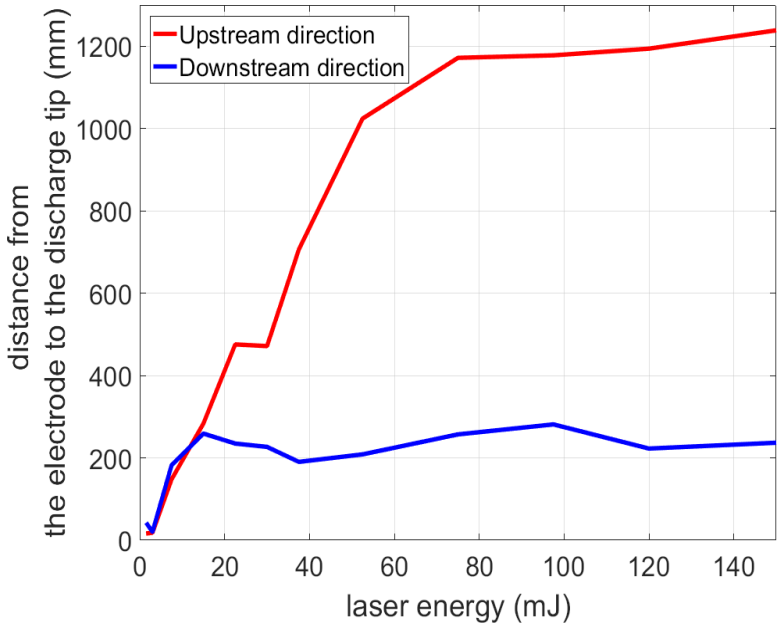

Figure 3.1.5: Maximum distance of the discharge propagation as a function of the laser energy in both directions, upstream and downstream of the laser propagation (as described in figure 3.1.4).

The propagation paths of the discharges were recorded for various laser energies ranging from 0 mJ (no laser) to 150 mJ. The measurements were repeated 5 times for each energy level and each time the highest discharge length was considered. The results, shown in figure 3.1.5, indicate a clear increase of the discharge length in the upstream direction as the energy increases from 0 to 75 mJ. Then, the evolution reaches a plateau, where the length does not increase anymore. The first initial increase is due to the apparition of an increasing number of filaments followed by their merging into a superfilament. The plateau is reached when the additional filaments resulting from the increase of energy are formed so far from the geometrical focus that they are too dispersed to merge (as seen in figure 2.2.1 (b)) and too far away to contribute to the discharge propagation (their position being further away from the electrode than the discharge length).

The evolution in the downstream direction is clearly different as a plateau is quickly reached for energy level above 15 mJ. This is semi consistent with the previous measurement. As observed in figure 2.1.2, the downstream length of the density channel is indeed constant between the measurement made at 20 mJ and 150 mJ which is consistent with apparition of the plateau. However, the amplitude of the measured density variation varies between the two energy values, which should lead to an increase of the discharge length and thus is inconsistent with the presence of a plateau.

3.2 Speed of the discharge for the two filamentation regimes

One other information that can be retrieved from the high-speed camera measurement is the velocity of the discharge propagation.

Time (µs)	Length at 20 mJ (cm)	Length at 150 mJ (cm)	Speed at 20 mJ (10^3 m/s)	Speed at 150 mJ (10^3 m/s)
5	4.7	7.6	9.4	15.2
10	40.7	48.2	72.0	81.0
15	44.2	57.2	7.0	18.0
20	47.2	95.2	6.0	76.0
25	47.8	104.0	3.2	18.0

30	49.2	106.0	0.8	4.0

Table 3.2.1: Evolution of the length and the speed of the discharge guided by the filament for a laser pulse energy set at 20 mJ and 150 mJ.

The velocity values measured in the superfilamentation and regular filamentation regimes are presented in table 3.2.1. The first thing to observe is the cyclical variation of the velocity. This is due to the oscillation of the Tesla voltage leading to a change of the discharge polarity during its propagation. The half period of the Tesla generator being of 5 µs, the change of sign is synchronized with the camera frame rate. Both polarities having different characteristic speeds of propagation, it explains the cyclical variation of the measured values.

The second important point is the difference between the measured speeds in the two initial frames. In the regular filamentation regime the speed is of 9.4 km/s, while it is of 15.2 km/s in the superfilamentation regime. This difference can be explained by taking into account that the factor limiting the speed of the discharge propagation is the time needed for the current to heat the medium (see the description of the propagation of a leader in the introduction). However, this time is different in the two regimes because the air density is different, a lower air density leading to a shorter heating time. If we look at the ratio between the propagation speeds in the two filamentation regimes, we get a value of 0.62, while the ratio of the density is of 0.66. The similarity of the two ratios is consistent with the previous explanation.

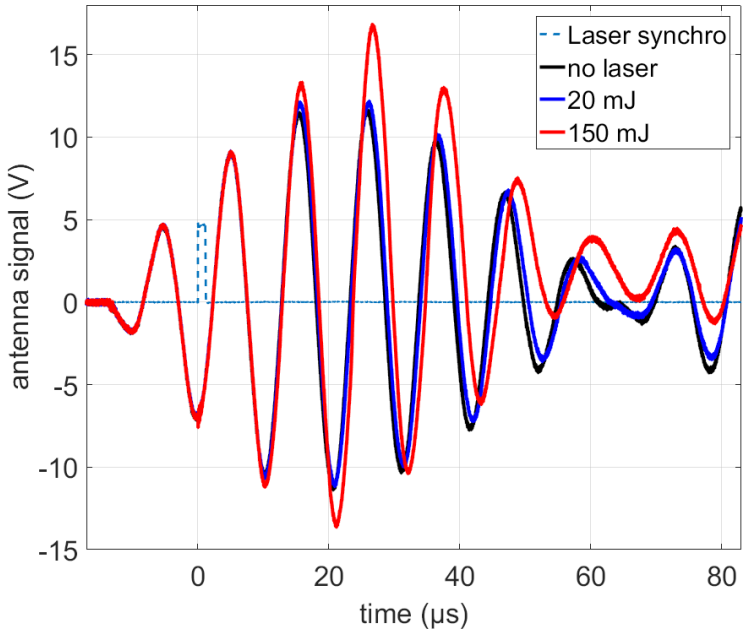

Figure 3.2.1: Plot of the oscilloscope measurement showing (in dashed blue) the signal of synchronization of the laser pulse, and the signal of the antenna measuring the voltage at the output of the Tesla generator without the laser (in black), in the presence of a laser pulse of energy 20 mJ (in blue), and in the presence of a laser pulse of energy 150 mJ (in red).

This observation of a dependence of the discharge velocity on the gas density is in contradiction with previous observation presented in [13], where measurements at different densities show the same propagation speed. This discrepancy can be explained by multiple factors. The first cause could be the modification of the Tesla voltage during the discharge propagation in the presence of superfilament, as shown in figure 3.2.1. This effect is however clearly present only at delay greater than 15 µs and should not affect the first steps of the propagation. A second explanation could be based on the difference of the homogeneity of the density. In [13], the density is reduced homogeneously by lowering the gas pressure. Thus, no specific direction is promoted during the

discharge propagation. On the contrary, in our experiment the pressure is not changed but the gas temperature is locally changed, resulting in a specific channel, where the discharge propagation will be enhanced. This will lead to a squeezing of the streamers present at the extremity of the discharge (all the streamers will favourably stay in the under-dense channel) and result to a local enhancement of the current density, thus an enhancement of the local heating. This enhancement of the heating could facilitate the propagation of a leader channel and result in a greater propagation speed. The efficiency of this squeezing being greater for high density variation (the boundary that delimits the streamer distribution being sharper), the presence of superfilament could lead to a higher propagation speed of the discharge.

3.3 Jump in the discharge path

While guided discharges over short distance in the range of several cm are characterized by a straight continuous path, the discharges measured in our experiments sometimes show a segmented path consisting of several straight parts parallel with each other but slightly displaced, which are connected by what we will call a discharge jump.

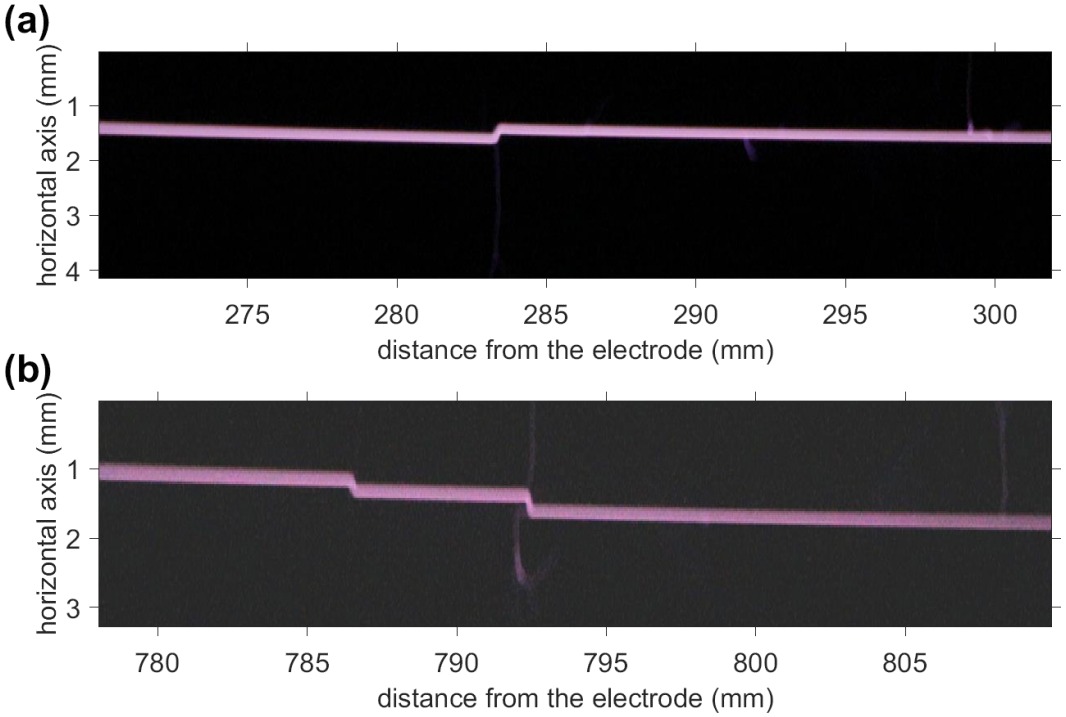

Figure 3.3.1: Still picture of the discharge path taken from under the discharge, with a camera. In the two different measurements, the discharge paths are clearly segmented.

Two examples of such segmentation can be observed in the pictures presented in figure 3.3.1. By repeating the same measurement, the segmentation appears and disappears randomly. While its position and presence seem random, one consistent value is the length of the jump. The two examples in figure 3.3.1 shows 3 jumps in total of lengths 146, 146 and 195 μm.

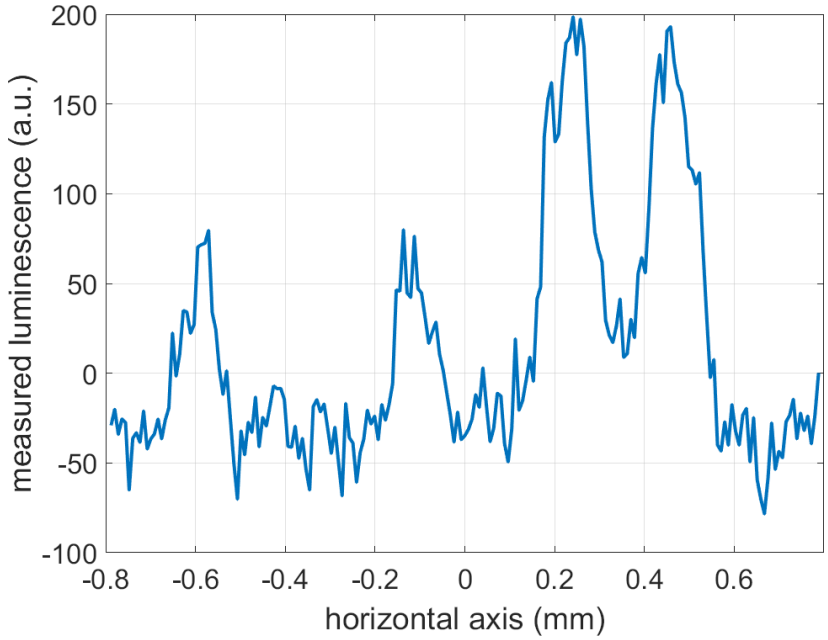

Figure 3.3.2: Profile of the plasma luminescence measured at the same position and with the same angle of view as in the picture of figure 3.3.1 (a).

The main actor of the guiding of the discharges being the under-dense channel, this jump should be linked to its structure. By looking at the luminescence profile (directly related to the under-dense variation) presented in figure 3.3.2, we can see two peaks indicating two strong and distinguishable under-dense channels. If we look at the distance separating the two, we have a distance of 210 µm, which is a distance similar to the jump length. This suggests that the jump is in fact the discharge jumping from the under-dense channel resulting from one superfilament to another. It is interesting to note that in our case, only the two superfilaments are close enough to be bridged by a jump, the closest regular filamentation being 370 µm away.

4 Conclusion

In this chapter, I presented that strongly focusing a high energy laser leads to a filamentation regime called superfilamentation. We observed in this regime an enhanced energy deposition in the region around the focusing region, resulting in an under-dense channel with a depth more important than the ones created by a regular filament. This enhanced under-dense channel greatly increases the reduction of the breakdown voltage as compared to the one of a regular filament.

This peculiar filamentation regime could be of utter importance to understand our capacity to efficiently guide electrical discharge. As it will be presented in the following chapter “Long-distance filamentation with kW ultrashort laser”, only experiments with a strongly focused beam, thus which could lead to superfilamentation, were observed to be able to guide electrical discharges.

Bibliography

[1] G. Point *et al.*, « Superfilamentation in Air », *Phys. Rev. Lett.*, vol. 112, n° 22, p. 223902, juin 2014, doi: 10.1103/PhysRevLett.112.223902.

[2] D. V. Pushkarev *et al.*, « Nonlinear increase in the energy input into a medium at the fusion of regularized femtosecond filaments », *JETP Lett.*, vol. 106, n° 9, p. 561-564, nov. 2017, doi: 10.1134/S0021364017210093.

[3] D. Pushkarev *et al.*, « Effect of phase front modulation on the merging of multiple regularized femtosecond filaments », *Laser Phys. Lett.*, vol. 15, n° 4, p. 045402, mars 2018, doi: 10.1088/1612-202X/aaa9ad.

[4] S. Henin *et al.*, « Saturation of the filament density of ultrashort intense laser pulses in air », *Appl. Phys. B*, vol. 100, p. 77, mars 2010, doi: 10.1007/s00340-010-3941-x.

[5] S.-M. Li *et al.*, « Unveiling stability of multiple filamentation caused by axial symmetry breaking of polarization », *Photonics Res.*, vol. 4, n° 5, p. B29-B34, oct. 2016, doi: 10.1364/PRJ.4.000B29.

[6] T.-T. Xi, X. Lu, et J. Zhang, « Interaction of Light Filaments Generated by Femtosecond Laser Pulses in Air », *Phys. Rev. Lett.*, vol. 96, n° 2, p. 025003, janv. 2006, doi: 10.1103/PhysRevLett.96.025003.

[7] Y. Brelet *et al.*, « Tesla coil discharges guided by femtosecond laser filaments in air », *Appl. Phys. Lett.*, vol. 100, n° 18, p. 181112, avr. 2012, doi: 10.1063/1.4711208.

[8] G. Méchain, A. Couairon, M. Franco, B. Prade, et A. Mysyrowicz, « Organizing Multiple Femtosecond Filaments in Air », *Phys. Rev. Lett.*, vol. 93, n° 3, p. 035003, juill. 2004, doi: 10.1103/PhysRevLett.93.035003.

[9] P. Walch, B. Mahieu, L. Arantchouk, Y.-B. André, A. Mysyrowicz, et A. Houard, « Cumulative air density depletion during high repetition rate filamentation of femtosecond laser pulses: Application to electric discharge triggering », *Appl. Phys. Lett.*, vol. 119, n° 26, p. 264101, déc. 2021, doi: 10.1063/5.0077635.

[10] G. Fibich, S. Eisenmann, B. Ilan, et A. Zigler, « Control of multiple filamentation in air », *Opt. Lett.*, vol. 29, n° 15, p. 1772, août 2004, doi: 10.1364/OL.29.001772.

[11] Y. Kamali, Q. Sun, J.-F. Daigle, A. Azarm, J. Bernhardt, et S. L. Chin, « Lens tilting effect on filamentation and filament-induced fluorescence », *Opt. Commun.*, vol. 282, n° 5, p. 950-954, mars 2009, doi: 10.1016/j.optcom.2008.11.009.

[12] J. P. Rajzer, J. P. Rajzer, et J. P. Rajzer, *Gas discharge physics*. Berlin Heidelberg: Springer, 1991.

[13] E. M. Bazelyan, Y. P. Raizer, et N. L. Aleksandrov, « The effect of reduced air density on streamer-to-leader transition and on properties of long positive leader », *J. Phys. Appl. Phys.*, vol. 40, n° 14, p. 4133-4144, juill. 2007, doi: 10.1088/0022-3727/40/14/007.

Chapter 5

Long-distance filamentation with kW ultrashort laser.

Figure 1: Picture of the frequency doubled beam propagating along the 140 m experimental zone.

In this chapter I will present a study of the filaments created by a laser system with J-range pulses of 1 ps duration at 1 kHz repetition rate. This study was done in the framework of the Laser Lightning Rod project to investigate the usability of such created filaments for atmospheric applications at long distance.

We investigated the spatial evolution over 140 m of the multiple filamentation regime obtained using both a collimated beam and a focused beam with different pulse durations and wavelength compositions. In the same conditions, we characterized the under-dense channel resulting from the filamentation process and its ability to control high-voltage discharges at different distances.

Table of content

1 Laser system

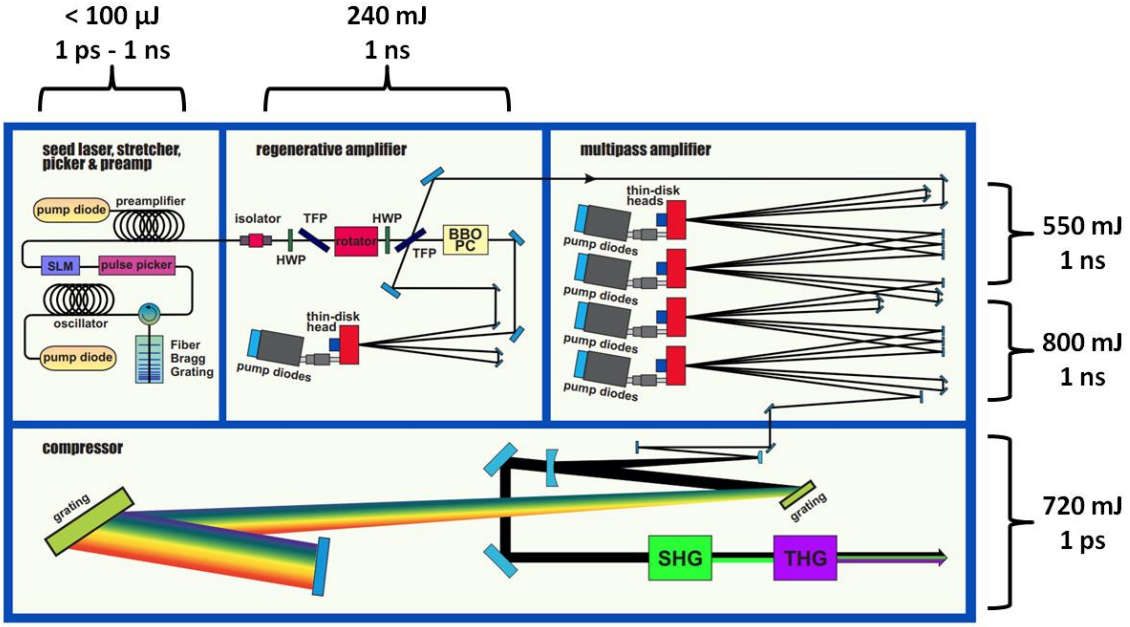

Figure 1.1: Layout of the LLR laser system

The laser system that was used in the experiments presented in this chapter is a specific laser prototype developed by TRUMPF scientific Laser (TSL) to meet the requirement of the LLR project (see chapter "The Laser Lightning Rod experiment"), with both high average and high peak power. It is based on a chirped-pulse amplification scheme and includes several amplification stages presented in figure 1.1, all operating at 1 kHz:

- The first stage consists of a commercially available regenerative amplifier (Dira200-1) developed by TSL, seeded by an industrial micromachining laser (TruMicro2000). Seed pulses are temporally stretched to a duration of ~1 ns by means of chirped fiber Bragg grating. This first amplification stage brings the low energy of the seed laser from 100 µJ to 240 mJ.
- The second stage is a multipass (MP) amplifier specifically developed in the framework of the LLR project. It consists of four industrial thin-disk laser heads used to increase the pulse energy from 240 mJ to 800 mJ (note that this stage can be divided into two distinctive stages, that will be called MP stage 1 and MP stage 2, respectively increasing the energy to 550 and 800 mJ).
- The last part of the laser is a grating compressor used to temporally compress the amplified pulses to a duration of 1 ps. Thanks to a diffraction grating with a high efficiency, the total compressor efficiency is approximately 90 %. Thus, laser pulses exiting the compressor can reach an energy of 720 mJ.

With this laser, pulses of max 720 mJ at 1030 nm with a pulse duration of 1 ps at a repetition rate of 1 kHz are available for our experiments.

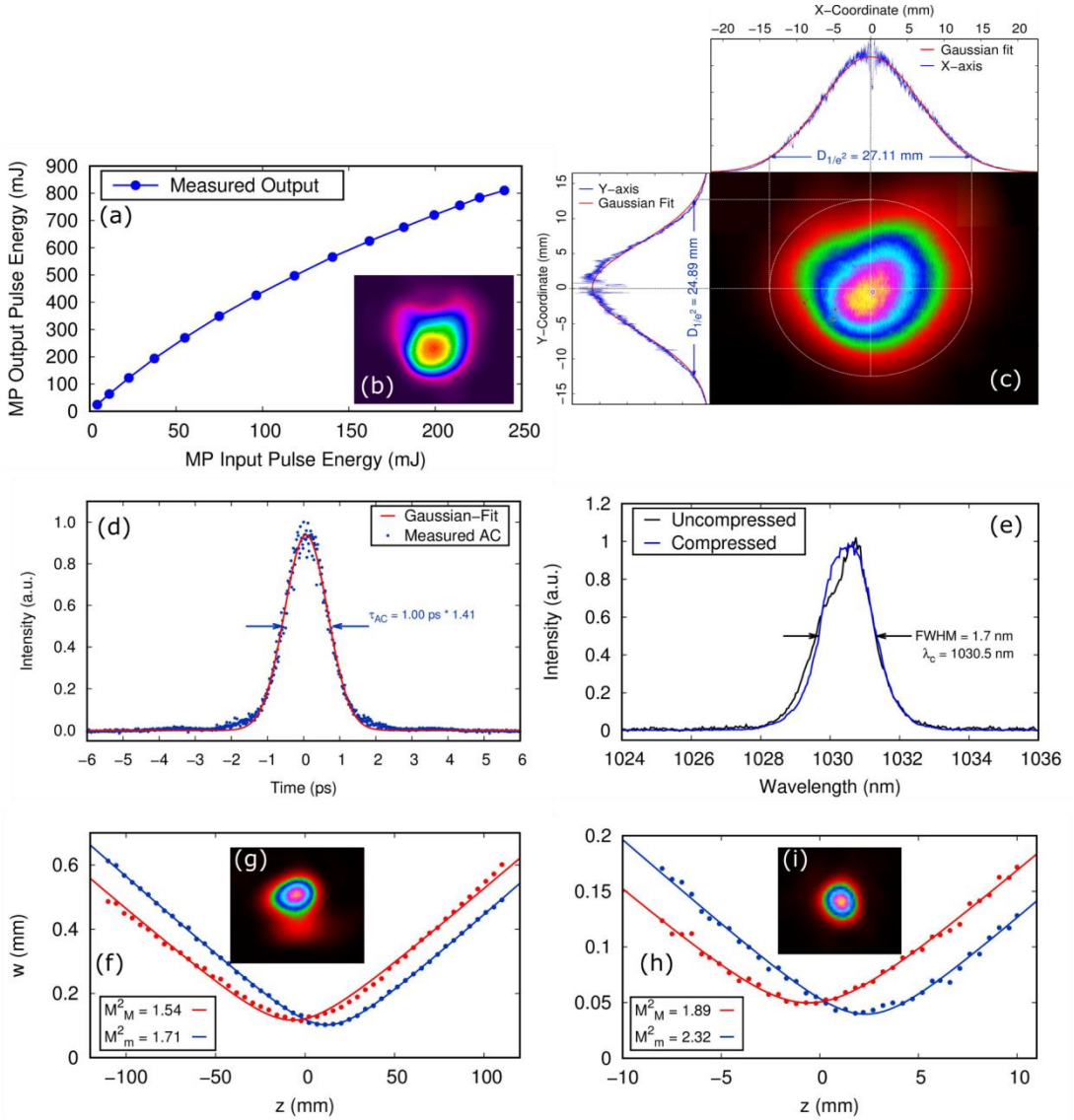

Figure 1.2: Measured characteristics of the final LLR laser system. (a) Evolution of the multipass output energy as a function of the injected regen energy. (b) Uncompressed output beam profile. (c) Compressed output beam profile (d) Pulse duration measured by autocorrelation at 720 mJ. (e) Pulse spectrum at 720 mJ. (f) M^2 measurement at 800 mJ before compression. (g) Beam profile at the focus position. (h) M^2 measurement at 720 mJ after compression. (i) Beam profile at the focus position.

The measured characteristics of the laser system are shown in figure 1.2. The main points are the following:

- The amplification of the MP stays constant over the range of the available input energy, showing no clear sign of saturation.
- The beam quality is not significantly changed while propagating through the compressor.
- The pulse duration, measured using an SHG autocorrelator, shows a full width at half maximum duration of 1.0 ps.
- The FWHM of the measured pulse spectrum is approximately 1.7 nm at full pulse energy and remains constant after compression.
- The beam quality of the output beam was measured before and after compression, resulting in an average M^2 of 1.6 and 2.1, respectively. The alteration of the beam quality after propagating through the compressor is typical of this type of grating compressors and is attributed to the imperfect surface quality of the gratings.

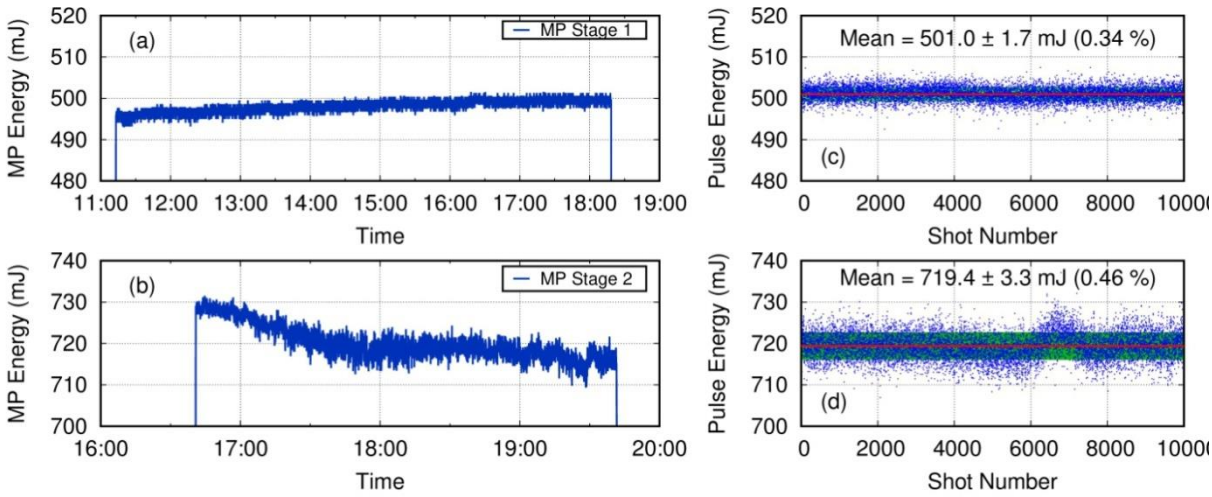

Figure 1.3: Long-Term measurement of the output energy of (a) MP stage 1 and (b) MP stage 2, and shot-to-shot pulse stability measured for (c) MP stage 1 and (c) MP stage 2.

To attest the reliability of the laser system needed for long experimentations, the MP energy and the shot-to-shot pulse stability were monitored over a period of 3 hours running at 800 mJ. The results are presented in figure 1.3 (note that the energy values are measured after compression). The long-term measurement of the energy of the MP shows a slight decrease of the energy over the hour timescale. This drift originates from the thermalization of the MP and leads to a modification of the extraction efficiency of each thin-disk laser heads. This thermalization effect results from both the laser thermalization and the temperature changes of the laboratory. The measured shot-to-shot pulse stability shows a standard deviation of 0.34 % for MP1 at 500 mJ and 0.46 % for the MP2 at 720 mJ, with a peak-to-valley range of 16 mJ and 30 mJ for each stage, respectively.

A more detailed description of the laser and its characteristic can be found in [1].

2 Second and third harmonic generation

To generate second and third harmonic of our laser (at 515 and 343 nm respectively), we used two lithium triborate crystals, grown by Cristal Lasers SA. LBO was selected as the nonlinear material because it fulfilled several requirements of our experiments:

- a high damage threshold (18.9 GW/cm^2 at 1053 nm) to withhold the beam high intensity,
- a low dilatation coefficient ($|\theta_L| = 10^5$ K), necessary to avoid mechanical stress due to the heating caused by the laser high average power,
- an excellent transmission (absorption $\mu < 10^2$ m^{-1} at 1.064 μm),
- a high nonlinear coefficient of (d_{32} = 1.02 pm/V [2]),
- the possibility to produce large aperture crystals (55 mm x 55 mm x 1.8 mm) with excellent optical quality.

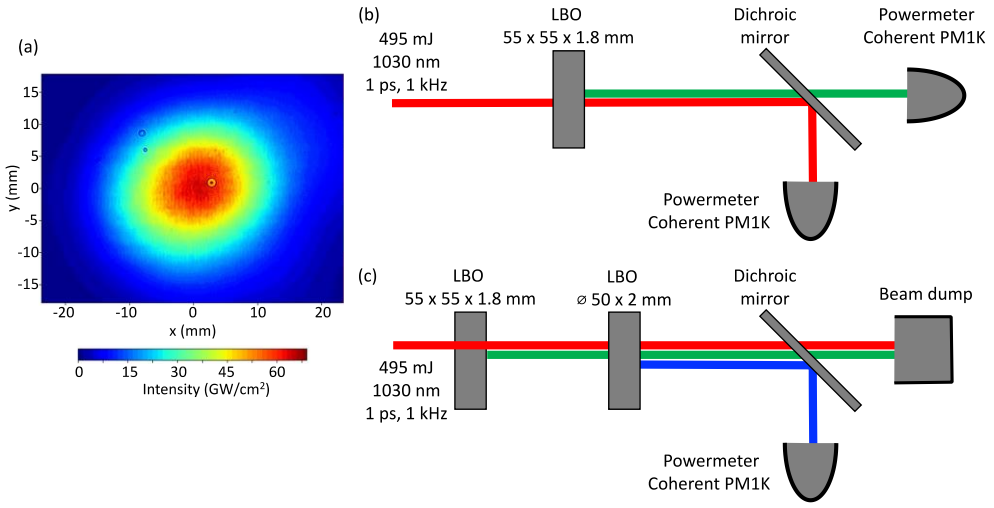

Figure 2.1. (a) Fundamental input beam profile. Experimental setup for (b) the SHG and (c) the THG conversion.

The conversion efficiencies were measured for both harmonic generations using the setup presented in figure 2.1.. The energy at each frequency was measured using specific dichroic mirrors to separate them.

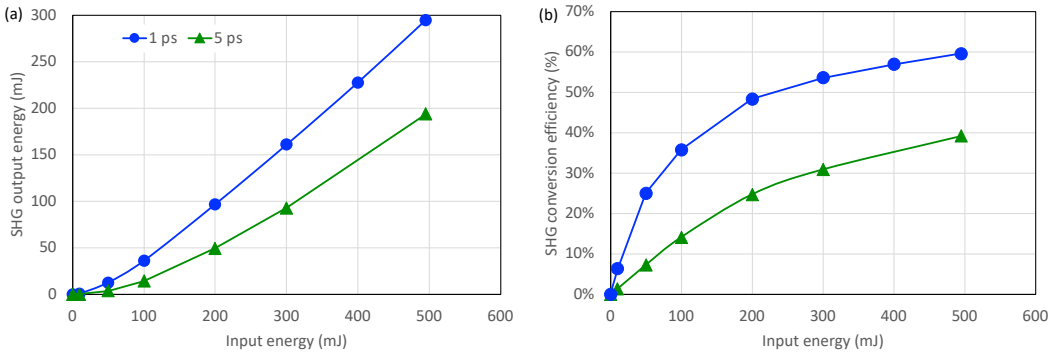

Fig 2.2: SHG energy (a) and energy conversion efficiency (b) of the SHG LBO crystal

The measured SHG conversion efficiency and output energy are presented in figure 2.2. The evolution exhibits the characteristic $\tanh^2$ behavior of a frequency-doubling process with depleted pump [3]. Even for an intensity of 70 GW/cm^2, the saturation is not reached as the conversion efficiency still rises. At the maximum investigated pump power (0.5 TW), the 515 nm output reaches 295 mJ, i.e., a peak power of ~ 0.3 TW and an average power of 295 W. This corresponds to an energy conversion efficiency of 59%. The measurement at two different pulse durations shows a higher efficiency for shorter pulse, which is expected due to the higher intensity of the shorter pulse.

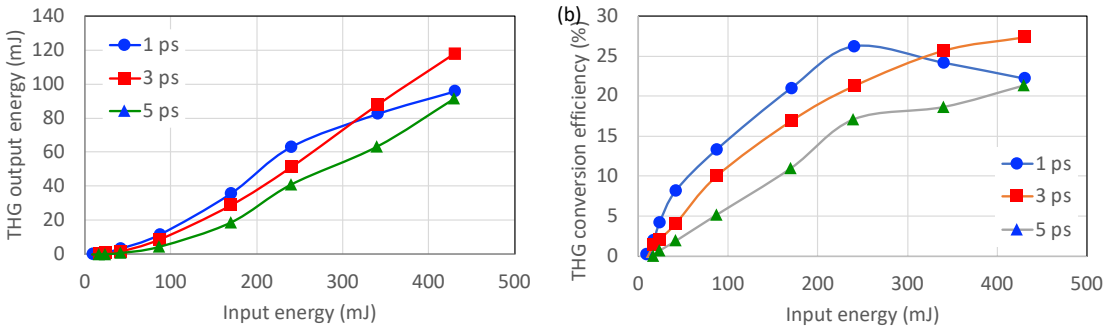

Fig 2.3: THG energy (a) and energy conversion efficiency (b) of the THG LBO crystal

The measured THG conversion efficiency and output energy are presented in figure 2.3. This time, the maximum output energy and conversion efficiency, 119 mJ and 27% respectively, are reached for the pulse duration of 3 ps, while the values for the pulse duration of 1 ps are smaller, (respectively 63 mJ and 26%). This is likely due to $\chi^{(3)}$-induced phase mismatch effects via cross- and self-phase modulation, back conversion [4], nonlinear absorption in the crystal and the associated thermal effects occurring at higher intensities.

One important point to note is that no loss of efficiency was observed during our whole experimental campaign (more than 100 hours of operations). This is important to assure the long-term stability of our system, stability that could have been jeopardized by a loss of efficiency due to multiphoton absorption in the UV that often induces photo-damage or long-term loss of conversion efficiency.

A more detailed characterization of SHG and THG can be found in [5].

3 Laser installation in the former LAL hall

The experimental campaign presented in this chapter has been performed at the former Laboratoire de l'accélérateur Linéaire (LAL) in the Orsay university campus, France, from September 2021 to March 2022.

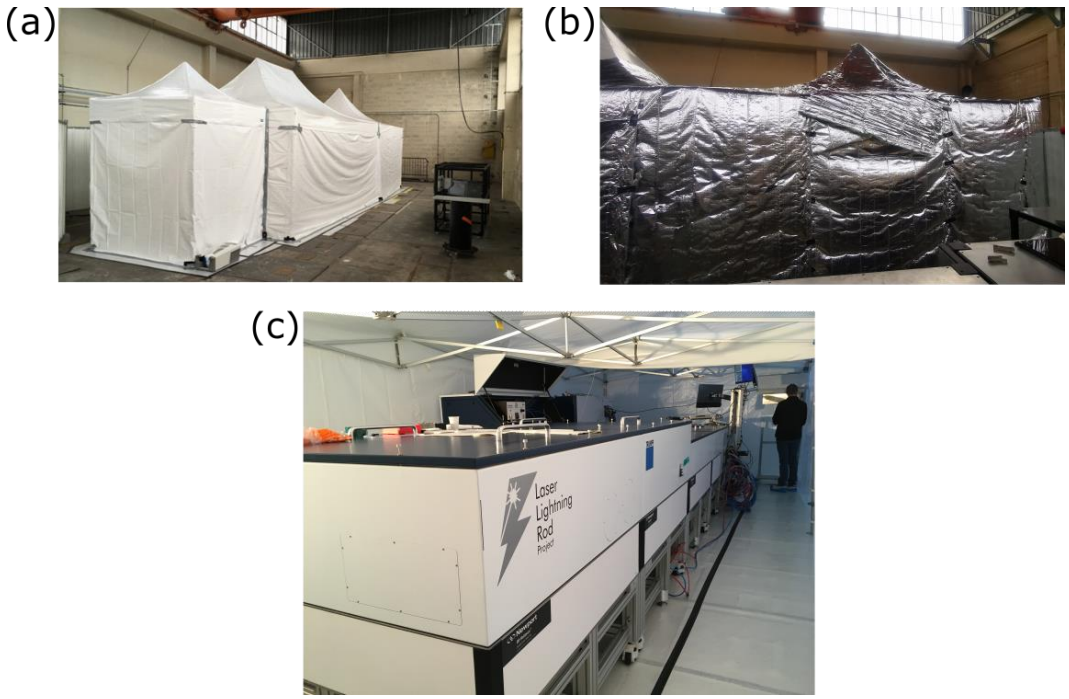

Figure 3.1: picture of (a) the tent, (b) the tent with its additional layer of insulative foil and (c) the laser inside the tent.

During this period, the laser was housed in a tent, providing a barrier to coarse temperature drifts, strong air drags, and large dust particles. In addition, a mobile fan-filter unit was used inside the tent to locally provide ISO-5 air quality when opening the laser housing for maintenance. The temperature change being greater than expected during the winter months, an additional layer of

insulation foil was added outside the tent to reduce the temperature variations. Pictures of the laser tent can be seen in figure 3.1.

This setup allowed us to operate the laser system using the full capacity of the MP amplifier at the maximum output energy of 720 mJ, despite the challenging environment conditions (weather-dependent temperature drift, non-cleanroom-class ambient air, temporary high-power electricity installation). It is however important to note that before reaching this stable operative state, several incidents leading to damaged thin-disk laser heads happened due to these environment conditions. The laser heads were each time replaced by the laser operating team, with remote assistance from Trumpf members that developed the laser.

Figure 3.2: Picture of the frequency-doubled laser beam propagating over the 140 m long experimental zone.

To ensure the protection of people in the vicinity of the building from any scattered light that could happen during the laser propagation, a wall of metallic fences on the side and a concrete wall at the end were installed in the LAL building, delimiting a ~3 m wide and 140 m long experimental zone. A picture of the frequency doubled laser beam propagating over the 140 m is shown in figure 3.2.

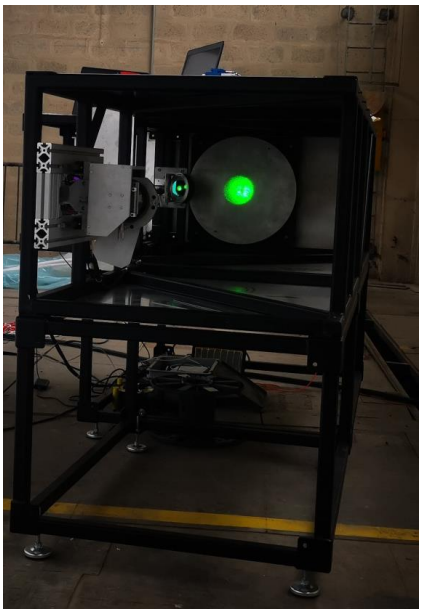

Figure 3.3: Picture of the LLR telescope.

In addition to the laser, a telescope was designed for the LLR experiment and tested at Orsay. It is composed of a plane folding mirror, a convex spherical secondary mirror (85-mm diameter) and a concave ellipsoidal primary mirror (430-mm diameter) set in an off-axis geometry. A picture of this telescope is presented in figure 3.3. This telescope has a magnification ratio of 7.14, expanding the beam diameter from 35 mm to 250 mm. Translation stages on the secondary mirror allowed us to have a tuneable focusing distance ranging from 55 m to ∞.

To carry out our experiment with the same setup as the one that would be used at the Säntis Mountain (see corresponding chapter), the telescope was placed so that the laser beam has to propagate eleven meters before reaching it. This long distance before reaching the telescope was a great cause of worries because of the accumulated nonlinear propagation resulting in hotspots in the beam profile or even the apparition of filaments, both irreversibly damaging our optics.

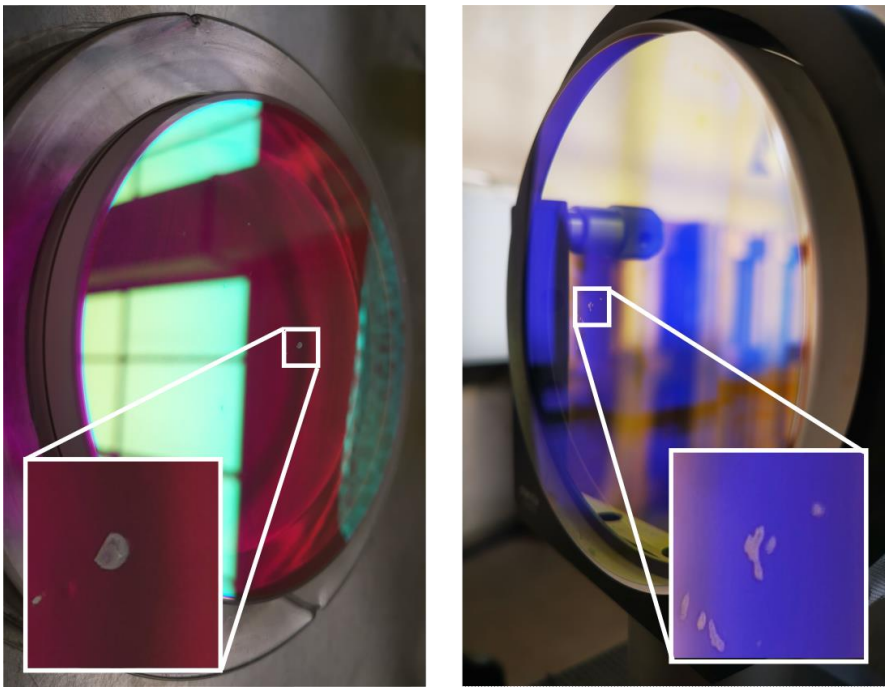

Figure 3.4: Pictures of two damaged telescope mirrors due to hotspots in the beam profile.

As presented in figure 3.4, several units of the 85-mm spherical mirror were damaged while operating the laser at maximum energy, despite the high resistance coating. As a consequence, only pulse energy up to 495 mJ was used during the experimental campaign to prevent further damage on optical devices that could have jeopardized our progression.

4 Characterization of the filament created by a collimated beam

We first investigated the filamentation of the free-propagating laser beam (without telescope). In such a configuration, the control of filamentation distance can be achieved simply by adjusting the laser pulse duration. This technique presents the main advantage of a simplified experimental setup with a reduced number of optical elements, thus with less chance to be damaged

4.1 Experimental setup

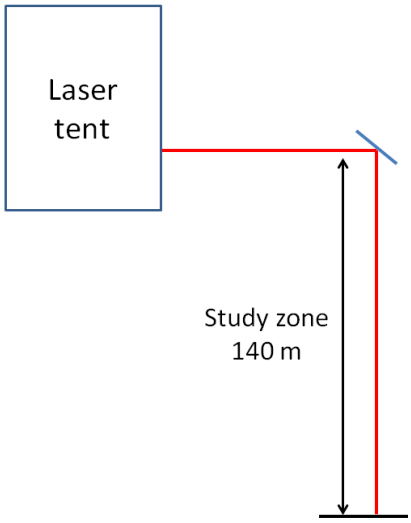

Figure 4.1.1: Experimental setup using the collimated beam.

The experimental setup for the study of the filaments created by the collimated beam, presented in Figure 4.1.1, is as follows: When the laser beam exits the tent, it is sent by a folding mirror to propagate in the direction of the 140 m long study zone. The beam is then stopped by the concrete wall at the end of the corridor.

4.2 Photosensitive paper measurement

To characterize the presence of filaments along the laser path, beam impact measurements were done using photosensitive paper (Ilford Multigrade IV RC 44M). Due to the high laser repetition rate, one needs to pass the paper through the beam fast enough so that the marks of each laser shot can be distinguished from each other. It is then possible to retrieve the number of filaments by counting the number of burned spots and the diameter of the filamentation zone by looking at their positions. An example of such measurement is presented in Figure 4.2.1. By repeating these measurements at different distances, we reconstruct the spatial evolution of the number of filaments along the laser propagation.

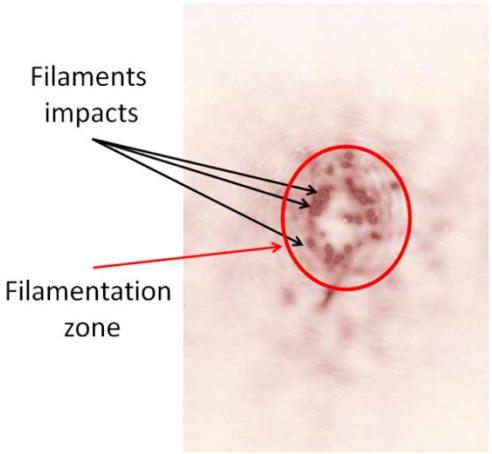

Figure 4.2.1: Example of a photosensitive paper measurement showing the filaments impacts and the filamentation zone.

The evolution of the number of filaments was measured using 1030 nm 500 mJ pulses at several pulse durations ranging from 1 to 7 ps. The results, presented in Figure 4.2.2, show that filaments are present over several tens of meters for all pulse durations. As expected from the reduced power, a longer pulse duration delays the onset of filamentation and increases the length of the region where filaments are present. Note that the distance available for the experiment was limited to 140 m, preventing to measure the full length of the filament region for the pulse duration of 7 ps.

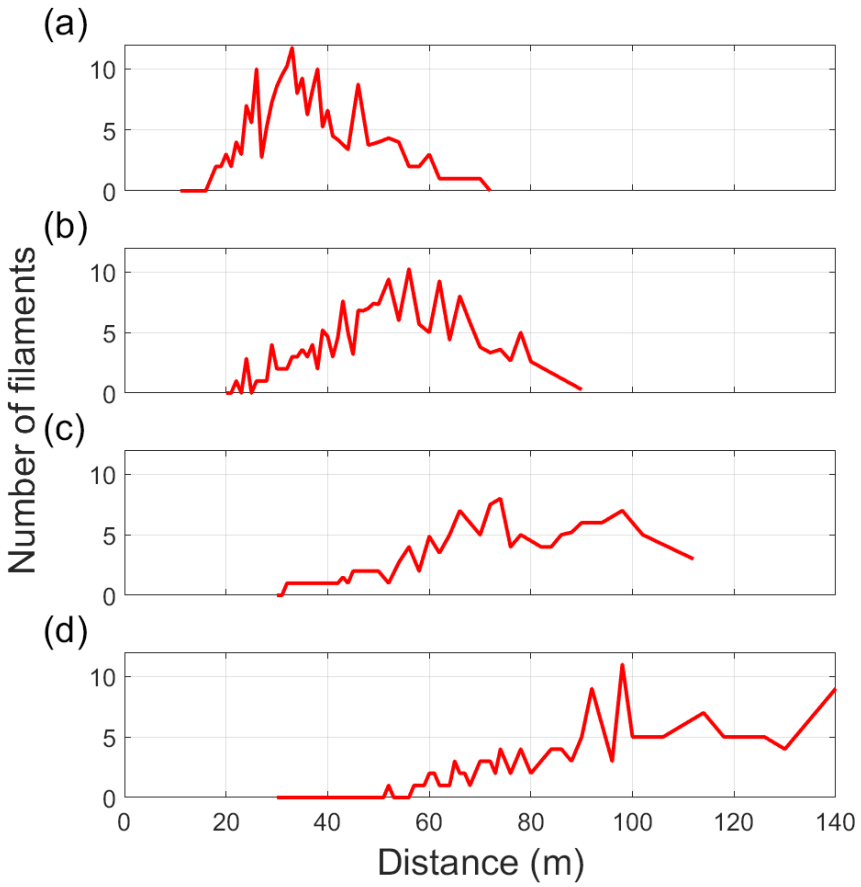

Figure 4.2.2: Evolution of the number of filaments along the laser propagation of a 500 mJ 1030 nm laser pulse for pulse durations of (a) 1 ps, (b) 3 ps, (c) 5 ps and (d) 7 ps.

As observed in Figure 4.2.2, the filament number rises slowly, and decays progressively after reaching a maximum. The distance of this maximum is compared to two distances:

- The distance of the whole beam self-focusing L_c given by the Marburger formula [6]:

$$L_c = \frac{0.367 \times z_r}{\sqrt{\left(\frac{P_{in}}{P_{cr}} - 0.852\right)^2 - 0.0219}},$$

with P_{in} = 430 GW the initial peak power of the laser pulse, P_{cr} = 4.9 GW the critical power for self-focusing in air at 1030 nm and z_r the Rayleigh length (z_r = 690 m at 1030 nm and 1370 m at 515 nm).

- The distance of the self-focusing adapted for multifilament $L_{c\ multifilament}$ given by:

$$L_{c\ multifilament} = \frac{0.367 \times \frac{z_r}{N}}{\sqrt{\left(\frac{\frac{P_{in}}{N}}{P_{cr}} - 0.852\right)^2 - 0.0219}},$$

with N being the maximum number of filaments retrieved from the measurement.

Laser pulse duration	1 ps	3 ps	5 ps	7 ps
Position of peak of filament number (m)	33	56	74	98
L_c (m)	30	56	76	94
$L_{c\ multifilament}$ (m)	12	31	67	312

Table 4.1.1: Comparison between the distance at which a maximum of filaments is detected, the whole-beam self-focusing distance L_c and the multifilament self-focusing distance $L_{c\ multifilament}$, for pulses durations of 1 ps, 3 ps, 5 ps and 7 ps.

The results, presented in table 5.a.1, show that the whole-beam self-focusing distance predicts well the location of the highest number of filaments. This underlines the importance of the photon bath in sustaining the multiple filamentation process, as the whole beam self-focusing corresponds to the distance of highest photon bath intensity.

On the other hand, the onset of filamentation is predicted neither by the whole-beam, nor by the multi filament self-focusing distance, suggesting that the nucleation of the observed small scale filamentation is not governed by the overall beam structure, but rather by local inhomogeneities originating either from the initial beam profile or from the effect of turbulence in the experimental hall.

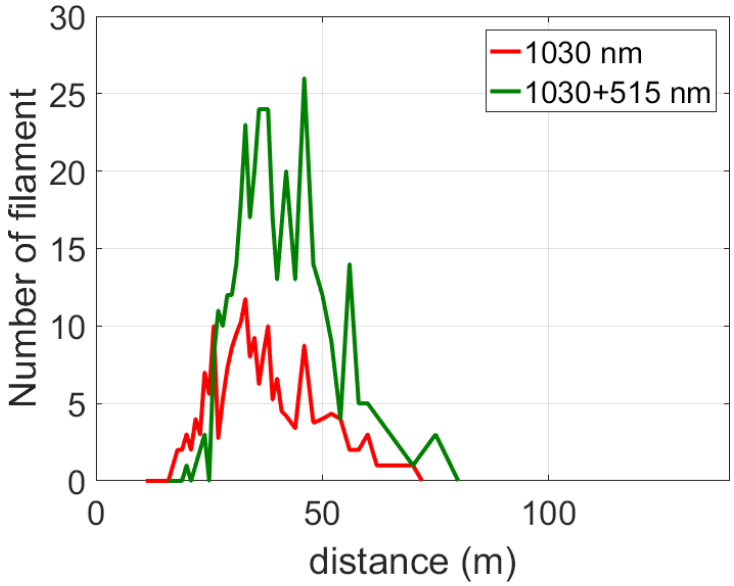

Figure 4.2.3: Evolution of the number of filaments along the laser propagation measured for the 1030 nm and 1030+515 nm pulses, with a pulse duration of 1 ps.

By using the frequency doubling LBO crystal, we repeated the measurement at pulse duration of 1 ps to compare the filaments created by the 500 mJ pulses at 1030 nm with those created by the dual color pulses consisting of 285 mJ at 515 nm and 215 mJ at 1030 nm [5]. The results are presented in Figure 4.2.3.

Compared with the fundamental beam, the effect of frequency doubling increases the number of filaments, multiplying this number by more than two over the whole filamenting range except the first few meters. This increase is in line with the fact that the SHG conversion efficiency is beyond 50% and that the λ^2 dependence of the critical power [7] results in more than doubling the normalized power P/P_{cr}.

More specifically, the critical power at 1030 nm amounts to 5 GW, so that 500 mJ in 1 ps corresponds to 100 P_{cr}. At a rate of 1 filament per 5 P_{cr} [8], we can therefore expect up to ~20 filaments, about twice the number observed. The 12 filaments observed correspond to ~8 P_{cr} / filament. In the case of the frequency-doubled beam at 515 nm, the critical power amounts to 1.24 GW, so that the 285 mJ, corresponding to 285 GW peak power, corresponds to 230 P_{cr}. The 26 filaments observed correspond to ~9 P_{cr} / filament, again slightly above the ratio expected from measurements for shorter pulses.

The beam diameter of 30 mm has a cross section of 660 mm^2, corresponding to more than 25 mm^2/filament. This value lies far from the geometrical saturation, which amounts to only a few mm^2/filament [9]. Therefore, spatial congestion is not the factor limiting the number of filaments.

One important aspect of the filamentation for atmospheric application is the diameter of the filamentation zone (see Figure 4.2.1). If the diameter is too large compared to the number of filaments, resulting in a low density of filaments, each filament is separated from the other one and they cannot collectively contribute to the desired effect (for example the guiding of electrical discharges or the clearing of cloud). On the contrary, if the density is high, their contribution will add up, resulting in a greater effect like in the case of superfilamentation [10].

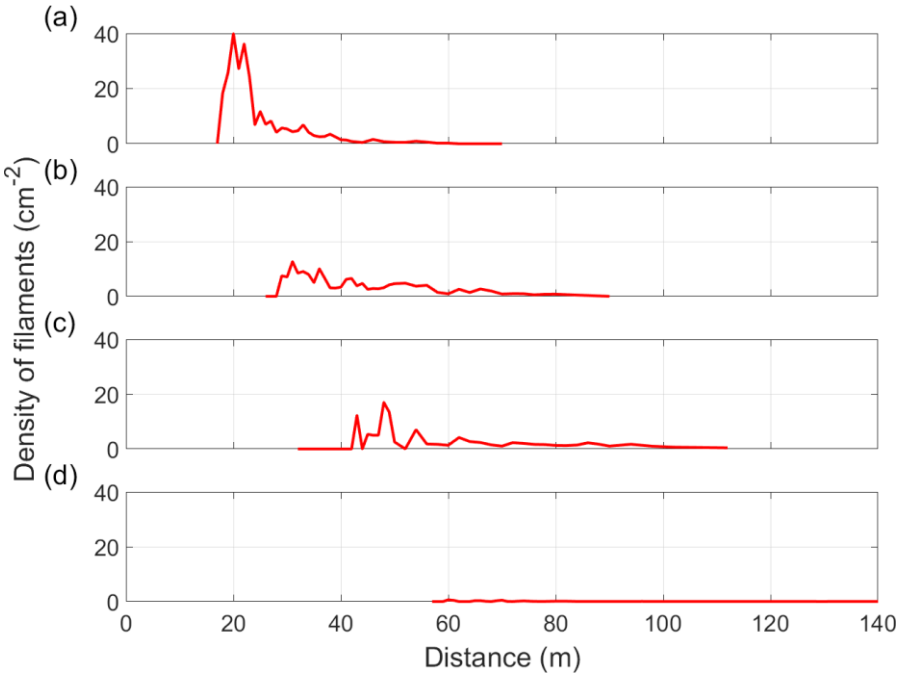

Figure 4.2.4: Evolution of the density of filaments along the laser propagation of a 500 mJ 1030 nm pulse for pulse durations of (a) 1 ps, (b) 3 ps, (c) 5 ps and (d) 7 ps.

Using the number of filaments and the diameter of the filamentation zone, we can retrieve the evolution of the density of filaments along the laser propagation. The results for 500 mJ 1030 nm pulses with duration ranging from 1 ps to 7 ps are presented in Figure 4.2.4.

While the maximums of the number of filaments were comparable for different pulse durations, a clear difference is seen on the density of filaments as a function of the pulse duration. The 1 ps pulse duration leads to a higher density compared to all the other durations, while the 7 ps shows the lowest density. Furthermore, the high density is present on a much smaller scale compared to the high number of filaments, the FWHM of the 1 ps density measurement being of only 6 m (the FWHM of the 1 ps measurement of the number of filaments is 25 m).

This suggests that even if the number of filaments is high over a long distance using a collimated beam, the distance over wich the density is high enough to be used for applications is more limited. Moreover, the use of a chirped pulse to do experiment at long distance severely reduces the density of filaments, thus the potential for certain applications requiring a high filament density.

4.3 Acoustic measurement

To attest the presence of filament, microphone measurements were made along the laser propagation path. During ionization the filamentary laser pulses quickly deposit energy in the medium resulting in the creation of a lateral acoustic wave that can be measured by the microphone [11], [12].

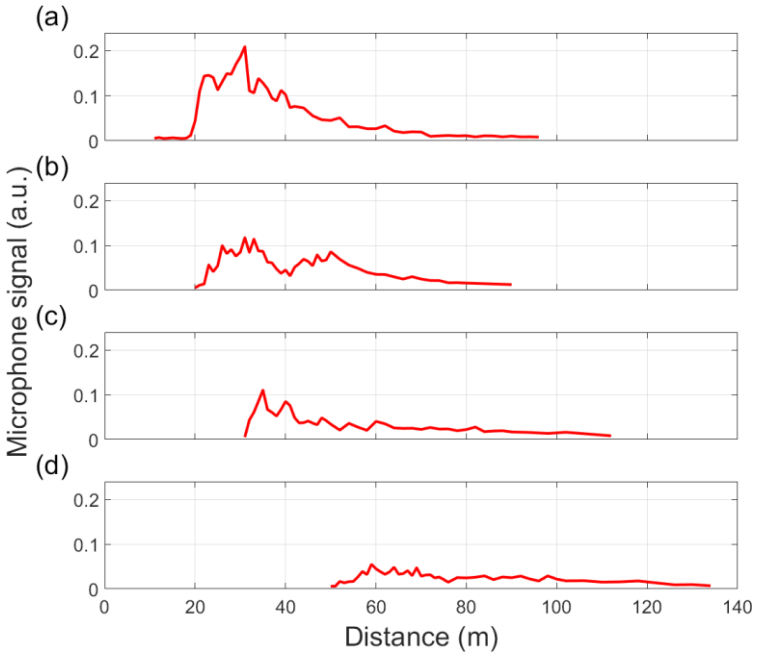

Figure 4.3.1: Acoustic signal measured along the laser propagation, for 500 mJ 1030 nm pulses with pulse duration of (a) 1 ps, (b) 3 ps, (c) 5 ps and (d) 7 ps.

The spatial evolution of the acoustic signal along the laser path was measured using 1030 nm 500 mJ pulses with pulse durations ranging from 1 to 7 ps. The results, presented in Figure 4.3.1, show a similar behaviour as the density of filament. The 1 ps pulse duration leads to a higher acoustic signal compared to all the other durations, while the 7 ps shows the lowest. However, the high acoustic signal is present over a similar distance compared to the high number of filaments, the FWHM of the 1 ps acoustic measurement being of 20 m (to compare with the FWHM of 25 m of the 1 ps measurement of the number of filaments and the FWHM of 6 m of the 1 ps measurement of the density of filaments).

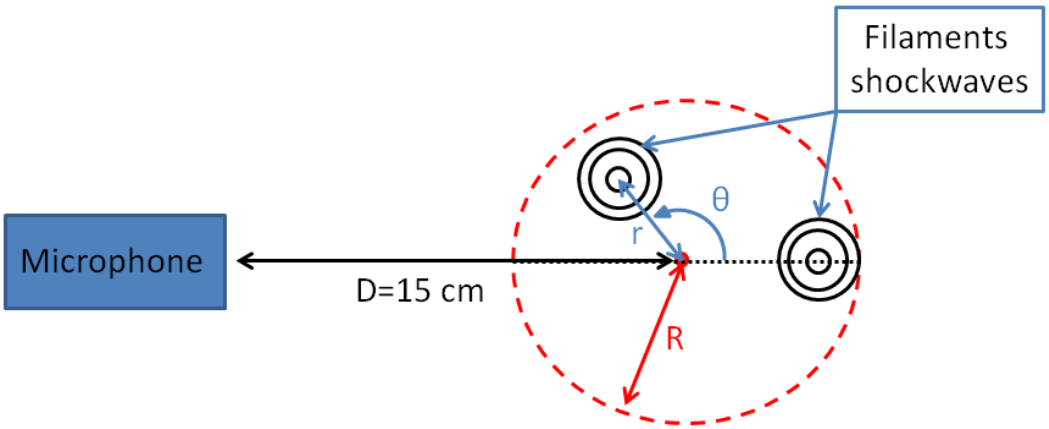

Figure 4.3.2: Schematic of the microphone measurement.

This discrepancy shows that the acoustic signal cannot be directly compared to either the number of filaments or the density of filaments. The correct quantity to compare the microphone signal to is one calculated from the contribution of the shockwaves of each filament after they propagate to reach the microphone. The expression used to calculate this quantity, that will be called the Deduced Signal DC, is

$$DC = \frac{Cst\ N}{2\,\pi\,R^2}\int_0^{2\pi}\int_0^{R}\frac{1}{(D-r\,cos(\theta))^2+(r\,\sin(\theta))^2}\,r\,dr\,d\theta,$$

where r and θ are the spherical coordinates as seen in Figure 4.3.2, R the radius of the filamentation zone, D the distance between the center of the beam and the microphone, N the number of filaments and Cst a constant that is related to the signal that should be measured from a single filament.

The use of this expression implies that the signal that should be measured from a single filament is constant in all our measurements, thus that the power deposited by each filament is constant. Moreover, it implies a homogeneous transverse distribution of the filaments in the filament area. As seen in Figure 4.2.1, it is not the case in our measurement, but the distribution is still mainly symmetrical.

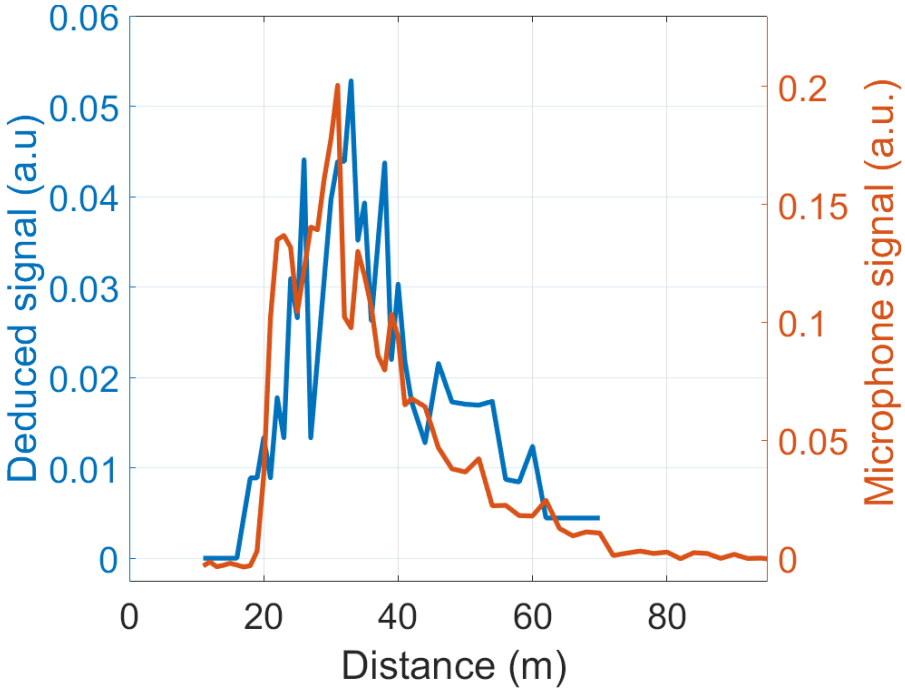

Figure 4.3.3: Comparison between the acoustic signal and the Deduced Signal DC for a laser pulse of 500 mJ at 1030 nm with a duration of 1 ps.

The comparison between the acoustic signal and the Deduced Signal calculated from the photosensitive paper measurements for a laser pulse of 500 mJ at 1030 nm with a duration of 1 ps is shown in Figure 4.3.3. The clear proportionality between the two signals shows that the use of the expression is valid. Thus, it confirms that the power carried by the filaments is constant over the propagation distance.

4.4 Filament population for each wavelength

One other important information that can be retrieved from the beam impact on photosensitive paper is the diameter of the filaments. This allows us to distinguish the filament from the beam at 515 nm from the ones from the beam at 1030 nm because the change of frequency during frequency doubling not only affects the number of filaments but also their diameter, as seen in Figure 4.4.1.

Figure 4.4.1: Example of a photosensitive paper measurement showing the impact of filaments of two different sizes attributed to the two laser wavelengths at 1030 nm and 515 nm.

The proportionality of the filament diameter with the wavelength is described by [13], [14]:

$$d_{filament} = \frac{1.22\,\lambda}{\sqrt{8\,n_0 n_2\,I_{max}}},$$

with λ the beam wavelength, n_0 the air refractive index, n_2 the nonlinear Kerr refractive index and I_{max} = 10^{14} W/cm^2 the intensity of the laser in the filament. The filament diameter being directly proportional to the wavelength, the filaments of the frequency doubled beam would be two times smaller than the ones from the fundamental beam.

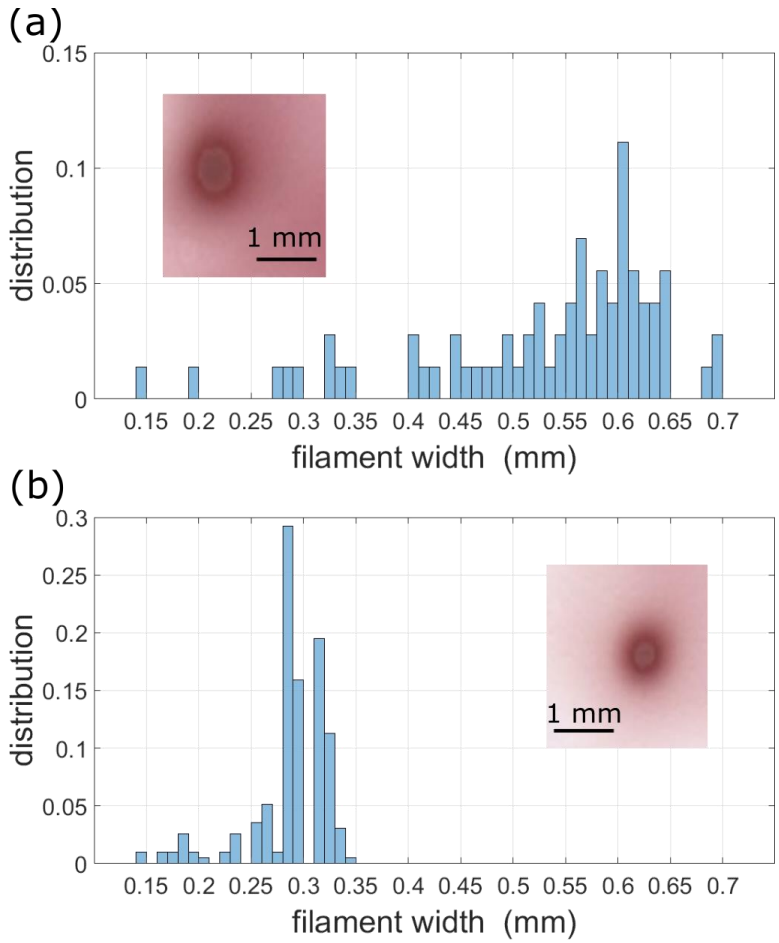

Figure 4.4.2: Distribution of the filaments diameters produced by (a) 500 mJ 1 ps laser pulses at 1030 nm and (b) 500 mJ 1 ps laser pulses at 1030+515 nm, measured on photosensitive paper.

By measuring the size of each filament impacts on each photosensitive paper measurement across the whole laser propagation for both the case of 500 mJ 1 ps pulses at 1030 nm and 500 mJ 1

ps pulses at 1030+515 nm (respectively 286 mJ at 515 nm and 214 at 1030 nm), we retrieved in these two cases the diameter distributions of the filaments.

The results, presented in Figure 4.4.2, show that the filaments generated by the fundamental beam have a diameter distribution peaked around 0.6 mm, while filaments generated by the frequency doubled beam have a diameter distribution peaked around 0.3 mm. The proportion ratio of 2 predicted by the theory is verified. However, the measured diameters of filaments are 5 times larger than previously reported and predicted by the theory (120 μm and 62 μm at 1030 nm and 515 nm, respectively) [7], [15]. This is explained by the low threshold of our photosensitive paper that is darkened not only by the filament core but also by the photon bath around it, resulting in a burned mark larger than the filament itself.

Remarkably, no filament with a diameter above 0.35 mm (which should be the case for filament at 1030 nm) is observed in the case of a beam at 1030+515 nm, suggesting that the unconverted fraction of the beam at 1030 nm does not produce filaments despite its 214 mJ energy per pulse (~43 P_{cr}). We confirmed the absence of NIR filaments in the NIR+SHG beam by separating the fundamental from the SHG using a 45° dichroic mirror ensuring less than 0.2% transmission, and more than 99.8% reflection in the NIR, and 70% transmission at 515 nm. After the doubling crystal the SHG beam alone generates filaments, while the NIR beam alone does not, confirming that only green filaments are observed in Figure 4.4.2.

To explain this effect, several hypotheses were considered:

- The contribution of each beam in a dual-colored co-filament could affect the filamentation process [16]. However, due to a phase velocity mismatch in air of 46.5 fs/m between these two spectral components, they do not temporally overlap anymore once the filament process begins after ~ 20 m of propagation. Furthermore, as the NIR pulse propagates ahead of the SHG, no perturbations from the latter preventing the filamentation of the former can occur.
- The non-linear depletion of the pump beam tends to self-regularize the beam, i.e., smooth the gradients within the beam profile due to higher conversion efficiency (hence higher losses) in the most intense regions. Such self-regularisation is expected to hinder filamentation by reducing the seeding of spatial modulational instability. However, modelling this effect based on the depleted pump formalism [3], in our conditions featuring ~57% conversion efficiency into the SHG [5], shows that the gradients are only reduced by a factor of $\sqrt{2}$, insufficient to prevent filamentation.

Currently, we do not have a theoretical explanation as to why the NIR beam exiting the SHG crystal does not produce filament. However, before searching too far and wide into the theory, it would be wise to ensure the validity of our observation. No filament produced by the remaining NIR beam over its propagation over 140 m was observed, but it could be that the filamentation simply starts at a larger distance than the one our current experimental setup allows to study. An experiment aiming to search for these filaments over a greater distance would be an effective way to confirm our current observation.

4.5 Spectrum measurement

The evolution of the spectrum of the triple frequency-converted (239 mJ, 195 mJ and 96 mJ at 1030 nm, 515 nm and 343 nm, respectively) pulse at 1 ps was measured along its propagation. The high beam intensity preventing direct measurement of its spectrum, we characterized the laser spectrum at different distances by measuring with a spectrometer the spectrum of the light scattered on a ceramic plate placed on the beam path.

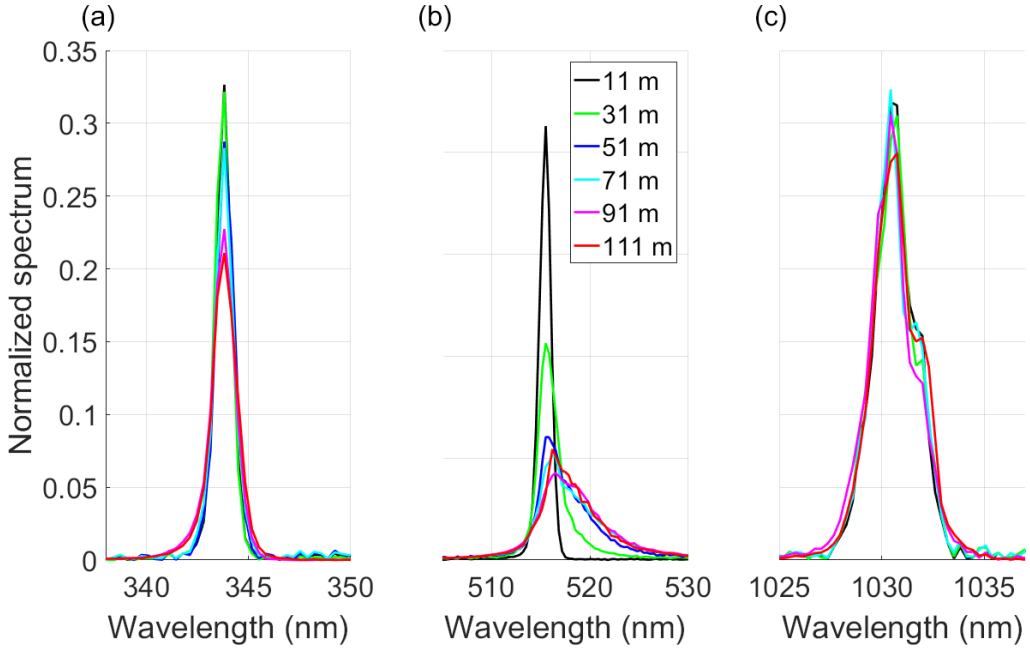

Figure 4.5.1: Evolution of the spectrum of the triple frequency-converted pulse along its propagation. (a), (b) and (c) being the measurement of the 343, 515 and nm beam, respectively.

As shown in Figure 4.5.1, the spectral broadening of the mixed beam is much more efficient for the green radiation than for the fundamental and the THG. This is consistent with the observations of filamentation produced with dual-color laser.

In the SHG pulse, the spectral width rises from 1.0 nm to 7.6 nm, which would allow the Fourier-limited pulse durations to drop from 389 to 51 fs. Note that this broadening occurs during the propagation, after the SHG crystal. The broadening in the crystal and the broadening due to the propagation of the beam before the crystal are already taken into account as an initial condition.

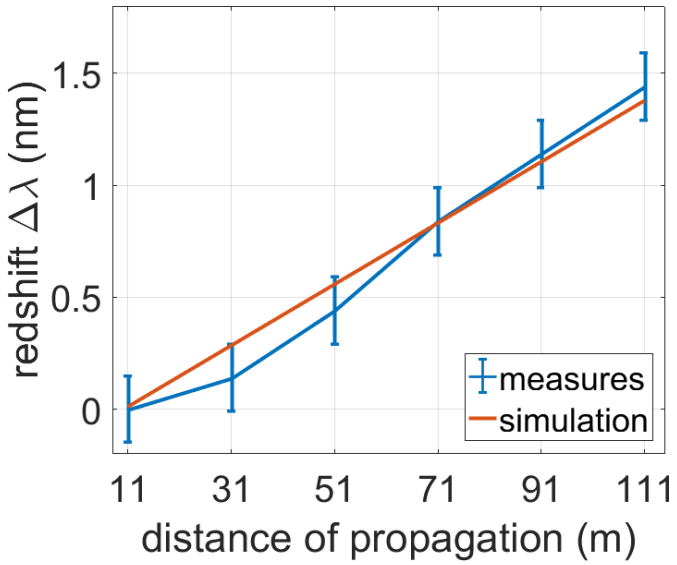

Figure 4.5.2: Comparison between the measured and calculated redshift along the laser propagation, for the pulse spectral component at 515 nm.

The redshift of the 515 nm beam can be explained by the retarded Kerr effect in air. Based on the model presented in [17], the red shift $\Delta\lambda$ is calculated along the laser propagation using the equation:

$$\Delta\lambda(z) = \lambda_0 \times \frac{k \times n_2 \times \mathrm{I}_0}{\tau \times \sqrt{2} \times w_0} \times \frac{\Delta t_0}{\Delta t} \times z,$$

with λ_0 the initial wavelength, k the wavenumber, n_2 the instantaneous nonlinear index of air, I_0 the laser intensity, τ the characteristic time of the partial alignment of the molecules, w_0 the initial angular frequency, Δt_0 the minimum pulse duration, Δt the used pulse duration and z the distance of propagation. The calculated values, presented in Figure 4.5.2, show a good agreement between the theory and the measurement.

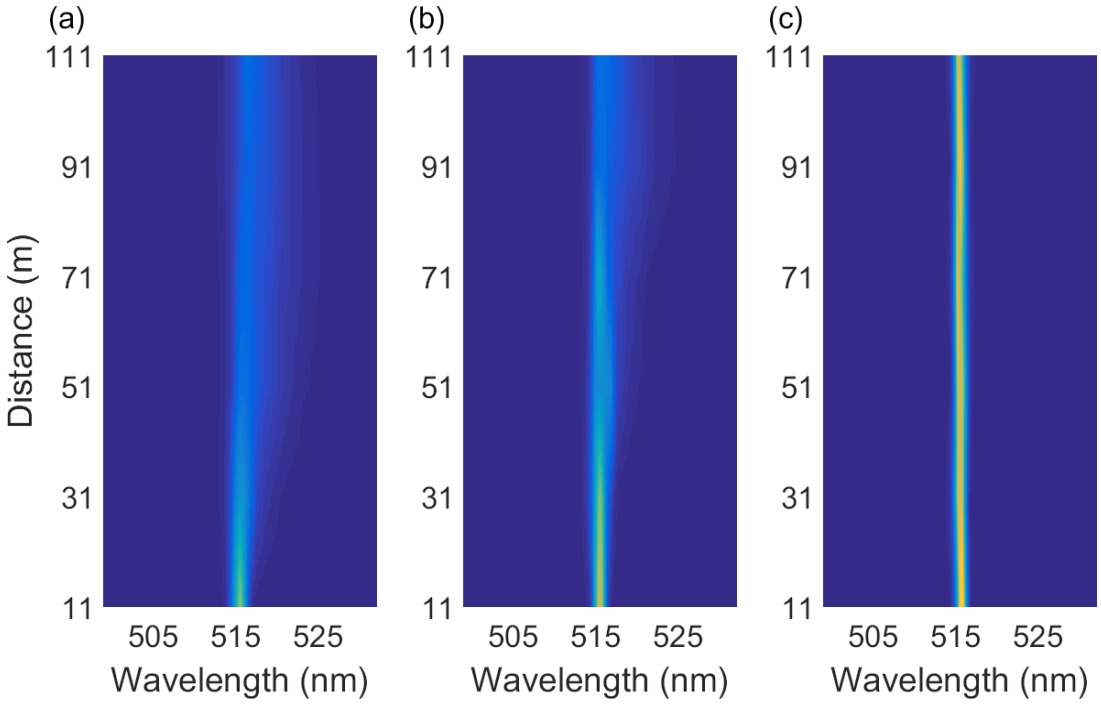

Figure 4.5.3: Evolution of the spectrum of the SHG part of the triple frequency-converted pulse along its propagation, for pulse durations of (a) 1 ps, (b) 3 ps and (c) 5 ps.

To further study the evolution of the spectrum, the same previous measurement was repeated for the pulse durations of 1 ps, 3 ps and 5 ps. For all tested pulse durations, the spectral broadening of the mixed beam is again more important for the green radiation than for the fundamental and the THG. As shown in Figure 4.5.3, longer pulse durations delay the onset of the spectral broadening and decrease its importance. The distances where the spectral broadening starts are consistent with the distances of apparition of filaments for all pulse durations. Moreover, the broadening only takes place over a limited distance after which no evolution of the spectrum is observed. This distance also corresponds to the distance over which filaments are observed.

5 Characterization of the filamentation produced by a focused beam

The other option to create filament at long distance is to change the diameter of the beam and its convergence using an expanding telescope as the one described earlier. This technique presents the advantage of having control over the collapse distance and thus the distance where filaments are present. Moreover, the tuning of this distance relies on the position of the optics of the telescope and can consequently be easily automatized using motorized translation stages.

However, this technique implies to add additional optics on the laser path and, as explained earlier, the damage threshold of these optics was the factor limiting the energy used in our experiment to 500 mJ.

5.1 Experimental setup

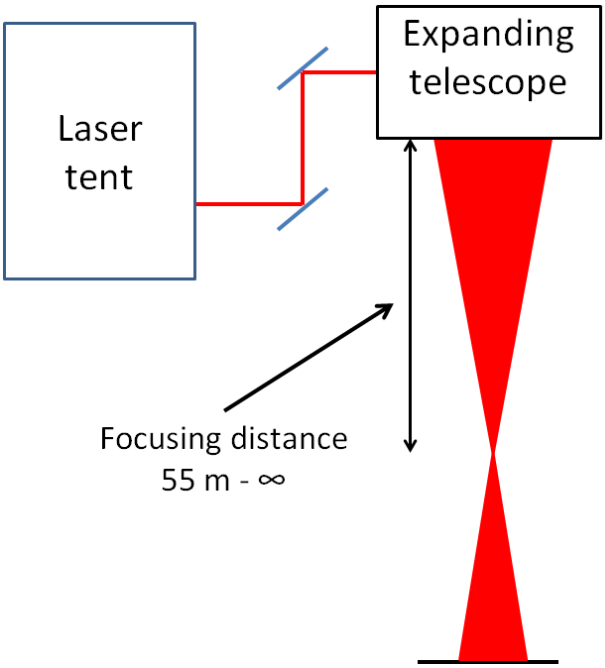

Figure 5.1.1: Experimental setup using the focusing telescope.

The experimental setup for the study of the filaments created by the telescope focused beam, presented in Figure 5.1.1, is similar to the setup for the collimated beam, with the addition of our telescope that increases the beam size to a diameter of 250 mm and allows to focus the beam at distances ranging from 55 m to ∞.

5.2 Photosensitive paper measurement for different focusing distances and wavelengths

As done previously, beam impact measurements were done using photosensitive paper (Ilford Multigrade IV RC 44M) to characterize the filamentation and the presence of filaments along the laser path.

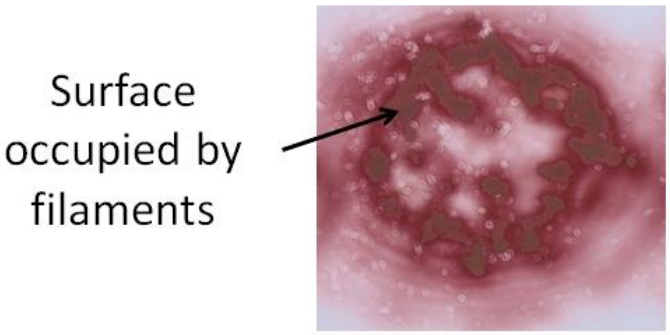

Figure 5.2.1: Example of a photosensitive paper measurement made using the telescope focusing beam.

The main difference compared to the previous beam impacts is that individual filaments cannot be distinguished from each other anymore, as seen in Figure 5.2.1. Therefore, the total surface occupied by filaments is used as an equivalent to the number of filaments.

To study the spatial evolution of the surface occupied by filaments and its dependence to the laser wavelength and focusing condition, measurements were made along the laser propagation using both the fundamental and frequency doubled beam, focused at 55 m (N.A. = 0.0023) and at 115 m (N.A. = 0.0011). In this measurement, the used laser energy is 500 mJ and the pulse duration 1 ps.

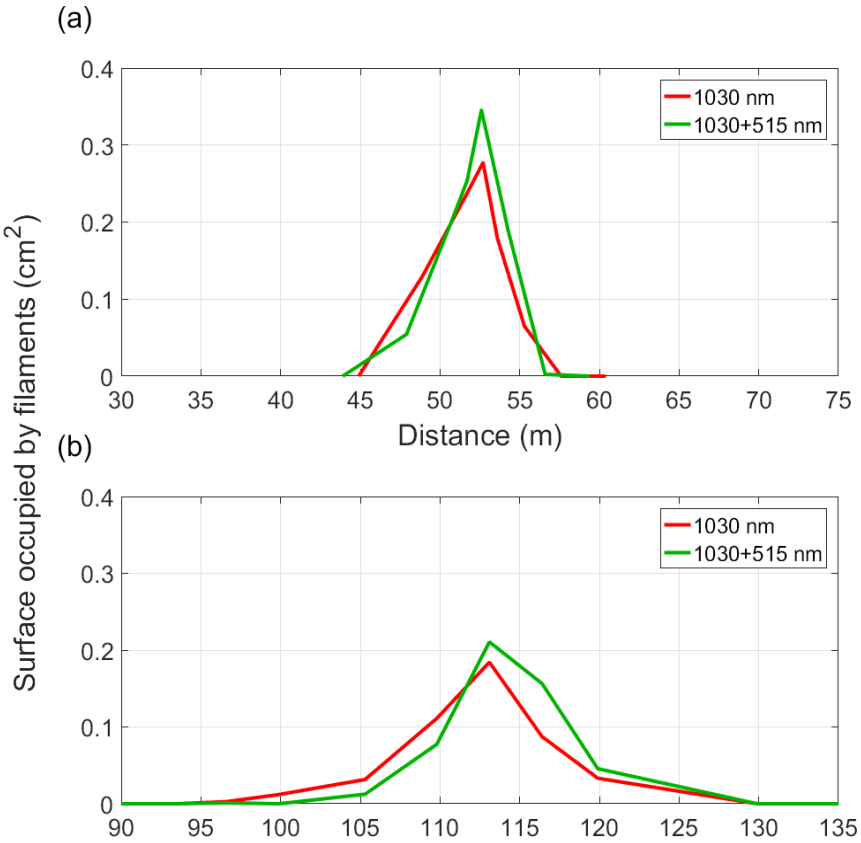

Figure 5.2.2: Spatial evolution of the surface occupied by filaments created by the 500 mJ 1 ps fundamental beam (red) or the frequency doubled beam (green), focused at either (a) 55 m or (b) 115 m.

The results, presented in Figure 5.2.2, show that the use of the frequency doubled beam leads to a higher surface occupied by filaments compared to the fundamental beam, albeit the difference is small. However, the difference is more pronounced when comparing the two focusing distances. The longer focusing distance of 115 m results in a lower maximum of the surface occupied by filaments but in a longer filamentation length, of more than 30 m compared to 12 m for the focusing distance of 55 m. This difference was expected and is coherent with the numerical aperture of both focusing conditions.

5.3 Photosensitive paper measurement for different pulse durations

The previous measurements being made at a fixed pulse duration, another set of measurement was performed at different pulse durations ranging from 1 ps to 7 ps using both the 500 mJ fundamental beam and the dual frequency beam at the focusing distance of 115 m.

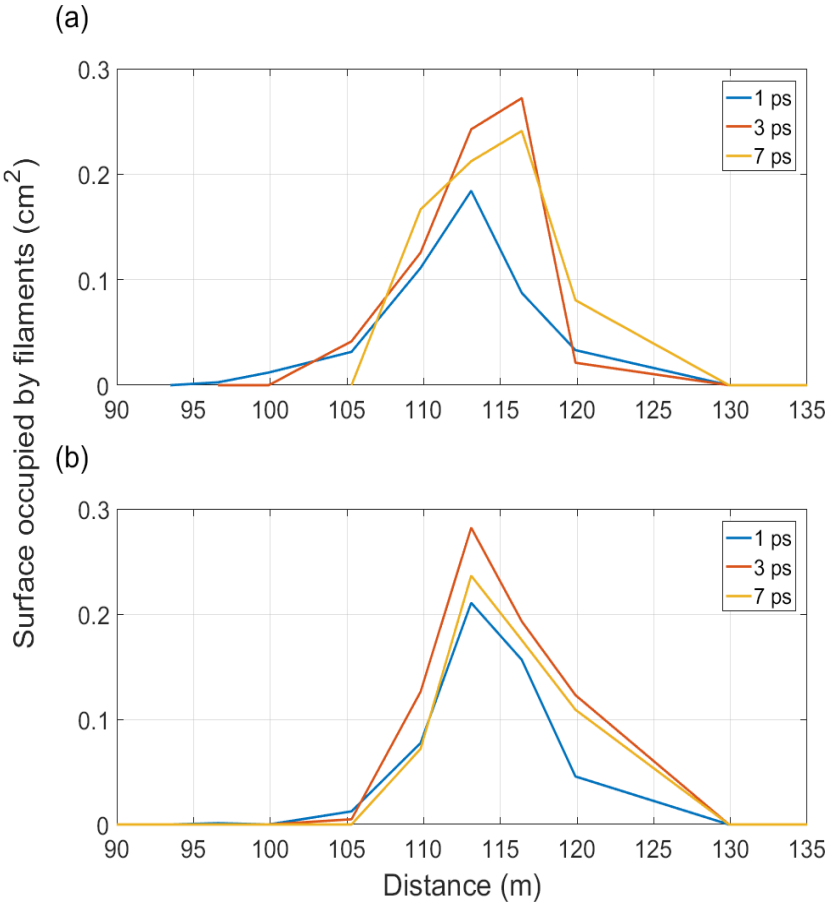

Figure 5.3.3: Spatial evolution of the surface occupied by filaments created by the 500 mJ (a) fundamental beam at 1030 nm and (b) the dual frequency beam at 1030+515 nm focused at 115 m, for several pulse durations ranging from 1 to 7 ps.

The results, presented in Figure 5.3.3, show a similar behaviour for both the fundamental and the dual frequency beam: smaller pulse duration leads to a smaller maximum of the occupied surface but over a longer distance. Again, the difference is small and the change of pulse duration does not drastically change the number of filaments.

This is an important observation because it allows us to use high pulse duration to reduce the laser intensity and prevent damage on the optics of our setup while maintaining a high number of filaments (in the same range as if we used the minimum pulse duration).

5.4 Picture of the plasma luminescence

One other measurement to unambiguously attest the presence of filaments is to capture the light emitted by the filament luminescence.

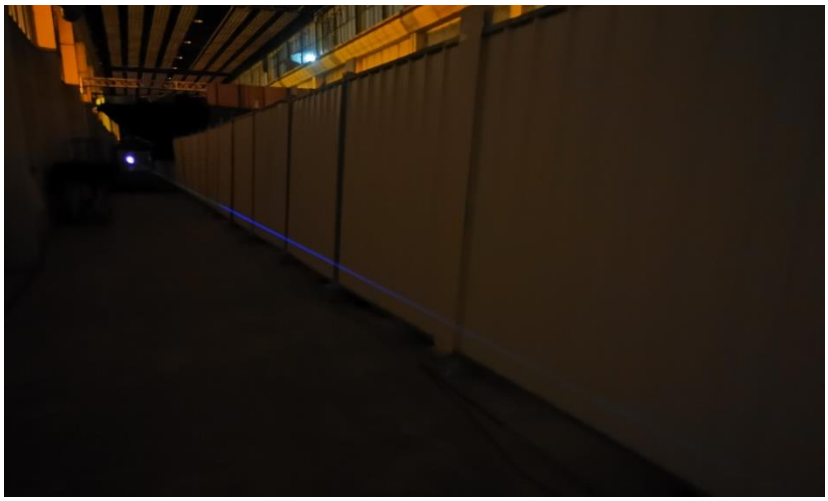

Figure 5.4.1: Picture of the luminescence emitted by filaments created by the 500 mJ laser focused at 55 m.

We tried to capture the luminescence of the filament for the two focusing distances 55 m and 115 m. Due to the high background light of the experimental environment, we could not observe the luminescence of the filament when the laser was focused at 115 m. However, as shown in picture 5.4.1, we recorded a clear signal of this luminescence when the beam was focused at 55 m. This suggest the presence of a higher ionisation when the beam is strongly focused, which seems reminiscent of the superfilamentation regime [10].

6 Evolution of the filament distribution over the filamentation zone: from ring-filamentation to superfilamentation

Another piece of information retrieved from the impact on photosensitive paper that was not discussed yet is the evolution of the filament distribution over the radial filamentation zone, hence how they are organised over the beam profile.

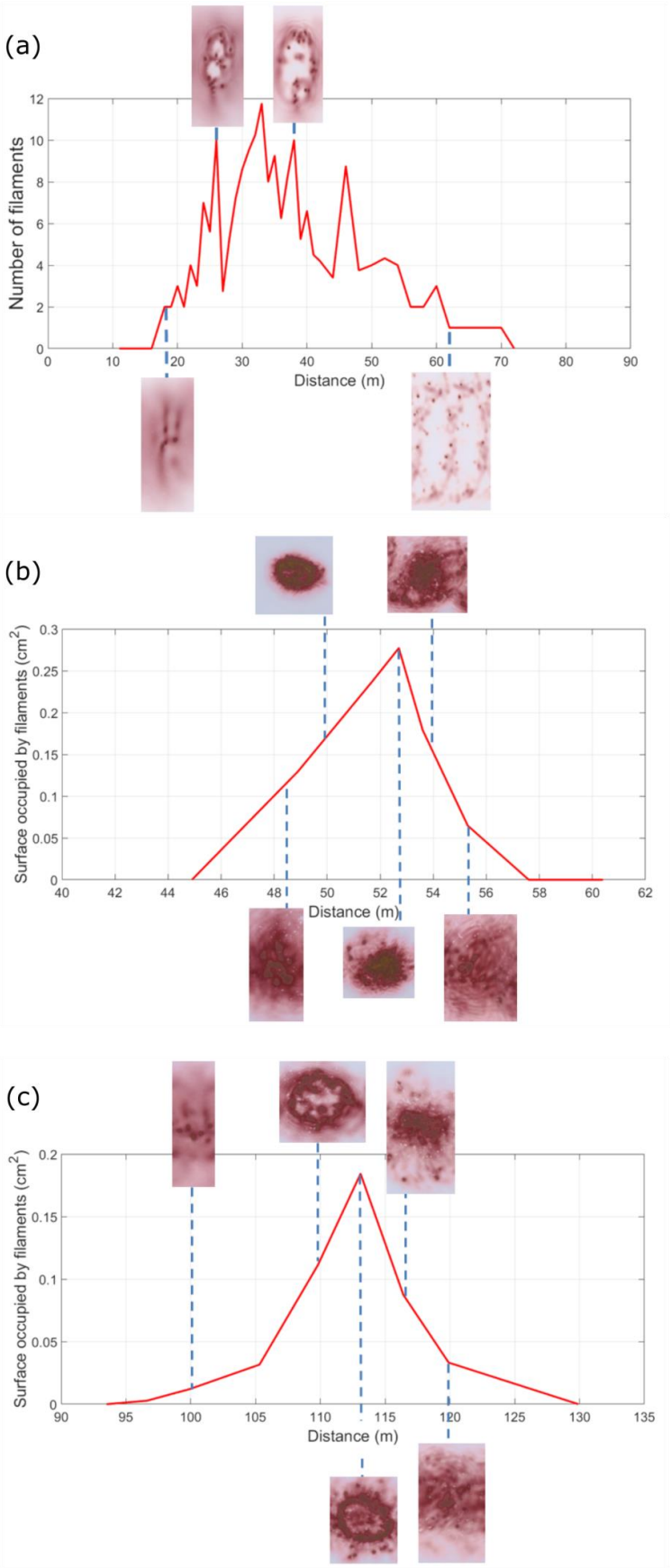

Figure 6.1: Evolution of the filament distribution for (a) the collimated beam, (b) the beam focused at 55 m and (c) the beam focused at 115 m. Note that due to the high repetition rate, two impacts partially overlap in the records at x = 62 m on Panel (a). The red curves are (a) the number of filaments, and (b) (c) the area of the beam profile covered by the filaments, used as an equivalent of the filament number. For all measurements, the laser energy was 500 mJ and its pulse duration 1 ps.

To analyse this evolution of the filament distribution we present in figure 6.1 a comparison of the cases of the collimated beam, the beam focused at 55 m and the beam focused at 115 m. In these measurements, the laser energy was of 500 mJ and the pulse duration of 1 ps. Some tens of meters after the filamentation onset, the filament pattern of the collimated beam self-organizes in a ring structure. This structure persists after the onset of filamentation, where the beam profile is rather homogeneously filled with filaments (See x = 18 m on figure 6.1 (a)). In free propagation regime, that ring pattern appears to be fully formed at the position corresponding to the maximum of the filament number. We interpret this ring pattern as a result of the propagation of our super gaussian laser beam profile, where the strong gradients on the edge of the beam profile promote local self-focusing and the subsequent onset of filaments. The ring pattern appears also with a focused beam. With a smooth focus we observe it till the focus (See x = 112 m on figure 6.1 (c)). However, with a stronger focusing, the ring disappears near the focal region and a dense pack of filaments is observed (See x = 52.5 m on figure 6.1 (c)). This behaviour is similar to the superfilamentation regime [10].

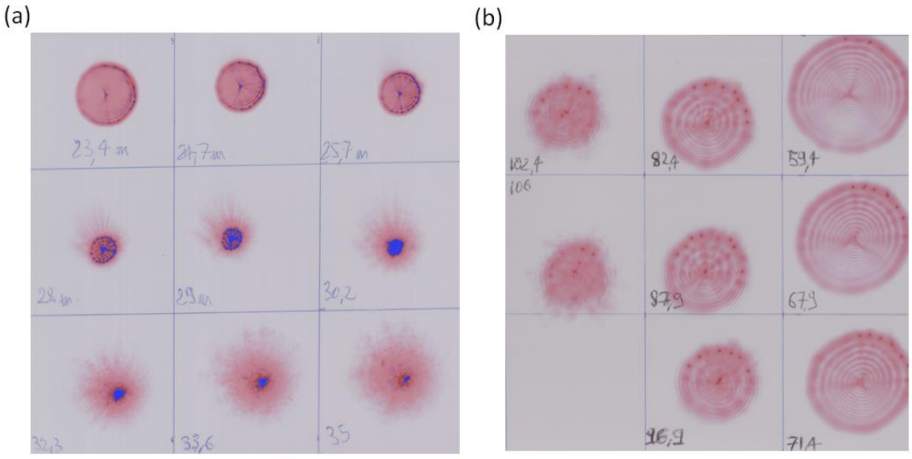

Figure 6.2: Evolution of the filament distribution of the 260 mJ 700 fs 800 nm ENSTAmobile beam focused at (a) f = 30 m and (b) f=100 m.

A similar behaviour was observed at a lower repetition rate (10 Hz), comparable pulse energy (260 mJ) and chirped duration (700 fs) at 800 nm. As observed in figure 6.2, the focusing of the 120 mm-diameter beam of the Enstamobile laser at 100 m (N.A. = 0.0006) and 30 m (N.A. = 0.002) leads to the apparition of a ring structure and for the case of the stronger focus, the apparition of superfilamentation.

7 Phase shift measurement

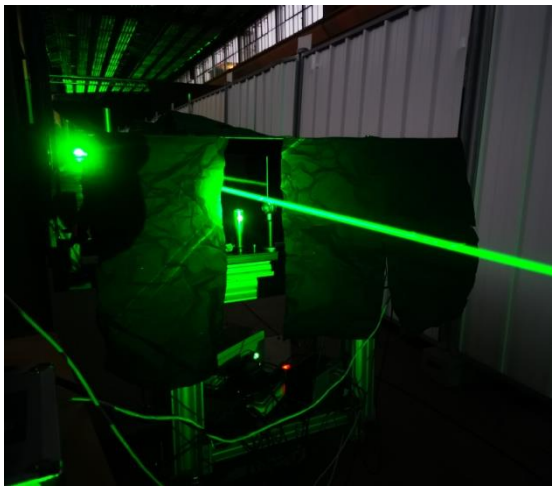

Figure 7.1: Picture of the Phase shift measurement setup during the experiment.

With a similar setup as described in chapter "Laser filamentation at high repetition rate: Study of the cumulative air density depletion and its application to electric discharge triggering", see figure 7.1, we characterized the low-density channel formed by the filament by measuring by interferometry the phase shift (linked to the neutral density variation) induced by the energy deposition of the filaments [18], [19]. The same measurements were made at several positions along the propagation path in the cases of a collimated beam and of a focused beam at distances of 55 m and 115 m.

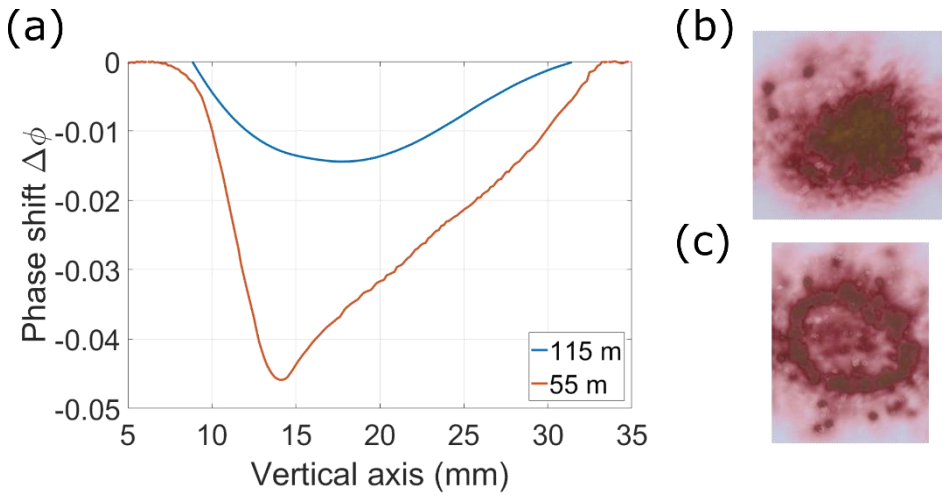

Figure 7.2: (a) Phase shift induced by the frequency doubled 500 mJ 1 ps pulse, focused at (red) 55 m and (blue) 115 m, measured at the geometrical focus of the beam 1 µs after the last laser pulse. Filaments distribution measured at the same position, (b) 55 m and (c) 115 m as where the phase shift is measured.

Signals with good signal to noise ratio were only measured with the focused beam, while none were measured using the collimated beam. This indicates that the under-dense channel created in this regime is too weak to be measured in the experimental conditions of the LAL. Results show that the measured phase shift is more important with the beam focused at 55 m compared to 110 m where it is nearly negligible, indicating respectively an important under-dense channel and a faint one. This can be seen in figure 7.2, where a comparison of the phase shift induced by frequency doubled 500 mJ 1 ps pulses focused at the two distances are shown. The more important phase shift appearing

with stronger focus is coherent and further supports the presence of superfilament, which deposit more energy and thus induce more air density depletion, in such conditions.

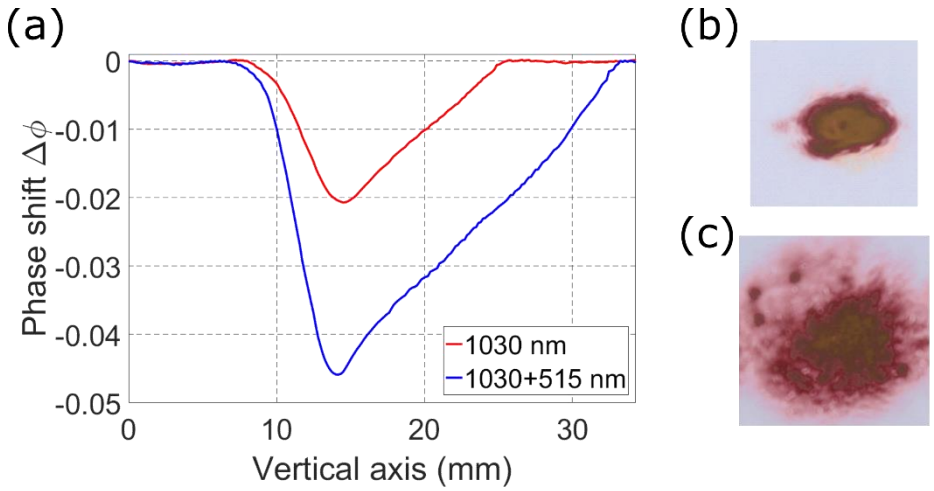

Figure 7.3: Phase shift induced by (in blue) the 500 mJ 1 ps frequency doubled beam and (in red) the fundamental beam, focused at 55 m, measured at the focal distance 1 µs after the last laser pulse. Filaments distribution measured at the same position as where the phase shift is measured for (b) the fundamental and (c) the frequency doubled beam.

To underline the importance of the use of the frequency doubled beam, a comparison between the phase shift induced by the fundamental beam and of the frequency doubled beam is presented in figure 7.3. A more important density variation is observed with the bicolour beam. The characteristic non symmetrical profile of phase shift measured at high repetition rate, as described in the chapter "Laser filamentation at high repetition rate", is clearly visible.

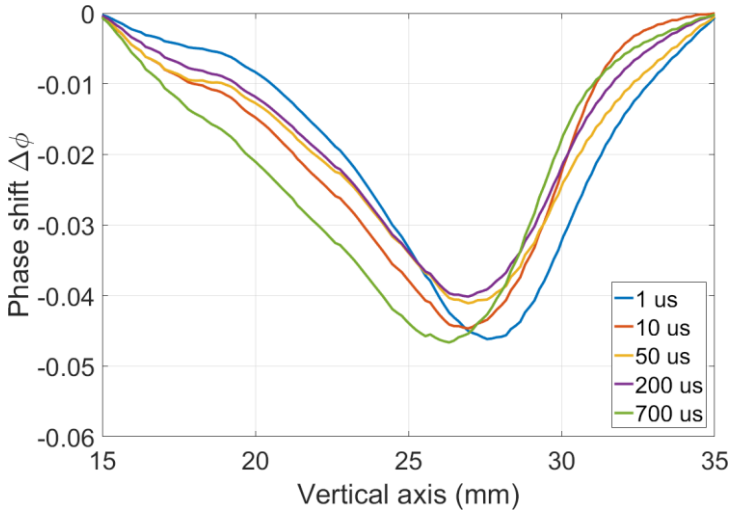

Figure 7.4: Phase shift induced by the 500 mJ 1 ps frequency doubled beam focused at 55 m, measured at the focal distance at several delays after the last laser pulse.

Moreover, the lack of temporal evolution between two consecutive pulses of the measured phase shift, as seen in figure 7.4, is again characteristic of the filamentation at high repetition rate. Thus, the under-dense channel created in this experiment seems to be constant over time.

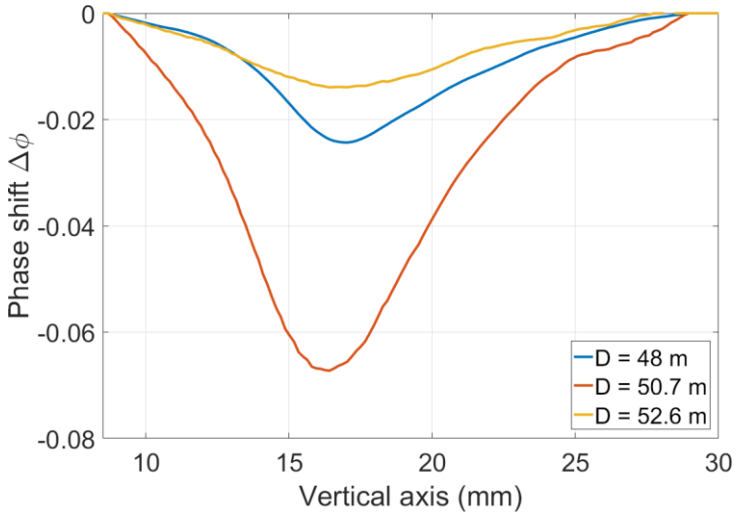

Figure 7.5: Phase shift induced by the 500 mJ 1 ps frequency doubled beam focused at 55 m, measured 1 µs after the last laser pulse at different distance near the focus distance.

One other important observation that can be retrieved from the phase shift measurement is the spatial evolution of the phase shift along the laser path. The measured phase shift being already fairly weak when the laser is focused at 115 m, no signal is measured at positions further than 50 cm away from the focal point. However, when the beam if focused at 55 m, a signal can be observed over a distance of ~3 m, centred around the focal point, as observed in figure 7.5. This distance is not consistent with the distance over which filaments are observed. It is however similar to the distance over which the dense pack of filaments characteristic of superfilaments is observed in such focusing conditions (see figure 6.1 (b)). This suggests that only the important phase shift induced by superfilament can be observed by our setup (which explains why no signals were measured with the collimated beam).

8 Effect on electrical discharges

After characterising the presence of filaments and the under dense channel created by them in the different focusing configuration, the next step was to test their ability to control high-voltage discharges in these different focusing conditions. This is an important test for the Laser Lightning Rod project because it would attest our capability to control high voltage at different distances and could impact the experimental setup that will be used be the following field campaign aiming to guide lightening.

The two main questions are:

- Can the collimated beam guide the electrical discharges? Or is the focused beam, and thus the telescope, mandatory?
- Does the use of the SHG crystal impact in a significant way the control of discharges?

The experiments performed to answer these questions were severely limited due to the time constraint of the campaign and unexpected damages on the telescope. As a consequence only a small number of experiments were conducted, with a maximum of laser energy of 200 mJ while using the telescope.

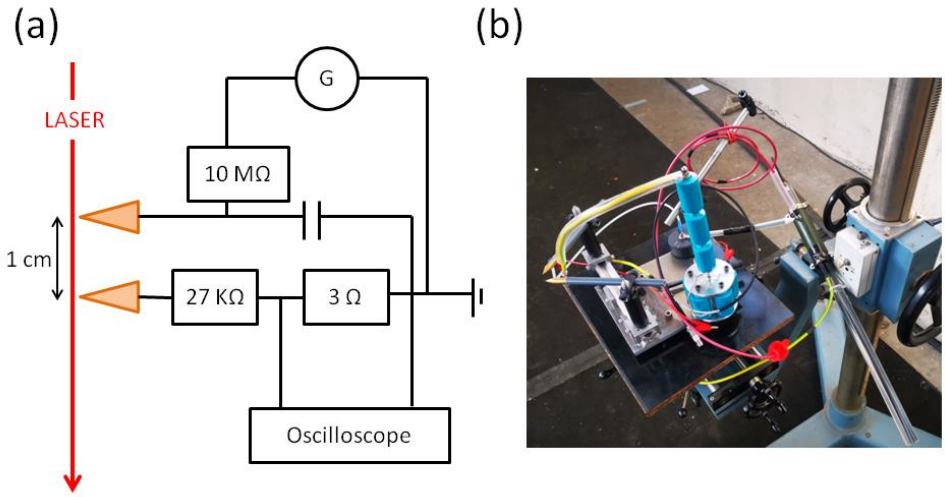

Figure 8.1: (a) Scheme and (b) picture of the setup allowing to test the guiding of discharges up to 30 kV.

The first set of experiment was done using the setup presented in figure 8.1. The setup consists of a tunable high voltage generator that can deliver tension up to 30 kV to a pair of needle electrode separated by a distance of 1 cm. Additional resistances were added to the circuit to allow us to monitor the current of the discharge. A photodiode was used to monitor the delay between the laser pulses and the discharge. By adjusting the tension on the electrode until a discharge is guided, we measured the breakdown voltage as the voltage for which a breakdown was observed for 5 consecutive tests.

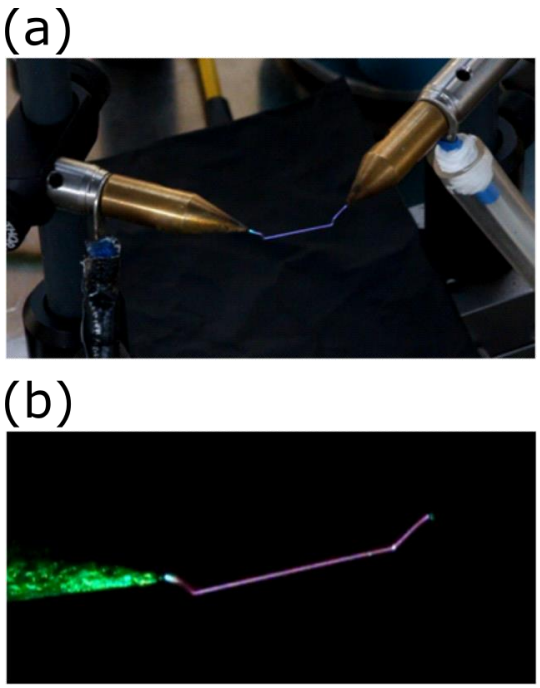

Figure 8.2: Picture of 1 cm long discharges guided at (a) 28.5 kV by the 1 ps 200 mJ laser pulses and (b) 27.5 kV by the 1 ps, 200 mJ frequency-doubled pulses, focused at 55 m.

This measurement of the breakdown voltage was done for the three propagation regime of the laser used in the previous sections: the propagation of a collimated beam, a beam focused at 115 m and a beam focused at 55 m. When using a focusing beam, the electrodes were placed near the non

linear focus and when using the collimated beam, they were placed at the position where the highest number of filaments were measured, as seen in figure 6.1.

No guiding effect nor reduction of the breakdown voltage were observed neither when using the collimated beam nor when the beam was focused to 115m. However, discharges guided by the beam focused at 55 m were observed, as presented in figure 8.2. This observation confirms us that the telescope and a strong focusing seem necessary to control discharges. When focused at 55 m, the breakdown voltage was reduced from the natural breakdown of 30 kV to 28.5 kV by the laser at 1030 nm, and to 27.5 kV by the frequency doubled laser at 1030+515 nm. The use of the SHG is thus confirmed to boost the breakdown reduction effect of the laser.

However, it is important to note that the reduction of the breakdown voltage is small compared to reduction of more than 60 % previously observed using a similar setup [18]. This can be explained due to the scale mismatch between the distance between the electrode of 1 cm and scale of the spatial distribution of the filament, as presented in figure 7.2 (b). At the focal point, when the beam was focused at 55 m, filaments were observed in an area of a diameter of 9 mm. Due to the size of the area being similar to the distance between the electrodes, only a portion of the filaments would be able to interact with the discharge and the one too far away are not able to contribute. Moreover, due to the configuration of the electrodes, the central part of the batch of filaments could not be used and only the edge of it was near the electrodes. When we tried to force the alignment of the central part of the filament's batch with the electrodes, the setup could not withhold the intense heating due to the high average power coming from the kHz repetition rate. This hypothesis of only a part of the filaments contributing to the breakdown voltage reduction is further strengthened by the observation that the reduction of the breakdown voltage was the same for laser energy varying from 20 mJ to 200 mJ. This means that the additional filaments generated by the increase of energy do not contribute to the breakdown voltage reduction. This could even explain the absence of observed guiding and breakdown voltage reduction when using the collimated beam and the beam focused at 115 m because in both of these cases the filaments batch (see figure 7.2 (b-c)) is even more loosely distributed.

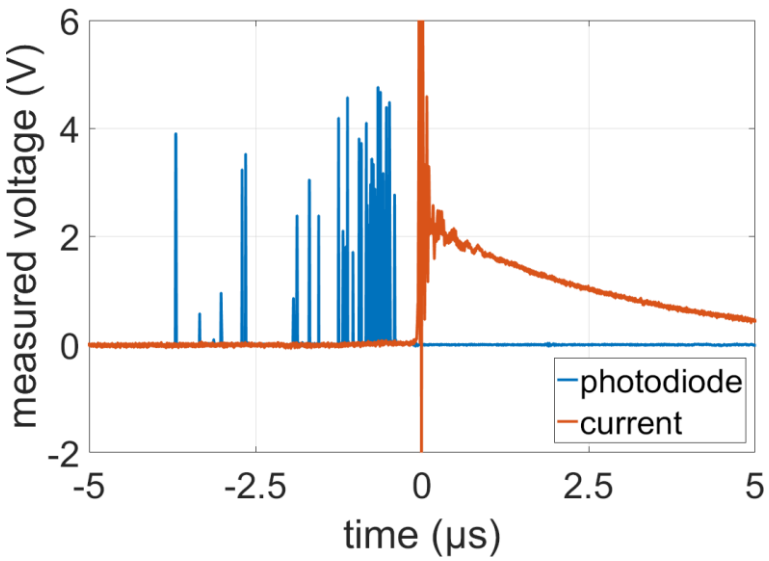

Figure 8.3: Measured voltage representing the (in red) discharge current and (in blue) the photodiode signal accumulated over 40 discharges. Each peak in the photodiode signal represents the temporal position of one of the 40 laser pulse as compared to the discharges.

One other important observation than can be done from the measurement is about the synchronisation between the laser pulses and the guided discharges. As presented in figure 8.3, by looking at the current signal and the signal from the photodiode over 40 discharges, we can retrieve the delay distribution between the laser pulse and the discharges. The measured delays ranged from

0 to 5 μs, and the mean delay was around 1 μs. These delay range and mean value are characteristic of the timescale needed to reach the pressure equilibrium after the laser filamentation and to form the under dense channel, as presented in the chapter “Laser filamentation at high repetition rate”.

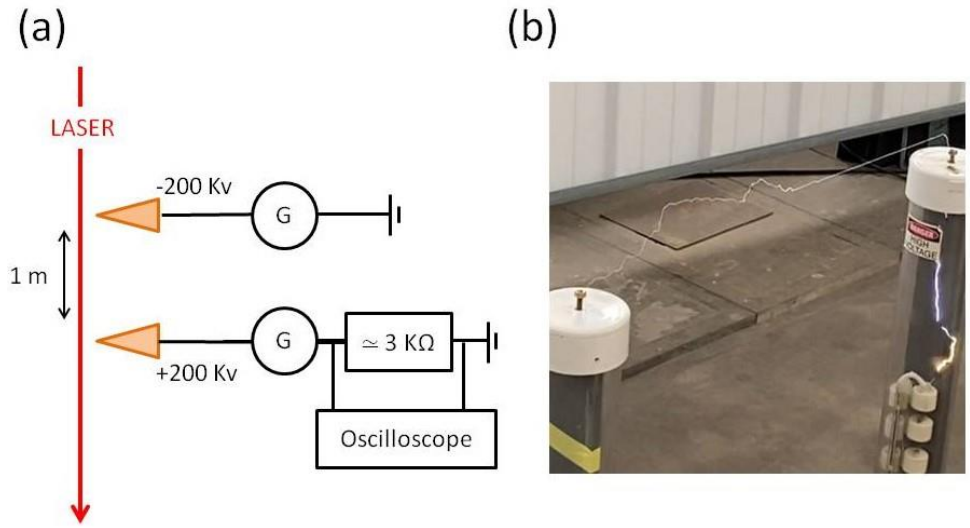

Figure 8.4: (a) Scheme of the 400 kV setup and (b) picture of a partially guided discharge guided by the beam focused at 55 m.

An additional experiment was performed using a high voltage delivering 200 kV to one electrode and -200 kV to the second electrode of 200 kV, netting in a 400 kV voltage between the electrodes. The electrodes were placed 1 m apart from each other, as seen in figure 8.4 (a). This setup was again used the three propagation regime of the laser used in the previous sections: the propagation of a collimated beam, a beam focused at 115 m and a beam focused at 55 m.

Similarly to what was observed with the 30 kV setup, no guided discharges were observed when using the collimated beam nor when the beam was focused to 115m, and discharges partially guided by the beam focused at 55 m were observed as shown in figure 8.4 (b). However, we could not continue the experimentation using this 400 kV setup due to technical issue rendering the generator unusable.

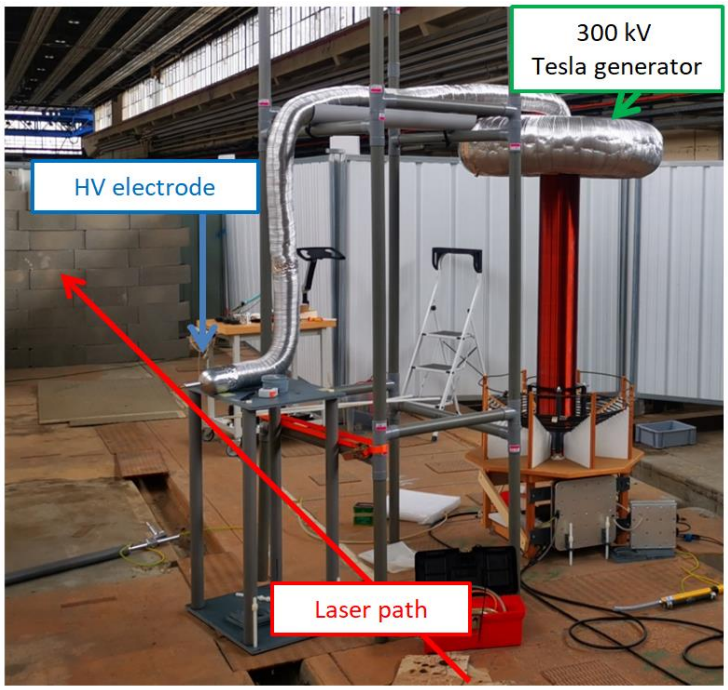

Figure 8.5: Experimental setup using the 300 kV Tesla generator.

The last experimentation to test the laser ability to control high-voltage discharges in the different focusing conditions was done using the 300 kV Tesla generator described in the chapter "Study of the feasibility of a plasma antenna using meter-long long-lived guided discharges at high repetition rate" [20], as shown in figure 8.5. The Tesla generator delivers 300 kV oscillating high voltage pulses to an electrode that are synchronised with the laser using a photodiode signal.

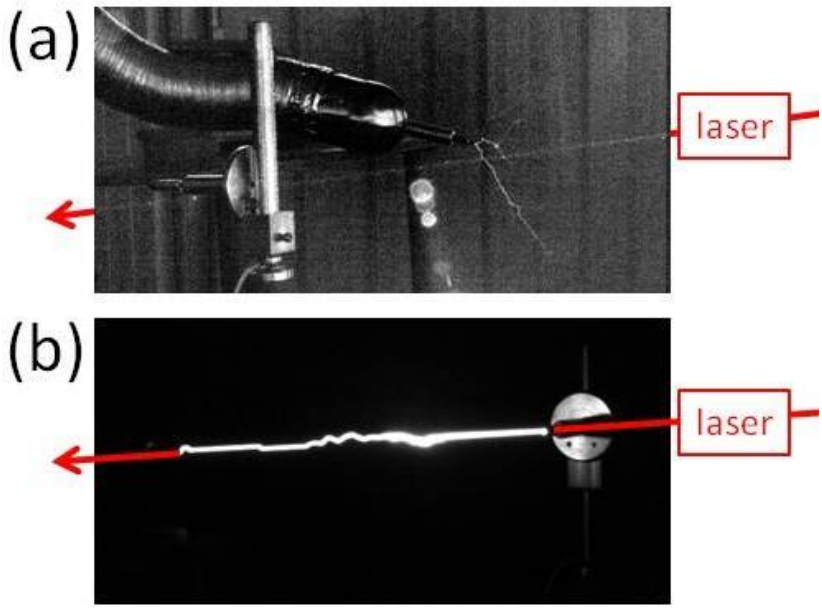

Figure 8.6: (a) Picture of the unguided discharge observed when using the laser focused at 115 m. (b) Picture of the partially guided 40 cm long discharge observed when using the laser focused at 55 m.

Once more, similar observations were made: no guided discharges were observed when using the beam was focused to 115m, and discharges partially guided by the beam focused at 55 m were

observed, as shown in figure 8.6 (a-b). One important observation of this partially guided discharge is the presence of jump in the discharge path, as if the discharge is hoping from one conductive channel to another, showing the contribution to the guiding effect of several filaments. The experiment was stopped due to time constraint caused by a damage appearing on one of the mirror telescope, rendering it unusable until repair.

With all these three different measurements, although they could not have been all finished due to technical difficulty, we can answer the two initial question of this section and affirm that the use of the telescope is mandatory to control electric discharges and that the use of the SHG crystal enhance the effect of the laser on discharges. Moreover, is important to note that while using the telescope, all focusing condition are not equal and a strong focusing is needed to control discharges. This condition seems reminiscent to the condition to have superfilament [10], and could point that their presence is an important contribution to the control of electric discharges.

9 Conclusion

In this chapter, I have shown the characterisation of the filamentation of the 500 mJ, 1ps, 1 KHz LLR laser system in different focusing condition. Using a collimated beam, the presence of filament over 50 m was observed and by changing the pulse duration from 1 to 7 ps, the onset of the filamentation was shifted from 18 m to 60 m. However, during all of our experiments these filaments failed to affect electrical discharges, probably due to their local density being too low.

Using the telescope developed in the framework of the LLR project, we characterized the filaments created by focusing the beam at 55 m and 115 m. Filaments created at 55 m are more locally dense than the ones created at 115 m, but they spread over a distance of 12 m compared to the 30 m covered by the ones created at 115 m. Only the beam focused at 55 m where observed to guide electrical discharges. The addition of a frequency doubling crystal was observed to increase the laser guiding efficiency.

These measurements were crucial for the main experiment of the Laser Lightning Rod project that will be presented in the following chapter, where we will use our laser to try to guide ascending lightning leader starting at the top of a tower. Our ability to create filaments at a distance of 115 m was a requirement as this is the tower height [21], and the measured presence of filaments over 30 m would be an important parameter to scale our expectation of the guiding effect. It is important to note that, while we failed to observed guides discharges using the beam focused at 115 m, the difference in the propagation of a lightning leader compared to our relatively short scale experiments and the beneficial conditions that will present during the main experiment (such as the verticality of the experiment, the presence of an electric field or the reduced air density) leaved me hopeful to observe a guiding effect of lightning.

Bibliography

[1] C. Herkommer *et al.*, « Ultrafast thin-disk multipass amplifier with 720 mJ operating at kilohertz repetition rate for applications in atmospheric research », *Opt. Express*, vol. 28, nº 20, p. 30164-30173, sept. 2020, doi: 10.1364/OE.404185.

[2] T. Schröder, K.-J. Boller, A. Fix, et R. Wallenstein, « Spectral properties and numerical modelling of a critically phase-matched nanosecond LiB3O5 Optical Parametric Oscillator », *Appl. Phys. B*, vol. 58, nº 5, p. 425-438, mai 1994, doi: 10.1007/BF01081885.

[3] R. W. Boyd, *Nonlinear optics*, 3rd ed. Burlington, MA: Academic Press, 2008.

[4] J. Ma, J. Wang, P. Yuan, G. Xie, et L. Qian, « Origin and suppression of back conversion in a phase-matched nonlinear frequency down-conversion process », *Chin. Opt. Lett.*, vol. 15, nº 2, p. 021901, févr. 2017.

[5] U. Andral *et al.*, « Second and third harmonic generation from simultaneous high peak- and high average-power thin disk laser », *Appl. Phys. B*, vol. 128, sept. 2022, doi: 10.1007/s00340-022-07887-8.

[6] J. H. Marburger, « Self-focusing: Theory », *Prog. Quantum Electron.*, vol. 4, p. 35-110, avr. 1975, doi: 10.1016/0079-6727(75)90003-8.

[7] A. Couairon et A. Mysyrowicz, « Femtosecond filamentation in transparent media », *Phys. Rep.*, vol. 441, nº 2-4, p. 47-189, mars 2007, doi: 10.1016/j.physrep.2006.12.005.

[8] G. Méjean *et al.*, « Multifilamentation transmission through fog », *Phys. Rev. E*, vol. 72, nº 2, p. 026611, août 2005, doi: 10.1103/PhysRevE.72.026611.

[9] M. Petrarca *et al.*, « White-light femtosecond Lidar at 100 TW power level », *Appl. Phys. B*, vol. 114, nº 3, p. 319-325, mars 2014, doi: 10.1007/s00340-013-5741-6.

[10] G. Point *et al.*, « Superfilamentation in Air », *Phys. Rev. Lett.*, vol. 112, nº 22, p. 223902, juin 2014, doi: 10.1103/PhysRevLett.112.223902.

[11] G. Point, E. Thouin, A. Mysyrowicz, et A. Houard, « Energy deposition from focused terawatt laser pulses in air undergoing multifilamentation », *Opt. Express*, vol. 24, nº 6, p. 6271-6282, mars 2016, doi: 10.1364/OE.24.006271.

[12] J. Yu *et al.*, « Sonographic probing of laser filaments in air », *Appl. Opt.*, vol. 42, nº 36, p. 7117-7120, déc. 2003, doi: 10.1364/AO.42.007117.

[13] R. G. Brewer, J. R. Lifsitz, E. Garmire, R. Y. Chiao, et C. H. Townes, « Small-Scale Trapped Filaments in Intense Laser Beams », *Phys. Rev.*, vol. 166, nº 2, p. 326-331, févr. 1968, doi: 10.1103/PhysRev.166.326.

[14] R. Chiao, M. Johnson, S. Krinsky, H. Smith, C. Townes, et E. Garmire, « A new class of trapped light filaments », *IEEE J. Quantum Electron.*, vol. 2, nº 9, p. 467-469, sept. 1966, doi: 10.1109/JQE.1966.1074117.

[15] L. Bergé, S. Skupin, R. Nuter, J. Kasparian, et J.-P. Wolf, « Ultrashort filaments of light in weakly ionized, optically transparent media », *Rep. Prog. Phys.*, vol. 71, nº 10, p. 109801, sept. 2008, doi: 10.1088/0034-4885/71/10/109801.

[16] P. Béjot, J. Kasparian, et J.-P. Wolf, « Dual-color co-filamentation in Argon », *Opt. Express*, vol. 16, nº 18, p. 14115-14127, sept. 2008, doi: 10.1364/OE.16.014115.

[17] M. Durand *et al.*, « Kilometer range filamentation », *Opt. Express*, vol. 21, nº 22, p. 26836-26845, nov. 2013, doi: 10.1364/OE.21.026836.

[18] P. Walch, B. Mahieu, L. Arantchouk, Y.-B. André, A. Mysyrowicz, et A. Houard, « Cumulative air density depletion during high repetition rate filamentation of femtosecond laser pulses: Application to electric discharge triggering », *Appl. Phys. Lett.*, vol. 119, nº 26, p. 264101, déc. 2021, doi: 10.1063/5.0077635.

[19] P.-Q. Elias *et al.*, « Improving supersonic flights with femtosecond laser filamentation », *Sci. Adv.*, vol. 4, nº 11, p. eaau5239, 2018, doi: 10.1126/sciadv.aau5239.

[20] L. Arantchouk *et al.*, « Large scale Tesla coil guided discharges initiated by femtosecond laser filamentation in air », *J. Appl. Phys.*, vol. 116, n° 1, p. 013303, juill. 2014, doi: 10.1063/1.4886582.
[21] T. Produit *et al.*, « The laser lightning rod project », *Eur. Phys. J. Appl. Phys.*, vol. 93, n° 1, Art. n° 1, janv. 2021, doi: 10.1051/epjap/2020200243.

Chapter 6

The “Laser Lightning Rod” experiment.

Figure 1: Picture of the laser experiment at the top of the Säntis Mountain.

In this chapter, I will present the results of the main experimental campaign of the Laser Lightning Rod project, during which we investigated the impact of laser filamentation at kHz repetition rate on real lightning strikes. We used the kHz-terawatt laser system developed for the LLR project and assess its ability to stimulate upward lightning flashes from the telecom tower at the top of the 2504 m high Säntis Mountain in Switzerland.

I will first focus on the experimental setup with a description of the Lightning observatory already present at Säntis and the laser installation that we set up. Next, I will present the various results that were obtained from the 16 lightning events recorded during this campaign. By comparing the characterization of the leader propagation, the X-ray emission and the polarity of flashes in the presence or the absence of the laser, I will show how the lightning flashes were affected by the filaments.

Table of contents

1 Context

Lightning is a spectacular phenomenon that has always fascinated mankind due it is raw destructive power and breathtaking nature. If we set aside the beauty of the phenomenon, we can easily see that lighting has a considerable impact on the environment and economy by causing supply outages, forest fires, damage to electronics and infrastructure, injury and death to either human or livestock. It is estimated that 6 000 to 24 000 casualties per year are related to lightning strikes worldwide [1]. Furthermore, these observations will only worsen due to the increase of the storms severity induced by the climate change and the increase of the number of precarious site such as wind turbines or telecommunications tower. It is then clear that lightning protection is a topic, whose relevance will increase in the following years. However, efficient lightning protection techniques are still lacking and the options are limited.

The first approach for a perfect lightning protection would be a Faraday cage with a sufficient wall thickness to shield the interior of the cage from any perturbation induced by the lightning. The frequency of the these perturbations ranging from few kHz to tens of MHz, a metallic shield of several mm would be an efficient lighting protection [2]. It is however clear that the usage of this technique is severely limited and can only be applied to specific objects of moderate scale.

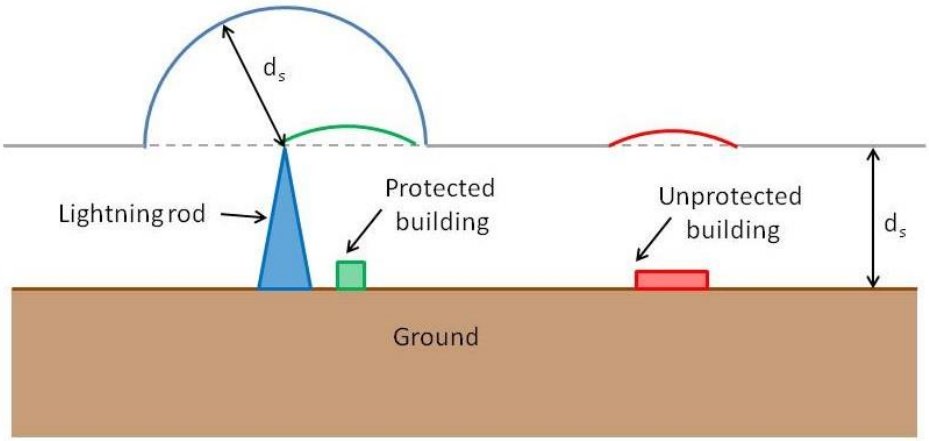

Figure 1.1: Illustration of a lightning rod capture region (in blue), showing a protected building whose capture region (in green) is inside the one of the lighting rod and an unprotected building whose capture region (in red) is outside the protection range of the lightning rod. d_s is the striking distance.

The other approach of lightning protection consists in defining a preferential path for the lightning that will draw it away from the target instead of shielding it. When a descending leader will propagate, before it is too close to the target, it will be "caught" by the lightning protection through the development of an upward leader. This is how the lightning rod described in 1749 by Benjamin Franklin operates [3]. This method is passive as it does not trigger a descending lightning. An important parameter to consider when implementing a lightning rod is called the striking distance d_s, which is the distance from the tip of the descending leader to an object where the electrical field is high enough to initiate electrical breakdown (note that d_s will mainly vary with the electric potential of the descending leader tip) [4]. We can then define a capture zone that is limited by the surface located at a distance d_s from the upper point of our lightning rod. Structures that are placed inside this zone are protected, as shown in figure 1.1. While effective, this technique is not always suitable, such as cases needing temporary protection, or even possible, such as for protection of rockets on their launching pad or landing lanes in airports.

Another approach to divert lightning is the rocket and wire technique where a small ascending rocket pulls a conductive wire. The sudden elevation of the potential in the wire will trigger a lightning flash that will follow the wire for a field value that would not be sufficient for a natural flash. As an example, a rocket attached to a 400 m wire can successfully trigger a flash when the ground electric field is around 10 kV/m [5].Such Rockets have been used to trigger lightning for research purposes since the 1960s. But this method presents several drawbacks [6], [7]. The success of this approach strongly depends on the location and the stage of the thunderstorm as well as the electric field close to the ground at the time of the triggering attempt. Launchpads are generally fixed and typically limited to 5 – 10 rockets, but mobile launchpads have also been used. Furthermore, the rockets fall back to the ground regardless of the success of the triggering attempt, generating debris. Finally, while the wire melts away during successful attempts, a few hundred meters of conductive wire fall to the ground with the rocket in the case of unsuccessful launches, implying risks for personnel and equipment on the ground.

To answer the shortcoming of these techniques, a new strategy was developed to try to find a continuously operating technique to trigger lightning, for which laser would be prime candidates. The first tests performed in the 1970s using nanosecond laser pulses demonstrated the guiding of megavolts discharges up to 2 m long [8], [9]. An attempt to trigger and guide natural lightning was made by Uchida *et al.* in 1999 using a combination of three lasers with kJ-level energy to form a 2 m long plasma spark at the tip of an experimental tower [10]. The researchers reported two successful events, but this low number of events did not lead to conclusive proof of the effectiveness of the lightning triggering technique [11]. The two main drawbacks of this technique, being the high energy cost to create the conductive plasma [12] and its discontinuity [13] led to his disappearance.

In contrast, with ps and fs laser pulses the energy necessary to create a column of plasma is way lower [14], [15]. Due to the filamentation process, the resulting plasma column is homogeneous and continuous. In the 2000s, several groups demonstrated their capability to trigger and guide high-voltage discharges over several meters with laser pulses of only 100 mJ [16], [17]. By connecting two electrodes separated by several meters, the laser filaments can reduce the breakdown voltage by 30%, and trigger the discharge. These triggered discharges are guided along the laser filaments path rather than following an erratic path typical of a classical discharge. Furthermore, filaments are able to divert a discharge from its preferential path [18].

Based on these successful results in laboratory, a mobile femtosecond-terawatt laser called "Teramobile" has been developed by a French-German-Swiss consortium. In a field campaign at the Langmuir Laboratory of the New Mexico Tech on the South Baldy Peak, micro-discharges synchronized with the laser pulses were detected in the presence of electric field, indicating that laser filaments can initiate corona discharges in thunderclouds [19]. However, they concluded that the short lifetime of plasma filaments (typically a few ns) prevented the initiation of upward leaders similar to the mechanism of rocket triggering. Increasing the plasma lifetime by heating the filament plasma with an additional, high-energy nanosecond laser was proposed by several groups [20]–[22]. However, this requires an additional laser of very high energy, typically in the kilojoule range. Coupling such a beam into the filament proved to be unpractical over distances exceeding a few meters.

On the other hand, an interesting feature of filaments recently highlighted is their ability to generate a low-density (air-depleted) channel [23], [24]. For a low-repetition rate multi-TW laser, the air density can be initially reduced by a factor 5 over a typical length of a few meters. After 1 ms this density depletion still amounts to typically 10% of the ambient density [25]. These straight, low-density channels favour the triggering and guiding of electric discharges in the atmosphere at a reduced voltage (proportional to the density reduction) [18], [26]. At repetition rates in the kHz range, one can expect this ms-long air density depletion (and the resulting triggering effect) to be amplified by a cumulative effect [23], [27], [28].

Based on these results, the European project Laser Lightning Rod used a specific kHz-terawatt laser system to try to guide lightning. This laser system, that was described in the previous chapter "Long-distance filamentation with kW ultrashort laser", have the particularities of having both high peak power, with energy of up to 500 mJ and minimum pulse duration of 1 ps, while having a kHz repetition rate. This combination should allow to create filament over a long-distance and at a high enough repetition rate, and to generate a permanent under-dense channel that will act as a preferential path for the lighting.

Based on the experiments described in the previous chapter "Long-distance filamentation with kW ultrashort laser", we can expect to create filaments over a distance of more than 30 m. Adding the beneficial effect of the verticality of our experiment, as described in the chapter "Laser filamentation at high repetition rate: Study of the cumulative air density depletion and its application to electric discharge triggering", we can expect an under-dense channel having a guiding effect over more than 50 m.

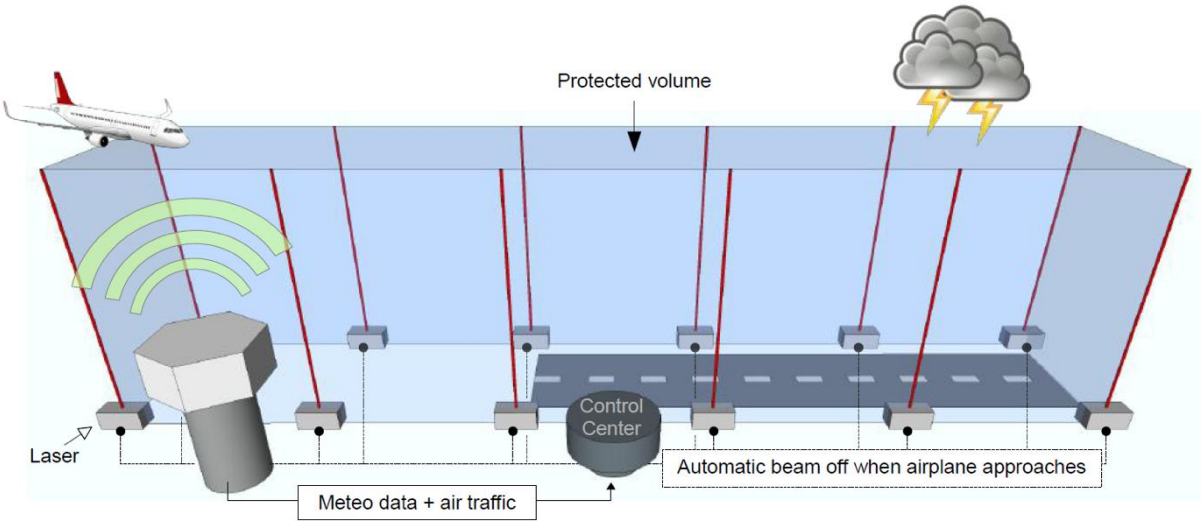

Figure 1.2: Potential laser network geometry for aircraft protection during landing and take-off, taken from [29].

If proven successful at guiding and triggering lightning, the laser lightning rod could be envisaged to be coupled with a lightning detection system locating the presence of lightning clouds. In the presence of imminent lightning flashes, the laser could be pointed toward the charged clouds to conduct lighting flashes toward defined safe areas and drain the charges in the cloud, reducing the possibility of lighting flash in an area that needed to be protected. By using several lasers working together, a large protected volume could be defined as shown in figure 1.2.

2 Lightning observatory at Säntis

2.1 Measurement system of the Säntis station

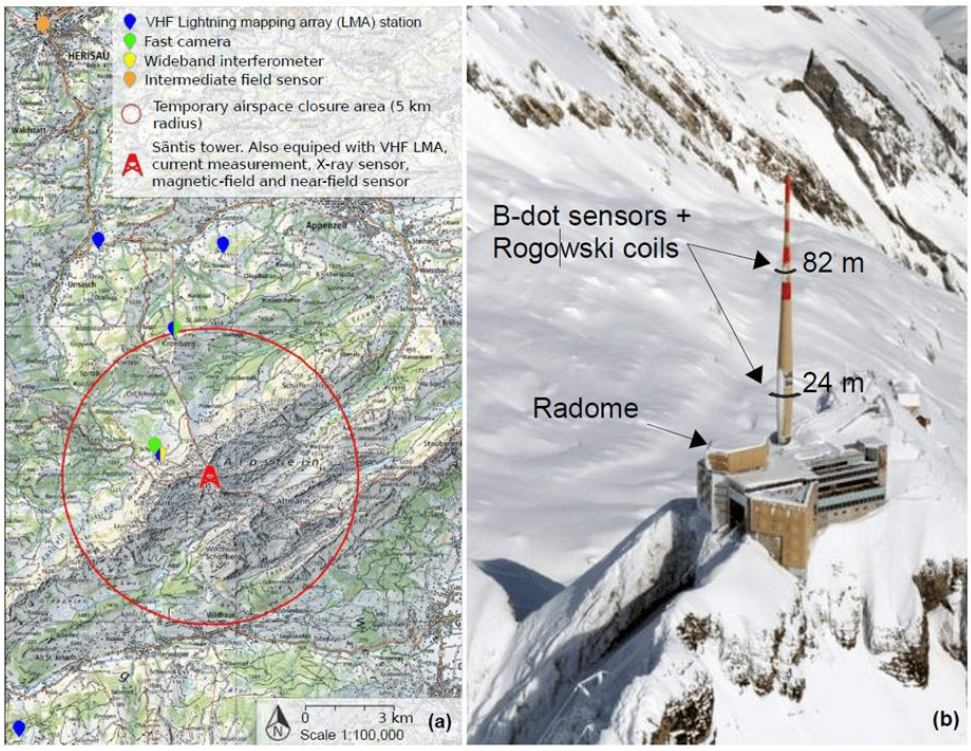

Figure 2.1.1: (a) Map of the experimental site, including auxiliary instruments and no-fly zone. (b) General view of the station and location of the Rogowski coils and B-dot sensors measuring lightning currents.

The field experiments of the LLR project has been performed at the top of the Säntis Mountain in Switzerland, at an altitude of 2481 m. This site has a weather station active since 1882 and it has been used for lightning research purposes since 2010.

The Säntis is one of the lightning hotspots in Europe with around 100 events per year, mostly concentrated between May and August, while the only snow free months are August and September. Typical Summer temperatures (0 °C to 10 °C), diurnal amplitudes (~6°C), relative humidity (80% – 90%) and wind gusts up to almost 180 km/h impose severe constraints on experiments, especially when sensitive instruments like a high-power ultrashort laser are needed.

Since 2010, two sets of instruments installed on the Säntis tower have been measuring both currents and current derivatives at 24 m and 82 m above ground level (see figure 2.1.1 (b)) under remote control and monitoring. Rogowski coils measure the low-frequency current from 10 mHz up to 3 MHz, while multigap B-dot sensors provide current-derivative waveforms with a 20 MHz bandwidth. The measured signals are transmitted over optical fibers to a National Instruments PXI-5122 high-speed digitizer that records each lightning flash over a measurement time window of 2.4 s at a sampling rate of 50 MS/s. The electromagnetic fields are measured by wideband electric and magnetic field sensors as well as a field mill installed inside the radome next to the tower. Wideband field sensors are also installed at a 14:7 km distance, on the roof of a 20 m tall building. The wideband vertical electric field is also measured at a distance of 380 km, in North western Austria, by flat-plate antenna belonging to the Austrian Lightning Detection and Information System (ALDIS).

Besides the electromagnetic field measurement, a Phantom high-speed video camera was installed in 2018, 2020 and 2021 on the Kronberg mountain, ~5 km North of the Säntis tower (See Figure 2.1.1 (a)). The camera overlooks the tower from a storage room at the Kronberg Luftseilbahn. An example of frames taken by the camera is presented in figure 2.1.2. In 2021 an additional high-speed camera was set up in a room of the Säntis - Das Hotel, located ~2 km away from the tower on the slope of Mount Säntis. Each camera operated, respectively, at 10,000 and 24,000 frames per second.

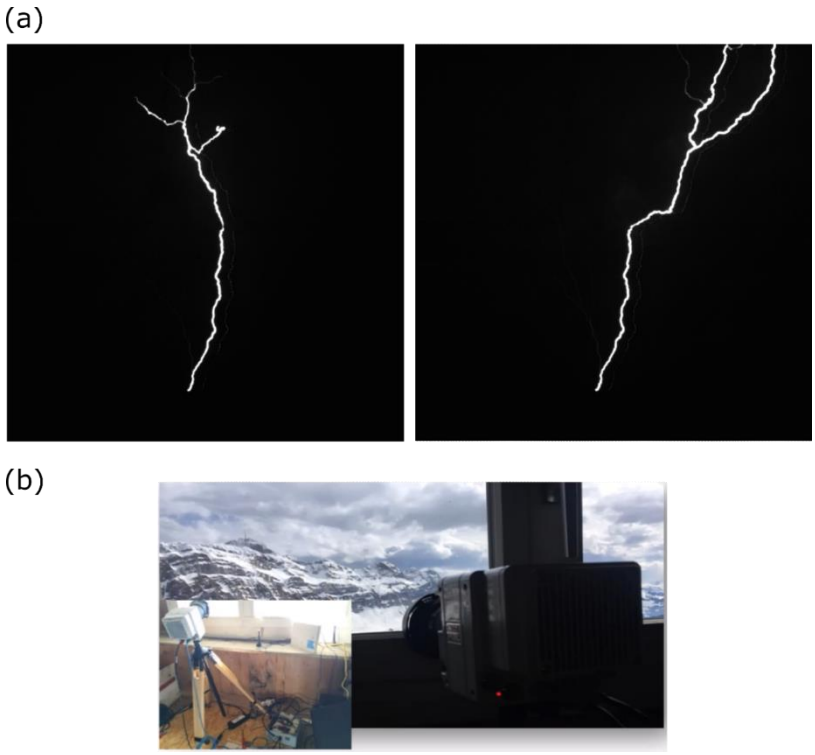

Figure 2.1.2: (a) Two frames recorded by the camera of an upward lightning strike on the 30th July 2021 at 15:38:10 UTC. (b) Picture of the camera in its room at the Kronberg Luftseilbahn.

An X-ray detector located in the radome measures the X-rays emitted in the range 20 keV-1 MeV. Moreover, data from the weather radar covering the Säntis Tower area are also made available by MeteoSwiss.

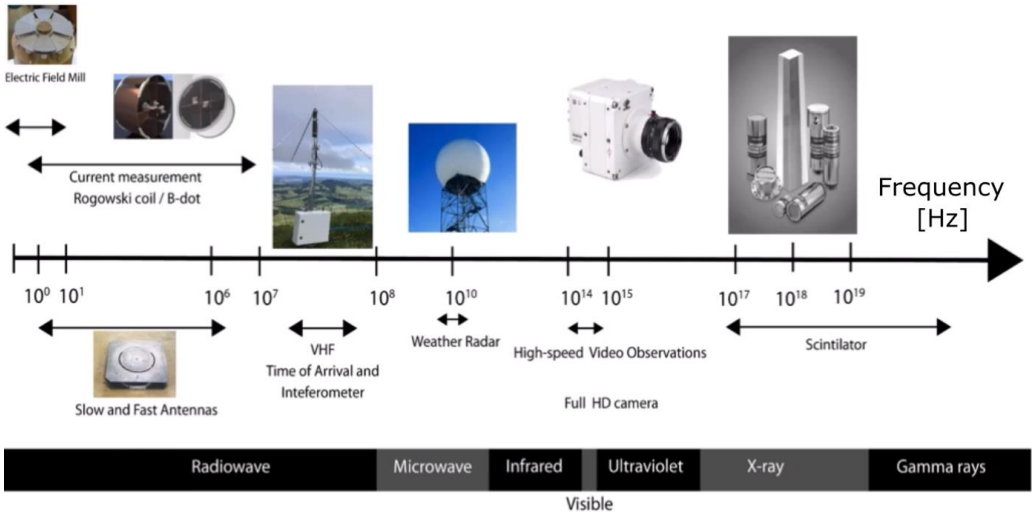

Figure 2.1.3: Different devices used in Säntis to characterize the lightning and their corresponding frequency range.

In figure 2.1.3 are presented all the different devices and their corresponding frequency range of recording. All the measurement devices record continuously with a pre-trigger window and once a certain threshold of measured current value is detected at the Säntis tower, a trigger signal is sent over the Internet to all the remote devices, allowing synchronized measurements.

2.2 Interferometer

In addition to the equipment presented in the previous section, an interferometer system belonging to the New Mexico Tech was installed during the 2021 summer in the vicinity of the Säntis - Das Hotel location [30], [31]. This system consists of three custom made inverted V-shape antennas that are connected to a PC equipped with a digitizer that samples the waveforms received by the antennas at a 250 MSamples/s rate. The three VHF antennas record the incoming electromagnetic waves from radiation sources in the 1–160 MHz band with a phase difference due to their different locations. By using a cross correlation algorithm, the location of the source can be obtained in a 2D space (azimuth, elevation) relative to the location of the system.

This system allows us to locate both spatially and temporally the lightning leader propagation, with a spatial resolution of several meters and a time resolution in the order of microseconds. We checked that with and without electric activity in the atmosphere, the interferometer is fully insensitive to the laser system and to the laser induced filaments.

3 Laser experimental setup at Säntis

To reach our goal of guiding upward lightning from the tip of the Säntis tower with the laser, the experimental setup should allow us to use the laser to create filaments starting from the tower top during thunderstorms.

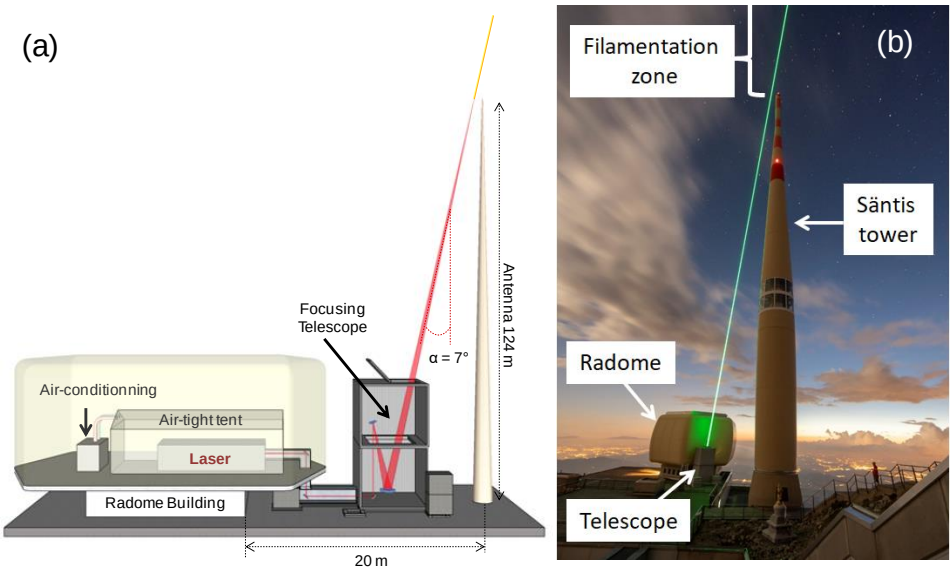

Figure 3.1: (a) Scheme of the laser experimental setup on top of the Säntis Mountain. (b) Photography of the experiment while the frequency doubled laser is propagating.

The first step is to provide a suitable environment for the laser system to ensure it can fully operate regardless of the harsh conditions of the thunderstorm. To do so, the laser was set up inside the Radome building that is located 20 m away from the tower (see figure 3.1). This building, generally used to host telecom antennas, provides a first layer of protection from the environment as well as access to the electrical supply. However, the building alone is not enough to ensure the clean and thermally stable conditions required to operate the laser (during the summer, the temperature in the building varied daily between 5 °C and 24 °C). Hence, the polyester tent described in the previous chapter was installed around the laser. This air-tight polyester tent equipped with an air conditioning system stabilizing the temperature at 20.2°C and 50% relative humidity. Moreover, after facing several issues due to perturbations in the state electrical distribution caused by the lightning strikes

(leading to the triggering of the laser interlock and shutting it down), the laser was set to be able to run on independent diesel power generators.

The second step is to create a beam path ensuring that the beam reaches the top of the tower and that the filaments will start there. To do so, after exiting the tent the laser beam is sent by a folding mirror downward to the terrace, through a metal tube inserted into the radome wall. There, a second folding mirror that directs it toward the beam expanding telescope. This telescope, already presented in the previous chapter, has a magnification ratio of 7.14 resulting in a final beam diameter of 250 mm at $1/e^2$. The translation stages on the secondary mirror of the telescope allow focusing the beam shortly after the tower tip to ensure that filaments start in its vicinity. The beam exits the telescope with an angle of 7° with respect to the zenith direction, propagating toward the top of the tower. The whole laser path, as presented in figure 3.1, was sheltered in an aluminium construction to protect it from precipitation, fog, and other environmental hazards as well as protect people in the path vicinity from any laser reflection. The construction consists of a horizontal section linking the radome to the telescope and in the telescope housing made of two stacked 3 m-high containers. The whole construction is anchored on a T-profile frame and stabilized against tilting and sliding by 20 concrete blocks of 930 kg each, a setup dimensioned to withstand winds up to 200 km/h.

The last step is to address the numerous laser safety issues related to such a massive open-air laser experiment, especially for both air traffic and public safety around the Säntis station. A no-fly zone has been defined in coordination with the Federal Office of Civil Aviation and the Swiss air navigation service provider (Skyguide) and was activated before each experiment (see figure 2.1.1). Furthermore, the laser was installed in the radome that is a private zone of the Säntis station, keeping the public beyond the minimal horizontal distance of 3 m required by Swiss regulations. Finally, the sheltering of the laser beam along its propagation toward the telescope ensures that any reflection or scattering can hit neither operators nor the public.

4 Result of the Laser Lightning Rod campaign

4.1 List of recorded events

Säntis is one of the locations in Europe which offers the highest lightning strike occurrence. The summer 2021 was no exception. During the operational period of the laser, from 21th of July until 30th of September 2021, 9042 lightning events were recorded by the interferometer. Out of these 9042 events, about 436 were classified as events that are likely to be in close proximity of the tower with sources possibly less than a hundred meters away from the tower tip. Note that the interferometer measurement alone cannot certify that an event happens in the tower plane due to the fact that they provide only 2D data.

Out of these 436 events during the campaign, 16 events were also recorded by the current measuring system, meaning that they unquestionably terminated to the tower structure. In this chapter, we will solely focus on these 16 events. Due to the limitation of the triggering system of the current measurement, event containing only an initial continuous current or with very low amplitude of fast pulses below the triggering threshold can be missed. As a consequence, there might be more events out of the 436 interferometer events that terminated to the tower.

However, the orographic situation of Säntis also promotes the presence of fog, which was highly detrimental to the LLR campaign. In particular, the fast cameras recording the events on the tower could only record lightnings during some hours on July 24 and July 30, due to the detrimental fog conditions around the tip of the mountain.

Additional difficulties appeared during the campaign: restricted time span yellowed by the air traffic control (permission after 3 pm only), but also unexpected restrictions due to the difficulty for aircrafts to fly in stormy conditions, electric power shutdown of the station due to lightning

strikes (before we started to use diesel generators), and difficulty of nowcasting lightning with the required accuracy in the mountainous region. Because of these difficulties, the laser effect could be recorded only during four upward events.

The information on all relevant recorded events is given in Table 4.1.1, where we provide information about the laser status during the flash and its polarity. In addition, we present the status of each measuring system during each flash, including HSC (high-speed camera), INT (Interferometer), X-ray (X-rays sensors), E-20 m (electric field 20 m from the tower) and E – 15 km (electric field 15 km from the tower).

Events	Date	UTC Time	Laser	Current	Flash polarity	HSC	INT	X-RAY	E (20m)	E (15km)
L1	24.7.2021	16:06:07	ON	YES	POS	NO	YES	YES	YES	YES
L2	24.7.2021	16:24:03	ON	YES	POS	YES	NO	YES	YES	YES
L3	30.7.2021	18:00:10	ON	YES	POS	NO	YES	YES	YES	YES
L4	30.7.2021	18:02:40	ON	YES	POS	NO	YES	NO	NO	YES
N01	30.7.2021	15:17:09	OFF	YES	NEG	NO	YES	YES	YES	YES
N02	30.7.2021	15:22:29	OFF	YES	NEG	NO	YES	NO	NO	NO
N03	30.7.2021	15:30:51	OFF	YES	NEG	NO	YES	YES	YES	NO
N04	30.7.2021	15:35:41	OFF	YES	NEG	NO	YES	YES	YES	YES
N05	30.7.2021	15:38:10	OFF	YES	NEG	YES	YES	YES	YES	YES
N06	30.7.2021	18:04:53	OFF	YES	POS	NO	YES	YES	YES	YES
N07	16.8.2021	02:00:27	OFF	YES	NEG	NO	YES	NO	NO	NO
N08	16.8.2021	02:34:10	OFF	YES	NEG	YES	YES	YES	YES	YES
N09	16.8.2021	05:53:24	OFF	YES	NEG	NO	YES	YES	YES	YES
N10	16.8.2021	10:16:32	OFF	YES	NEG	NO	YES	NO	NO	NO
N11	16.8.2021	15:06:45	OFF	YES	NEG	NO	YES	YES	YES	NO
N12	16.8.2021	15:08:34	OFF	YES	NEG	NO	YES	YES	YES	NO

Table 4.1.1 – Lightning strike events during the campaign, and available diagnostics for each event.

Out of the 16 flashes, 5 were positive flashes (POS) and 11 were negative flashes (NEG). Only 3 were recorded by at least one high-speed camera (two without laser and one with the laser on), while all but one were recorded by the interferometer. All investigated lightning strikes were upward, like 97% of the strikes observed at Säntis since 2010. All four recorded laser events were positive.

4.2 High speed camera measurements

The only 2 days of the campaign during which the visibility was suitable for recording flashes with the high-speed cameras at Schwaegalp and Kronberg were July 24 and July 30, 2021. As mentioned above, fast cameras constituted the most reliable diagnostics during the campaign to assess the guiding effect of the laser. On the 30th, the visibility was, however, highly variable, and dropped to such low values that no picture could be taken when the laser was switched on. On July 24, The LLR P2 event was observed with the two high speed cameras, one operating at 24 000 frames per second, installed on the Kronberg mountain, and the second operating at 10 000 frames per second installed inside Santis Das Hotel (Schwaegalp). Note that high-speed camera records of upward positive flashes are exceedingly rare and there are only a few reported in literature [32], [33].

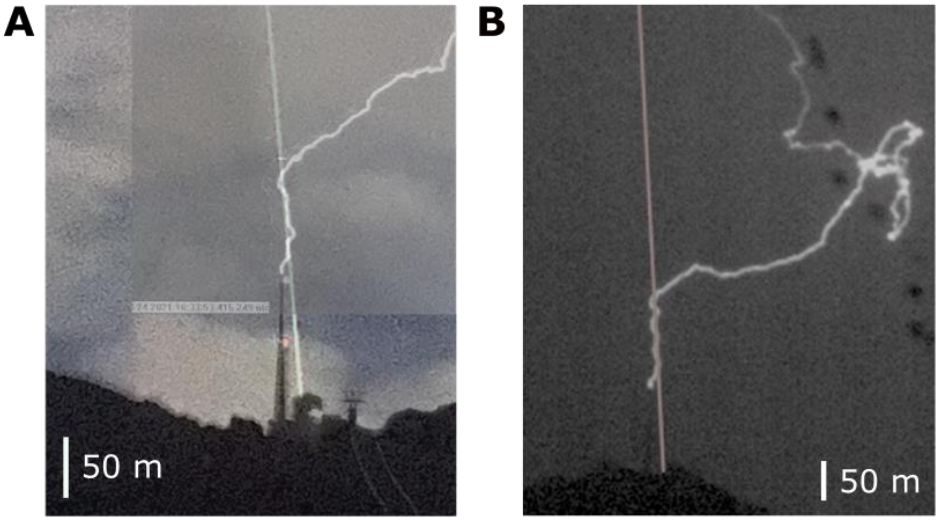

Figure 4.2.1: Snapshots of the lightning event of July 24 (L2) recorded in the presence of the laser by the two high-speed cameras located at Schwaegalp (A) and Kronberg (B). The trajectory of the laser path taken subsequently in cloudless sky through second harmonic generation is also overlaid.

Figure 4.2.1 displays two representative frames taken from the two fast cameras. To precisely calibrate the position of the laser, several comparative procedures were carried out: images from the fast cameras on daylight for better identifying the position of the tower and the surrounding topography, high resolution pictures at night with a D810 Nikon next to the fast cameras, when the laser was operating, reconstruction of the laser direction and position using precise GPS data.

On the 2 pictures in figure 4.2.1, depicting an upward positive flash, an initial segment of about 70 m from Schwaegalp and 120 m from Kronberg is observed following the path of the laser beam. Let us notice that the discharge is not completely straight along this initial segment, as it would be in the case of triggering with a rocket pulling wire. This difference is, however, well known from laser triggered and guided discharge performed at High Voltage facilities. Moreover, it was already observed with discharged guided by our laser, as presented in the previous chapter.

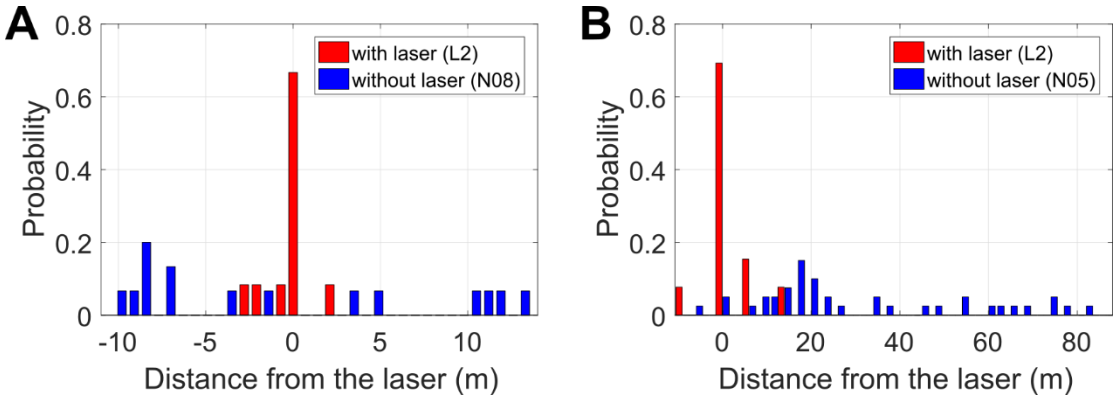

Figure 4.2.2: Projected 2D histograms based on single image, comparing (A) event L2 with N08 viewed from Säntis, and (B) L2 with N05 viewed from Kronberg.

To quantify the guiding along the laser path, we determined the actual lateral distance distribution towards the laser in these 2 pictures. In order to assess the probability for natural discharges to follow the laser path, we compared these lateral distances to fast camera pictures taken without laser, mainly on July 30th. The result, presented in figure 4.2.2, shows a clear difference between the events with and without laser, the one with laser having a narrower distribution. Thus, the leader propagation seems to stay closer to the laser path when the laser is operating.

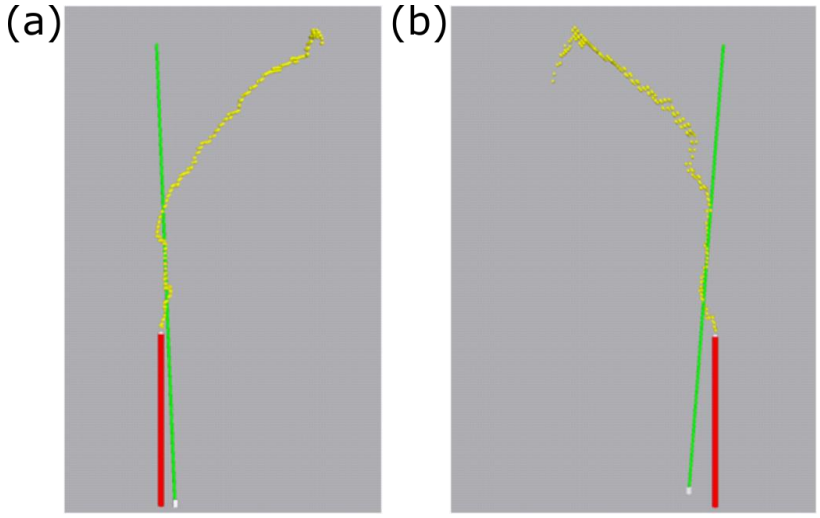

Figure 4.2.3: 3D reconstructed lightning path obtained using the image from the two high speed camera observed from 2 angles.

The images from Kronberg and Schwaegalp are only 2D projections and thus may partially lead to perspective errors. However, simultaneous acquisition of the 2 pictures allowed us to reconstruct the 3D path of the flash, as shown in figure 4.2.3. This reconstruction confirms that the straight segments are indeed straight and not just the projection of an erratic part in the plane perpendicular to that of the image.

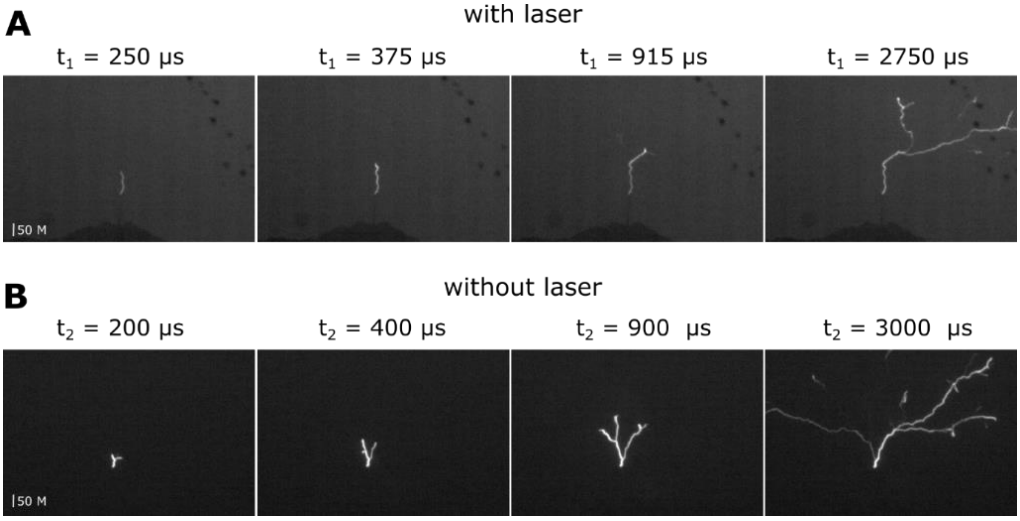

Figure 4.2.4: High speed camera images of upward leaders: (A) Images of the lightning path in the presence of the laser recorded on July 24 2021 at (L2) 250, 375, 915, and 2750 µs after initiation of the discharge. (B) Images of the lightning path recorded on July 2. 2019 in the absence of laser 200, 400, 900, and 3000 µs after initiation of the discharge.

Another aspect of the leader propagation that can be retrieved from our observations is its branching, while it propagates. Figure 4.2.4 presents a comparison between the recorded frames from two events, one with laser and the other without. A clear distinction between these two events can be observed. In the case of the event with the laser, the number of the branches in the region close to the tower is significantly smaller compared to the case without the laser.

4.3 Interferometer measurements

During the campaign, four flashes have been recorded by the interferometer system, while the laser was active (LLR P1, LLR P3, LLR P4 and LLR L5). The interferometer accuracy is about several tenths of degrees corresponding to tens of meters in the plane of the tower tip.

Note that the laser filamentation can only occur over a length of several tens of meters above the tower. As a consequence, guiding effects of the laser are expected only in this region. Therefore, analysis of the results is focused on the region close to and above the tower tip.

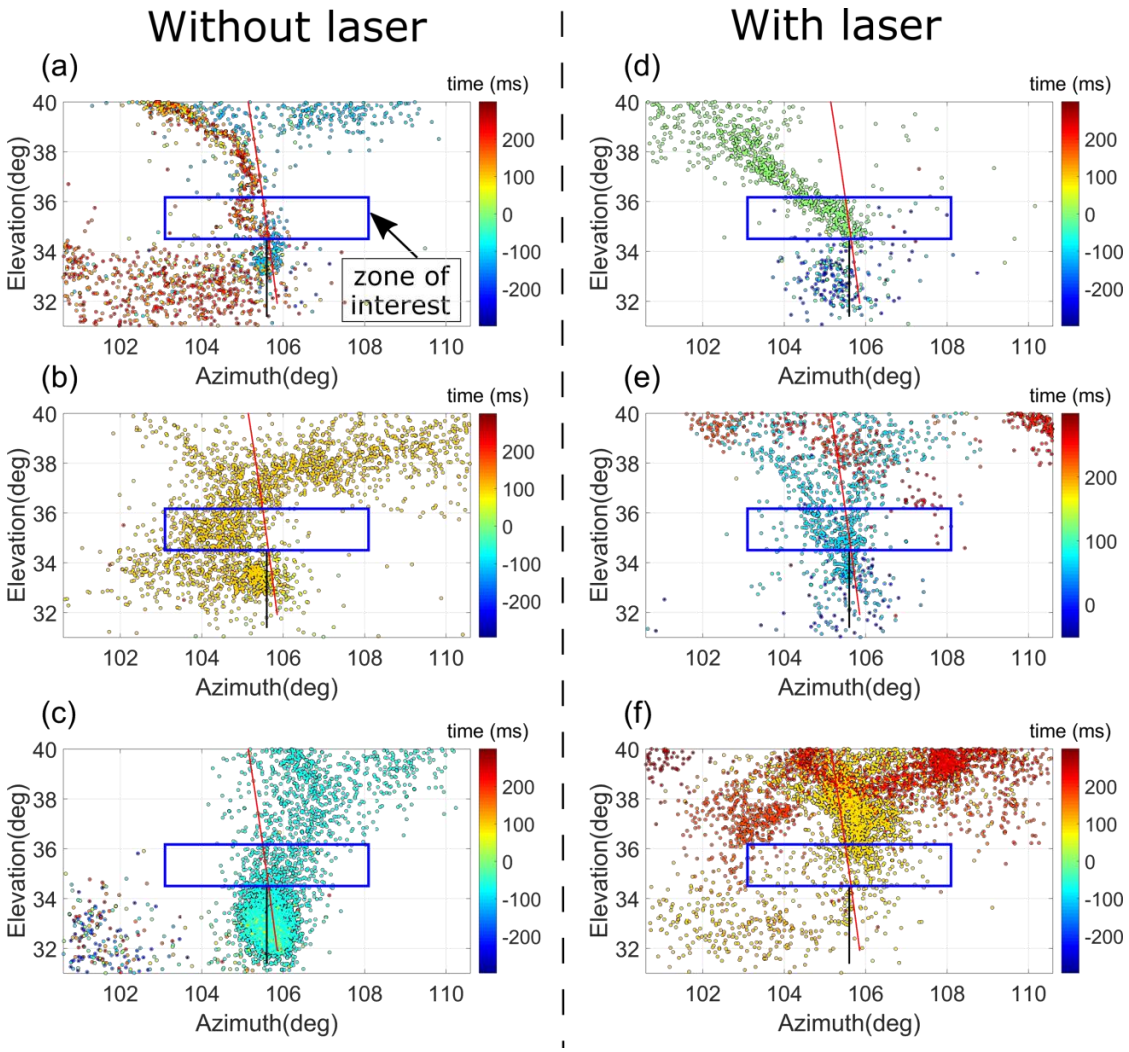

Figure 4.3.1: Plot of temporal and spatial distributions of the VHF sources for the events without laser (a) LLR N2, (b) LLR P5, (c) LLR N7 and the events with laser (d) LLR P1, (e) LLR P3, (f) LLR P4 (see table 1 and 2 for the date of the events). The Säntis tower is represented on each plot as a black line, the laser path is represented as a red line. The blue rectangles correspond to the zones of interest where guiding effect is observed (height = 60 m, width = 185 m).

Figure 3.5 (e) to (h) present 4 different events of lightning hitting the tower recorded by the interferometer without the laser. Each plot is a 2D map of the VHF sources detected during 600 ms around the tower (represented by the black line).
By contrast, in the four events with laser, presented in Figure 3.5 (a) to (d), we observe VHF sources always aligned along the laser path. This guiding effect is visible at the beginning of the upward propagation of the lightning leader, corresponding to the length, where laser filamentation occurs. Note that each event is recorded during 600 ms, corresponding to 600 laser shots.

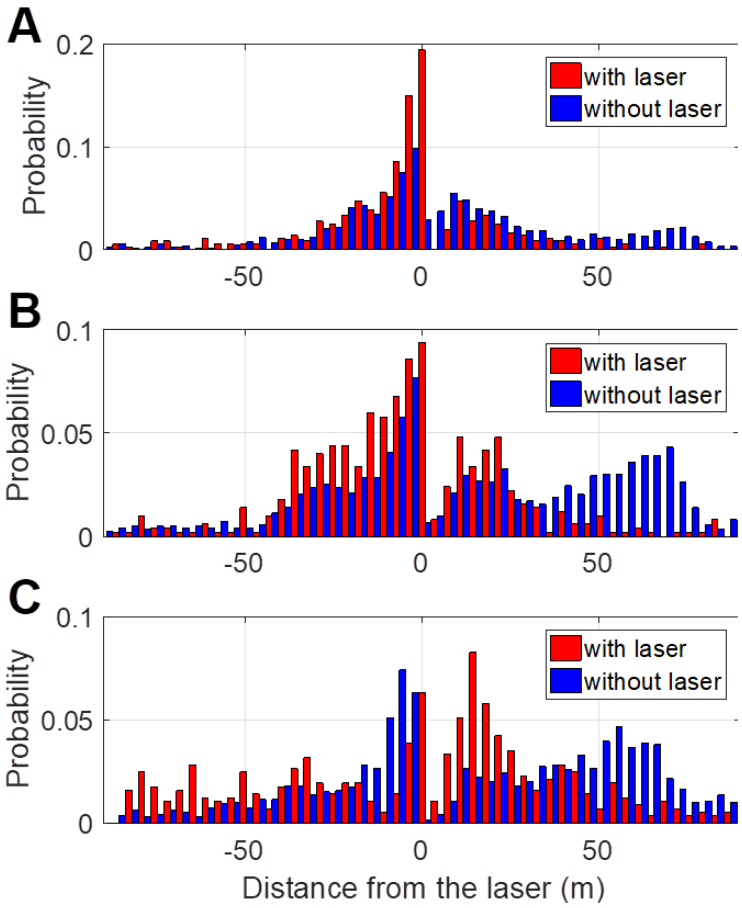

Figure 4.3.2: Cumulative histograms of VHF sources distance to the laser beam as per height slice of 30 m for all the events with and without laser. (A), (B) and (C) corresponding respectively to the height slices 0-30 m, 30-60 m and 60-90 m.

To assess more quantitatively the laser guiding effect, we calculate the distribution of the nearest distance from the VHF sources to the laser path for all recorded flashes. These distributions are calculated for three different heights above the tower (0 to 30 m, 30 to 60 m and 60 to 90 m), to attest over which scale the laser have a guiding effect. We then compare the distributions coming from flashes where the laser was active from those without the laser. The results are presented in figure 4.3.2. We observe narrower distributions in the presence of laser for both distances 0-30 m and 30-60 m above the tower, while no major differences are observed over the distance 60-90 m.

Elevation range	Laser status	Mean distance (m)	Standard deviation (m)
00-30	OFF	28.03	23.86
	ON	17.46	18.24
30-60	OFF	35.64	24.31
	ON	21.93	18.48
60-90	OFF	35.89	24.94
	ON	32.68	24.22

Table 4.3.1: Mean value and standard deviation of the distribution of the distance from the VHF sources to the laser path for all the events with and without laser, for the three height slice 0-30 m, 30-60 m and 60-90 m.

As shown in table 4.3.1, for the elevation range 0-30 m above the tower, the means distance from the VHF sources to the laser path is of 28.03 m without laser and 17.46 m with laser. For the elevation range 30-60 m, the means distance is of 35.64 m without laser and 21.93 m with laser. One should note that the average distances being smaller for both cases with and without laser when comparing the two elevation range is normal and due to the tower tip attraction being more important in the few meters above it. For both elevation ranges, the mean distance is significantly smaller when the laser is active, suggesting a guiding effect. The reduction is in the same proportion range with a decrease of 37.7% and of 38.5% for the elevation ranges 0-30 m and 30-60 m, respectively, suggesting a homogeneous guiding effect. A similar conclusion can be deduced by looking at the standard deviation of the distributions. For the elevation range 0-30 m the standard deviation is of 23.86 m without laser and 18.24 m with laser, while for the range 30-60 the values are respectively of 24.31 and 18.24 m. We can thus conclude that a guiding effect is observed over 60 m above the tower tip.

On the other hand, the means distance for the range 60-90 m is of 35.89 m without laser and 32.68 with laser, while the standard deviation is 24.94 m and 24.22 m, respectively. For this elevation range the difference of the mean distance is less significant (decrease of 8.9 %) and the standard deviations are similar for both cases, leading us to the conclusion that no guiding effect is observed over the distance 60-90 m.

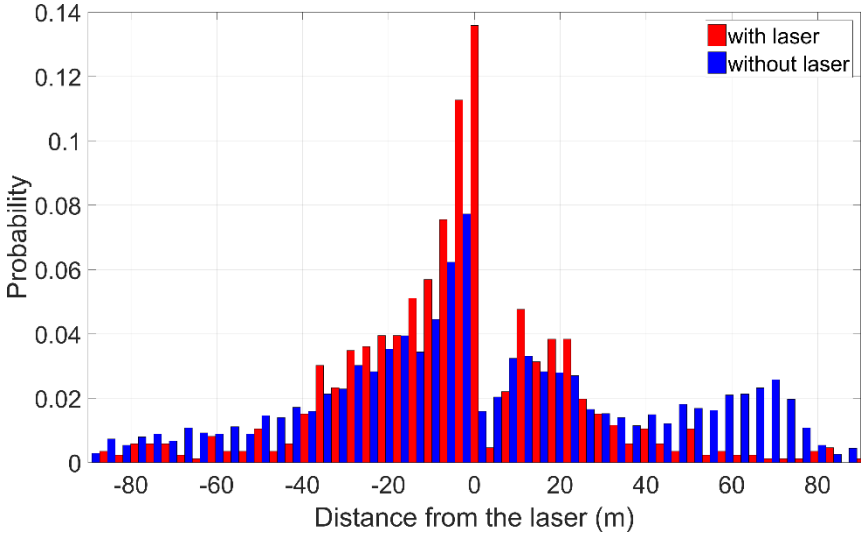

Figure 4.3.3: Distributions of the nearest distance from the VHF sources to the laser path for flashes with laser, and flashes without laser. The value of the mean absolute distance is presented for both with and without laser.

Figure 4.3.3 shows the distributions calculated over 60 meters above the tower (corresponding to the zone of interest of Figure 3.5). The mean distance from the VHF sources to the laser path is of 0.8393° without laser and 0.5573° with laser, corresponding to 20.06 m and 31.66 m, respectively. This decrease of 37 % of the mean distance with laser supports the assertion that the lightning leader propagates over the first 60 m along the path of the laser beam when the laser is on. If we look at the standard deviation over these distributions, we have a value of 18.51 m with laser and 24.37 without laser. The smaller standard deviation when the laser is active is again a proof of the more narrow propagation of the leader, supporting the guiding effect of the laser.

By looking at these observations made with the interferometer data and adding the observation coming from the high-speed camera presented in the previous section, it is clear that the laser has a guiding effect on the lightning propagation. The total length over which the effect is present may vary from one event to another, but will nonetheless stay in the range of ~60 m. It is interesting to note that this distance is in the ranges of guiding distance that we could have expected based on the previous experiments (as described in section 1 of this chapter).

4.4 X ray measurements

Current, electric field and X-rays were recorded for the 3 events with laser L1, L2 and L3.

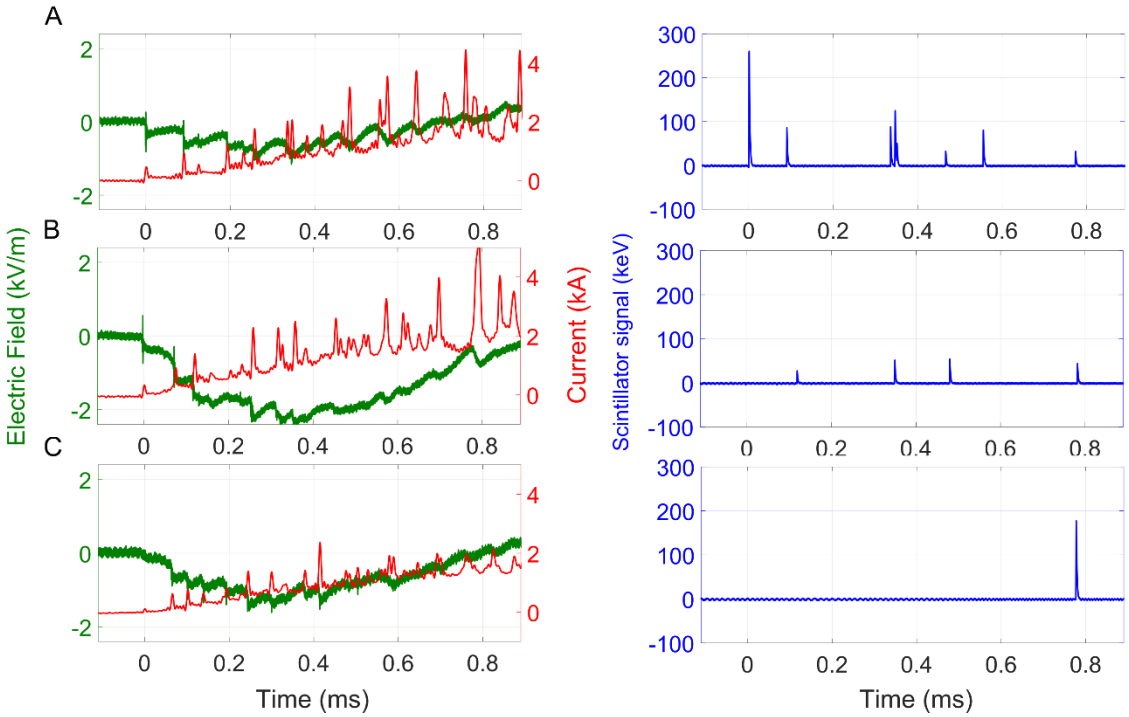

Figure 4.4.1: Electric signals measured for the 3 positive upward flashes L1 (A), L3 (B) and N6 (C). Top subplot for each event: The electric field scale is given on the left y-axis and the current on the right y-axis. Bottom subplot: X-ray signal detected by the Scintillator, where each peak corresponds to the integrated x-rays energy collected during the 50 ns sampling.

Figure 4.4.1 presents the plots of these measurements for the events L1, L3 and N6, an event without laser. Because the characteristic of a lightning event depends a lot on its polarity, only events of same polarity could be compared. And all the events with laser being positive, only positive events will be discussed here. For the events with laser L1, L2 and L3, 7, 2 and 4 x-ray bursts were observed, respectively. In the event without laser N6, only one x-ray burst was observed. Two other positive upward events recorded in 2021 prior to the laser installation show the same number of x-rays.

Both events with and without laser exhibit similar current and electric field waveforms in terms of amplitudes and step intervals. However, the number of X-rays bursts was much higher in the presence of the laser beam, with a mean value of 4.3 per event with laser and only of 1 per event without. The X-rays bursts energy levels were similar in both of these two categories.

Based on our observations alone, it is yet however impossible to discern between two cases: one being that the total number of x-rays is increased; the other being that the number of x-rays emitted in the direction of our detector is increased while the total number stays the same (in this case, it is important to note that the solid angle of our x-ray detector is nearly centered around the laser path).

The emission of x-ray being closely related to the stepping happening during the laser propagation, thus its propagation, a difference in their number is another proof that the laser affects the propagation of the leader.

4.5 Laser incidence on the number of flashes

The occurrence statistics of upward flashes at the Säntis Tower has a strong seasonal variation [34], as show in Figure 4.5.1 where the monthly distribution of the number of flashes recorded at the

Säntis tower from May 2009 to August 2019 is presented. Typically, the peak months are July and August with an average of about 12.5 events during July and about 15.6 events during August. The laser was running for 10 days in July and for the complete month of August. During this period, only 16 events were recorded, again suggesting that there was no significant increase of the number of events due to the presence of the laser for certain periods during these months. However, this does not mean that the laser was not responsible for the initiation of lightning.

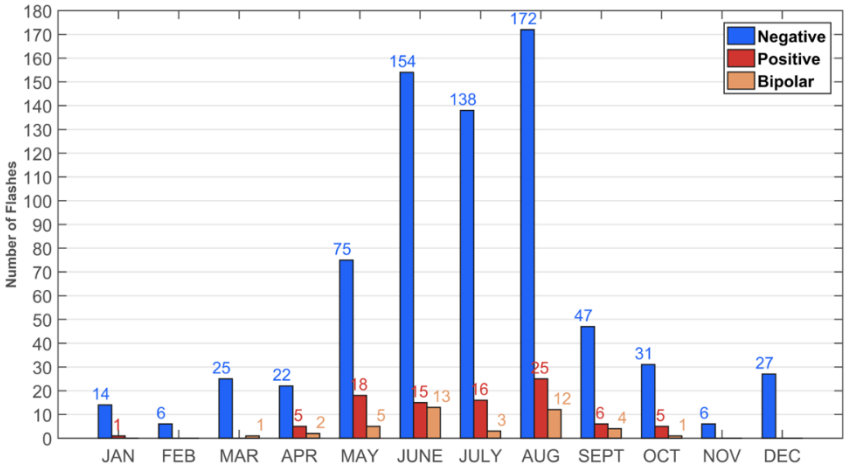

Figure 4.5.1: Monthly variations of the number of upward flashes from the Säntis Tower.

There are several explanations why the presence of the laser beam did not result in a significant increase in the number of flashes. The most obvious reason is the short operational time of the laser due to the problems we faced (laser failures, electric power shutdowns, restrictions due to air traffic etc.). Moreover, the tower itself is already attracting more than 100 flashes per year, so it is possible that the additional effect of the laser is too minor compared to the attracting effect of the mountain and the tower.

However, the most intriguing fact is that all four recorded events with laser were positive. By contrast, of all the flashes recorded from May 2009 to August 2019, 84% are negative flashes, 11% are positive flashes, and 5% are bipolar flashes. This raises the question whether the influence of the laser might be stronger at facilitating the initiation of upward positive flashes, leading to a higher prevalence of this polarity compared to the others during laser operating time.

4.6 Model simulation of the effect of the filamentation on the lightning flashes initiation

In order to understand more the effect of the laser on the initiation of upward lightning and especially distinguish the incidence it has on the lightning polarity, simulations were performed by professor Vernon Cooray of Uppsala University, Sweden. The goal of the simulation is to understand the circumstances under which the conducting plasma channel created by the laser filamentation could trigger a lightning flash from the Säntis tower.

It is important to note that both the under-dense channel left by the filaments and the plasma channel contribute to the guiding/triggering of a lightening. However, the under-dense channel affect both the electron and the ions in the same way by forming a preferential path for the discharge propagation where the mean free paths of the charges. As a consequence, it does not promote leaders of a specific polarity over another On the other hand, the modeling described here was developed to understand the overrepresentation of positive lightning events while using the laser despite their usual rarity. This bias in the leader polarity is explained by the effect of the conductive plasma as described in the modeling. One could add the effect of the hot air column to the model, but it would only add an offset to all value of breakdown voltage. For the sake of simplicity, the model only focused on the contribution of the conductive plasma.

First, it is important to point out that if the background electric field is large enough, the tower alone can initiate a lightning flash without the presence of the laser beam. To initiate a leader, the local electric field at the tip of the tower must exceed 3 x 10^6 V/m. In the case of the Säntis tower, this value has to be multiplied by a factor 0.75 to take into account the low atmospheric pressure at 2500 m height [35]. Thus, to have an effect on the lightning initiation the laser filament should be able to initiate a leader when the electric field at the top of the tower is below this above threshold.

The initiation of a lightning flash from an object takes place in two stages. First, a streamer burst is initiated from the object. The streamers will travel to a distance where the electric field goes below a threshold field necessary for streamer propagation. This threshold depends on the sign of the streamer and on the ambient pressure. If the charge associated with the streamers is larger than 1 μC, then the stem of the streamers will be converted into a leader. Leaders can propagate in fields much lower than the threshold necessary for streamer propagation, and can thus propagate over greater distance. These steps appear in the simulation as follow:

- For a given background electric field, the spatial variation of the local field that depends on the geometry of the different elements (in our case, the tower tip and the plasma channel) is calculated using the charge simulation method.
- Then, the growth of electron avalanches in the high electric field region where the electric field exceeds the breakdown electric field is studied.
- If the number of positive ions at the electron avalanche head exceeds the critical value 10^8, the avalanche is assumed to be converted to a streamer discharge.
- Once a streamer is initiated, its propagation distance into the gap is estimated using critical electric fields necessary for streamer propagation. For the propagation of positive streamers, a background electric field of about 500 kV/m is required at atmospheric pressure and, for negative streamers, the required field is higher, about 1.5 MV/m. Both these values have to be multiplied by a factor of about 0.75 to take into account the low atmospheric pressure at the Säntis tower. Once streamers are initiated, they extend in the gap to a distance where the average electric field along the length of the streamer region is equal to the critical electric fields mentioned above.
- Knowing the extension of the streamers in the gap, the charge associated with it is estimated following the procedure used by Becerra and Cooray. If the charge in the streamers is larger than 1 μC, the streamers will give rise to a leader discharge. Leaders can propagate in fields much lower than the threshold necessary for streamer propagation and thus over greater distance.

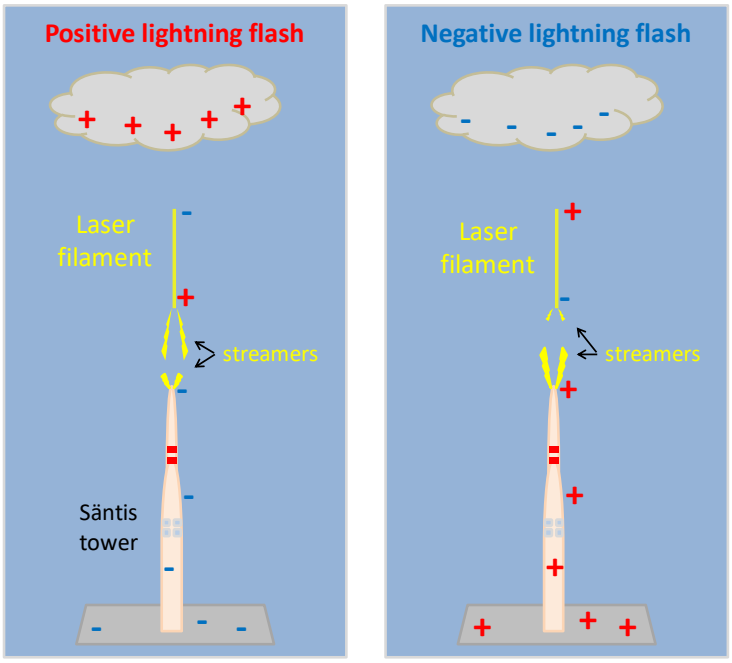

Figure 4.6.1: Geometry of the simulation. The laser filament is assumed to be located vertically and directly above the tower tip.

For the specific case of our experiment, two elements are taken into account in the geometry: the tower tip of the Säntis tower with a radius of curvature of 1 m and, located above it at a distance D, the bottom tip of the plasma channel with a radius of 1 cm and a total length L. The simulation will be repeated for several distances D and lengths L. The geometry and the different charges locations for negative and positive flashes are presented in Figure 4.6.1.

As a first approach, the plasma of the filament is considered fully polarized by the background electric field. As it will be discussed later, this approach does not truly represent the real behavior of the filament plasma, but will however be sufficient to get us a first understanding of the laser effect on lightning flashes of the two polarities.

Using the above-mentioned geometry and hypothesis, we evaluate the electric field distribution between the lower tip of a 10 m long filament plasma channel and the tower tip for different background electric fields and for two distance D between the two elements, 1 and 2 m.

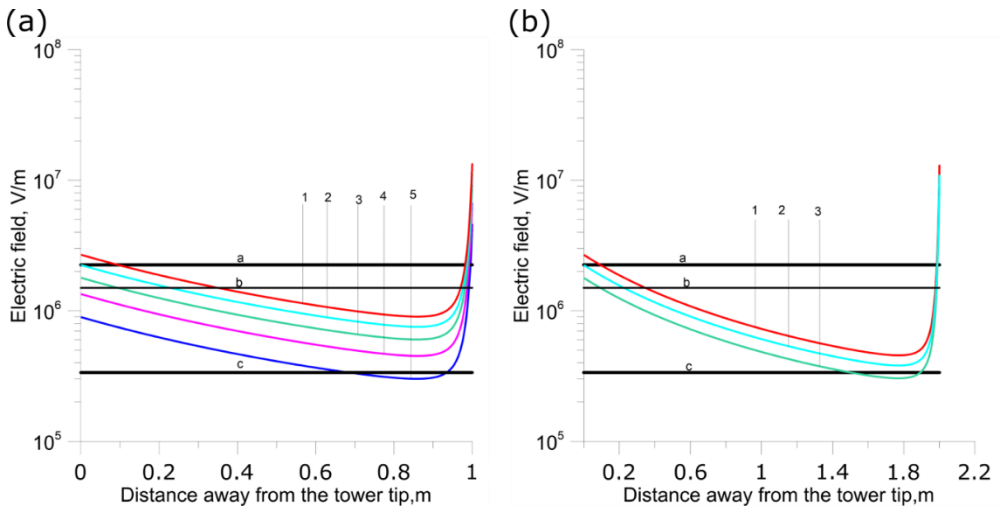

Figure 4.6.2: (a) Magnitude of the electric field between the lower tip of the laser beam and the tower tip, for a distance of 1 m between them, for different background fields: (1) 30 kV/m, (2) 25 kV/m, (3) 20 kV/m, (4) 15 kV/m and (5) 10 kV/m. (b) Magnitude of the electric field between the lower tip of the laser beam and the tower tip, for a distance of 2 m between them, for different background fields: (1) 30 kV/m, (2) 25 kV/m and (3) 20 kV/m. The curves marked a, b, c are respectively the breakdown electric field in air at the tower height, the threshold field necessary for negative streamer propagation and threshold field necessary for positive streamer propagation.

The results are shown in figure 4.6.2, along with the threshold electric field necessary for electrical breakdown of the tower tip itself, the threshold electric field necessary for negative streamer propagation and the threshold electric field necessary for positive streamer propagation.

The first observation is that for a background electric field below ±30 kV/m, the electric field at the tip of the tower is below the threshold electric field necessary for the initiation of a lightning flash by the tower. Thus, the chances that the tower itself will initiate a lightning flash under this condition are minimal.

The second observation is that in the case of the gap distance of 1 m, for all values of the background field between 15 to 30 kV/m, the electric field between the filament tip and the tower tip is larger than or equal to the threshold field for positive streamers. However, it is below the threshold for negative streamers. For a background electric field of 10 kV/m, the curve slightly drops below the threshold, but once streamers have been initiated and propagated some distance, they increase the electric field ahead of them and this effect may be able to lift up the field ahead of the streamers, making it possible for them to cross the gap. Thus, for background electric fields between 10 and 30 kV/m, breakdown is possible with positive streamers travelling from the lower filament tip to the tower tip. Such breakdowns will give rise to a positive ground flash. No negative flashes will be possible at these background electric fields. No breakdown can be initiated without laser filaments either. If the background electric field is increased beyond about 30 kV/m, negative streamers will also be able to breach the gap between the tip of the filament and the tower. However, at these fields, the tower itself is capable of initiating lightning flashes without the assistance of the laser beam.

Similar observation can be made for a gap distance of 2 m, the values of the electric field limits being slightly different.

A more detailed study of the incidence of the plasma channel length and of the gap length is done by repeating the simulation for the four channel lengths 10, 20, 30 and 40 m, and for gap lengths varying from 1 to 5 m.

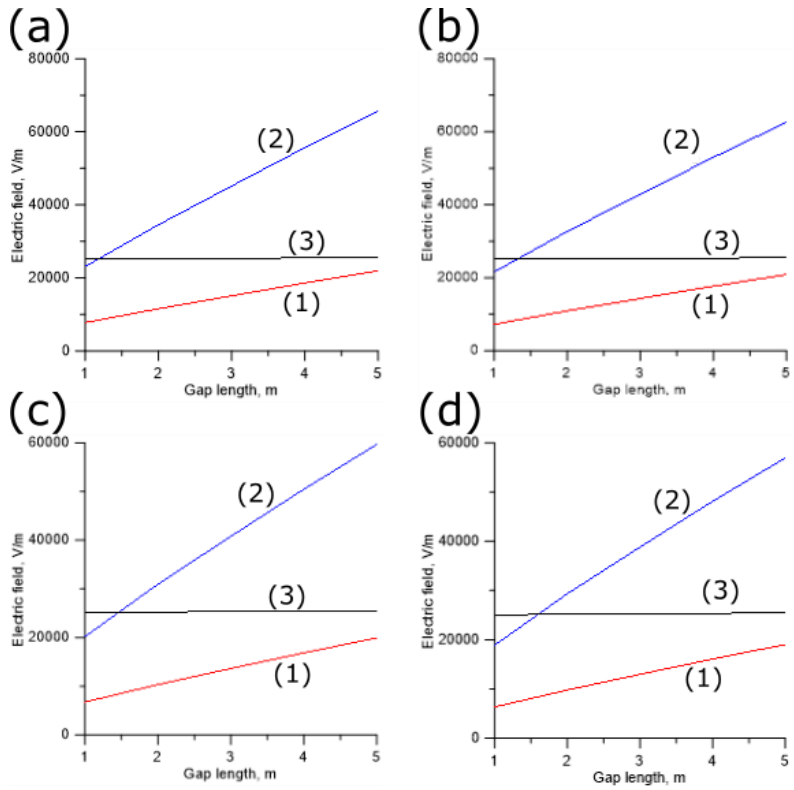

Figure 4.6.3: Magnitude of the background electric fields necessary to initiate (1) laser assisted positive lightning flashes and (2) laser assisted negative lightning flashes and as a function of the gap length between the lower tip of the laser filament and the tower tip. The curve marked (3) depicts the magnitude of the background electric field necessary for the tower to initiate a negative lightning flash without the assistance of the laser filament. The lengths of the laser filaments used in the calculation are (a) 10 m, (b) 20 m, (c) 30 m and (d) 40 m. Note that the polarity of the background electric field necessary to initiate a positive lightning flash is opposite to the background electric field necessary to initiate a negative lightning flash.

The results are presented in figure 4.6.3. The first observation is that, for all tested gap length and channel length, the background electric field necessary for the generation of a laser assisted positive lightning flash is always below the background electric field necessary for the tower to initiate flashes without the assistance of the laser filament. The maximum gap lengths where the laser can influence the initiation of positive flashes are 6, 6.5, 7 and 7.5 m for filament length of 10, 20, 30 and 40 m. With the experimental setup used during our experiments, the distance between the tower and the start of filament is in the right interval. Therefore, the laser filament can help the initiation of positive flashes.

The second observation is that, apart from short gap length (this limit, of 0.3 m and 1.2 m for a plasma length of respectively 10 m and 40 m, is more lenient for longer plasma channel), the background electric field necessary for the generation of a laser assisted negative lightning flash is always greater than the background electric field necessary for the tower to initiate flashes without the assistance of the laser filament. The laser will thus have no influence on the initiation of negative flashes.

By looking at the simulation results, we see that the laser will promote the apparition of positive flashes and not of negative ones, and putting into perspective the results of the previous section showing that all events will laser were positive (although those positive flashes are usually the least probable outcome at the Säntis tower), a clear indication that the laser has also an effect over the initiation of lightning flash appears.

4.7 Discussion about the wind speed effect

4.7.1 Discussion of the wind effect on the event N08

One aspect that is still not discussed and could affect the filament effect is the impact on the wind speed on the observations.

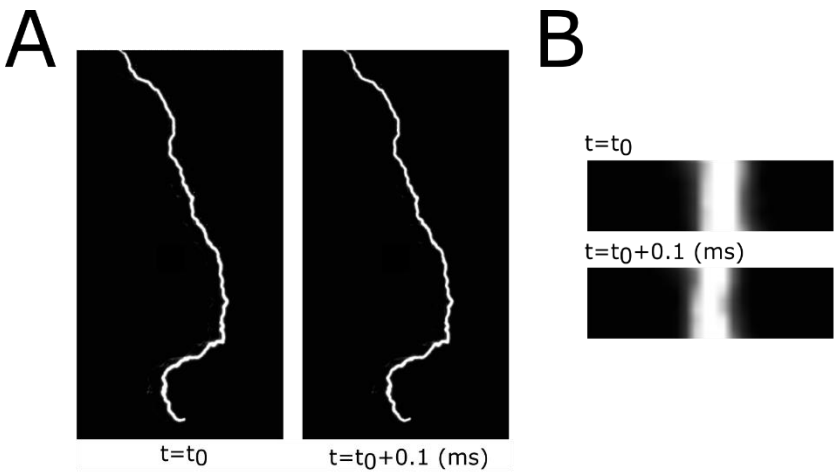

Figure 4.7.1.1: Consecutive frames recorded by the high-speed camera located at Schwagalp for the event N08, separated by 1 ms. (a) Full frames. (b) zoom on a part of the frames to highlight the movement of the leader path.

Figure 4.7.1.1 presents two consecutive frames of the event N08 recording by the high-speed camera located at Schwagalp. The camera working at 10 000 frame/s, the delay between the two frames is 0.1 ms. By looking at the slight displacement of the lightning channel between the two frames, highlighted in figure 4.7.1.1 (b), we can measure the displacement speed. The obtained value is of 5.4 m/s. Furthermore, by taking into account the position of the camera, we know that the direction of the displacement is north east (note that the camera can only distinguish between the north east and the south west directions).

Using the meteorological data obtained from the Federal Office of Meteorology and Climatology, MeteoSwiss, we have access to the characteristic of the wind at the time of the vent N08, with a time resolution of 10 min. The values are as follows:

- Angle of the direction of the wind: 239° from the angle of view the interferometer looking at the Santis tower (and angle of 0° being on the axis between the interferometer location and the Säntis tower). This angle roughly translates in the north direction.
- Peak speed: 10.3 m/s.
- Mean speed: 4.9 m/s.

The speed of the wind and the speed of the displacement are similar in value and direction, thus we can make the hypothesis that the wind affects the channel of the lightning and should affect the laser filament too.

4.7.2 Discussion of the wind effect on the event N06

Of all the recorded events, the event N06 is one of the most particular, being the only positive event without laser. An important fact regarding this event is that the laser was stopped just before the flash happened due to a sudden accumulation of hail on the telescope mirrors. This delay was not measured but was short. As the laser operator at this specific moment, I roughly estimate it to be a few tens of seconds.

Using the meteorological data obtained from MeteoSwiss, the wind characteristic at the time of the vent N0 were as follows:

- Angle of the direction of the wind: 254° from the angle of view the interferometer looking at the Santis tower. This angle roughly translates in the north direction.
- Peak speed: 23.3 m/s.
- Mean speed: 14.5 m/s.

Using the mean value of 14.5 m/s and projecting on the interferometer measurement axis, we have a speed of visible displacement that could be seen on the interferometer of 14 m/s (not that the direction of this displacement will be in the direction of the negative value of the used x axis of the following figure 4.7.2.1).

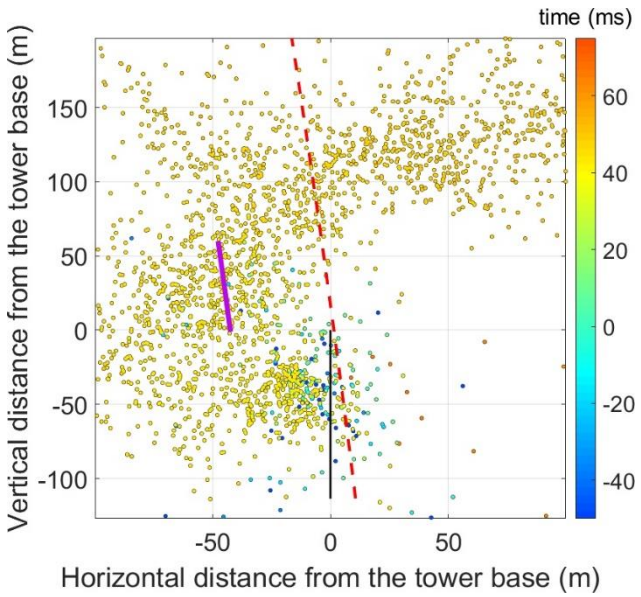

Figure 4.7.2.1: 2D maps of the VHF sources emitted during the lightning event N06. The Säntis tower is represented on each plot as a black line, the laser path is represented as a red dotted line. Each point corresponds to a VHF emission. The delay between the VHF source and the initiation of the current on the tower is shown by the color code displayed on the right. The violet line shows the region where the channel resulting from the laser filamentation would be located after the wind moved it during 3 s.

In figure 4.7.2.1 is presented the interferometer measurement of the event N06 showing the lighting propagation, along with the example of the position where a conductive channel created by the filament 3 s after its creation would be, position calculated from the wind speed data at the time of this event.

Even if the laser was stopped just before the lightning flash, lingering effects of the filamentation, as described in previous chapters, could still affect it on the timescale of several seconds. Moreover, these lingering effects, as shown with the example in the figure 4.7.2.1, would be moved right where the leader path was being recorded (note that the figure only shows the contribution of one laser pulse whereas in reality all the numerous pulses happening every ms should be taken into account).

Another point suggesting the laser contribution is that this hypothesis would explain the curved trajectory of the event compared to the other events (see figure 4.3.1). The other laser events being mostly affected by the continuous train of pulses creating conductive channels over the tower, the leader propagation moves relatively straight up. On the other hand, the event N06 could only be affected by the lingering effects of the laser pulses, the laser being stopped at the moment of the flash.

This lingering effect being moved away from the tower by the wind, it would facilitate the propagation of the leader in a non-straight path, as it is indeed recorded by our measurement.

Moreover, the positive polarity of this event could corroborate a possible inception effect of the laser on it.

All these observations strongly suggest that this event was affected by the laser several seconds after it was stopped. This effect, that would need further experiments to be confirmed, could play a key role on the usability of the laser as a lightning rod by removing the need of a precise synchronization between the laser pulse and the lighting flash that we want to affect.

5 Conclusion and outlook

During the Laser Lightning Rod experimental campaign, a 500 mJ, 1 ps, 1 kHz laser was installed at the top of the Säntis Mountain, and was pointed to the Säntis Tower to guide upward lightning flashes. The laser was active for more than 3 month, from the 21th of July until the 30th of September 2021, during which four positive upward flashes were recorded in the presence of the laser.

Based on the measurements of high-speed cameras, a lightning tracking interferometer system, electric field sensors, current sensors and X-rays sensors, we answered two important questions: Is the laser able to guide lightning flashes, and is it able to initiate these flashes?

As it was presented in this chapter, a guiding distance of 60 m was observed. The laser is thus capable of guiding lightning flashes. No strong evidence of laser triggered lightning were observed, however, the polarity of all flashes during laser activity being positive seems to point toward a possible triggering effect.

The Laser Lightning Rod experiment could thus be considered a success. Obviously, more data would be necessary to complete the experiment and characterize the laser effect on lightning propagation, but a great step in the right direction was achieved during this campaign. In future experiments, the exploration of different laser settings (such as the use of the frequency doubled or tripled beam) and setup geometry (such as trying to guide lightning in a homogeneous electric field with no tall building like the tower) would be the next recommended steps.

Bibliography

[1] R. L. Holle, « The Number of Documented Global Lightning Fatalities », San Diego, California, 2016, p. 4.

[2] M. A. Uman, *The Art and Science of Lightning Protection*, 1re éd. Cambridge University Press, 2008. doi: 10.1017/CBO9780511585890.

[3] M. W. Jernegan, « Benjamin Franklin's "Electrical Kite" and Lightning Rod », *N. Engl. Q.*, vol. 1, nº 2, p. 180, avr. 1928, doi: 10.2307/359764.

[4] Ė. M. Bazelian, J. P. Rajzer, et E. M. Bazeljan, *Lightning physics and lightning protection*. Bristol: Inst. of Physics Publ, 2000.

[5] J. C. Willett, D. A. Davis, et P. Laroche, « An experimental study of positive leaders initiating rocket-triggered lightning », *Atmospheric Res.*, vol. 51, nº 3-4, p. 189-219, juill. 1999, doi: 10.1016/S0169-8095(99)00008-3.

[6] M. M. Newman, J. R. Stahmann, J. D. Robb, E. A. Lewis, S. G. Martin, et S. V. Zinn, « Triggered lightning strokes at very close range », *J. Geophys. Res. 1896-1977*, vol. 72, nº 18, p. 4761-4764, 1967, doi: 10.1029/JZ072i018p04761.

[7] P. Hubert, P. Laroche, A. Eybert-Berard, et L. Barret, « Triggered lightning in New Mexico », *J. Geophys. Res. Atmospheres*, vol. 89, nº D2, p. 2511-2521, 1984, doi: 10.1029/JD089iD02p02511.

[8] D. W. Koopman et T. D. Wilkerson, « Channeling of an Ionizing Electrical Streamer by a Laser Beam », *J. Appl. Phys.*, vol. 42, nº 5, p. 1883-1886, avr. 1971, doi: 10.1063/1.1660462.

[9] M. Miki, Y. Aihara, et T. Shindo, « Development of long gap discharges guided by a pulsed CO2 laser », *J. Phys. Appl. Phys.*, vol. 26, nº 8, p. 1244-1252, août 1993, doi: 10.1088/0022-3727/26/8/014.

[10] S. Uchida *et al.*, « Laser-triggered lightning in field experiments », *J. Opt. Technol.*, vol. 66, nº 3, p. 199, mars 1999, doi: 10.1364/JOT.66.000199.

[11] V. A. Rakov et M. A. Uman, *Lightning: physics and effects*. Cambridge: Cambridge University Press, 2007.

[12] V. V. Apollonov *et al.*, « Electric-discharge guiding by a continuous spark by focusing CO2-laser radiation with a conic mirror », *Quantum Electron.*, vol. 32, nº 2, p. 115, févr. 2002, doi: 10.1070/QE2002v032n02ABEH002140.

[13] E. M. Bazelyan et Y. P. Raĭzer, « The mechanism of lightning attraction and the problem of lightning initiation by lasers », *Phys.-Uspekhi*, vol. 43, nº 7, p. 701-716, juill. 2000, doi: 10.1070/PU2000v043n07ABEH000768.

[14] A. Braun, G. Korn, X. Liu, D. Du, J. Squier, et G. Mourou, « Self-channeling of high-peak-power femtosecond laser pulses in air », *Opt. Lett.*, vol. 20, nº 1, p. 73-75, janv. 1995, doi: 10.1364/OL.20.000073.

[15] S. Tzortzakis *et al.*, « Nonlinear propagation of subpicosecond ultraviolet laser pulses in air », *Opt. Lett.*, vol. 25, nº 17, p. 1270, sept. 2000, doi: 10.1364/OL.25.001270.

[16] D. Comtois *et al.*, « Triggering and guiding leader discharges using a plasma channel created by an ultrashort laser pulse », *Appl. Phys. Lett.*, vol. 76, nº 7, p. 819-821, févr. 2000, doi: 10.1063/1.125595.

[17] M. Rodriguez *et al.*, « Triggering and guiding megavolt discharges by use of laser-induced ionized filaments », *Opt. Lett.*, vol. 27, nº 9, p. 772-774, mai 2002, doi: 10.1364/OL.27.000772.

[18] B. Forestier *et al.*, « Triggering, guiding and deviation of long air spark discharges with femtosecond laser filament », *AIP Adv.*, vol. 2, nº 1, p. 012151, mars 2012, doi: 10.1063/1.3690961.

[19] J. Kasparian *et al.*, « Electric events synchronized with laser filaments in thunderclouds », *Opt. Express*, vol. 16, nº 8, p. 5757-5763, avr. 2008, doi: 10.1364/OE.16.005757.

[20] X. M. Zhao, J.-C. Diels, C. Y. Wang, et J. M. Elizondo, « Femtosecond ultraviolet laser pulse induced lightning discharges in gases », *IEEE J. Quantum Electron.*, vol. 31, n° 3, p. 599-612, mars 1995, doi: 10.1109/3.364418.

[21] G. Méjean *et al.*, « Improved laser triggering and guiding of meqavolt discharges with dual fs-ns pulses », *Appl. Phys. Lett.*, vol. 88, n° 2, p. 021101, janv. 2006, doi: 10.1063/1.2162430.

[22] M. N. Shneider, A. M. Zheltikov, et R. B. Miles, « Tailoring the air plasma with a double laser pulse », *Phys. Plasmas*, vol. 18, n° 6, p. 063509, juin 2011, doi: 10.1063/1.3601764.

[23] Y.-H. Cheng, J. K. Wahlstrand, N. Jhajj, et H. M. Milchberg, « The effect of long timescale gas dynamics on femtosecond filamentation », *Opt. Express*, vol. 21, n° 4, p. 4740, févr. 2013, doi: 10.1364/OE.21.004740.

[24] G. Point, C. Milián, A. Couairon, A. Mysyrowicz, et A. Houard, « Generation of long-lived underdense channels using femtosecond filamentation in air », *J. Phys. B At. Mol. Opt. Phys.*, vol. 48, n° 9, p. 094009, mai 2015, doi: 10.1088/0953-4075/48/9/094009.

[25] G. Point, E. Thouin, A. Mysyrowicz, et A. Houard, « Energy deposition from focused terawatt laser pulses in air undergoing multifilamentation », *Opt. Express*, vol. 24, n° 6, p. 6271-6282, mars 2016, doi: 10.1364/OE.24.006271.

[26] S. Tzortzakis, B. Prade, M. Franco, A. Mysyrowicz, S. Hüller, et P. Mora, « Femtosecond laser-guided electric discharge in air », *Phys. Rev. E*, vol. 64, n° 5, p. 057401, oct. 2001, doi: 10.1103/PhysRevE.64.057401.

[27] P. Walch, B. Mahieu, L. Arantchouk, Y.-B. André, A. Mysyrowicz, et A. Houard, « Cumulative air density depletion during high repetition rate filamentation of femtosecond laser pulses: Application to electric discharge triggering », *Appl. Phys. Lett.*, vol. 119, n° 26, p. 264101, déc. 2021, doi: 10.1063/5.0077635.

[28] J. K. Wahlstrand, N. Jhajj, et H. M. Milchberg, « Controlling femtosecond filament propagation using externally driven gas motion », *Opt. Lett.*, vol. 44, n° 2, p. 199, janv. 2019, doi: 10.1364/OL.44.000199.

[29] T. Produit *et al.*, « The laser lightning rod project », *Eur. Phys. J. Appl. Phys.*, vol. 93, n° 1, Art. n° 1, janv. 2021, doi: 10.1051/epjap/2020200243.

[30] M. G. Stock *et al.*, « Continuous broadband digital interferometry of lightning using a generalized cross-correlation algorithm », *J. Geophys. Res. Atmospheres*, vol. 119, n° 6, p. 3134-3165, mars 2014, doi: 10.1002/2013JD020217.

[31] A. Sunjerga *et al.*, « LMA observations of upward lightning flashes at the Säntis Tower initiated by nearby lightning activity », *Electr. Power Syst. Res.*, vol. 181, p. 106067, avr. 2020, doi: 10.1016/j.epsr.2019.106067.

[32] Y. Pu *et al.*, « Upward negative leaders in positive triggered lightning: Stepping and branching in the initial stage: Triggered Upward Negative Leaders », *Geophys. Res. Lett.*, vol. 44, n° 13, p. 7029-7035, juill. 2017, doi: 10.1002/2017GL074228.

[33] M. M. F. Saba, C. Schumann, T. A. Warner, J. H. Helsdon, et R. E. Orville, « High-speed video and electric field observation of a negative upward leader connecting a downward positive leader in a positive cloud-to-ground flash », *Electr. Power Syst. Res.*, vol. 118, p. 89-92, janv. 2015, doi: 10.1016/j.epsr.2014.06.002.

[34] C. Romero, F. Rachidi, M. Rubinstein, et M. Paolone, « Lightning currents measured on the Säntis Tower: A summary of the results obtained in 2010 and 2011 », in *2013 IEEE International Symposium on Electromagnetic Compatibility*, Denver, CO, USA, août 2013, p. 825-828. doi: 10.1109/ISEMC.2013.6670524.

[35] V. Cooray, « Mechanism of electrical discharges », in *The Lightning Flash*, V. Cooray, Éd. Institution of Engineering and Technology, 2014, p. 41-117. doi: 10.1049/PBPO069E_ch3.

General conclusion

This thesis was dedicated to the study of high repetition rate laser filamentation and its application for the development of a laser lightning rod.

I studied the influence of the laser repetition rate on filamentation and the subsequently created under-dense channel. I observed the apparition of a cumulative effect for repetition rates higher than 100 Hz, due to the accumulation of heating by multiple pulses, this effect being amplified as the repetition rate increases. This cumulative effect results in a permanent under-dense channel larger and deeper than the ones created by a single filament. I developed a model describing the evolution of each under-dense channel and how they contribute together to the cumulative effect. The under-dense channel being responsible for the reduction of the breakdown voltage of a laser guided discharge, I simulated and measured how this cumulative effect induces a more efficient guiding at high repetition rate. To explain some discrepancies in the measurement, I investigated the importance of the gas composition and highlighted an enhancement of the guiding effect due to the accumulation of long-lived ions 0_2^-. To prepare for outdoor applications, I studied the ability of a transverse air flow to cancel weak cumulative effects, and the importance of the setup geometry, showing that the cumulative effect is much more important when the filaments are created vertically.

This cumulative effect could play an important role for all applications of the under-dense channel by increasing its efficiency and more importantly, by creating a permanent channel. This steady state effect would greatly enhance the range of possibilities of application such as the laser lightning rod, laser cloud clearing or laser generated optical air waveguide. Moreover, with the advancement of laser technology, laser systems with higher repetition rates and average power become available, leading to the creation of ever more important cumulative effect, which would need to be fully understood and controlled. As such, I would recommend for future studies to complete the work presented in this thesis by adding a study of the air chemistry in this high repetition rate regime and of the interaction between the consecutive under-dense channels, which have been neglected so far.

Another aspect of the repetition rate that I studied was consecutive laser guided discharges, in order to obtain a permanent conductive plasma column that could be used as a plasma antenna. To approach the goal of a steady state antenna, I first investigated how an additional electrical circuit injecting current into the discharge could increase its lifetime. This approach proved to be successful and increased the discharge lifetime by two order of magnitude, up to the ms timescale. I then studied the behaviour of consecutive guided discharges created at 10 Hz, and observed an interaction between them where an initial discharge lead to a perturbation preventing the guiding by the subsequent filament. I developed a model of the discharge thermal expansion describing this phenomenon, and proved that using an airflow could cancel this perturbation.

These two approaches are important steps toward the realisation of a continuous plasma antenna and the next steps are quite straightforward to conceptualize: increase the repetition rate of the guided discharges to 100 Hz and increase the lifetime of the discharge to more than tens of ms. However, this is a technical challenge due to the difficulty of setting up a charging system fast enough to load the high voltage generator that could initiate meter long guided discharges at 100 Hz.

The investigation on the superfilamentation regime was conducted to explain the discrepancies observed in the guiding efficiency of different filaments. This was especially important to me because the wide range of laser energies that I used during my thesis lead to the creation of different quality of plasma. I observed that strongly focusing a high-energy beam leads to an enhanced energy deposition and an under-dense channel more important than the one created by the regular filamentation regime. This enhanced under-dense channel results in a greater increase of the reduction of the air breakdown voltage.

This filamentation regime with an improved guiding efficiency are quite important for any application and, as it was observed during the first campaign of the Laser Lightning Rod project, only filaments created in a setup with a high beam focusing were observed to guide electrical discharges. Thus, it would be beneficial in the future to fully characterize the transition between the two filamentation regimes. Moreover, this effect leading to more important under-dense channels, it would be interesting to investigate how this filamentation regime affects the apparition of the cumulative effect.

Finally, the main work I conducted during my thesis was done during two experimental campaigns of the Laser Lightning Rod project. The first campaign was important to our project because we needed to confirm the possibility to use the J-range, 1 kHz repetition rate, laser system developed for this project to induce filamentation and guide electrical discharges at long distance. The observation of filament created at a distance of 115 m was of great interest as it was the distance used during the main lightning campaign. This work was especially important from a technical point of view, due to the difficult experimental conditions that we faced during this campaign. The various solutions considered to overcome them proved to be successful and could be useful for any outdoor laser application. This second campaign was a real scale experiment, aimed at guiding ascending lightnings from the top of a tower on Mount Säntis in Switzerland. By an analysis of the different data collected for the 16 lightning events recorded on the tower, I have shown that the ascending lightning precursor was guided by the laser over 60 m on 4 occurrences. Moreover, study of the polarity of the lightning flashes and of their X-rays emission also demonstrated an interaction of the filaments with the lightning.

These fascinating results are the first successful observations of a laser guided lightning and will be of utmost importance for the development of the laser lightning rod technology in the upcoming years. While improvement in the laser technology would surely be the most important aspect beneficial to this development, it would be wise to also investigate how parameters such as the laser wavelength, pulse duration, repetition rate or energy affect the proficiency of the filament to guide lightning. This would expand our still limited knowledge of the phenomenon, and would be useful to steer in the most efficient direction the development of specific laser systems.

ECOLE DOCTORALE

Titre : Etude de la filamentation d'impulsions laser à haute cadence pour le développement d'un paratonnerre laser

Mots clés : laser ultrabref, filamentation, optique non-linéaire, foudre, décharge, plasma

Résumé : Mes travaux de thèse ont porté sur l'étude de la filamentation laser à haute cadence pour le développement d'un paratonnerre laser. Quand une impulsion laser intense de durée femtoseconde se propage dans l'air, elle donne lieu à la filamentation, un processus spectaculaire où une partie de l'énergie du faisceau se contracte pour former un long canal dans lequel l'intensité est maintenue à ~10^{13} W/cm^2. Ce régime de propagation autoguidée s'accompagne par la formation d'une colonne de plasma qui va évoluer en un canal d'air chaud sous-dense capable de guider des décharges électriques.
Plus particulièrement, la filamentation à haute cadence (supérieure à 100 Hz) permet à chaque impulsion laser de créer un canal sous-dense alors que celui créé précédemment est toujours présent, résultant en un effet d'accumulation. Par une série d'expériences et par le développement d'un modèle théorique, j'ai démontré qu'utiliser un laser à haute cadence permettait de générer un canal sous-dense plus important et permanent, plus efficace pour guider les décharges électriques. Par ailleurs, je me suis intéressé au régime dit de superfilamentation, montrant l'apparition de filaments plus intenses ainsi que leur capacité à améliorer le guidage de décharges électriques.
Dans le but de développer une antenne plasma émettrice dans la gamme RF, j'ai aussi étudié le guidage à haute cadence de décharges électriques successives dans le but de réaliser une colonne de plasma rectiligne conductrice quasi-continue.
Dans le cadre du projet européen « Laser Lightning Rod » visant à développer un paratonnerre laser, j'ai participé à une campagne expérimentale de guidage de la foudre en grandeur nature réalisée au sommet du mont Säntis en Suisse avec le premier laser térawatt haute cadence. 16 éclairs ont été mesurés lors de cette campagne dont 4 en présence de filaments laser. En se basant sur la caractérisation de la propagation par interférométrie VHF ainsi que sur les vidéos prises par deux caméras ultra-rapides, nous avons ainsi démontré pour la première fois, un effet de guidage de la foudre par le laser sur une distance de 60 m. Une étude de la polarité des éclairs et de leur émission de rayons X a aussi mis en évidence un effet significatif lié à l'interaction de la foudre avec les filaments laser.

Title : Study of high repetition rate laser filamentation for the development of a laser lightning rod

Keywords : ultrashort laser, filamentation, nonlinear optics, lightning, discharge, plasma

Abstract : This thesis reports the study of high repetition rate laser filamentation for the development of a laser lightning rod. When an intense femtosecond laser pulse propagates in air, a spectacular process called filamentation occurs, where part of the beam contracts to form a long channel in which the laser intensity is maintained at ~10^{13} W/cm^2. This self-guided propagation regime creates a plasma column in the wake of the pulse and evolves in a long-lived under-dense air channel that can be used to guide electrical discharges.
Filamentation at high repetition rate (higher than 100 Hz) allows each laser pulse to create an under-dense channel, while the previously created one is still present, resulting in a cumulative effect. Through a series of experiments and the development of theoretical models, I show the apparition at high laser repetition rate of a more important and permanent under-dense channel, which is more efficient in guiding electrical discharges. I also studied the superfilamentation regime, showing the apparition of denser filaments that improve the guiding of electric discharges.
Aiming to maintain a permanent conductive plasma column that could be used as an emitting RF antenna, I have studied both experimentally and theoretically the guiding of successive electric discharges at high repetition rate.
As part of the European "Laser Lightning Rod" project, I was strongly involved in a real scale experimental campaign at the top of Mount Säntis in Switzerland aiming to guide lightning using the first terawatt high repetition rate laser. 16 lightning flashes were measured during this campaign including 4 in the presence of filaments. Based on the characterization of the propagation of these flashes by VHF interferometry and by two high-speed cameras, we demonstrated for the first time a guiding effect by the laser over a distance of 60 m. Study of the polarity of the lightning flashes and of their X-rays emission also demonstrated a significant effect due to the interaction of the filaments with lightning.

Institut Polytechnique de Paris
91120 Palaiseau, France